

**Characterization of Hysteresis in Magnetic Systems:  
A Preisach Approach**

by

Patricia Darlene Mitchler

A Thesis  
Submitted to the Faculty of Graduate Studies  
in Partial Fulfillment of the Requirements  
for the Degree of

DOCTOR OF PHILOSOPHY

Department of Physics and Astronomy  
University of Manitoba  
Winnipeg, Manitoba

© July, 2000



National Library  
of Canada

Acquisitions and  
Bibliographic Services

395 Wellington Street  
Ottawa ON K1A 0N4  
Canada

Bibliothèque nationale  
du Canada

Acquisitions et  
services bibliographiques

395, rue Wellington  
Ottawa ON K1A 0N4  
Canada

*Your file* *Votre référence*

*Our file* *Notre référence*

The author has granted a non-exclusive licence allowing the National Library of Canada to reproduce, loan, distribute or sell copies of this thesis in microform, paper or electronic formats.

The author retains ownership of the copyright in this thesis. Neither the thesis nor substantial extracts from it may be printed or otherwise reproduced without the author's permission.

L'auteur a accordé une licence non exclusive permettant à la Bibliothèque nationale du Canada de reproduire, prêter, distribuer ou vendre des copies de cette thèse sous la forme de microfiche/film, de reproduction sur papier ou sur format électronique.

L'auteur conserve la propriété du droit d'auteur qui protège cette thèse. Ni la thèse ni des extraits substantiels de celle-ci ne doivent être imprimés ou autrement reproduits sans son autorisation.

0-612-53071-X

Canada

**THE UNIVERSITY OF MANITOBA  
FACULTY OF GRADUATE STUDIES  
\*\*\*\*\*  
COPYRIGHT PERMISSION PAGE**

**Characterization of Hysteresis in Magnetic Systems:**

**A Preisach Approach**

**BY**

**Patricia Darlene Mitchler**

**A Thesis/Practicum submitted to the Faculty of Graduate Studies of The University**

**of Manitoba in partial fulfillment of the requirements of the degree**

**of**

**Doctor of Philosophy**

**PATRICIA DARLENE MITCHLER © 2000**

**Permission has been granted to the Library of The University of Manitoba to lend or sell copies of this thesis/practicum, to the National Library of Canada to microfilm this thesis/practicum and to lend or sell copies of the film, and to Dissertations Abstracts International to publish an abstract of this thesis/practicum.**

**The author reserves other publication rights, and neither this thesis/practicum nor extensive extracts from it may be printed or otherwise reproduced without the author's written permission.**

# Abstract

The phenomenon of hysteresis is perhaps the most widely recognized microscopic manifestation of magnetic ordering, and is the principal feature which is responsible for technologically-oriented applications of magnetic materials such as permanent magnets and recording media. Interest in a phenomenological model of hysteresis originally proposed by Preisach in 1935 has been renewed recently, particularly in engineering applications, such as the characterization of magnetic recording media and magnetostrictive materials. Thus, a rigorous assessment of the capabilities and limitations of the Preisach model for characterizing magnetic materials is of considerable importance from both fundamental and technological perspectives. The fundamental characteristics of hysteresis are discussed and a theoretical background for the processes involved in magnetic systems is established. A generalized version of the scalar Preisach model, which includes original contributions, is developed to extend the model's abilities to describe the effects of the structure of the initially demagnetized state, the presence and nature of interactions, the system's coercive field distribution, and especially, the effects of temperature and experimental wait time, on the observed hysteretic properties of a variety of magnetic systems including spin glasses, ferromagnets, ferrimagnets, and superparamagnets. The moment and remanence of magnetic systems are measured as a function of applied field and temperature, using both a vibrating sample magnetometer (VSM) and a SQUID-based magnetometer. A Preisach analysis of the data is used to characterize the irreversible response of six magnetic systems: CrO<sub>2</sub> audio tape;

magnetoferritin; a  $\text{Nd}_2\text{Fe}_{14}\text{B}$  permanent magnet; a floppy disk medium; and longitudinal and perpendicular cobalt-chromium-based hard disk materials. The ambiguous nature of tools presently used to analyze the nature of magnetic systems, such as the application of Henkel plots to the analysis of interaction effects, is demonstrated and alternative Preisach-based analysis schemes are presented. The physical significance of parameters, which emerged from the Preisach calculations, is discussed in detail and modifications are proposed to model this array of real magnetic systems. These changes to the scalar Preisach model extend its capabilities, while maintaining the inherent simplicity of a scalar model. Limitations of the model are also discussed critically, and suggestions for future generalizations are made.

# Acknowledgements

Special thanks to my thesis advisor Dr. R. M. Roshko, who first inspired me to study physics. His guidance, support, patience, and encouragement during the course of my research and throughout my undergraduate studies are deeply appreciated.

I also thank the advisory committee, Dr. A. H. Morrish, Dr. J. H. Page, and Dr. D. Thomson, for their time and suggestions throughout my graduate program, and Dr. C. Campbell, for acting as external examiner.

Thank you to Dr. P. W. Zetner for our many discussions and for his advice and encouragement during the completion of this thesis.

I extend my sincere appreciation to Wanda Klassen for her invaluable assistance in the preparation of this manuscript.

I acknowledge the financial support of NSERC, which provided fellowships and grants for this research, and I am grateful to the School of Physics and Astronomy, University of Minnesota, which made available the equipment used to gather the data presented in this thesis.

A special thank you to my sister, Mary-Ann, for her friendship and for providing me with transportation.

Finally, I express heartfelt gratitude to my parents, Dan and Stephanie Mitchler for their unwavering support, patience, and unconditional encouragement for all my academic endeavours, throughout my life. Thank you, Mom, for instilling in me a love of science. I am forever in your debt.

# Table of Contents

	<b>Page</b>
<b>Abstract</b>	iv
<b>Acknowledgements</b>	vi
<b>Chapter 1: An Overview of Hysteresis</b>	1
1.1 The Hysteresis Loop	1
1.2 Physical Origins of Hysteresis	2
1.3 The An hysteretic Curve	4
1.4 Technical Applications of Hysteresis	7
1.5 Modelling Hysteresis	9
1.6 Investigating Hysteresis Using the Preisach Approach	10
<b>Chapter 2: The Theoretical Basis of Hysteresis</b>	14
2.1 Magnetization	14
2.2 Magnetostatic Energy	15
2.3 Exchange Interaction	16
2.4 Magnetic Anisotropy	16
2.5 Domain Structure	18
2.6 Single Domain Particles	19
2.7 Mechanisms of Magnetization Reversal	20
2.7.1 Coherent Reversal: The Stoner-Wohlfarth Model	20
2.7.2 Incoherent Reversal Modes	27

2.7.3 Dipole-Dipole Interactions	30
2.7.4 Domain Wall Motion	34
2.7.5 Brown's Paradox	38
2.7.6 Becker's Model	40
2.8 Types of Magnetic Materials	45
2.8.1 Paramagnetism	45
2.8.2 Ferromagnetism	46
2.8.3 Ferrimagnetism	48
2.8.4 Superparamagnetism	50
2.8.5 Spin Glasses	53
<b>Chapter 3: The Preisach Model: Generalizing the Formalism</b>	<b>58</b>
3.1 Scalar Preisach Model	59
3.2 Moving Preisach Model	62
3.3 Preisach Plane	67
3.3.1 Using the Preisach Plane	69
3.3.2 The Demagnetized Plane	69
3.4 Henkel Plots	72
3.4.1 Wohlfarth Relation Derivation	73
3.4.2 The Lower Limit	74
3.4.3 Interpretation of Henkel Plots	78
3.4.4 Henkel Plots and the Random Thermally Demagnetized Plane	79

3.4.5 Compensated Henkel Plots	84
3.5 Thermal and Time Relaxation Effects	85
3.5.1 Generalized Preisach Model	85
3.5.2 Effects of Relaxation on Hysteresis Loops and on Henkel Plot Curvature	89
3.6 Reversibility in the Preisach Model	98
3.7 The Moving Coercive Field Distribution: The Preisach Model and Spin Glasses	99
<b>Chapter 4: Equipment, Experimental Protocols,     and Magnetic Systems</b>	112
4.1 Magnetic Measurement Equipment	112
4.1.1 SQUID Magnetometer	112
4.1.2 Vibrating Sample Magnetometer (VSM)	118
4.2 Experimental Protocols	125
4.2.1 Generating Magnetization Curves as a Function of Temperature	125
4.2.2 Demagnetization	126
4.2.3 Magnetization and Remanence Measurements: Generating a Henkel Plot	127
4.2.4 Magnetization as a Function of Time	128
4.3 Magnetic Systems	129
4.3.1 Chromium Dioxide Audio Tape	129

4.3.2 Magnetoferritin	132
4.3.3 Neodymium Iron Boron: A Permanent Magnet	136
4.3.4 Commercial Floppy Disk	138
4.3.5 Commercial Hard Disk: Cobalt Chromium-Based	139
4.3.6 Perpendicular Hard Disk: Cobalt Chromium	140

## **Chapter 5: A Preisach-based Analysis and Discussion**

### **of the Hysteretic Properties of Magnetic Systems** 142

5.1 Parameter Selection and Fitting	142
5.1.1 Initial Parameter Values	143
5.1.2 The Preisach Distribution	146
5.1.3 The Reversible Component	151
5.1.4 The "Fitting" Procedure	154
5.2 Commercial Floppy Disk	157
5.3 Commercial Cobalt-Chromium-Based Hard Disk	164
5.4 Perpendicular $\text{Co}_{80}\text{Cr}_{20}$ Hard Disk	168
5.5 Chromium Dioxide Audio Tape	175
5.5.1 General Features of the Magnetic Response	175
5.5.2 Analysis of AC Demagnetized Sample Data (25 °C ≤ T ≤ 120 °C)	177
5.5.3 Comparison of AC and Thermally Demagnetized Sample Data (25 °C ≤ T ≤ 120 °C)	189
5.5.4 Alternative Parameter Selection (25 °C ≤ T ≤ 120 °C)	196

5.5.5 Analysis of AC and Thermally Demagnetized Low Temperature Data ( $10\text{ K} \leq T \leq 300\text{ K}$ )	202
5.6 Magnetoferritin	216
5.6.1 General Features of the Magnetic Response	216
5.6.2 Analysis of Thermally Demagnetized Hysteresis Data	218
5.7 Neodymium Iron Boron	233
5.7.1 General Features of the Magnetic Response	233
5.7.2 Analysis of the Hysteresis Data: Modifying the Elementary Hysteresis Loop	233
<b>Chapter 6: A Critical Appraisal of the Preisach Approach</b>	247
<b>Appendix 1: Additional Data and Fits</b>	258
<b>Appendix 2: Fortran Programs for Preisach Calculations</b>	279
A2.1 Fortran Program for Preisach Calculations (General)	280
A2.2 Fortran Program for Preisach Calculations ( $\text{Nd}_2\text{Fe}_{14}\text{B}$ )	301
<b>References</b>	312

# Chapter 1

## An Overview of Hysteresis

The phenomenon of magnetic hysteresis refers to the observation that strongly exchange-coupled magnetic materials (ferromagnets (Section 2.8.2), antiferromagnets (Section 2.8.3), spin glasses (Section 2.8.5), etc.) exhibit a nonunique, *path dependent* response to a variable external field stimulus. Essentially, hysteresis originates from the presence of many local metastable minima in the free energy landscape of the system in configuration space. These minima trap the system in various metastable and often long-lived configurations, and prevent the system from exploring all of the local energy minima ergodically and, thus, from reaching thermal equilibrium within the time scale of the measurement.

### 1.1 The Hysteresis Loop

Magnetic hysteresis is a phenomenon exhibited by a variety of magnetic materials whereby the magnetic state depends not only on the applied magnetic field but also on

magnetic history, that is, on the previous state. Hysteretic behaviour is presented graphically as a hysteresis loop (Figure 1.1), where the component of the magnetization,  $M$ , along the direction of the applied field  $H_a$ , is plotted as a function of  $H_a$ . (The quantity measured experimentally is the total moment rather than the magnetization (Section 2.1).) For an initially unmagnetized material, the magnetization increases with field to saturation, thus defining the initial magnetizing curve. A saturation state is reached when the applied field is sufficiently large to ensure that the material possesses a uniform magnetization. For a hysteretic material, reducing the applied field to zero does not completely demagnetize the material and the residual magnetization is called the *remanence*. Following saturation, the residual magnetization is referred to as the *saturation remanence*,  $I_s$ . The reverse field required to demagnetize the material, is named the *coercive field* or *coercivity*,  $H_c$ . A zero remanence state, that is a demagnetized state in *zero* field, is achieved by recoiling to zero from a particular value of the field called the remanent coercivity,  $H_{cr}$  that is necessarily larger in magnitude than  $H_c$ . The loop in Figure 1.1 is completed by saturating the magnetization in the reverse direction and then reducing the applied field to zero, and finally, increasing the field until positive saturation is once again established. This cycle defines the major hysteresis loop. Minor loops can also be produced when the maximum applied field is insufficient to saturate the magnetization.

## 1.2 Physical Origins of Hysteresis

Hysteresis loops have many different forms and by analysing them, information on the basic physical mechanisms controlling the observed phenomenology can be

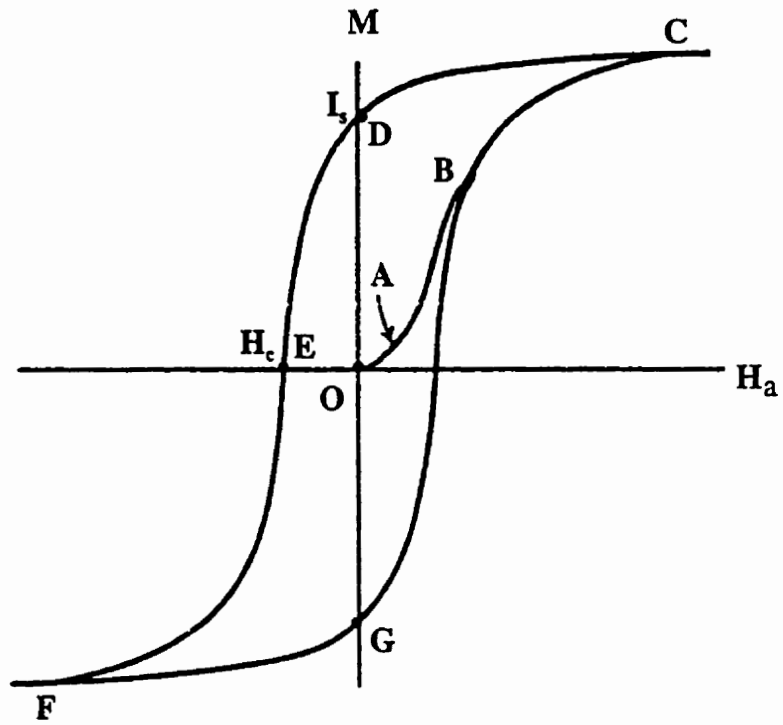


Figure 1.1 . An initial magnetization curve (OABC) and a hysteresis loop (CDEFGBC) of a typical ferromagnet (after Morrish, Fig. 7-1.1, 1965). O denotes the initially unmagnetized state, C and F denote the saturated states, D corresponds to the saturation remanence  $I_s$ , and E marks the coercive field  $H_c$ .

gained. Much of the understanding of hysteresis is due to Weiss (1907), who proposed the existence of the molecular field (Section 2.8.2) to account for spontaneous magnetization, and also proposed the existence of domains (Section 2.5) within magnetic materials, which have since been observed directly.

The variety of different forms observed in measured hysteresis loops are directly due to a number of factors that affect domain structure: exchange energy (Section 2.3), related to the molecular field, which favours uniform magnetization, magnetocrystalline anisotropy (Section 2.4), due to interactions with the lattice, which defines preferred directions in the lattice along which the magnetization can lie, the magnetostatic energy (Section 2.1), which prefers zero total moment or zero magnetization, on average, and the external field that establishes a preferred direction for the magnetization.

### 1.3 The Anhysteretic Curve

As a consequence of hysteresis, a given point of the field-magnetization plane can be reached in an infinite number of ways, depending on the field history. A complete description of the system is not given by the applied field,  $H_a$  and the magnetization,  $M$ . The state of the system is defined by its magnetic domain structure and, for a given point on the plane, the domain structure of the system depends on the history, which also determines how the magnetization will evolve with subsequent field variation.

As discussed, one of the hallmark characteristics of hysteresis in a material is the presence of a nonzero moment, or remanence, at zero applied field. However, the origin of the hysteretic plane ( $M = H_a = 0$ ) can be reached by particular cycling of the field. The simplest way to achieve this state, known as dc demagnetization, consists of following

the return branch from a field called the remanent coercivity,  $H_{cr}$ . Moreover, there are an infinite number of ways to achieve this state by cycling to two, three or more appropriately selected reversal fields. Experimentally, the demagnetized state is usually produced using an oscillating applied field of ever-decreasing amplitude starting from some large initial value, which is sufficient to saturate the sample. This procedure is called ac demagnetization. Applying a sufficiently large magnetic field ensures that the sample possesses a uniform magnetization. Once in this saturation state, field history is rendered irrelevant; subsequent evolution with field is independent of any field path taken prior to saturation. Technical saturation is evident from the absence of changes in the hysteresis properties of the material when larger fields are applied.

The ac demagnetization procedure can be generalized to a nonzero target field  $h_0$ , where field cycling occurs about  $h_0$  rather than zero. In this way, points on an *anhysteretic*, or *equilibrium*, curve ( $M$  vs.  $h_0$ ), passing through the origin, are generated. The dashed curve, shown in Figure 1.2, is history independent, its memory of previous states of the system erased by the oscillating field.

Another way of producing a similar history-independent curve is to heat the material above its Curie temperature and then slowly cool it at constant field,  $h_0$ . These two curves have similar but not identical properties (Bertotti, 1998, p. 19). Both are an attempt to attain a state of minimum free energy, that is the state that would be occupied if there were no barrier to achieving this minimum energy configuration. The existence of these barriers results in hysteresis.

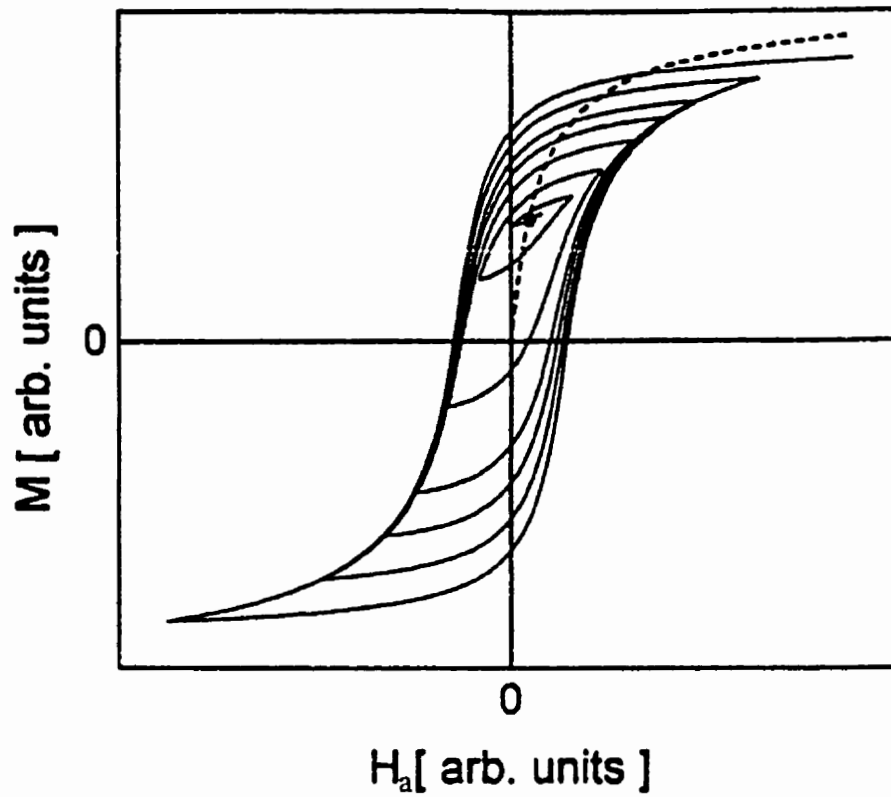


Figure 1.2 . The field history generating a point on the *anhysteretic* curve oscillating around a constant bias  $h_0$  with an amplitude that decreases from infinity to zero.

Repeating this procedure with different values of the bias field generates the anhysteretic (dashed) curve (Bertotti, Fig. 1.8, 1998).

## 1.4 Technical Applications of Hysteresis

There is a wide variety of hysteresis loop shapes and consequently, loop features, such as the coercive field, the remanence, and the susceptibility  $\chi = M/H$ , differ greatly among magnetic materials. Ferromagnets are often classified on the basis of their coercivity. Historically, experiments on mechanically hard iron and steel samples showed high coercivities, while low coercivities were found for soft specimens. So, materials that saturate in a small applied field are considered *magnetically soft*; those which require very large fields for saturation are called *magnetically hard* (Figure 1.3). There is no sharp delineation between hard and soft ferromagnets; however, those with coercivities less than 12.5 Oe are considered soft, while hard magnetic materials possess coercivities above 125 Oe (Jiles, 1991, p. 74). A magnetic substance which does not exhibit hysteresis is completely reversible and has both zero coercivity  $H_c = 0$  and zero saturation remanence  $I_s = 0$ .

The magnetic properties of ferromagnets make them particularly useful in permanent magnets, electrical motors, inductors, power generation, and magnetic recording. Soft magnetic materials are used in electromagnets, motors and transformers where low coercivity and high permeability,  $\mu = 4\pi\chi + 1$ , are important features. Hard magnetic materials are important for applications in magnetic recording and permanent magnets where high values of the remanence and coercivity are important.

In hysteretic systems, the remanent magnetization is a memory of both the magnitude and direction of the last field maximum experienced by the material, thus enabling the use of magnetic materials as information storage media. For retrieval of

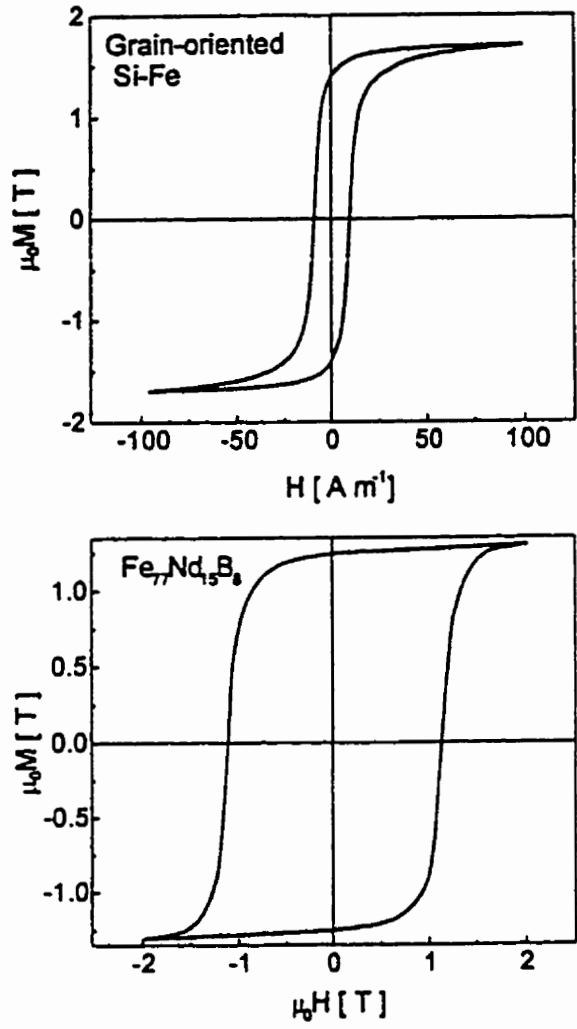


Figure 1.3 . Hysteresis loops corresponding to a soft ferromagnet (top), 3 wt. % Si-Fe alloy used in transformer cores, and a hard ferromagnet (bottom), a sintered aligned  $\text{Fe}_{77}\text{Nd}_{15}\text{B}_8$  permanent magnet. The loop widths differ by a factor of approximately  $10^5$  (Bertotti, Fig 1.1, 1998).

stored data, the material must possess a high saturation magnetization and a relatively square hysteresis loop, so that the remanence will be high enough to produce a sufficiently large signal in reproduction. The coercivity, or loop width, is also critical; it must be large enough to prevent erasure by stray fields, but small enough so that the magnetic disk or tape can be reused. This typically requires values of between about 250 and 1250 Oe (Jiles, 1991, p. 232).

## 1.5 Modelling Hysteresis

Both field and magnetization are vectors and, as such, models of hysteresis should be based on vector principles. However, many experiments and theoretical interpretations are scalar-based analyses, which relate the *component* of magnetization along the field axis to the field intensity.

*Micromagnetic* approaches to hysteresis in ferromagnetic materials treat the system on a length scale *intermediate* between the microscopic scale of atomic spins arranged on a discrete lattice, and the macroscopic scale of domains or fine magnetic particles. The individual atomic spins are replaced by a magnetization vector  $\vec{M}(\vec{r})$  whose magnitude is fixed at the spontaneous value, but whose direction is a continuous function of position  $\vec{r}$ . The equilibrium orientation of  $\vec{M}$  at every point  $\vec{r}$  is determined by minimizing the free energy, which includes contributions from magnetostatic, anisotropy, and exchange sources, as well as from the external field. Micromagnetic models are capable of simulating very specific microstructural features such as grain size, grain shape, the dispersion of the magnetocrystalline anisotropy among the crystallites, structure at the sub-grain level, clustering of grains, and possibly, nonuniform

magnetization processes within grains (Schrefl, 1997).

By contrast, the Preisach approach to hysteresis (Preisach, 1935) is based on very general physical considerations that transcend the microstructural details of the specific systems and even the nature of the hysteresis itself, so that the Preisach formalism is not limited to magnetic systems alone. In the Preisach representation of hysteresis, the complex multiplicity of metastable states in the free energy landscape, which is ultimately responsible for hysteresis, is decomposed into a superposition of many *bistable elements*, each characterized by *two* local energy minima separated by an energy maximum. Each elementary *two level subsystem* thus incorporates the two essential mechanisms common to all systems that exhibit hysteresis: *anisotropy energy barriers*, that tend to trap the subsystem “temporarily” in one of its two possible states, thus preventing equilibration, and *interactions* between subsystems, which lift the degeneracy of the two states yielding one stable and one metastable state.

## **1.6 Investigating Hysteresis Using the Preisach Approach**

This thesis explores both theoretical and practical applications of the Preisach model to the study of metastability in magnetic systems, and hysteresis in particular. This is motivated by the fact that hysteresis makes magnetic systems useful in applications such as permanent magnets and recording media. Applying this phenomenological model, the behaviour of magnetization, remanence, interactions, and the role of thermal effects in a system can be established. Since interest in the model has been renewed recently, especially in engineering applications (Basso & Bertotti, 1994 and references therein), this study is an important contribution to the determination of the capabilities and the

limitations of the Preisach model for characterizing magnetic materials.

Preisach's (1935) original model is introduced (Section 3.1) and the formalism is extended to include mean field-like interaction effects (Section 3.2). The illustrative capabilities of Preisach's diagrammatic representation of the model's constituent loops, resulting from decomposition of macroscopic hysteresis, are presented with particular emphasis on the magnetizing and demagnetizing processes and the structure of various demagnetized states (Section 3.3). The model is extensively applied to the interpretation of remanence characteristics in this thesis as a means to understanding interaction processes within magnetic systems. The connection of Henkel plots (Section 3.4), which are a popular graphic diagnostic tool for analyzing interactions, to the Preisach model is made with special consideration given to clarifying this often ambiguous guide. To treat the effects of finite time and temperature, relaxation effects are incorporated into the Preisach formalism (Section 3.5), which allows application of the model to the analysis of data from magnetic systems over a wide range of temperatures (Sections 5.5 to 5.7) Using this generalized Preisach model can provide a more complete understanding of Henkel plot behaviour. The addition of a phenomenological reversibility term to the model (Section 3.6) completes the modifications that are implemented in the analysis of real magnetic systems. A theoretical treatment of the remanence behaviour in spin glass systems is proposed in Section 3.7.

Experimental considerations including the equipment (Section 4.1) utilized for measuring magnetic moments and the techniques (Section 4.2) employed to obtain demagnetized states, to generate Henkel plots, and to explore the temperature dependence

of the moment as well as the temporal magnetic response to application of a field are related. In addition, the six magnetic systems are discussed in depth: CrO<sub>2</sub> audio tape, consisting of elongated, aligned CrO<sub>2</sub> particles (Section 4.3.1); magnetoferritin, a potential magnetic resonance contrast agent consisting of roughly spherical, nanodimensional, ferrimagnetic particles (Section 4.3.2); a permanent magnet, Nd<sub>2</sub>Fe<sub>14</sub>B which is a granular medium comprised of sintered Nd<sub>2</sub>Fe<sub>14</sub>B ferromagnetic particles (Section 4.3.3); a flexible disk medium, similar to audio tape in that it consists of fine particles, but these particles are oriented randomly in the plane (Section 4.3.4); and two cobalt-chromium-based hard disk materials, one of which is longitudinal, with particles that lie in the plane of the disk (Section 4.3.5), and the other a perpendicular medium, comprised of columnar grains oriented perpendicular to the plane of the disk (Section 4.3.6).

Details of the model parameters and fitting procedures used in the Preisach analysis of real systems are presented in Section 5.1. The particular choice of a functional representation for distributions describing coercive fields and interactions, as well as evidence for the absence of interactions for demagnetizing-like mean-field interactions, and for magnetizing-like interactions are explored in Sections 5.2 through 5.4, as exposed by the Preisach analysis of data from the three magnetic disk media. Theoretical assertions regarding the influence of the initial demagnetized state are explored in great depth with regard to both CrO<sub>2</sub> (Section 5.5) and magnetoferritin (Section 5.6) systems. The generalized Preisach formalism, used to treat the effects of temperature and experimental wait time, is central in the analysis for CrO<sub>2</sub>, magnetoferritin, and

$\text{Nd}_2\text{Fe}_{14}\text{B}$  (Section 5.7). In addition, the analysis of  $\text{Nd}_2\text{Fe}_{14}\text{B}$  introduces a substantial restructuring of the bistable element used in the basic Preisach implementation to account for domain wall nucleation and motion within the grains of the permanent magnet.

The basic principles of magnetism involved in hysteresis, presented in Chapter 2, provide a solid foundation for the experimental study of processes and interactions in magnetic systems. The theoretical predictions of the standard Preisach model are investigated and Henkel plots are interpreted via the application of a generalized version of the model. The model is a tool to gain an understanding of the magnetic processes that dominate in the six magnetic systems. The detailed analysis of the experimental data within the Preisach formalism employs the theoretical conclusions established in Chapter 3 to exploit the model's predictive capabilities and to expose its limitations.

## Chapter 2

# Theoretical Basis of Hysteretic Properties

Two basic mechanisms are at the root of the behaviour of magnetic materials, exchange and anisotropy. The origins of the spontaneous moment is a microscopic problem where exchange interactions are important. The magnetization process is a macroscopic problem which can be a consequence of domain wall motion or the reversal of single domain particle moments by coherent or incoherent rotation. From the latter perspective, dipole-dipole interactions, magnetostatic energy, and anisotropy are important.

### 2.1 Magnetization

Magnetic fields can be described mathematically as originating from small regions of space called *magnetic poles*. Two types of poles, defined as north and south, exist and exert opposite forces on a common magnetic test pole. However, poles do not exist in isolation, but in pairs. A north-south pole pair defines a dipole. The magnitude of the

magnetic moment of a dipole is

$$m \equiv \text{pole strength} \times \text{distance between poles.}$$

The energy,  $E$ , of a dipole of moment,  $\vec{m}$ , in a field,  $\vec{H}$ , is defined by  $E = -\vec{m} \cdot \vec{H}$ . The lowest energy state is given by the moment lying parallel to the field. Magnetization,  $\vec{M}$ , describing the extent to which the magnetic body is magnetized, is defined as the total magnetic moment per unit volume  $\vec{M} = \frac{1}{V} \left( \sum_i \vec{m}_i \right)$ , and is an *average* value when the sum is defined over the volume  $V$  of the entire body. However, magnetization is often defined locally, at some position  $\vec{r}$ , as  $\vec{M}(\vec{r}) = \frac{1}{\Delta V} \left( \sum_i \vec{m}_i \right)$  where the sum is taken only over dipoles in a small element of volume  $\Delta V$ .

## 2.2 Magnetostatic Energy

Magnetostatic energy is the self energy of a magnetic body. Treating the body as an assembly of magnetic dipoles  $\vec{m}_i$ , the magnetostatic energy,  $E_{ms}$  is calculated using the internal field,  $\vec{H}_{int}$ , which is the field due to the dipoles themselves, and summing over all the dipoles in the assembly  $E_{ms} = -\frac{1}{2} \sum_i \vec{m}_i \cdot \vec{H}_{int}$  (Morrish, 1965, p. 12). In the continuum limit this becomes  $E_{ms} = -\frac{1}{2} \int_V \vec{M} \cdot \vec{H}_{int} dV$  where  $V$  is the volume of the magnetic body. Specifically, for an ellipsoid of uniform magnetization, the internal field due to uncompensated surface poles is just a demagnetizing field and is opposite and proportional to the magnetization,  $H_D = -DM$  where  $D$  is the demagnetizing coefficient. Thus, the magnetostatic energy for an ellipsoid is proportional to the square of the magnetization  $E_{ms} = \frac{1}{2} DM^2$ . Magnetostatic energy leads to anisotropy (Section 2.4) and the formation of domains (Section 2.5).

## 2.3 Exchange Interaction

The exchange interaction arises from a combination of the electrostatic coupling between electron orbitals and the necessity to satisfy the Pauli exclusion principle. The overall antisymmetric character of electronic states gives rise to a coupling between the spin momentum and the wave function in real space. Parallel spins give rise to a symmetric spin wave function and an anti-symmetric spatial wave function. These spins cannot stay close together, so this reduces the average energy for the electrostatic interaction. This fundamentally electrostatic effect is the basis for ferromagnetism (Section 2.9.2). The exchange interaction is quantum mechanical and is described by the Hamiltonian  $\mathcal{H} = -\sum_{i,j} J_{ij} \vec{S}_i \cdot \vec{S}_j$  where  $\vec{S}_i$  is the spin angular momentum located at the  $i^{\text{th}}$  lattice site and  $J_{ij}$  is the exchange integral that measures the coupling strength between spins  $i$  and  $j$ . The sign of  $J_{ij}$  determines whether the spins prefer to orient themselves parallel ( $J_{ij} > 0$ ) or antiparallel ( $J_{ij} < 0$ ) to each other. The spin-spin interactions are an exchange interaction, favouring long-range ordering over macroscopic distances. Nevertheless, exchange is a short-range interaction, which falls off rapidly with distance and it is usually sufficient to include only nearest neighbours. Then, the interaction strength only varies with the angle between neighbouring moments. The exchange interaction is the most important interaction between atomic magnetic moments.

## 2.4 Magnetic Anisotropy

Magnetic anisotropy refers to the directional dependence exhibited in measurements of magnetic properties. Magnetic anisotropy can appear in different ways,

including intrinsic properties of the crystal that define preferred directions for the magnetization, extrinsic properties, such as the specimen's shape, or through the application of stress to the material. *Magnetocrystalline*, or *crystal*, anisotropy is the force that tends to bind the magnetization vector  $\vec{M}$ , to particular directions in the crystal. The interaction, known as spin-orbit coupling, or the coupling between electronic orbitals and spin, is the dominant mechanism of magnetocrystalline anisotropy since the magnetization is tied to the spin. (Experiments have established that the atomic origin of magnetism is not an orbital motion but the spin moment of the electron, with a small orbital contribution (Morrish, 1965, p. 48)). Within the crystal, there exists an electric potential, or crystal field, created by the charged ions on the crystal lattice and sharing the symmetry of the lattice. Interactions between the orbital angular momentum,  $\vec{L}$ , and this potential can be such that the orbital momentum orientations are fixed strongly to the lattice. Due to spin-orbit coupling, proportional to  $\vec{L} \cdot \vec{S}$ , the spin orients itself along certain symmetry axes of the lattice that are energetically favoured. Alternatively, the spin-orbit coupling may be stronger than that between the electronic orbitals and the lattice. In this case, the orbital angular momentum rigidly follows the spin and anisotropy results from the variation of energy due to changes in the orientations of  $\vec{L}$  with respect to the lattice. Crystalline anisotropy is not due to the exchange interaction. Although this latter spin-spin coupling is strong, it does not depend on orientation with respect to the lattice, but only on the angle between the spins themselves. The spin-orbit coupling is weak, but it defines easy axes within the crystal, since energy is required to rotate the spin system away from these preferred directions.

*Shape* anisotropy appears when the shape of the magnetic body deviates from spherical form; if no crystalline anisotropy exists, a spherical sample is equally easy to magnetize in any direction. Ultimately, the origin of shape anisotropy is magnetostatic energy and is a consequence of demagnetizing fields resulting from uncompensated surface poles. The field within a magnetic body is a vector sum of the applied and demagnetizing fields. Considering an ellipsoid, a stronger field must be applied along the short axis than the long axis to produce the same true field inside the specimen, to compensate for the stronger demagnetizing field. This means that an easy direction is defined along the long axis.

Anisotropy in magnetic materials exists when the magnetization vector favours lying along certain directions in the sample, and *stress* alone can create an easy axis within a material through magnetoelastic coupling to the lattice. This coupling is a consequence of the energy variation when positions of the magnetic ions on the lattice are modified (Bertotti, 1998, p. 158).

## 2.5 Domain Structure

First postulated by Weiss (1907), domains are regions in a material that have a uniform magnetization. Each domain is spontaneously magnetized to the saturation value. The exchange interaction explains this spontaneous magnetization in an individual domain since parallel spin orientations are favoured by this interaction when the coupling constant  $J_{ij}$  is positive. Neighbouring domains have different orientations of the magnetization. The interface between regions where the spontaneous magnetization has different directions defines a domain wall. Within the extent of the wall the

magnetization must change direction. This means that the wall is defined by atoms with spins that are not parallel, but which make some angle with one another. This introduces exchange energy that is minimized when the spin direction changes gradually over many atoms. However, where crystal anisotropy exists, a competition arises between the reduction of exchange energy, favouring a thick wall, and the corresponding increase in crystalline anisotropy energy, favouring a thin wall. Spins prefer to lie along easy directions of the crystal and a thin wall minimizes the number of atomic moments that orient themselves in noneasy directions. Thus, the wall energy has both exchange and crystalline anisotropy contributions.

For a particle having just one domain, the magnetostatic energy is  $E_{ms} = \frac{1}{2}DM_s^2$  where  $D$  is the demagnetization factor and  $M_s$  is the saturation magnetization. If the particle splits into two domains of opposing magnetization, thus bringing north and south surface poles closer together and decreasing the spatial extent of the field, the magnetostatic energy is reduced. Formation of additional domains accomplishes further reduction of the magnetostatic energy, until the energy introduced into the material by additional walls exceeds this reduction.

## **2.6 Single Domain Particles**

Some particles can exist as single domain if they are small enough such that the reduction of magnetostatic energy induced by the formation of domain walls is dominated by an increase in the total energy from the wall energy contribution. The critical size for single domain behaviour in zero applied field can be predicted by minimizing the expression for the total energy with respect to size (Cullity, 1972, p. 300). This type of

particle cannot be demagnetized. Because there are no domain walls, the magnetization can only be reversed by rotation. Shape or crystalline anisotropy hinder this rotational process. A multi-domain particle can become single domain if it has been saturated in a sufficiently strong magnetic field.

The critical size for a single domain can be calculated under two different conditions, static and dynamic. In the static case, a particle is single domain when all spins are parallel in  $H_a = 0$ , and the particle will spontaneously break up into domains when the critical size has been exceeded. According to the dynamic definition of critical size, a particle is only considered single domain if and only if the spins of the particle remain parallel in zero field *and* during reversal in  $H_a \neq 0$ , that is, the particle exhibits coherent reversal (Cullity, 1972, p. 398).

## **2.7 Mechanisms of Magnetization Reversal**

There are many mechanisms for magnetization reversal. Domain wall motion is a mechanism of magnetization reversal in multi-domain materials. Small single domain particles change their direction of magnetization by coherent rotation. Incoherent mechanisms for rotation are suggested by experiments that yield coercive fields that are too low to be accounted for by coherent reversal.

### **2.7.1 Coherent Reversal: The Stoner-Wohlfarth Model**

The Stoner-Wohlfarth model provides a classical calculation of hysteresis. It examines the behaviour of a single domain particle in a magnetic field. In single-domain particles, no domain walls exist, and rotation, as a mechanism of magnetization reversal,

can be considered in isolation. Rotation occurs against restoring forces of shape, stress, and/or crystal anisotropy. The model considers a prolate spheroid, as shown in Figure 2.1, with a constant spontaneous magnetization,  $M_s$ , having uniaxial shape anisotropy, but for which crystalline anisotropy and strain are zero; however, since these anisotropies are of the same form,  $E_K = K \sin^2\theta$  (Cullity, 1972, p. 216), they can be treated similarly. For the Stoner-Wohlfarth particle in question, the semi-major axis is given by  $c$ , and  $a$  is the semi-minor axis. The long axis is the easy axis of magnetization. The angle formed by the magnetization vector and  $c$  is  $\theta$ , and  $K$  is the uniaxial anisotropy constant, which in the case of shape anisotropy can be expressed in terms of the demagnetizing coefficients along the semi-minor and semi-major axes as  $K = \frac{1}{2}(N_a - N_c)M_s^2$ .

In the expression for the total energy, a potential energy term for a magnet in an applied field,  $\vec{H}_a$ , combines with the anisotropy energy to give:

$$E = K \sin^2\theta - H_a M_s \cos(\alpha - \theta) \quad (2.1)$$

where  $\alpha$  is the angle that  $\vec{H}_a$  makes with  $c$ . The equilibrium position of the magnetization vector is given by minimizing the energy equation, that is, setting  $\frac{dE}{d\theta} = 0$  and ensuring that  $\frac{d^2E}{d\theta^2} > 0$ . Defining reduced parameters for the magnetization and the field by  $m = M/M_s$  and  $h_a = H_a M_s / 2K$  respectively, the following well-known result is obtained:

$$\sin\theta \cos\theta - h_a \sin(\alpha - \theta) = 0 \quad (2.2)$$

Solutions to Equation 2.2 define hysteresis loops for the particle, where the projection of the magnetization vector on the easy axis is given by  $M = M_s \cos(\alpha - \theta)$ , or in terms of reduced variables,

$$m = \cos(\alpha - \theta).$$

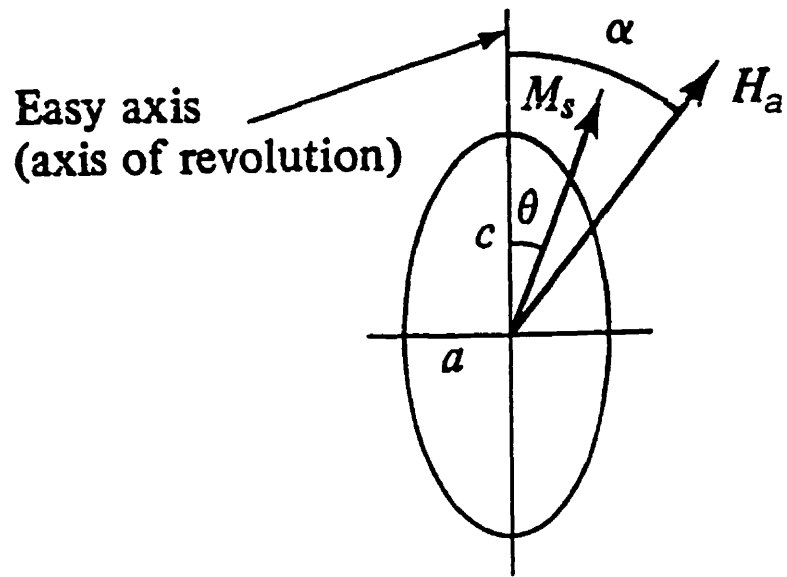


Figure 2.1 . A Stoner-Wohlfarth particle (from Cullity, Fig. 9.37a, 1972). The uniform spontaneous magnetization  $M_s$  forms an angle  $\theta$  with the easy axis  $c$  of the ellipsoid. A magnetic field  $H_a$  is applied at an angle  $\alpha$  with respect to this axis.

For this simple model, the critical field, where switching takes place, is given by simultaneously solving Equation 2.2 and the equation obtained by setting  $\frac{d^2E}{d\theta^2} = 0$ .

The hysteresis loops generated from these calculations are shown in Figure 2.2. These loops vary in character from a square loop (identical to the elementary hysteresis loops for a pseudoparticle, implemented in the Preisach model discussed in Chapter 3) when the applied field is aligned with the easy axis, to a linear anhysteretic curve when the field is applied normal to the long axis. The hysteresis loops generated by applying the field at different angles indicate the presence of both reversible and irreversible changes in magnetization in the process of domain rotation. These irreversible changes are sometimes referred to as Barkhausen jumps.

These loops display information about the *critical* or *switching field*, where the magnetization jumps irreversibly, and the reduced *coercive field*  $h_c$ , where the particle exhibits zero moment. The critical field varies between reduced values 0.5 and 1.0, as shown in Figure 2.3. The reduced coercive field, ranges from a maximum value of  $h_c = 1$  for the square hysteresis loop to a minimum value  $h_c = 0$  where the magnetization is a linear function of the field and completely reversible. So, the maximum coercive field for a single domain particle with uniaxial anisotropy is  $H_c = \frac{2K}{M_s}$  and is sometimes called the anisotropy field  $H_K$ .

An energy level diagram can be generated by plotting the total energy as a function of the angular position of the magnetization vector. In Figure 2.4, the curves have been generated for a field applied antiparallel to the easy axis,  $\alpha = 180^\circ$ . In the case of zero applied field, the result is two degenerate minima. The local energy minimum at

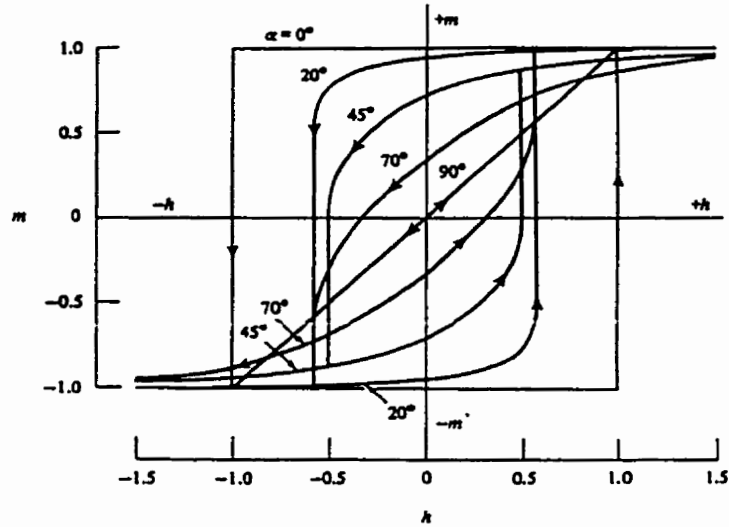


Figure 2.2 . Hysteresis loops for a particle with uniaxial anisotropy showing the dependence of loop shape and switching field on the angle  $\alpha$  between the applied field and the easy axis of the particle (Cullity, Fig. 9.38, 1972). Here  $m$  is the reduced magnetization and  $h$  is the reduced field.

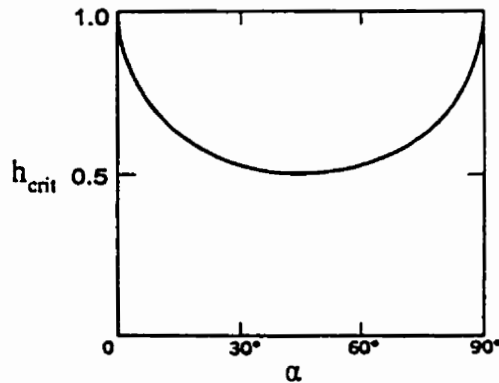


Figure 2.3 . Dependence of the critical field  $h_{crit}$  on the orientation  $\alpha$  of the applied field (after Chikazumi, Fig. 14.2, 1964).

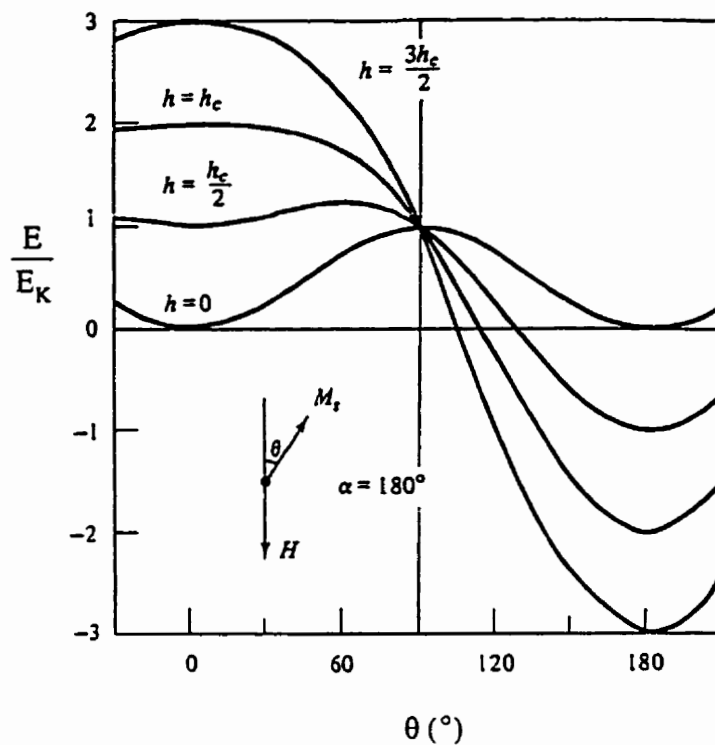


Figure 2.4 . Rotation of the magnetization in an ellipsoid. Energy  $E$  (divided by the anisotropy energy,  $E_K$ ) as a function of the rotation of the magnetization in an ellipsoid through angles  $\theta$  (after Cullity, Fig. 9.37b, 1972).

$\theta = 0^\circ$  becomes a maximum when the applied field matches the particle's critical field.

The Stoner-Wohlfarth model (Stoner & Wohlfarth, 1948) makes several assumptions that represent an idealized state. In real materials, these conditions are impossible to meet. The assumption of spheroidal geometry is thwarted since particles and grains have irregular shapes. Strong dipolar fields may be present at sharp corners or surface irregularities and these may favour magnetization reversal. In the absence of other sources of anisotropy, the coercivity of a spherical particle ( $\frac{c}{a} = 1.0$ ) is zero, but calculations show that for a single domain particle, small deviations from a perfect sphere dramatically increase the coercivity. For example, increasing  $\frac{c}{a}$  to 1.1 results in a coercivity of 810 Oe (Cullity, 1972, p. 338). Furthermore, particles are never perfectly aligned in the field. The relation between coercivity and anisotropy field is affected by the degree of misalignment, and for random orientations, coercivity predictions are about halved. Zero temperature is also assumed. At finite temperatures, magnetization reversal can start in small regions by thermal activation. This is a consequence of the inhomogeneity of magnetic properties that can exist in real materials, where some regions of lower anisotropy may provide nucleation sites for reversal. Even in a state of technical saturation, the tiny reverse domains that survive the application of very large applied fields can act as nucleation sites. It is also important to consider particle interactions in real materials with particles and grains that are packed together, and in bulk polycrystalline materials. The dipolar or exchange interactions affect the collective magnetization reversal properties.

Stoner and Wohlfarth (1948) and Rhodes (1949), as cited by Cullity (1972),

extended this model to an assembly of particles with two restrictions: the assembly must be magnetically isotropic with the orientation of the easy axes randomly distributed in space, and the particles must be noninteracting, that is, the contribution of a particle's own magnetic field to the external field experienced by its neighbours is neglected. The resultant hysteresis loop (Figure 2.5) is characterized by a remanence of 0.5, normalized to the saturation magnetization, a reduced critical field 0.5, and a reduced coercivity of 0.48.

In Stoner-Wohlfarth rotation, the spins of all atoms in a particle remain parallel throughout rotation. However, measurements of coercivity in iron whiskers yielded only a fraction (18%) (Luborsky, 1961) of the theoretical value expected for shape anisotropy, and yet were too large to be explained with crystal anisotropy, thus prompting a search for *incoherent* rotation mechanisms. The most important of these modes are *fanning* and *curling*.

### **2.7.2 Incoherent Reversal Modes**

The chain of spheres model suggested by periodic bulges observed in electron micrographs of electrodeposited iron, was used by Jacobs and Bean (1955) to investigate these two possible incoherent reversal modes. In symmetric fanning, the magnetization vectors of successive spheres in the chain fan out in a plane by rotating in opposite directions in neighbouring spheres (Figure 2.6). Each sphere is considered single domain, with the reversal mechanism of an isolated sphere being coherent. In the model, each sphere is treated as a dipole. The resulting equations have the same form as for uniaxial coherent reversal (Eq. 2.2) so the fanning mode is also characterized by a rectangular

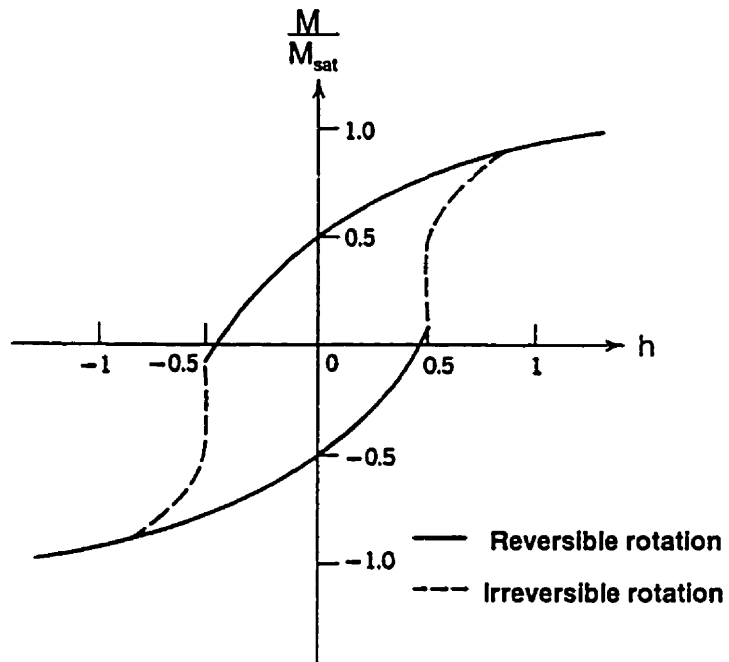


Figure 2.5 . Hysteresis loop describing the magnetic response of an aggregate of single domain fine particles with uniaxial anisotropy (after Chikazumi, Fig. 14.10, 1964).

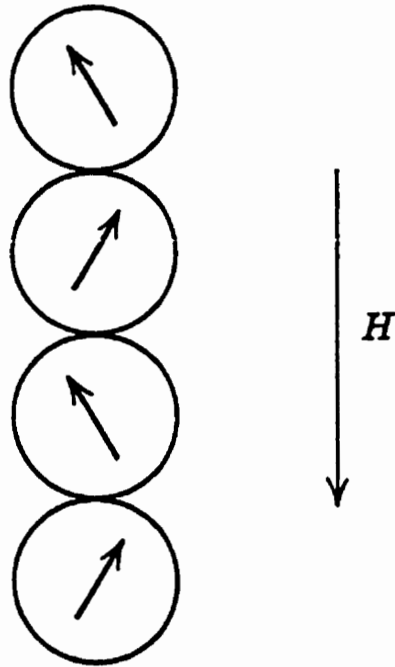


Figure 2.6 . Incoherent magnetization reversal by *fanning* (from Morrish, Fig. 7-2.14, 1965). The magnetization vectors in adjacent particles rotate in opposite directions when a magnetic field  $H$  is applied.

hysteresis loop but with reduced coercivity.

The curling mode can be investigated by micromagnetics. This mode is most easily visualised for an infinite cylinder. Each spin rotates about the radius parallel to the plane on which it is located, so that halfway through the reversal, spins are parallel to that plane and form closed circles of flux in all cross-sections (Figure 2.7). No magnetostatic energy is involved since no uncompensated poles are on the surface, but exchange energy resulting from the angles formed between spins in this mode is the barrier to reversal. Coercivity in the curling mode depends on both particle size and shape.

A given particle will reverse by whatever mechanism has the lowest coercivity. Below a critical diameter, coherent reversal is favoured whereas for larger particles incoherent mechanisms are favoured, and the specific mechanism depends on particle shape. Curling is favoured for cylindrical particles (Cullity, 1972, p. 396), whereas fanning is favoured for “peanut-shaped” particles (Luborsky, 1961).

### **2.7.3 Dipole-dipole Interactions (Bertram & Zhu, 1992)**

Interactions between dipoles can yield more insight into reversal patterns. Consider two particles with parallel anisotropy axes, and with anisotropy constants  $K_1$  and  $K_2$ . The applied field is parallel to these axes. The dipole particles have a centre-to-centre separation of  $\vec{r}$ , directed at an angle,  $\theta$  with respect to their anisotropy axes. Their magnetizations are equal in magnitude, but are oriented at angles  $\theta_1$  and  $\theta_2$  to their respective particle axes in the plane defined by the particles (Figure 2.8).

The energy of the system can be calculated as the sum of single particle terms from the Stoner-Wohlfarth model plus an interaction term. The demagnetization energy is

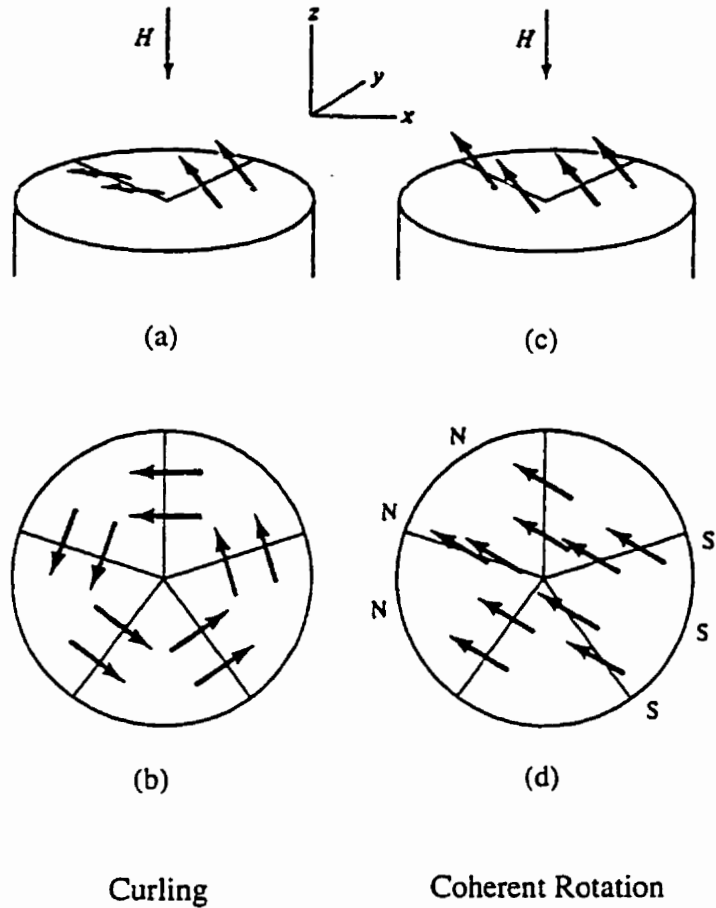


Figure 2.7 . Magnetization reversal by (a) curling and (c) coherent rotation. (b) and (d) show cross-sections normal to the z-axis after 90 °C a rotation from the +z direction (from Cullity, Fig. 11.8, 1974).

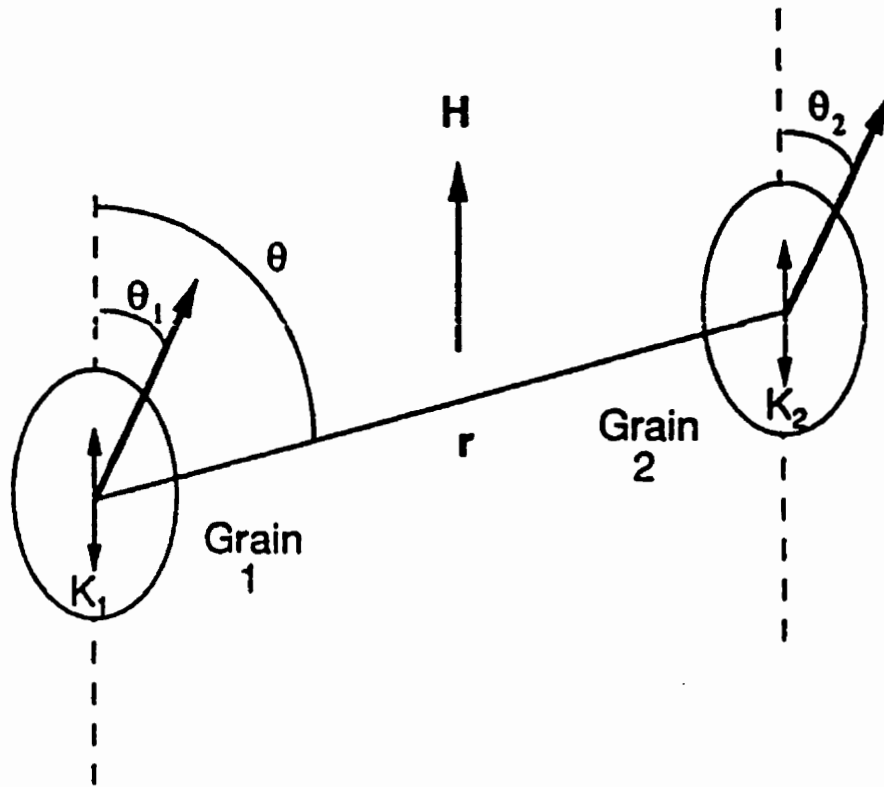


Figure 2.8 . An interacting dipole pair with bond angle  $\theta$  and separation  $r$ . The grains possess uniaxial crystal anisotropy with easy axes parallel to each other and the applied field,  $H$ .

described in terms of shape anisotropy for the  $i^{\text{th}}$  particle as  $K_i \sin^2 \theta_i$ . So, in this notation, the energy per unit volume for a single particle in a field  $H$  is given by

$E_i = K_i \sin^2 \theta_i - HM_s \cos(\theta_i)$  as in Eq. 2.1. Moreover, the dipole energy for a point dipolar interaction is given by

$$E = \frac{m_1 m_2 - 3(\vec{m}_1 \cdot \hat{r})(\vec{m}_2 \cdot \hat{r})}{r^3}$$

where  $m_i = M_s V_i$  is the particle moment and  $V_i$  is the volume of the particle. The total energy density is therefore

$$E = -HM_s(\cos \theta_1 + \cos \theta_2) + K_1 \sin^2 \theta_1 + K_2 \sin^2 \theta_2 \\ + H_{\text{int}} M_s (\cos(\theta_1 - \theta_2) - 3 \cos(\theta - \theta_1) \cos(\theta - \theta_2))$$

where  $H_{\text{int}} = \frac{M_s V}{r^3}$  is an effective internal field. Equilibrium states of the magnetization

vectors are defined by simultaneously minimizing the first derivatives of the energy,

$\frac{\partial E}{\partial \theta_1} = 0$  and  $\frac{\partial E}{\partial \theta_2} = 0$ . To find the critical points, the determinant of the second

derivatives is evaluated

$$\delta E^2 = \begin{vmatrix} \frac{\partial^2 E}{\partial \theta_1^2} & \frac{\partial^2 E}{\partial \theta_1 \partial \theta_2} \\ \frac{\partial^2 E}{\partial \theta_1 \partial \theta_2} & \frac{\partial^2 E}{\partial \theta_2^2} \end{vmatrix}.$$

Mathematically, finding the nucleation field and the equilibrium states is treated as an eigenvalue problem. Physically, nucleation occurs at the lowest reverse field where a

saddle point develops in the energy surface.

Interactions between particles or grains affect the switching field. For identical particles with zero bond angle  $\theta = 0$ , the easy axes coincide, and there is only one equilibrium state. At high fields, the moments of both particles lie along this line,  $\theta_1 = \theta_2 = 0$ . This configuration is stable until a negative applied field reaches a value  $|H_n| = H_K + H_{int}$ , where  $H_K = \frac{2K}{M_s}$  is the uniaxial anisotropy field. The initial reversal mode is fanning, where the particle moments rotate opposite to one another,  $\delta\theta_1 = -\delta\theta_2$ . The final equilibrium state is the parallel reverse spin configuration, with both spins opposite to their initial direction. For side-by-side particles, where  $\theta = \frac{\pi}{2}$ , the ferromagnetic state ( $\theta_1 = \theta_2 = 0$ ) is stable, and nucleation in the opposite direction requires a negative field  $|H_n| = H_K - 3H_{int}$ , and the reversal mode is coherent  $\delta\theta_1 = \delta\theta_2$  when  $H_K > 3H_{int}$ . However, if  $H_K < 3H_{int}$ , then the motion is reversible and occurs by fanning. So, bond angles along the applied field ( $\theta = 0$ ) raise the nucleation field, whereas bond angles that are orthogonal to the applied field serve to reduce the nucleation field. For nonidentical grains, where  $K_1 \neq K_2$ , the reversal mode and nucleation fields depend on the strength of the interactions (Bertram & Zhu, 1992).

#### 2.7.4 Domain Wall Motion

When domain walls are present, magnetizing the sample is a process of converting the specimen from a multi-domain state into a single domain whose magnetization is aligned with the applied field. A saturation state is reached when an applied field is large enough to remove the domain structure. (If the field is further increased, an increase in the magnetization over the spontaneous value is observed. This

phenomena is also seen in systems where saturation is achieved by other mechanisms, such as rotation. This is called *forced magnetization*, and is a result of perfecting the thermal spin alignment within an atom (Chikazumi, 1964, p. 246). This effect is due to changes in the Boltzmann factors ( $e^{-E/k_B T}$ ) governing the populations of the atomic Zeeman energy levels that depend on the applied field. Imperfect spin alignment is due to thermal agitation. Field induced moment growth is particularly important near  $T_C$ , where the molecular field, and hence the Zeeman splitting, is small.)

In a multi-domain specimen, free of imperfections, with  $180^\circ$  walls, that is antiparallel domains, applying a field along the magnetization direction on one side of the domain wall, can displace that wall. Thus, domains initially parallel to the field grow at the expense of the antiparallel domains. In a perfect crystalline material, the field required to induce motion of the wall is expected to be small, since only a small number of spins, within the thickness of the wall, must change their orientation (Figure 2.9), and provided no significant changes in surface pole distribution accompany the wall motion. Real materials have imperfections that impede the motion. Furthermore, the total energy of the sample will depend on the location of the domain wall due to the imperfections throughout the crystal, since the energy of the wall itself will depend on its position. This means that the magnetization process by movement of domain walls through the crystal can be understood in terms of the energy landscape.

Consider the position dependence of the energy for the example given in Figure 2.10a. In zero applied field, the wall will reside at a minimum, such as O, where it is *pinned*. Applying a field will move the wall to the right by an amount contingent upon the

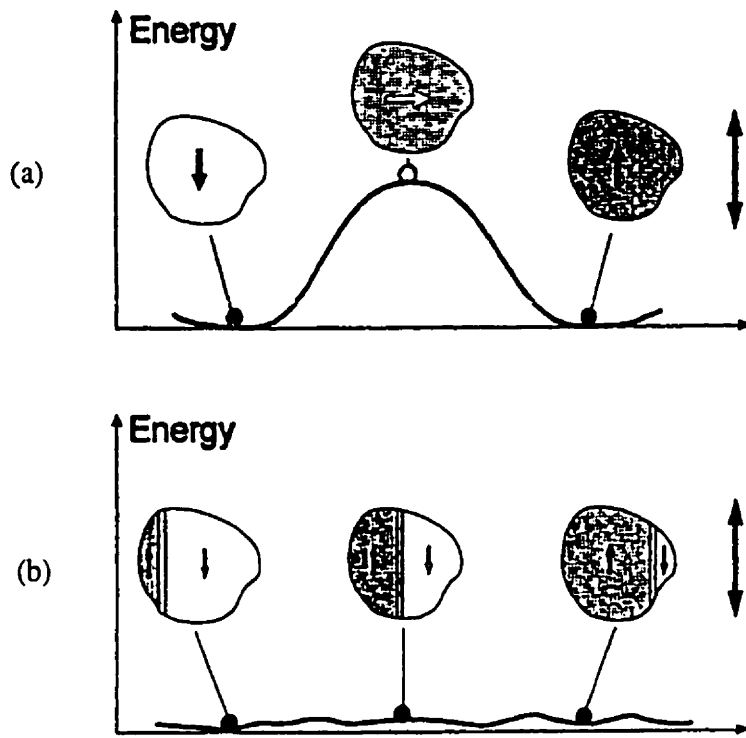


Figure 2.9 . Energy barriers opposing magnetization for (a) coherent rotation and (b) domain wall motion (from Bertotti, Fig. 11.1, 1998).

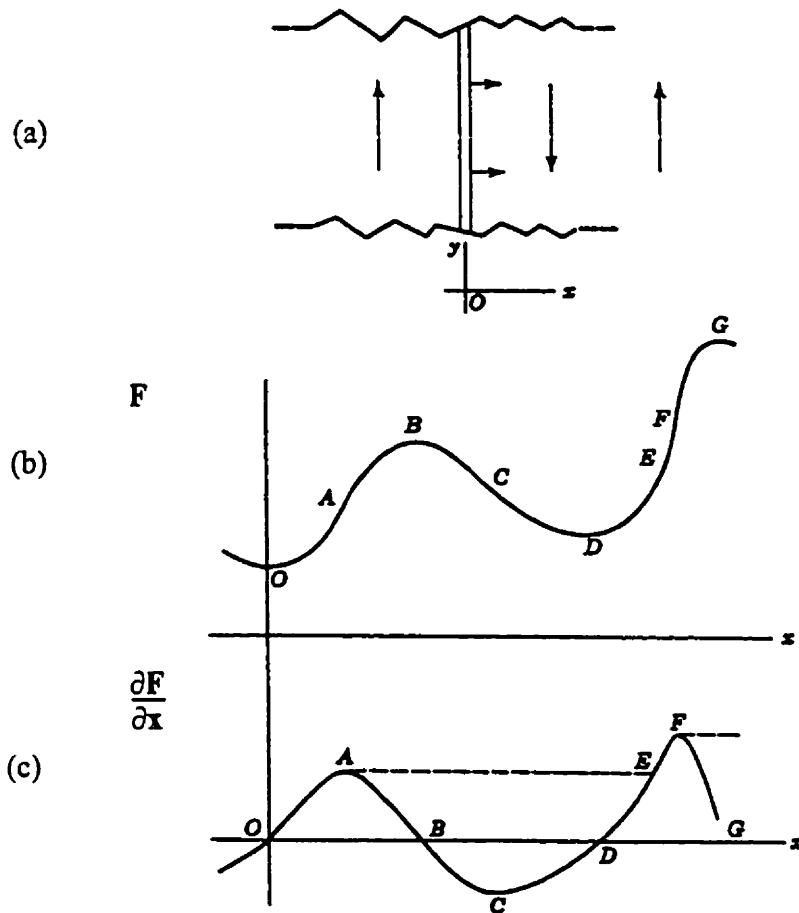


Figure 2.10 . Domain wall motion in a soft material with imperfections (from Morrish, Fig. 7-7.1, 1965). The direction of motion of  $180^\circ$  wall is indicated in (a). A representation of the dependence of the wall's free energy with respect to position  $x$  is given in (b). The slope of this curve, plotted against position, is shown in (c).

slope of the curve in this region. Between O and A, the domain wall motion is reversible; however, once the wall reaches a location A, where it is unpinned, it will spontaneously flash across the sample to a position E, having equal slope, where the *total energy*  $E = F(x) - 2\Delta m H x$  is a *minimum*. Decreasing the field, the wall will move toward D, and upon reversal, the wall will continue moving toward position C. Increasing the field, when the wall is located at E, will move the wall toward F where the motion is also unstable and the wall will spontaneously jump again.

Figure 2.10b shows the derivative of the free wall energy with respect to position. The coercivity is a measure of the field required to move a wall past energy barriers and it depends directly on the maximum slope of the energy curve, that is on the maximum value of its derivative. When a local coercive field is exceeded, the wall moves from one energy well to another, resulting in an irreversible energy change. This irreversibility yields hysteresis and remanence.

### 2.7.5 Brown's Paradox

Two problems present themselves with coercivity measurements. Given that domain wall motion is a relatively easy process, the coercivities observed in multi-domain particles are unusually high, and the coercivity falls with increasing particle size. Brown (as cited in Cullity, 1965, p. 400) used micromagnetic calculations to show that for a perfect crystal, the *internal* field required for magnetization reversal is  $H_c = \frac{2K}{M_s}$ , regardless of particle size. This is the same value as that for coherent rotation. However, experiments show a dramatic decrease of coercivity with increases in particle diameter. The discrepancy of these results for large particles with theory and experiment is known

as Brown's paradox. Obviously, coherent rotation cannot be the mechanism of reversal in particles sufficiently large to be multi-domain. One alternative is that one or more domain walls are nucleated in the particle, and move through the particle, reversing its magnetization. Once nucleated the wall will flash across the particle in one Barkhausen jump if the applied field exceeds the demagnetizing field. To nucleate a wall requires spin rotation of a few atoms near the surface, against crystal anisotropy, which needs the same field,  $H_c$ , as for coherent rotation in a perfect crystal. A perfect crystal will spontaneously break into domains when the demagnetization field is larger than the anisotropy field. Real crystals possess irregular shapes, aspherical in form, with pits, bumps, cracks and scratches, and internal imperfections of all descriptions, including dislocations, solute atoms, interstitials, and vacancies. To resolve Brown's paradox these imperfections are required to lower the nucleation fields. To nucleate a wall for a single particle, the total field,  $H = H_a + H_D$ , which is the sum of the applied and demagnetizing fields, must exceed the anisotropy field,  $\frac{2K}{M_s}$ . A small applied field is sufficient for nucleation if the demagnetization field,  $H_D$ , is large, the spontaneous magnetization,  $M_s$ , is large and/or the anisotropy constant,  $K$ , is small. The demagnetizing field, although bounded for ideal spheroids (Morrish, 1965, p. 10), can approach infinity near sharp corners.  $M_s$  is determined by the magnetic moment and exchange coupling per atom and can change locally. The local value of the anisotropy constant,  $K$ , due to spin orbit coupling is changed by imperfections, like small-scale inhomogeneities in the chemical composition of the particles. The most likely nucleating agents are local variations in the demagnetizing field. Considering surface imperfections, pits hinder the nucleation

process since their local fields oppose the applied reversing field, whereas a bump produces local fields that reinforce the applied field and encourage nucleation (Cullity, 1965, p. 403).

### 2.7.6 Becker's Model

Experimentally, the difference between absolute saturation and a magnetization that is a few tenths of a percent lower can go unnoticed, so reverse domains occupying a very small volume fraction of the particle can go undetected. Then, nucleation of a wall is no longer required, but rather only the *unpinning* of walls already existing within the material.

The coercivity of a particle cannot be predicted given the size and material, since details of the surface topography are essential. Becker (1967) showed that an additional factor could determine the measured coercivity of a particle, the magnitude of the magnetizing field. He noticed that coercivity increases with increasing applied fields in certain permanent magnets. For an unsaturated sample, this result is expected; however, the fact that the coercivity increases with the maximum value of the magnetizing field *after saturation* is very surprising (Figure 2.11). These results seem to indicate that the strength of a pinning site depends on how hard the wall is driven into it during the magnetizing process, although the mechanism for this is not understood. Furthermore, Becker has proposed that a single particle can have a number of pinning sites, each characterized by a field,  $H_n$ , required to nucleate or unpin a domain wall, and that the particular site that operates depends on the value of the previously applied field.

A hysteresis loop will exhibit low coercivity if walls are present and free to move.

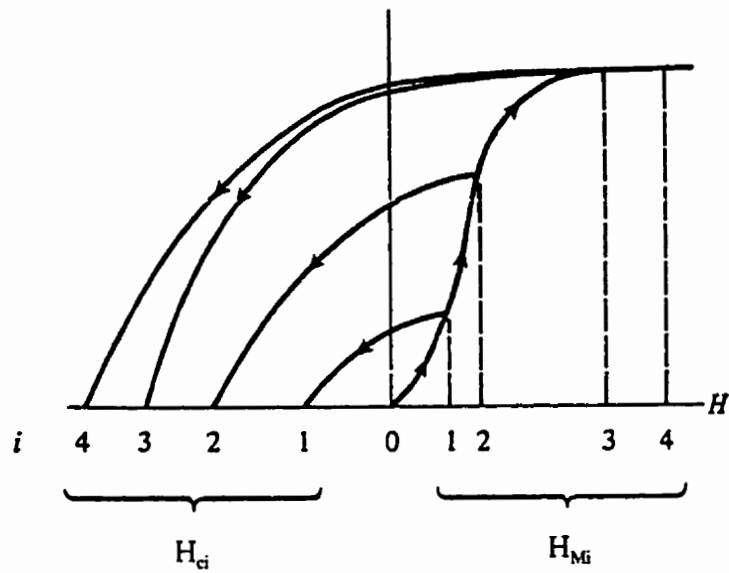


Figure 2.11 . A schematic diagram of the dependence of the coercivity  $H_{ci}$  on the maximum magnetizing field  $H_{Mi}$  (Becker, 1968, as cited by Cullity, Fig. 11.15a, 1972). Even after saturation (point 3)  $H_{ci}$  continues to increase if larger magnetizing fields are applied.

Moreover, if the defect concentration is sufficiently low, there is negligible resistance to wall motion, so, as shown in Figure 2.12, the loop is very narrow, having coercivity  $H_w$  and a slope  $\frac{1}{D}$ , where  $D$  is the demagnetizing factor (Cullity, 1972, p. 408). The loop saturates at a field  $H_D$ . Increasing the magnetizing field to  $H_M$ , walls are pinned so that nucleating fields are required to reverse wall motion. Depending on the nucleating field, the character of the loop can change dramatically. For a nucleating field,  $H_{n1}$ , the magnetization will drop and follow the upper wall branch and the coercive field will be that of the wall,  $H_w$ . For a nucleating field  $H_{n2}$ , the observed coercive field will also be  $H_{n2}$ . A square hysteresis loop results for a sufficiently large nucleating field  $H_{n3}$ .

Reversal nuclei may be material defects, but they may also be any small region of reverse magnetization enclosed by a locally pinned domain boundary (Becker, 1973). By this definition, the nuclei may be obliterated by a sufficiently high  $H_M$ . If the nucleating fields indicated in Figure 2.12 were of this type, applying a field  $H_M < H_D + (H_D - H_{n1})$  would yield a reversing field, determined by the site corresponding to the nucleating field  $H_{n1}$ , while for  $H_D + (H_D - H_{n1}) < H_M < H_D + (H_D - H_{n2})$ ,  $H_M$  is sufficiently large to remove this site, and  $H_{n2}$  would become the lowest nucleating field for reversal. By contrast, defects cannot be removed by field application and so, the strongest defect in the sample determines the reversing field  $H_n$ , where a *strong* defect is defined as one at which a *small* field can nucleate or unpin a wall. The larger the particle the greater the probability that it possesses a strong defect, due to the larger surface area.

By comparing the initial magnetization curve of a system with its major hysteresis loop, two different behaviours will be exhibited by hard magnets depending on the

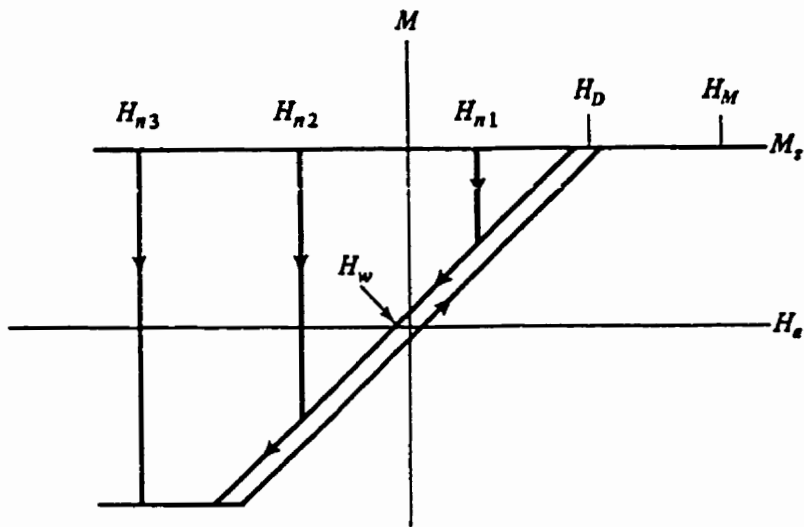


Figure 2.12 . Theoretical hysteresis loop of a single particle having defect nucleating fields  $H_{ni}$ , based on Becker's model (1969, as cited by Cullity, Fig. 11.16a, 1972). The loop saturates at a field  $H_D$ ,  $H_w$  is the wall coercive field, and  $H_M$  denotes the magnetizing field.

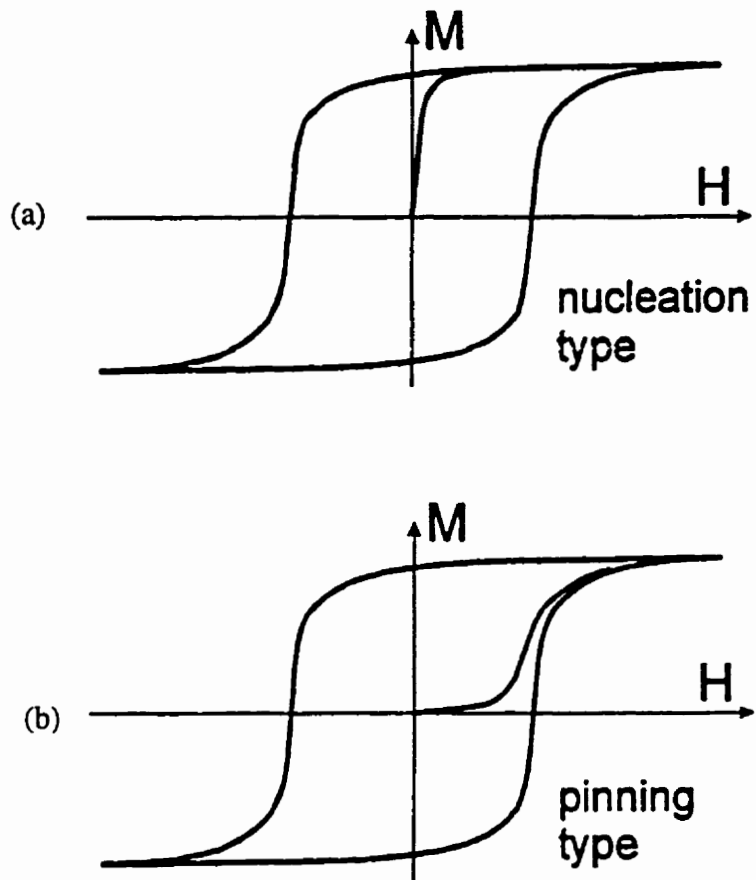


Figure 2.13 . A schematic representation of magnetization curves and hysteresis loops in (a) nucleation and (b) pinning type magnets (from Bertotti, Fig 10.10, 1998).

dominant mode of reversal (Figure 2.13). When *reversal nuclei* are present in the material, reverse domains already exist within a saturated region. If the initial magnetization curve is steep and saturation is reached in a field much lower than the saturated loop coercive field then this indicates freely moving walls where pinning effects are unimportant. If *pinned* walls are present in the material, stronger fields are required to move the walls and a field on the order of the saturation coercive field will be required to reach saturation along the initial magnetization curve.

## 2.8 Types of Magnetic Materials

### 2.8.1 Paramagnetism

In a paramagnetic material, the coupling between magnetic moments of individual atoms is small or zero. Thus, the magnetization of a paramagnet is only affected by the application of an external magnetic field and thermal agitation due to finite temperature. In zero external field, atomic moments assume random orientations in space because they are uncoupled and subject only to thermal agitation, and a net magnetization of zero results. A nonzero magnetization can be induced by application of an external field since the coupling between magnetic moments  $\vec{m}$  and an applied field  $\vec{H}$  energetically favours alignment of magnetic moments along the field direction according to  $E = -\vec{m} \cdot \vec{H}$ . Assuming classical dipoles, the magnetization exhibited by an ideal paramagnet, as a function of an applied field and temperature, can be expressed in a simple equation (Langevin, 1905)

$$M(H,T) = M_0 \left( \coth a - \frac{1}{a} \right)$$

where  $\coth a - \frac{1}{a}$  is called the Langevin function,  $a = \frac{mH}{k_B T}$  is a dimensionless parameter,

where  $m$  is the magnetic moment,  $k_B$  is the Boltzmann constant, and  $T$  is the temperature,

and the maximum possible magnetization is  $M_0$ . The result of a quantum mechanical

treatment, where only discrete moment orientations are allowed, is

$$M(H,T) = M_0 \left[ \frac{2J+1}{2J} \left( \coth \frac{2J+1}{2J} a' \right) - \frac{1}{2J} \coth \frac{a'}{2J} \right]$$

where the square bracketed quantity is the Brillouin function, with  $a' = \frac{m_H H}{k_B T}$  and  $m_H$

represents a component of the net magnetic moment of an atom along  $H$ . The Brillouin

function reduces to the classical Langevin result in the limit  $J \rightarrow \infty$ , a condition

corresponding to unrestricted orientations of the magnetic moment (Cullity, 1972, p.

105). For quantum spins  $S = \frac{1}{2}$ , there are only two possible orientations, and the

Brillouin function simplifies to  $M = M_0 \tanh a'$ . Regardless of whether a classical or a

quantum approach is used, the relationship between magnetization and field is linear at

low fields and high temperatures  $\left( \frac{mH}{k_B T} \ll 1 \right)$ , and a paramagnet exhibits no hysteretic

behaviour.

## 2.8.2 Ferromagnetism

Ferromagnetism is a label that describes materials with strongly coupled atomic

dipole moments that tend to be aligned parallel to each other. These materials can exhibit

a spontaneous magnetization,  $M_s$ , even in the absence of a magnetic field. This

spontaneous moment disappears when the material is heated above a certain temperature

called the ferromagnetic Curie temperature,  $T_C$ . The maximum possible value of  $M_s$  is

achieved only at absolute zero, but the value of the spontaneous magnetization is only weakly dependent on temperature below the magnetic ordering temperature, until the temperature exceeds  $0.75T_C$ . Then, the spontaneous moment rapidly decreases to zero at  $T_C$ . Above  $T_C$ , the material behaves paramagnetically.

Classically, ferromagnetism is treated phenomenologically, where a strong interaction between atomic dipoles is assumed to be proportional to the magnetization. This interaction can be considered equivalent to some internal magnetic field, as in the theory developed by Weiss (1907). The internal field is referred to as the molecular, Weiss, or exchange field, and can be written as  $H_m = N_m M$ , where  $N_m$  is the molecular field constant. For finite temperatures, the thermal energy of the atoms breaks alignment with this internal field, and so  $T_C$  defines the temperature at which thermal energy is sufficient to destroy the spontaneous magnetization. The size of the molecular field is several orders of magnitude larger than the demagnetizing or dipole-dipole interaction fields (Morrish, 1965, p. 261). Analogously, below  $T_C$ , ferromagnetism is given the same quantum mechanical treatment as paramagnetism (Section 2.8.1), except that the applied field,  $H$ , in the magnetization expression is replaced by the total field, a sum of the applied and molecular fields,  $H + N_m M$ , so that simultaneous equations must be solved to find the spontaneous magnetization  $M(T, 0)$ .

The shapes of hysteresis loops are affected by many factors including temperature and measuring technique, that is whether the applied field is parallel (square loops) or perpendicular (nearly linear loops) to the specimen's easy axis (Cullity, 1972, p. 348), as well as the type of magnetism exhibited by the system (Souletie, 1983). As discussed,

paramagnets exhibit no hysteresis, whereas ferromagnets are classic hysteretic systems (Figure 2.14). The thermal hysteretic behaviour of ferromagnets is characterized by a drop in both coercivity and saturation moment as temperature increases. These changes are a consequence of the loss of spontaneous moment with increasing temperature and the corresponding reduction in the energy barriers to flipping moment orientation, as these barriers generally depend on magnetization. For example, when the particle's coercivity is determined by shape anisotropy, and thus, by the magnetostatic energy (Section 2.2) of a spontaneously magnetized particle, the anisotropy constant varies as  $K \sim M_s^2$ . The equilibrium curve (Section 1.3) shown in Figure 2.14 resembles that of a two level system with no coercivity, hence switching can occur with a negligible applied field at all temperatures.

### 2.8.3 Ferrimagnetism

In a ferromagnetic system, all atomic moments positioned on a lattice are coupled and spontaneously align in parallel; however, some magnetic systems have coupling that can be described in terms of a sublattice structure. Atoms occupying sites on the same sublattice possess moments that are coupled to each other and aligned parallel to one another. Magnetic moments of atoms on different sublattices lie antiparallel to one another. Where the magnitude of these moments are identical, the system exhibits *antiferromagnetism*; however, when the atomic moments residing on different sublattices are not the same, the result is a net moment and the system is described as *ferrimagnetic*. The strict definition has been broadened to include more than two sublattices.

Ferrimagnets also exhibit critical behaviour and the temperature above which the

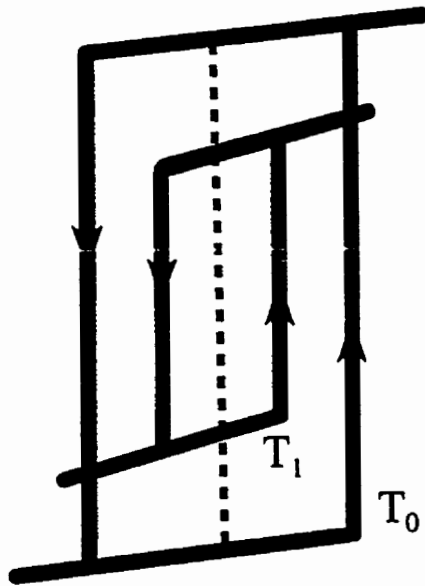


Figure 2.14 . A schematic representation of a hysteresis loop and its evolution with temperature ( $T_1 > T_0$ ) in the case of a ferromagnet (after Souletie, Fig. 9a, 1983). Both the amplitude and coercivity are reduced by increased temperature. The equilibrium curve for the system is given by the dashed line.

spontaneous magnetization vanishes is referred to as the Curie or Néel temperature . Like ferromagnets, this class of materials possesses a spontaneous magnetization that arises from long-range order, and displays hysteresis similar to that observed in ferromagnets.

#### 2.8.4 Superparamagnetism

The existence of superparamagnetic particles was first predicted by Néel (1949). Superparamagnetic particles behave much like paramagnetic particles, but their magnetic moments are much larger. In a superparamagnetic particle, the entire assembly of spins is thermally excited to rotate together to overcome the potential barrier due to anisotropy. The coercive force is decreased by thermal excitation and the process requires a time that is dependent on particle size.

The energy of a single domain particle with uniaxial anisotropy depends on the angle between the magnetization vector and the particle's easy axis,  $\theta$ . The energy as a function of angle is given by  $E = \frac{1}{2}CV \sin^2\theta$ . In zero applied magnetic field, the height of the energy barrier is  $\frac{1}{2}CV$ , where  $C$  is the anisotropy constant and  $V$  is the particle volume. This anisotropy can be due to shape, in which case  $C = (N_a - N_c)M^2$ , where  $N_a$  and  $N_c$  are demagnetizing factors for an ellipsoid.  $C$  can also refer to the crystalline anisotropy, in which case  $C = 2K$ . If anisotropy is due to strain then  $C = 3\lambda_s\sigma$ , where  $\lambda_s$  is the saturation magnetostriction, or the change in length per unit length when the sample is saturated, and  $\sigma$  is the applied tension. Obviously, two energy minima exist and so, in the absence of any perturbation, the magnetization will lie along the easy axis at an angle  $\theta$  equal to 0 or  $\pi$ . The magnetization can reverse direction if the energy barrier separating the two states is exceeded. This can be initiated by thermal agitation if the volume of the

particle is small, or the temperature is high.

The reversal process is characterized by a relaxation time,  $\tau$ , the time for the magnetization to decrease to  $1/e$  or 37% of the initial value. Consider a powder of uniaxial particles whose easy axes are aligned along the z-axis. The sample's magnetization has been saturated in the direction of alignment by a magnetic field applied along the z-axis. In the absence of the field the magnetization will decay from a value  $M_0$  according to

$$M = M_0 e^{-\frac{t}{\tau}}$$

where  $\frac{1}{\tau}$  is proportional to the Boltzmann factor  $e^{-\frac{1/2CV}{kT}}$ , which gives the probability that a particle has enough thermal energy to overcome the energy barrier, as required for reversal. The upper limit for the inverse relaxation time,  $\frac{1}{\tau}$ , is the frequency of precession from the +z to the -z direction (Morrish, 1965, p. 361). This frequency is given by  $\frac{\gamma H_c}{2\pi}$  where  $\gamma \approx 10^7$  and  $H_c = \frac{C}{M} \approx 10^2$  or  $10^3$  in real particles (Morrish, p. 267 & p. 361), and is the equivalent applied field necessary to produce a magnetization in a stable particle. Thus,  $\frac{1}{\tau} \approx 10^9 e^{-\frac{1/2CV}{kT}}$ , assuming coherent reversal. For incoherent reversal mechanisms, the energy barrier is reduced. Furthermore, applied fields also modify these results, essentially reducing the energy barrier (Chikazumi, 1964, p. 313).

A critical size, for which superparamagnetic behaviour is expected, can be determined using  $\tau = 100$  s. This value is rather arbitrarily selected and is the approximate time required for a remanence measurement (Cullity, 1972, p. 413). Increasing this time parameter by an order of magnitude only changes slightly the

predictions of critical dimensions. Above the critical size the magnetization is stable, while below the critical dimension, an assembly of particles is always in thermal equilibrium and exhibits superparamagnetism. A small change in particle size drastically changes the relaxation time constant. In fact, a 30% change in particle diameter changes  $\tau$  by a factor of  $10^9$ .

Moreover, this condition for stability against thermally activated transitions can be used to predict the temperature at which the thermal energy of the particle is insufficient to make an overbarrier transition. This temperature is called the *blocking temperature*,  $T_B$ . Substitution of  $\tau = 100$  s into the expression for  $\frac{1}{\tau}$  yields  $\frac{1}{2}CV \approx 25kT$ , and for a given particle shape and volume, the temperature that satisfies this equality is  $T_B$ .

For an assembly of superparamagnetic particles possessing no anisotropy, the classical theory of paramagnetism applies above  $T_B$  since the moment of each particle can point in any direction, and the Langevin function describes the character of the magnetization. For a finite anisotropy, where easy axes are aligned with each other and with the field, the orientations of the moments are severely restricted, so quantum theory applies and a hyperbolic tangent magnetization curve is expected. In the general case of nonaligned particles with finite anisotropy, neither equation applies.

Furthermore, neither of these forms of magnetization curves can actually be observed since the theories which lead to these equations assume uniform particle size and moment, but there is usually a distribution of particle sizes and the moment per particle is not uniform. This results in a distribution of blocking temperatures. Above the highest blocking temperature, the assembly behaves paramagnetically, while below the

lowest blocking temperature the individual moment orientations are fixed. However, the moment of the particle is still free to grow with decreasing temperature by virtue of the temperature dependence of its spontaneous moment.

For a superparamagnetic sample, magnetization curves at different temperatures always superimpose when the magnetization is plotted against  $H/T$  (Cullity, 1972, p. 411). There is no hysteresis; the coercivity and remanence are zero. Hysteresis will appear when particles of a particular size are cooled below a certain temperature (blocking temperature), or alternatively, when particles of increasing size are investigated at constant temperature. Because of the distribution of particles sizes and blocking temperatures, the hysteresis loops are somewhat rounded (Figure 2.15). The thermal character of the superparamagnetic hysteresis loop differs greatly from that of a ferromagnet. Although coercivity drops with increasing temperature as a consequence of the increased thermal energy available for transition, the saturation moment remains almost the same. In the superparamagnet region the moment is relatively constant if, as is generally the case, the temperature is well below the critical temperature of the system. Temperature strongly affects the equilibrium curves shown in the figure. The steepness of the curve depends inversely on temperature through  $M = M_0 \tanh a'$  where  $a' = \frac{m_H H}{k_B T}$  (Section 2.8.1) so, for low fields, increasing temperature decreases the slope of the equilibrium curve.

### 2.8.5 Spin Glasses

Spin glasses are a class of magnetic materials whose atomic spins are disordered in terms of both their location and the interatomic interactions. Spin glasses display a

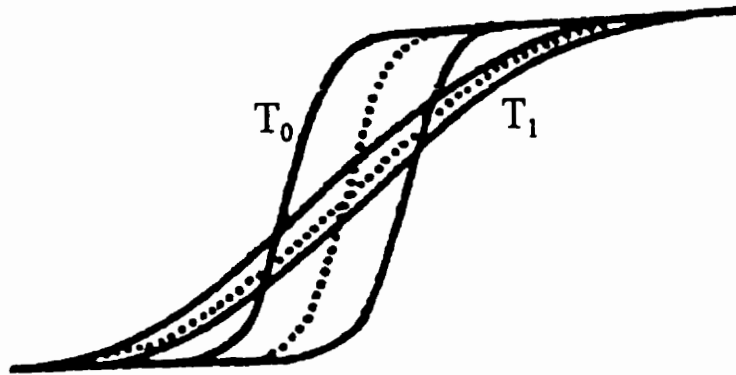


Figure 2.15 . Schematic shape and evolution with temperature ( $T_1 > T_0$ ) of the hysteresis cycle for a superparamagnet (after Souletie, Fig. 9b, 1983). Temperature strongly affects the equilibrium curves (dashed lines).

*coexistence* of both ferromagnetic and antiferromagnetic couplings, due to the structural disorder. An atom of a given spin may not be able to orient itself to satisfy its interaction with all the other atoms in the spin glass, and this is called *frustration*. Physically, a *canonical* spin glass is defined as a dilute, random distribution of magnetic impurities in a nonmagnetic host metal.

Consider three spins as shown in Figure 2.16, where Spin A interacts ferromagnetically with Spin B and antiferromagnetically with Spin C, but the interaction between Spins B and C is ferromagnetic. If Spin C aligns with Spin A it violates the ferromagnetic interaction with Spin B, but if it aligns itself with Spin B it violates the antiferromagnetic interaction with Spin A. Thus, there is no way to satisfy all alignment requirements simultaneously and the system is said to be frustrated. The result is that a spin glass system can have several low-energy states based on the minimum number of interaction violations within the system.

There is still controversy over whether a spin glass is a genuine magnetic phase or simply a paramagnet whose dynamic properties are sufficiently slowed so as to appear to constitute a static phase, analogous to common glass, which appears to be a solid, but is really a liquid flowing at an astonishingly slow rate. Both infinite range and short range theories of spin glasses have been proposed, and they are discussed in detail by Fischer and Hertz (1991).

The hysteretic properties of spin glasses are somewhat different from those described for ferromagnets and superparamagnets (Figure 2.17). The sole effect of increasing temperature is a narrowing of the loop. The saturation moment remains

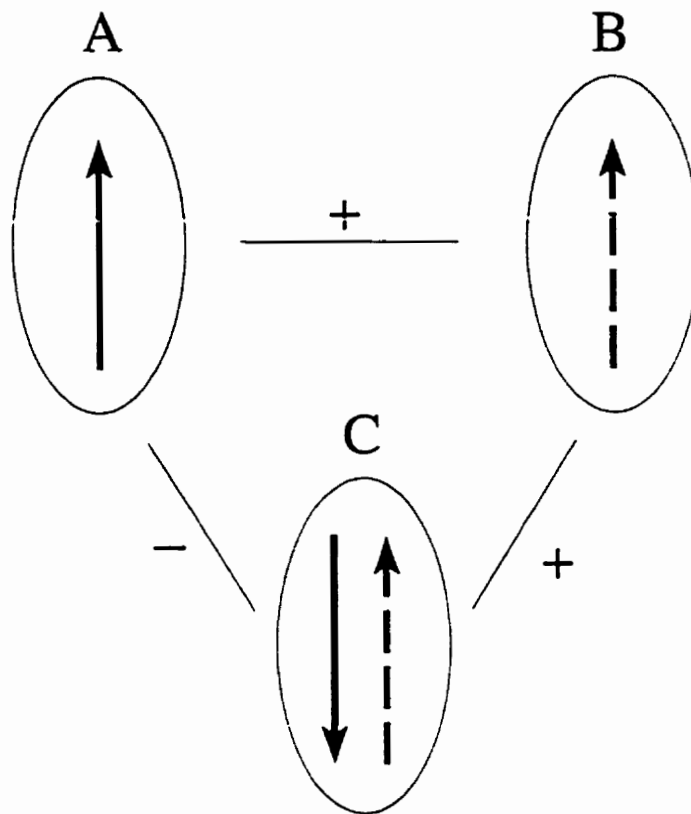


Figure 2.16 . A frustrated three spin system. If the ferromagnetic interaction between spins A and B, the ferromagnetic coupling between spins A and C and the antiferromagnetic coupling between spins B and C *cannot* be satisfied simultaneously. Ferromagnetic couplings are indicated by “+”, while antiferromagnetic couplings are marked “-.”

unchanged with respect to temperature, as expected for systems which exhibit a constant moment under field cooled conditions (3.7). For this reason, the equilibrium curves generated for spin glasses are also nearly completely independent of temperature (Souletie, 1983).

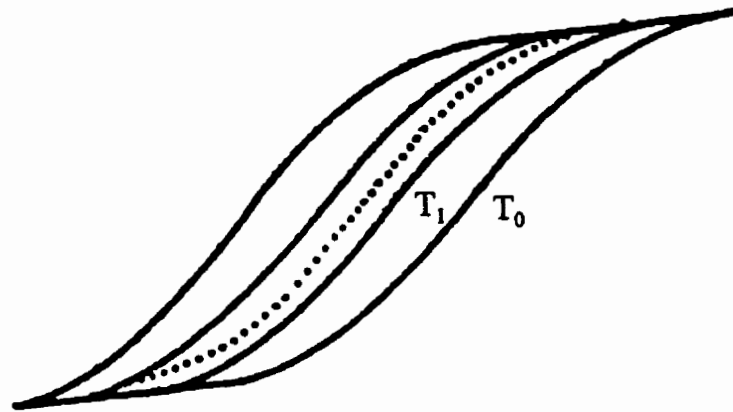


Figure 2.17 . Hysteresis loops for a spin glass system at temperatures  $T_1 > T_0$  (after Souletie, Fig.9c, 1983). The equilibrium curve (dashed line) does not depend on temperature.

## Chapter 3

### Preisach Model: Generalizing the Formalism

First regarded as a physical model of *magnetic* hysteresis when F. Preisach published his paper in 1935, the Preisach model makes several plausible hypotheses concerning the physical mechanisms of magnetization, and its fundamental simplicity is quite attractive for the study of hysteresis. A better understanding of the general nature of the model was achieved when Krasnosel'skii separated the model from its physical meaning and represented it in purely mathematical form (Krasnosel'skii & Pokrovskii, 1983, as cited by Mayergoyz, 1991). This mathematical description can be used to replicate hysteresis processes of different physical origins. The Preisach model as applied in magnetics (Section 3.1), is often criticized for making unsatisfactory physical interpretations and the mathematical approach is preferred by some because its treatment of hysteresis, based on hysteresis operators, does not encounter the difficulties inherent in connecting the model to physical definitions (Mayergoyz, 1991). Nonetheless, recent

interest in the Preisach model has been spurred by its potential to clarify the interpretation of Henkel plots (Section 3.4), widely used to characterize interaction effects in a wide variety of magnetic materials.

### 3.1 Scalar Preisach Model

The Scalar Preisach Model (SPM) describes macroscopic hysteresis phenomena by superposing a continuum of elementary asymmetric rectangular hysteresis loops. An elementary hysteresis loop as depicted in Figure 3.1a represents a magnetic *pseudoparticle* having moment  $\mu$ , and two possible magnetic states  $\varphi = \pm\mu$ , corresponding to moment orientations that are up or down. The field at which the particle flips from  $-\mu$  to  $+\mu$  is the up-switching field,  $\alpha$ . Theoretically, this switching field can assume any value  $-\infty < \alpha < +\infty$ . The down-switching field, where the moment flips from  $+\mu$  to  $-\mu$ , is given by  $\beta$  where  $-\infty < \beta < \alpha$ , since the down-switching field must always be less than the up-switching field. To avoid the difficulties inherent in the physical interpretation of this magnetic form of the Preisach model, the term “pseudoparticle” has been used, rather than explicitly connecting the elementary hysteresis loops to real magnetic particles. In the Preisach model, no reference is made to the shapes or spatial location of these particles within the system (Mayergoyz, 1991).

An ensemble of these loops can be described by a distribution  $p(\alpha, \beta)$  or alternatively,  $p(h_c, h_s)$ , called the *Preisach distribution* where  $h_c = (\alpha - \beta)/2$  is the elementary loop coercive field, which is the half-width of the loop, while  $h_s = (\alpha + \beta)/2$  is an asymmetry field, which measures the shift of the loop with respect to the origin

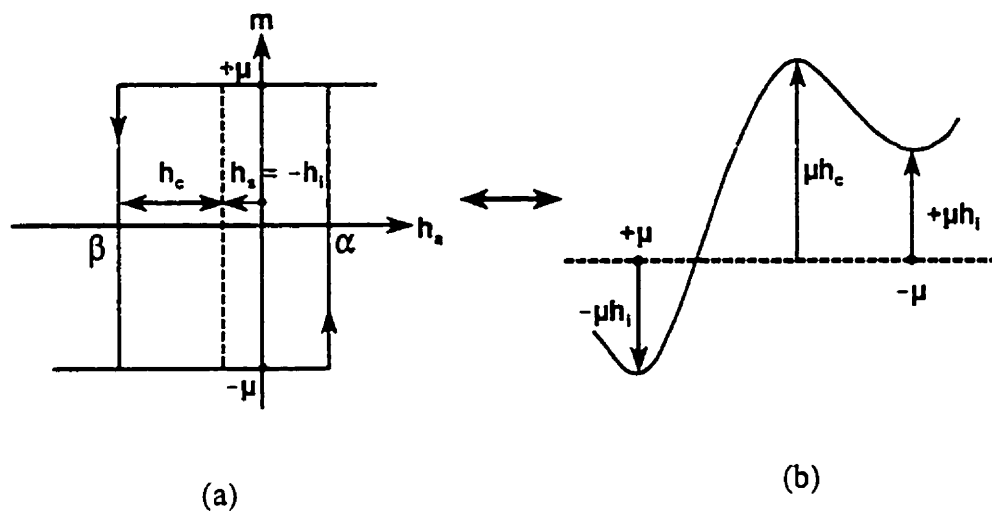


Figure 3.1 . (a) An elementary Preisach hysteresis loop with states  $m = \pm\mu$ , a shift field  $h_s = -h_i$ , where the interaction field is  $h_i > 0$ , and a coercive field  $h_c$ . (b) The double well potential corresponding to the hysteresis cycle in (a) when  $h_a = 0$ .

(Figure 3.1a). For an isolated particle, there is no mechanism that can shift the loop from its symmetric position about zero field; the shift is a consequence of *interactions* with adjacent particles. Consequently, the shifted loop can be described in terms of an interaction field,  $h_i$ , where  $h_i = -h_s$  and is the preferred notation to illuminate the physics of the model. These two loop parameters are generally assumed to be independent of each other (Basso & Bertotti, 1994), and so the Preisach distribution can be factored into a product of two functions, such that  $p(h_c, h_s) = f(h_c)g(h_s)$ . The coercive field is an intrinsic property. Physically, the distribution of coercive fields  $f(h_c)$  is a consequence of fluctuations in the anisotropy constants or in the spontaneous magnetization of a particle. The shifted loops, invoked in the magnetic Preisach model, are criticized as being unphysical for single particles (Mayergoyz, 1991). However, when considered as a consequence of interactions between particles, which implies that particles feel the sum of the applied field and a field due to adjacent particles, a distribution of shift fields can result from variations in the internal field due to variations in particle size, shapes, or spacing. The resulting distribution is utilized in calculations despite the absence of an explicit inclusion of these parameters in the model. Treating the shift field as a measure of local interactions that are random,  $g(h_s)$  must be symmetric about  $h_s = 0$ , mirroring the symmetry of macroscopic hysteresis loops. Moreover, this symmetry ensures that  $p(h_c, h_s) = p(h_c, h_i)$  because  $g(h_s) = g(-h_i) = g(h_i)$ .

The simplest metastable system is a double well potential with two possible configurations and two local minima whose energies are a function of some external parameter. Particles represented by an elementary Preisach hysteresis loop can be

equivalently represented by such a two level potential energy diagram. Figure 3.1 shows the equivalence between the particle hysteresis loop and energy well representations.

Applying a magnetic field effectively alters the barrier height, by changing the depth of the potential wells as shown in Figure 3.2. Thus, the barrier can be ostensibly removed by applying a sufficiently large field.

### 3.2 Moving Preisach Model

If, in addition to local random interactions, the system also possesses a global induced interaction field  $h_m = km$ , then the original local interaction field  $h_i$  is supplemented by  $km$  to produce a total effective interaction field

$$h_i' = h_i + km$$

Also,

$$\alpha - \alpha' = \alpha - km$$

$$\beta - \beta' = \beta - km$$

so the switching of the particle now takes place at applied fields  $h_a = (\alpha', \beta')$  instead of  $h_a = (\alpha, \beta)$ . Alternatively, the new distribution,  $p'(h_c', h_i')$ , of coercive fields,  $h_c'$ , and total interaction fields,  $h_i'$ , is

$$p'(h_c', h_i') = p(h_c, h_i) = p(h_c, h_i' - km)$$

so, the new distribution is just the original distribution shifted by  $km$  along the original  $h_i$ -axis. Figure 3.3a shows this effect on the Preisach plane.

The Moving Preisach Model (MPM) is a state-dependent generalization of the Scalar Preisach Model, in which the distribution function itself is allowed to evolve in

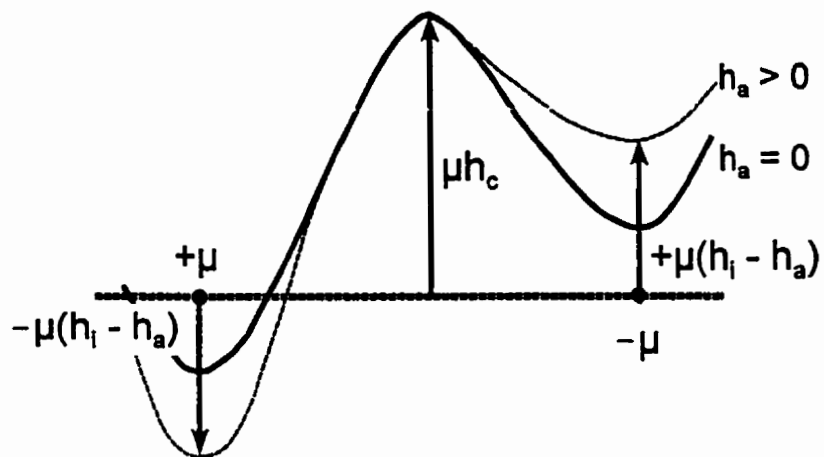


Figure 3.2 . Applying a magnetic field  $+h_a$  changes the depth of the potential wells (dashed lines), effectively increasing the barrier height for the  $+$  to  $-$  transition by  $\mu h_a$ , while decreasing the barrier height for the  $-$  to  $+$  transition by  $\mu h_a$ .

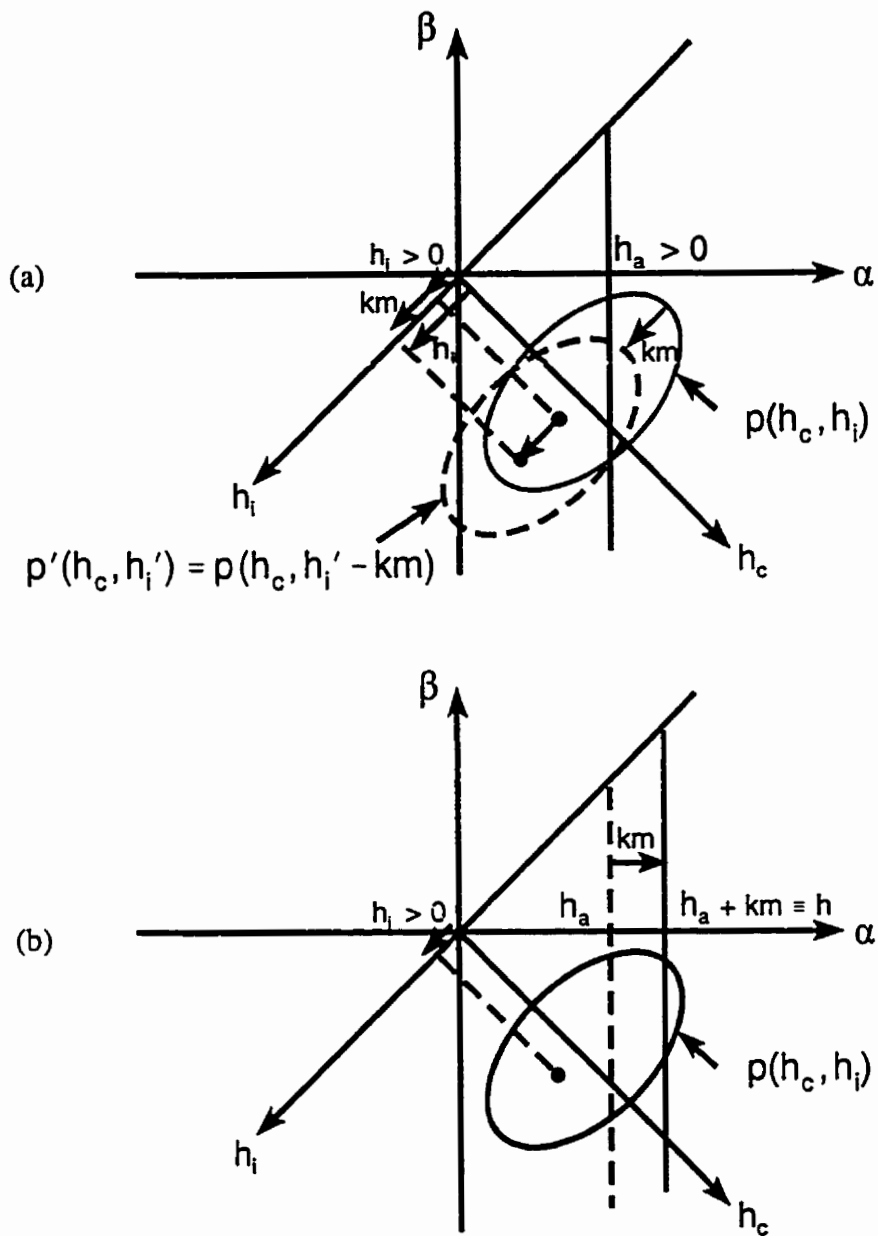


Figure 3.3 . (a) In the Moving Preisach Model, the Preisach distribution  $p(h_c, h_i)$  shifts by  $km$  along the original  $h_i$ -axis. (b) To first order, this is the same as replacing the applied field with an effective field  $h = h_a + km$ .

response to changes in the macroscopic magnetization of the system (Della Torre, 1966). The moving, or mean field, parameter  $k$  reflects a more realistic picture of interaction fields, which are expected to be symmetrically distributed around a magnetization-dependent mean  $\langle h_{int} \rangle = km$ . Vajda and Della Torre (1993) showed that to first order shifting the Preisach distribution is equivalent to magnetizing the original Preisach plane with the SPM, but replacing the applied field with an effective field,

$$h = h_a + km(h) \quad (3.1)$$

where the regenerative contribution  $km(h)$  is necessarily explicitly dependent on the field (Figure 3.3b). This allows us to retain the original switching fields of the particle.

If  $k > 0$ , the physical origin of this mean field can be considered similar to that of a molecular field, resulting from strong ferromagnetic interactions favouring *collective* alignment of the moments along the same direction. The degree of alignment is measured by the magnetization and to a first approximation, the molecular field can be written as  $H_m = N_m M$  (Section 2.9.2). A mean field term can also result from the presence of domain walls (Bertotti, 1998, p. 452). The magnetostatic, or self energy of a body, associated with dipolar interactions, can also contribute to a mean field effect with  $k < 0$ ; its associated demagnetizing field is proportional to the magnetization (Section 2.2). This means that both interactions and shape effects can combine into a global mean field described by a single phenomenological mean field parameter,  $k$ .

The MPM introduces a skew transformation for the hysteresis loops generated by the SPM. As shown in Figure 3.4, an oblique line passing through the origin of the magnetization versus effective field identifies zero applied field, and this axis is

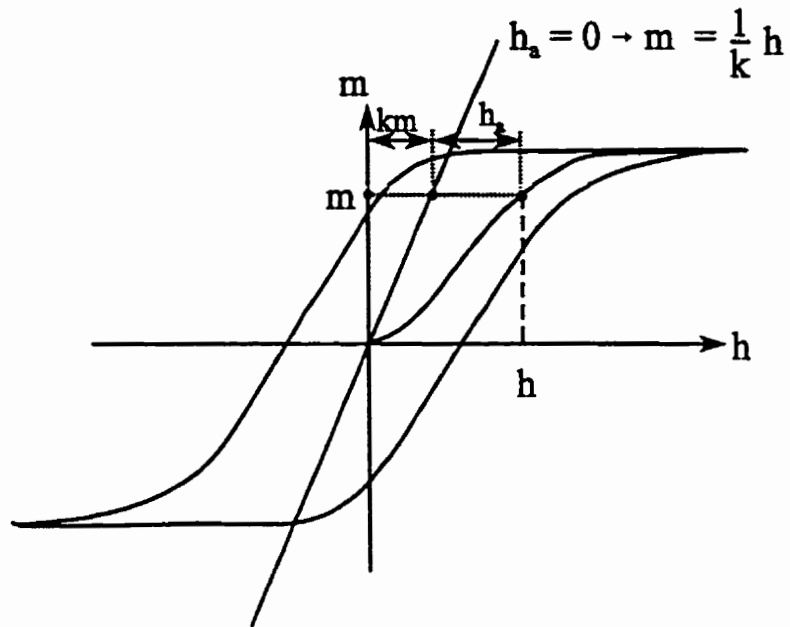


Figure 3.4 . Skew transformation. The oblique line having slope  $\frac{1}{k}$  and passing through the origin of the magnetization  $m$  versus the *effective* field  $h$ , identifies the location of zero *applied* field, which corresponds to a magnetization  $m = \frac{h}{k}$ .

equivalent to a magnetization,  $m = \frac{h}{k}$ . In Preisach calculations, the same hysteresis loop will result regardless of the mean field parameter if the magnetization is plotted against the effective field. Generating hysteresis curves as a function of the applied field reveals mean field effects. The characteristics of these loops can be seen qualitatively from the skew transformation. For positive values,  $k > 0$ , the saturation remanence increases over its mean field-free value, the initial magnetization process is faster, and the hysteresis loop is steeper; whereas for negative values of this parameter, the saturation remanence is reduced and the magnetization varies more slowly with increasing field. The coercivities are *not* affected by the mean field term.

### 3.3 Preisach Plane

A special diagrammatic technique, developed by Preisach, constitutes the mathematical foundation for magnetic calculations using this model. This geometric interpretation utilizes the Preisach plane (Figure 3.5). The energy level representation of Preisach particles and their corresponding elementary loops are included in the diagram to show the significance of the three relevant quadrants of the plane. Recall that no particles can exist above the diagonal  $\alpha = \beta$ ; that region of the plane is *forbidden* for physical reasons, as particles must have down-switching fields that are less than their up-switching fields. For quadrants I and III, only one energy minimum exists in zero field. The energy levels are degenerate along the coercive field axis since  $h_i = 0$ . In the fourth quadrant, the energy minima are nondegenerate with an “up” state energetically favoured beneath the  $h_c$ -axis, and the “down” state favoured above it.

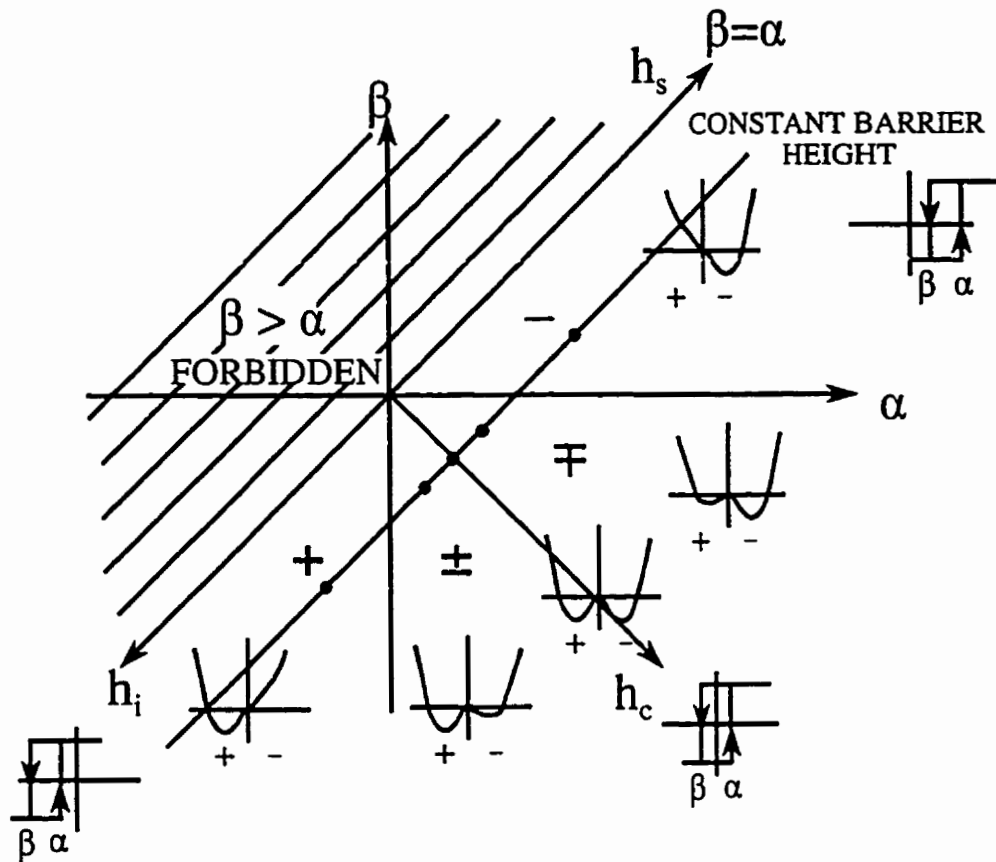


Figure 3.5 . The Preisach Plane. The energy level representation and corresponding elementary particle hysteresis loops for selected particles. In Quadrant I and III, particles possess only one energy minimum, corresponding to the “+” state in Quadrant III and the “-” state in Quadrant I. Along the coercive field axis,  $h_c$ , the energy levels are degenerate, corresponding to a centred loop. In Quadrant IV, the energy minima are nondegenerate and the “+” state is favoured beneath the  $\alpha$ -axis, while the “-” state is favoured above it.

### 3.3.1 Using the Preisach Plane

The magnetization induced by applying a positive field, is simulated by sweeping a vertical line across the plane to a value of field  $\alpha = +h_a$  (Figure 3.6a). The region between the  $\beta$ -axis and the vertical line represents the particles that have transition barriers that are less than the applied field,  $h_c - h_i < h_a$ . The magnetizing remanence is depicted by sweeping a horizontal line, beginning at the intersection point of the applied field line and the  $h_i$ -axis, down to the  $\alpha$ -axis, representing zero applied field (Figure 3.6b). In general, the demagnetization process, in negative applied fields, involves sweeping horizontal lines downward to  $\beta = -h_a$ . Calculating the moment at any given stage is accomplished by integrating over the entire plane, accounting for the state  $\phi(h_c, h_i, h)$  of each particle within the Preisach distribution:

$$m = \int \int_{h_c, h_i} \phi(h_c, h_i, h) p(h_c, h_i) dh_i dh_c .$$

### 3.3.2 The Demagnetized Plane

When we refer to an initially demagnetized state, it refers to the origin of the hysteretic plane  $M = H = 0$  that also lies on the anhysteretic curve (Section 1.3). This state is commonly generated by ac demagnetization, dc demagnetization, or thermal demagnetization. Figure 3.7 depicts the Preisach plane representation of these states. Ac demagnetization is experimentally ensured by saturating a specimen with a sufficiently large applied magnetic field and oscillating the field with ever-decreasing amplitude. The Preisach plane resulting from the ac demagnetizing procedure (Figure 3.7a) is the *lowest* zero-field energy state possible since all the higher energy metastable states are vacant

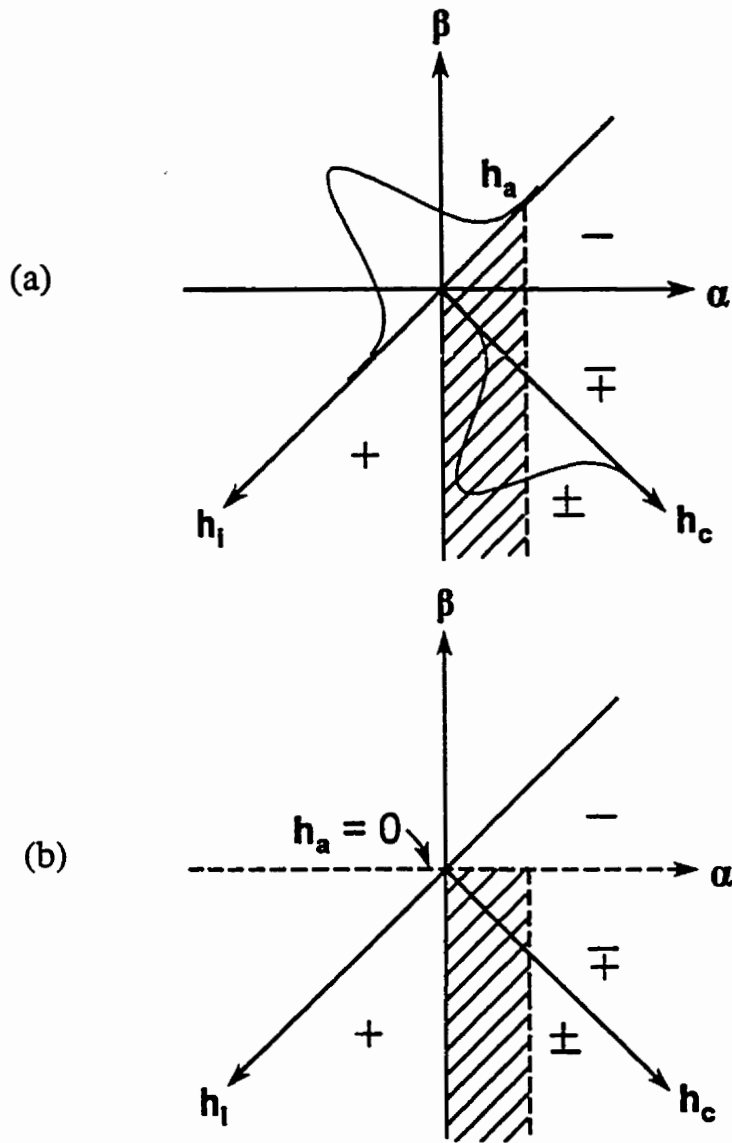


Figure 3.6 . The Preisach plane is used to calculate the total moment of the system it represents. (a) The distribution of particle interaction and coercive fields is shown.

Applying a positive field  $h_a$  (dashed line) flips the moment of all particles originally in the “-” state that have transition barriers less than  $h_a$ . These particles lie in the shaded region of the plane. (b) The particles which contribute to the magnetizing remanence when  $h_a$  is reduced to zero are included in the shaded area.

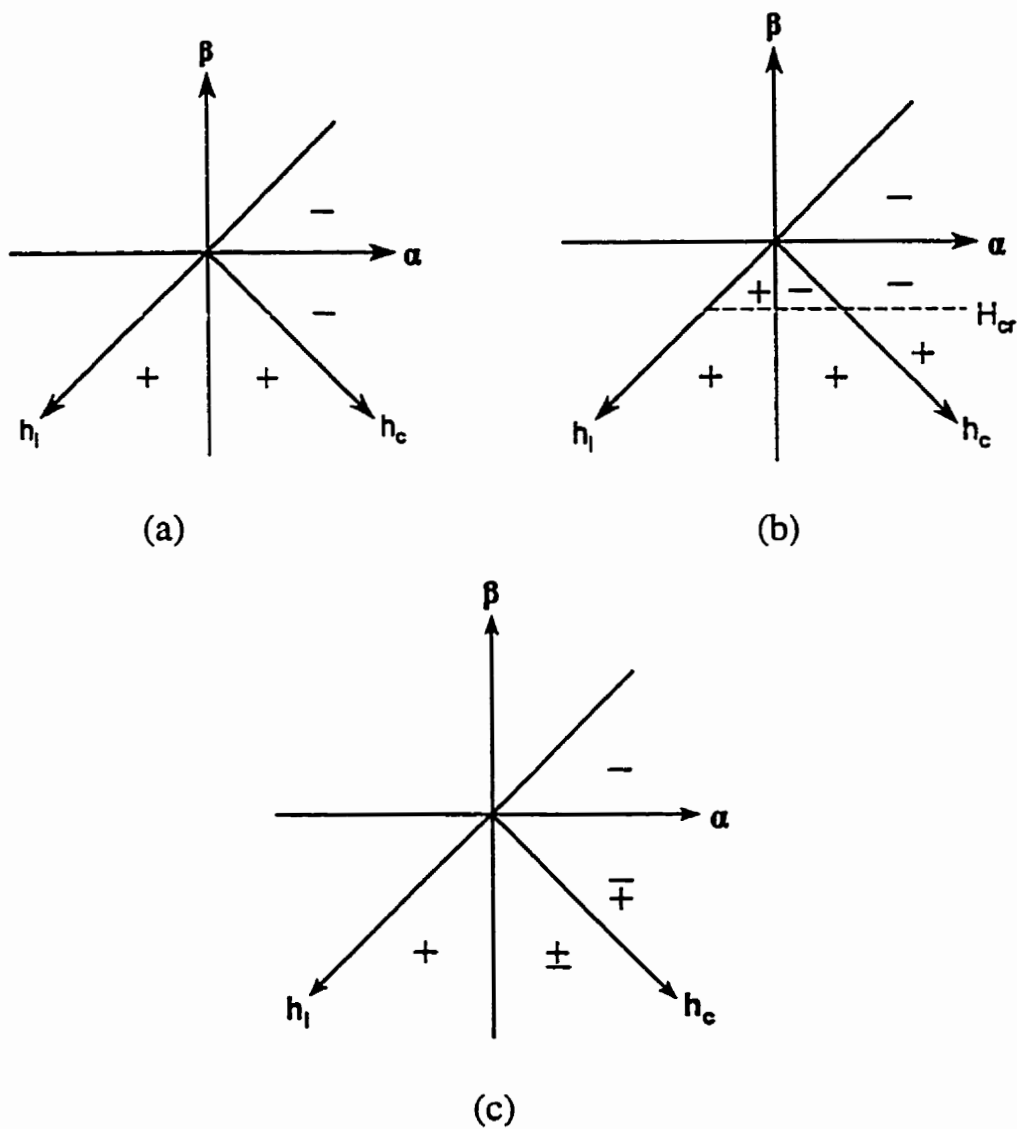


Figure 3.7 . Preisach planes depicting (a) the ac demagnetized state, (b) a dc demagnetized state, where  $H_{cr}$  is the remanent coercive field, and (c) the thermally demagnetized state where occupation probabilities of both energy minima are non-zero in the fourth quadrant. Equal occupation probabilities ( $1/2, 1/2$ ) mean that the plane depicts a random thermally demagnetized state.

and only the lowest energy levels are occupied. The probability ( $p_-$ ,  $p_+$ ) of a pseudoparticle occupying its two allowed states ( $-\mu$ ,  $+\mu$ ) is therefore expressed as (0,1) for particles below the coercive field axis or (1,0) for the particles above it. Dc demagnetization (Section 1.3) is most simply performed by returning the field to zero from the remanent coercive field, and its character in the plane is strongly dependent on the Preisach distribution of pseudoparticles (Figure 3.7b). When thermal energy is sufficiently large, the two pseudoparticle states are essentially degenerate, since the thermal energy not only exceeds the energy barriers, but is also much greater than the difference between the energies of the states. Thus, if the system is cooled in zero field, from a very high temperature, the particles may be frozen into a random state. This is the thermally demagnetized state, which defines a Preisach plane where each particle is equally likely to be found in either of the two local energy minima (Figure 3.7c). Both minima only exist in the fourth quadrant of the plane and here the occupation probability for the two states is expressed as ( $1/2, 1/2$ ). Mitchler, Dahlberg, Engle and Roshko (1995) linked these random occupation probabilities, important in the analysis of magnetization properties using Henkel plots (Section 3.4), to the physically significant thermal demagnetization procedure that can be used to achieve it (Section 3.4.4).

### **3.4 Henkel Plots**

Recently there has been a considerable revival of interest in the Preisach model and particularly in its potential to improve the interpretation of Henkel plots (Henkel, 1964). Henkel plots are parametric plots of the demagnetizing remanence as a function of

the magnetizing remanence, with the applied field acting as an implicit matching parameter. They are used extensively to characterize interactions in magnetic materials. Henkel plots naturally lie between two limits, an upper limit, given by the Wohlfarth relation  $i_d = i_\infty - 2i_m$  (Wohlfarth, 1958), and a lower limit, given by  $i_d = -i_m$ .

### 3.4.1 Wohlfarth Relation Derivation

Following the analysis of Stoner and Wohlfarth (1948), the properties of an assembly of single domain particles can be determined by treating the collection as a superposition of single-particle contributions, where interactions between particles are neglected. A uniaxial particle possesses two energetically equivalent states in zero applied field. The minima correspond to opposite magnetization states. The axis of particle magnetization is determined by anisotropy and the field history determines which direction the magnetization assumes. In an assembly of particles, there is a distribution of anisotropy axes as well as a distribution of populations over the energy minima.

Consider an assembly of particles with aligned easy axes that have a distribution of coercive fields or energy barriers and which have an *equal* probability of existing in either orientation in the demagnetized state. Applying a field, along the common easy axis to saturate the assembly, results in one half of the particles changing their orientation, so that all moments lie in the same direction. Reducing the field to zero yields a saturation remanence  $i_\infty$ , equal to the saturation magnetization. If a reverse field,  $-h_a$ , is applied, then all particles having coercive fields,  $h_c$ , less than  $h_a$  switch, and returning the field to zero yields the demagnetizing remanence  $i_d$ . The *loss* of magnetization from the saturation remanence is simply equal to twice the magnitude of the magnetizing

remanence,  $i_m$ , found by applying and then removing a field  $+h_a$  to the original demagnetized state. This is evident since these particles with  $h_c < h_a$  are the same particles activated by the demagnetizing field and the factor of two arises from the fact that in the original demagnetized state both minima are equally populated and only half of the particles switch. This yields the well-known Wohlfarth relation  $i_d = i_\infty - 2i_m$ .

The Wohlfarth relation is expected to hold for an assembly of independent, single-domain particles. The particles must be uniaxial as well as non-interacting because the symmetry of the loop, assumed in deriving the Wohlfarth relation, is destroyed when an interaction field contributes to the external field. However, it is *not* necessary for the axes to be aligned. Randomly oriented easy axis yield the same result because the particles are always in pairs with opposite magnetic moments. In the Preisach Model, the Wohlfarth relation holds when elementary loops exhibit *no* shift along the field axis

$p(h_c, h_i) = f(h_c)\delta(h_i)$ . This relation also applies to domain walls moving through a fixed distribution of pinning sites (McCurrie & Gaunt, 1964). In terms of a graphical relation, a Henkel plot of the Wohlfarth relation yields a straight line as shown in Figure 3.8.

### 3.4.2 The Lower Limit

The key to understanding deviations from the Wohlfarth relation lies in the initial population that is active during the magnetizing process. Referring to Figure 3.9, under random, or thermally demagnetized conditions the “magnetizing” metastable (higher energy) state is occupied with probability  $1/2$ , as was implicit in the derivation of the Wohlfarth relation. By contrast, ac demagnetization leaves the system in its lowest energy state, so that all metastable states are initially unoccupied. Under these conditions,

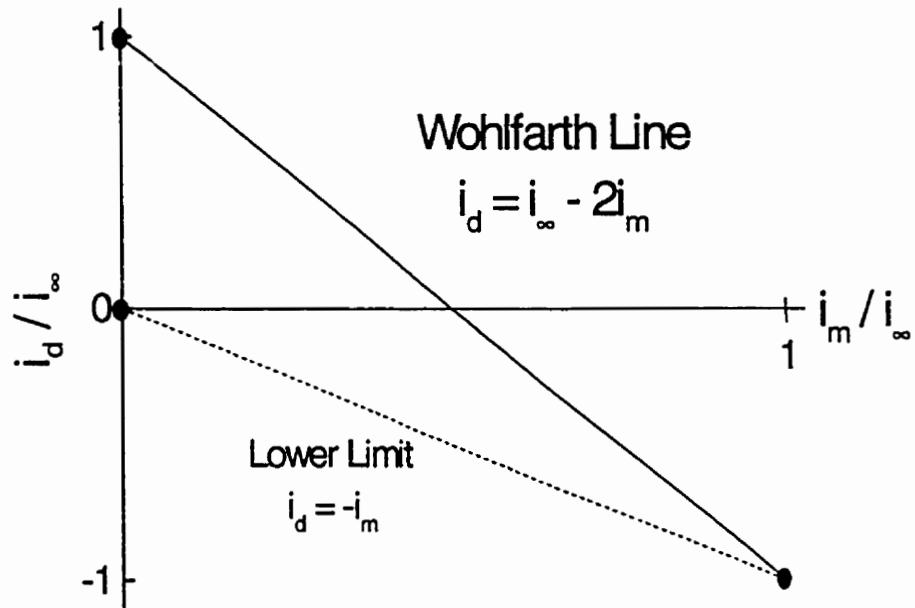


Figure 3.8 . The Wohlfarth line and lower limit line for Henkel plots. The Henkel plot resulting from an assembly of particles which have equal probability of existing in either “+” or “-” orientation in the demagnetized state (random thermal demagnetization) is the Wohlfarth line. The lower limit defines the greatest deviation from the Wohlfarth line that can occur when all metastable states are unoccupied (ac demagnetization).

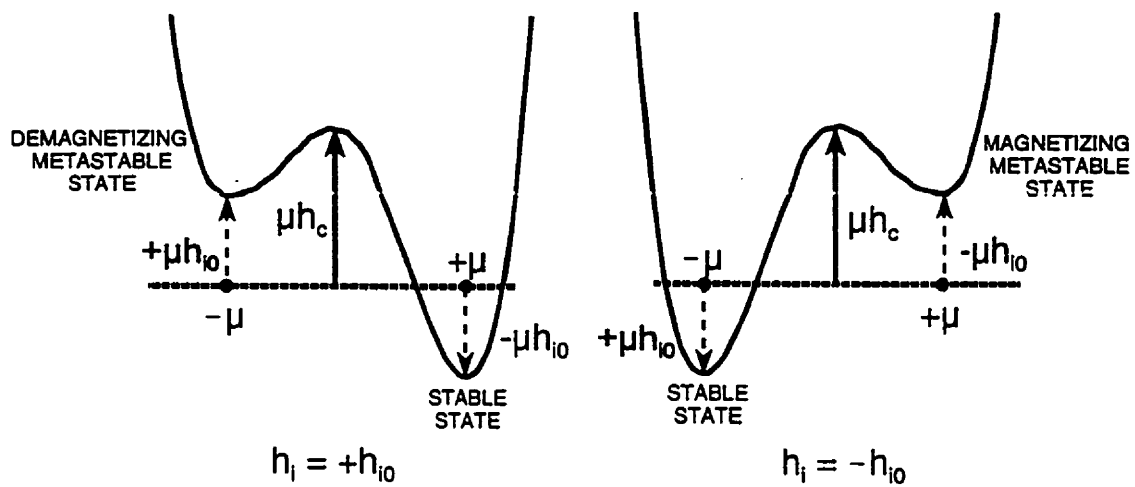


Figure 3.9 . Energy level representation of a pair of Preisach particles with equal and opposite interaction fields  $h_i = +h_{i0}$  and  $h_i = -h_{i0}$ .

the “magnetizing” metastable state contributes nothing to the magnetizing remanence, while the “demagnetizing” metastable state continues to contribute after saturation, so that the Henkel plot for random interaction fields must curve *below* the Wohlfarth line. The lower limit defined for a Henkel plot is shown in Figure 3.8. The lower limit of the Henkel plot can be understood by considering a Preisach distribution  $p(h_c, h_i) = \delta(h_c - h_0) g(h_i)$  where  $g(h_i) = \frac{1}{2}[\delta(h_i - h_{i0}) + \delta(h_i + h_{i0})]$ . The energy level representation of the Preisach particles is shown in Figure 3.9. Consider the system in its lowest energy state. If a field smaller than the smallest metastable barrier is applied,  $h_a < h_c - |h_{i0}|$ , there will be no field induced transition, and the magnetizing remanence will be zero,  $i_m = 0$ . If a saturating field is applied, the spin-down particle will flip and remain in this orientation even if a matching reverse field  $-h_a$  is applied, and so the demagnetizing remanence attributed to this flipped particle is  $i_d = \mu$ , yielding a Henkel point  $(i_m/i_\infty, i_d/i_\infty) = (0, 1)$ . Now considering a field  $h_a'$  larger than the metastable barrier but smaller than the stable barrier  $h_c - |h_{i0}| < h_a' < h_c + |h_{i0}|$ , the field will not induce a transition and yields no remanence  $i_m = 0$ . The demagnetizing remanence, however, will also be zero since the reverse field  $-h_a'$  can activate a transition from the demagnetizing metastable state over the smaller barrier. This gives the point  $(0, 0)$  on the Henkel plot. Finally, applying a sufficiently large field  $h_a''$  to overcome both barriers  $h_a'' > h_c + |h_{i0}|$ , yields a magnetizing remanence  $i_m = \mu$  and the matching demagnetizing remanence of  $i_d = -\mu$  since the field can flip both particles from the positive saturated state into the negative saturated state, producing the Henkel point  $(1, -1)$ . The continuous line segments shown in Figure 3.8 can be generated by a continuum of interaction fields, and points on

the lines are related to the fraction of particles activated by the applied field. The lower limit,  $i_d = -i_m$  is exhibited by pseudoparticle distributions that have a fixed coercivity  $p(h_c, h_i) = \delta(h_c - h_0) g(h_i)$ . Basso and Bertotti (1994) provide a mathematical derivation of this result.

### 3.4.3 Interpretation of Henkel Plots

Traditionally, the curvature of Henkel plots has been used to infer the types of interactions present in a magnetic system; whereby, positive curvature, below the Wohlfarth line, is interpreted as an indication that interactions favour the demagnetizing process, whereas negative curvature, above the Wohlfarth line, implies interactions that favour the magnetizing process. For particles that are noninteracting,  $g(h_i) = \delta(h_i)$ , the Henkel plot follows the Wohlfarth line. So, curvature is a natural consequence of intrinsic disorder. The presence of local interaction fields is indicated by using a function of finite width to describe the distribution of interaction fields. However, the behaviour of Henkel plots is more complicated than this simple assertion suggests and the shape of a Henkel plot is known to be sensitive to the precise method by which the original unmagnetized state is achieved (Vajda, Della Torre & McMichael, 1994). In particular, calculations that assume an ac demagnetized initial state predict that demagnetizing-like curvature will occur for any Preisach distribution that includes shifted loops, in the absence of mean field effects. With the exception of a trivial  $\delta$ -function local interaction field distribution  $\delta(h_i)$ , no unique relationship exists between the sign of the mean (or moving) field parameter  $k$  and the curvature of the Henkel plot. Furthermore, the shape of the plot often has complex, oscillatory structure, so that the identification of mean field interaction

effects is rendered quite problematic. Similar remarks apply to a dc-demagnetized Preisach plane (Vajda et al., 1994). As we will show, in the following section, many of these ambiguities are removed, and the interpretation of Henkel plots are considerably simplified if the initial, unmagnetized state is *random*, such as may be achieved by *thermal demagnetization* (Mitchler, Dahlberg, Engle & Roshko, 1995).

### 3.4.4 Henkel Plots and the Random Thermally Demagnetized Plane <sup>1</sup>

Henkel plots cannot be interpreted without reference to the initial demagnetized state. For a random thermally demagnetized initial state, with level occupation probabilities ( $\frac{1}{2}, \frac{1}{2}$ ), a system will exhibit a linear Henkel plot in the absence of mean field effects. The calculation of the magnetization of a Preisach system involves integrating the coercive and interaction field distributions over the entire Preisach plane corresponding to the system's initial demagnetized state and modified by the application of the field

$$m = \int_{-\infty}^{\infty} dh_i \int_0^{\infty} dh_c p(h_c, h_i) \varphi(h_c, h_i, h). \quad (3.2)$$

Details of the calculations for the ac-demagnetized plane are given by Basso, Bue, and Bertotti (1994). The Preisach calculation for a thermally demagnetized system is similar. The initial magnetization curve  $m(h)$  and the magnetizing remanence,  $i_m(h)$  are described by different Preisach integrals than those for ac demagnetization due to the occupation of metastable states that are vacant in the ac demagnetized state, while the saturation remanence,  $i_\infty$ , the demagnetizing curve,  $m_d(h)$ , and its associated demagnetizing

remanence,  $i_d(h)$  remain unchanged. In particular, the appropriate Preisach integrals for a thermally demagnetized MPM with mean field parameter  $k$  are as follows:

(a) initial magnetization curve ( $k \geq 0$ )

$$m(h) = 2 \int_0^h d\alpha \int_0^\alpha d\beta p(\alpha, \beta) + \int_0^h d\alpha \int_{-\infty}^0 d\beta p(\alpha, \beta) \quad (3.3)$$

with  $h_a$  determined by the skew transformation  $h = h_a + km(h)$ ;

(b) magnetizing remanence ( $k > 0$ )

$$i_m(h) = m(h) - 2 \int_{ki_m}^h d\alpha \int_{ki_m}^\alpha d\beta p(\alpha, \beta) \quad (3.4)$$

with  $i_m$  determined iteratively;

(c) magnetizing remanence ( $k < 0$ )

$$i_m(h) = m(h) - 2 \int_{ki_m}^h d\alpha \int_{ki_m}^\alpha d\beta p(\alpha, \beta) - \int_h^\infty d\alpha \int_{ki_m}^0 d\beta p(\alpha, \beta) \quad (3.5)$$

with  $i_m$  determined iteratively;

(d) saturation remanence ( $k \geq 0$ )

$$i_\infty = m(h = \infty) - 2 \int_{ki_\infty}^h d\alpha \int_{ki_\infty}^\alpha d\beta p(\alpha, \beta) \quad (3.6)$$

with  $i_\infty$  determined iteratively;

(e) demagnetizing curve ( $k \geq 0$ )

$$m_d(h) = i_\infty - 2 \int_h^{k_i} d\alpha \int_h^\alpha d\beta p(\alpha, \beta) - 2 \int_{k_i}^\infty d\alpha \int_h^{k_i} d\beta p(\alpha, \beta) \quad (3.7)$$

with  $h_a$  determined by the skew transformation  $h = h_a + k m_d(h) < 0$ ;

(f) demagnetizing remanence ( $k \geq 0$ )

$$i_d(h) = i_\infty + 2 \int_h^{k_i} d\alpha \int_h^\alpha d\beta p(\alpha, \beta) \quad (3.8)$$

with  $i_d$  determined iteratively.

When  $k = 0$  (no mean field effects), the shape of the Henkel plot can be established analytically. In fact, when  $k$  is set to zero in Equations 3.3 to 3.8, a number of the integrals collapse, and direct comparison shows that

$$i_d(-h_a) = i_\infty - 2 i_m(+h_a).$$

This means that the Wohlfarth relation is obeyed, independent of the specific form of the Preisach distribution, as long as  $p(\alpha, \beta) = p(-\beta, -\alpha)$ . Thus, provided the intrinsic disorder is symmetric, *producing a symmetric distribution of local interaction fields* about  $h_i = 0$  the Henkel plot of a thermally demagnetized system cannot be curved. This result is in sharp contrast to the behaviour of both ac and dc demagnetized systems (Basso, Lo Bue, & Bertotti, 1994; Vajda, Della Torre & McMichael, 1994), and the result is independent of the representation, so the same will apply to calculations in the  $(h_c, h_i)$ -representation. Hence, the result is equally applicable to both magnetic particle assemblies and to materials where domain wall motion is the dominant magnetization mechanism.

Numerical calculations were actually performed in the  $(h_c, h_i)$ -representation, and

the specific form of the Preisach distribution was selected to be the product of two normalized Gaussian functions where the interaction field distribution is symmetric about zero with a width  $\sigma_i$  and the coercive field distribution is symmetric about some mean coercive field  $\bar{h}_c$  with a width  $\sigma_c$ :

$$p(h_c, h_i) = \frac{1}{2\pi\sigma_c\sigma_i} \exp\left[-\frac{h_i^2}{2\sigma_i^2}\right] \exp\left[-\frac{(h_c - \bar{h}_c)^2}{2\sigma_c^2}\right]. \quad (3.9)$$

The numerical integration and iteration of Eqs. 3.3 to 3.8, expressed in the  $(h_c, h_i)$ -representation and the substitution of parameter values  $k = 0$ ,  $\bar{h}_c = 10.0$ ,  $\sigma_c = 3.0$ , and  $\sigma_i = 1.0$  into Eq. 3.9, indeed confirms that a linear Henkel plot is produced for the thermally demagnetized Preisach plane with no mean field effects (Figure 3.10).

When  $k \neq 0$ , we must rely on a numerical solution and the curved lines in Figure 3.10 show Henkel plots generated for several nonzero values of  $k$ . Clearly, the most striking consequence of the thermal demagnetization process is the unique relationship between the curvature and the sign of the mean field parameter: demagnetizing-like interactions ( $k < 0$ ) always yield a Henkel plot lying below the Wohlfarth line while magnetizing-like interactions ( $k > 0$ ) always curve above this line. Furthermore, the complex oscillatory behaviour present in ac and dc demagnetization calculations is eliminated. The Preisach formalism predicts that Henkel plots are most effective as a probe of mean field interaction effects when the system has been thermally demagnetized. This procedure may not be feasible for some physical systems, including many particulate

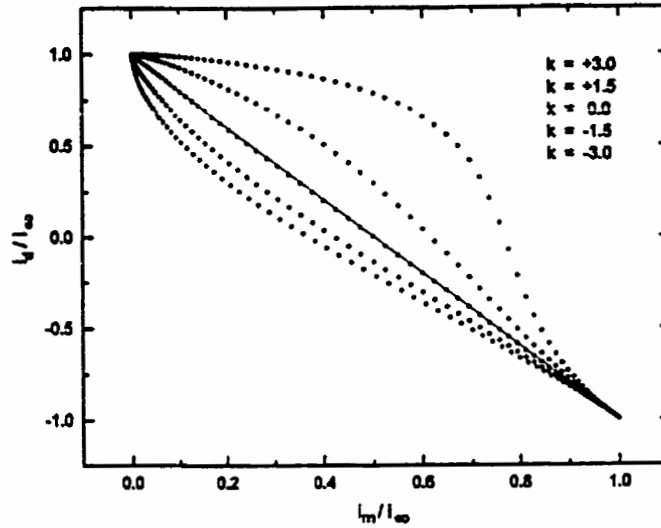


Figure 3.10 . For a thermally demagnetized initial state, the relationship between the sign of the mean field parameter  $k$  and the curvature of the Henkel plot is unique. For  $k > 0$  the plot always lies above the Wohlfarth line, while for  $k < 0$ , it always lies below. The plot for  $k = 0$  is coincident with the Wohlfarth line, as shown. The numerical calculations were performed with parameter values  $\bar{h}_c = 10.0$ ,  $\sigma_c = 3.0$ , and  $\sigma_i = 1.0$ .

magnetic recording media, where exceeding  $T_c$  leads to the physical deterioration of the material and/or its substrate. Nonetheless,  $\text{CrO}_2$  audio tape (Section 4.3.1) can be investigated using the thermal demagnetization procedure as will be shown in Chapter 5 (Mitchler, Roshko, & Dahlberg, 1998; Mitchler, Roshko, Dahlberg & Moskowitz, 1999).

### 3.4.5 Compensated Henkel Plots <sup>2</sup>

The curvature of the Henkel plots in Figure 3.10 for nonzero values of  $k$  originates from two sources: the remanences  $i_m$  and  $i_d$  are calculated in zero *applied* field, and the remanences are matched to generate the Henkel plot using the magnitude of the applied field as the implicit variable. If, instead, the remanences were defined as the residual magnetization in zero *effective* field,  $h \equiv h_a + km = 0$  (corresponding to nonzero applied fields of  $h_a = -ki_m$  and  $h_a = -ki_d$ ), and then matched with respect to the effective field, all Henkel plots would be linear for thermally demagnetized systems. A similar procedure has, in fact, been suggested as a possible means of compensating experimentally for shape demagnetizing effects, which contribute to a term  $h_D = -Dm$  to the local field. This is like the usual mean field contribution with  $k = -D$ . For perpendicular recording media (Section 5.4) this term will dominate the curvature of the Henkel plot and mask “genuine” interaction effects arising from sources other than dipole-dipole coupling. The experimental procedure is, however, flawed because it compensates for the demagnetizing field,  $h_D = -Dm$  associated with the magnetized state  $m$  rather than for the remanent demagnetizing fields  $h_D = -Di_m$  or  $h_D = -Di_d$ . Of course, such a compensating field cannot be applied experimentally, since  $i_m$  and  $i_d$  are not known beforehand. However, the error incurred by this approximation is particularly easy to

evaluate within a thermally demagnetized Preisach model because under these conditions, exact compensation is equivalent to perfect linearity. We have replicated the experimental compensating procedure outlined by Samwell, Bissell and Lodder (1993) numerically (Mitchler, Dahlberg, Engle & Roshko, 1995); the system was in a random initial state, was magnetized to a state  $m$  in a positive effective field  $h = h_a + km$ , and then demagnetized to remanence  $i_m$  that was calculated iteratively in an effective field  $h_m = -km + ki_m$ , corresponding to an applied field  $h_a = -km$ . A similar procedure was followed along the demagnetization curve ( $h < 0$ ). Figure 3.11 shows both the uncompensated and the (approximately) compensated Henkel plots for  $k = -D = -8$ , with all other parameters as given for Figure 3.10. The linear curve in Figure 3.11 indicates that, with the current assumptions regarding the factorization properties and the shape of the Preisach distribution, the model predicts no discernible difference between the approximate and exact compensation techniques, and thus offers convincing support for the experimental analysis. In practice, the result appears to be very sensitive to small errors in  $D$  (Samwell, Bissell & Lodder, 1993).

## 3.5 Thermal and Time Relaxation Effects

### 3.5.1 The Generalized Preisach Model<sup>3</sup>

The energy required to switch magnetic states can be supplied by applying an external magnetic field. Alternatively, the energy required to overcome energy barriers  $W$  can be provided thermally. The characteristic time for barrier activation can be written as  $\tau = \tau_0 \exp\left(\frac{W}{k_B T}\right)$ . At a given temperature,  $T$ , and for a given experimental wait time,

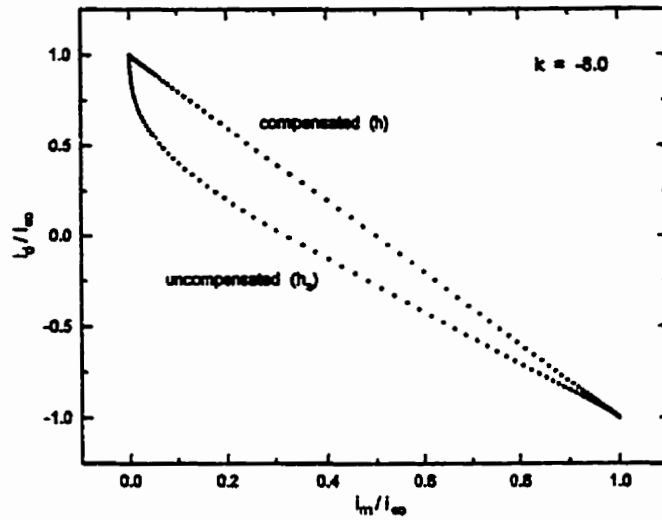


Figure 3.11 . The *uncompensated* Henkel plot, using  $h_p$  for the matching field and the *compensated* Henkel plot, where  $h$  is the matching field, for  $k = -8$ . Preisach distribution parameters used in the calculation were  $\bar{h}_c = 10.0$ ,  $\sigma_c = 3.0$ , and  $\sigma_i = 1.0$ .

$t_{\text{exp}}$ , the height of the largest energy barrier that can be surmounted is  $W^* = kT \ln \left( \frac{t_{\text{exp}}}{\tau_0} \right)$  and all barriers  $W < W^*$  are thermally activated. The parameter  $\tau_0$  is a time constant of order  $10^{-9}$  to  $10^{-12}$  seconds, and can be considered the time required to make a transition in the limit where the barrier height is zero and there is no impediment to motion. On an atomic scale, the upper limit of  $\tau_0^{-1}$  is just the Larmor precessional frequency of the moment in the field (Morrish, 1965, p. 361). Furthermore,  $\tau_0^{-1}$  is related to the curvature of the potential well, where curvature increases with increasing barrier height (Préjean & Souletie, 1980). The first overbarrier transitions activated are those from the state of higher potential energy to the lower energy state. Thermal transitions can also be expressed in terms of an *effective thermal viscosity field*,  $h_T^*$ , where  $\mu h_T^* = W^*$ .

Thermally or temporally activated transitions are depicted in the Preisach plane, after applying a positive field  $h_a$ , by simultaneously sweeping a horizontal line downward from  $\beta = h_a$  to  $\beta = h_a - h_T^*$ , and a vertical line across the plane, from  $\alpha = h_a$  to  $\alpha = h_a + h_T^*$ , as shown in Figure 3.12. The boundary line between these two processes is the dashed diagonal line  $h_i = -h_a$ , parallel to the  $h_c$ -axis. The intersection of the two thermal instability lines with this line  $h_i = -h_a$  is the effective thermal viscosity field,  $h_T^*$ .

In our model calculations, the “equilibrium” or “reversibility limit” is obtained by letting  $t_{\text{exp}} \rightarrow \infty$ , or equivalently  $h_T^* \rightarrow \infty$ , and this yields the maximum possible magnetization for a fixed spontaneous particle moment, which is always larger than the superparamagnetic moment at the same temperature, since thermal or Boltzmann populations are not incorporated into the model. There is a square region in the Preisach plane defined by  $(h_a < \alpha < h_T^* + h_a, h_a - h_T^* < \beta < h_a)$ , as shown in Figure 3.12, where

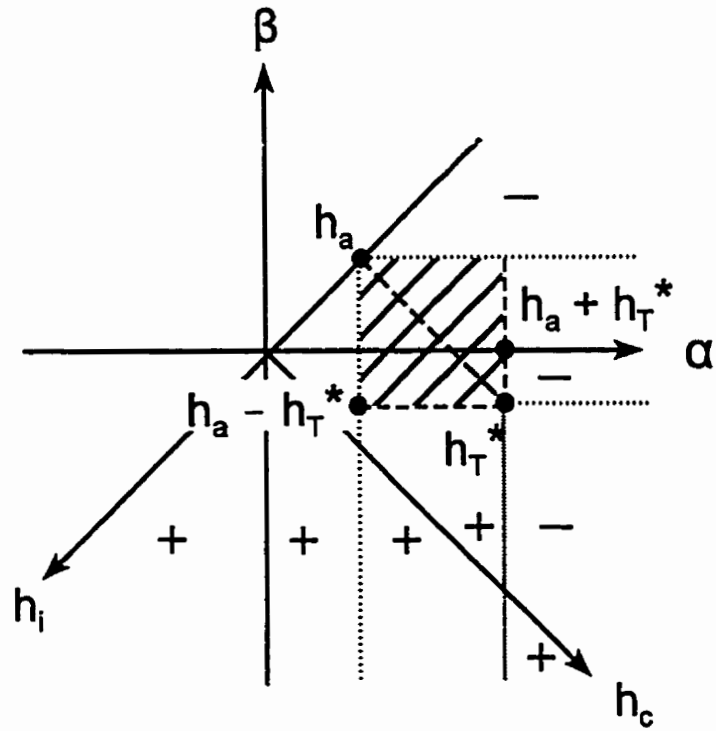


Figure 3.12 . The magnetized Preisach plane. The thermally activated magnetizing transitions occur between the two dotted vertical lines while the demagnetizing transitions occur between the two dotted horizontal lines. Thermal relaxation will be equally effective for both barriers in the shaded square.

thermal relaxation will be equally effective for both barriers and will yield paramagnetic (or superparamagnetic) populations  $\exp\left[\pm\frac{\bar{\mu}(h_i + h_a)}{k_B T}\right]$  for a given double well potential. The effect of neglecting this thermally demagnetized square can be estimated for typical experimental temperatures  $T$  and experimental wait times  $t_{\text{exp}}$ . In this superparamagnetic region of the Preisach plane, the difference between the equilibrium moment of the pseudoparticles  $\bar{\mu} \tanh\left[\frac{\bar{\mu}(h_i + h_a)}{k_B T}\right]$  and the saturation moment  $\pm\bar{\mu}$  is negligible except within a narrow strip of width  $|h_i + h_a| - k_B T/\bar{\mu} = h_T^* \ln(t_{\text{exp}}/\tau_0) \sim h_T^*/20$  on either side of the diagonal line  $h_i = -h_a$ . Furthermore, the contribution from this region tends to be small for small values of the effective thermal parameter, since the Preisach distribution ensures that only a relatively small number of particles exist in this region.

### 3.5.2 Effects of Relaxation on Hysteresis Loops and on Henkel Plot Curvature <sup>4</sup>

While the geometric constructions in the previous sections that describe the relaxation process are similar to those employed earlier in the literature by Néel (1950) and Souletie (1983), our work represents the first attempt to apply these constructions to the numerical calculations of hysteresis loops, remanences, and Henkel plots for an arbitrary Preisach distribution and over the entire magnetic field range from positive to negative saturation.

The upper and lower boundaries for Henkel plots introduced in Sections 3.4.1 and 3.4.2, are expected to hold in the limit of zero temperature, independent of the details of the initially demagnetized state. Finite temperature or relaxation time, introduced in the generalized, finite-temperature version of the Preisach model, can have a profound effect

on the shapes of the Henkel plots. Furthermore, varying the relaxation times  $t_{\text{exp}}$  from one branch to another of a given hysteresis cycle can produce spurious mean field-like curvature or even violations of the nominal lower boundary  $i_d = -i_m$  (Mitchler, Dahlberg, Wesseling & Roshko, 1996b), as observed in some canonical spin glasses (Section 2.9.5).

To illustrate these violations, the model system was prepared in both ac and thermally demagnetized initial states as shown in Figures 3.7a and 3.7c respectively. The latter assumes an instantaneous quench in zero field from above to below  $T_C$ , so that the two states in the fourth quadrant are characterized by their paramagnetic ( $T > T_C$ ) occupation probabilities ( $1/2, 1/2$ ). According to Figure 3.7a, ac demagnetization is equivalent to a thermal quench followed by an “infinite” (or thermally equilibrating) experimental wait time  $t_{\text{exp}} \rightarrow \infty$ .

Figure 3.13 shows (a) the magnetization  $m$ , (b) the remanences  $i_m$  and  $i_d$ , and (c) the Henkel plots for an ac demagnetized system with distribution parameters  $\bar{h}_c = 10$ ,  $\sigma_c = 3$ ,  $\sigma_i = 1$ ,  $k = 0$ , with each data set corresponding to a fixed value of the “thermal field” parameter  $h_T^* = W^*/\mu = 0, 5, 7, 10, 18$ . Since changes in  $h_T^*$  may be interpreted as either changes in temperature  $T$  at fixed observation time  $t_{\text{exp}}$  or changes in observation time  $t_{\text{exp}}$  at fixed temperature  $T$ , the model predicts a systematic loss of irreversibility with increasing temperature or observation time, and an eventual collapse of hysteresis for  $h_T^* \gg \bar{h}_c$ , which is precisely what is expected to occur experimentally. In addition, increases in temperature and observation time also tend to enhance the “natural” ( $k=0$ ) demagnetizing curvature (Basso, Lo Bue & Bertotti, 1994) of the Henkel plots as shown in Figure 3.13, and this process appears to converge to a specific curve for

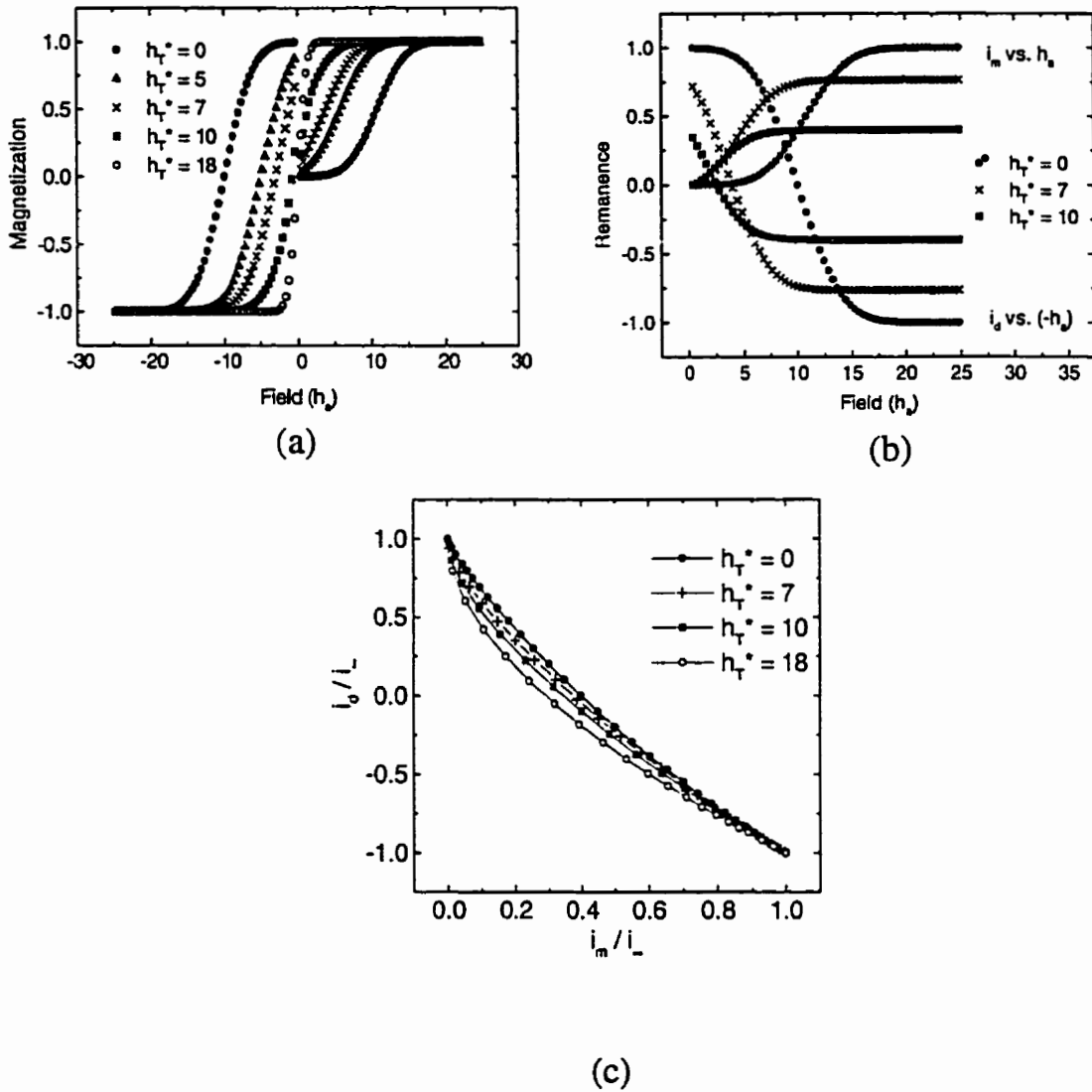


Figure 3.13 . The effects of relaxation on hysteresis loops and Henkel plot curvature. (a) Magnetization, (b) remanences, and (c) Henkel plots for an initially ac demagnetized Preisach plane with  $k = 0$ , distribution parameters  $\bar{h}_c = 10$ ,  $\sigma_c = 3$ , and  $\sigma_i = 1$ , and thermal field parameter values  $h_T^* = 0, 5, 7, 10$ , and  $18$ .

$h_T^* \geq 18$ . Of course, the details of this convergence must ultimately depend on the precise functional form of the coercive field distribution and, in particular, on its asymptotic properties, as well as on the restriction that neither the coercive field nor the interaction field distributions have been allowed to vary with  $h_T^*$ . In fact, measurements performed on samples of CrO<sub>2</sub> audio tape (Mitchler, Roshko & Dahlberg, 1998) indicate the *opposite* trend where less demagnetizing curvature is exhibited at higher temperatures. The analysis of CrO<sub>2</sub> data (Section 5.5.2) indicates that the *collapse of the field distributions* as  $T - T_C$  explains the apparent contradiction. Both the coercive and interaction field distributions must eventually collapse into  $\delta$ -functions centred at  $h_c = h_i = 0$  above the ordering temperature  $T_C$ . By contrast with ac demagnetization, the Henkel plots generated from a thermally demagnetized initial state show no tendency to favour either the magnetizing or demagnetizing processes in the absence of mean field effects ( $k = 0$ ), and are coincident with the linear Wohlfarth relation for all values of  $h_T^*$ .

Figure 3.14 shows a sequence of Henkel plots for an ac demagnetized system with a nonzero positive mean field parameter  $k = +1$ . While the curve for  $h_T^* = 0$  has less demagnetizing curvature than its counterpart in Figure 3.13, as expected when a ferromagnetic bias is imposed on the interaction field distribution, the sequence converges to the same limiting curve as that for  $k = 0$ , which supports our contention that this limit is determined by the characteristics of the specific Preisach distribution.

The preceding discussion assumed that all branches of the hysteresis cycle have a common thermal field parameter corresponding to a fixed temperature  $T$  and a single time constant  $t_{exp}$ ; however, if a common experimental time constant  $t_{exp}$  does *not* imply a

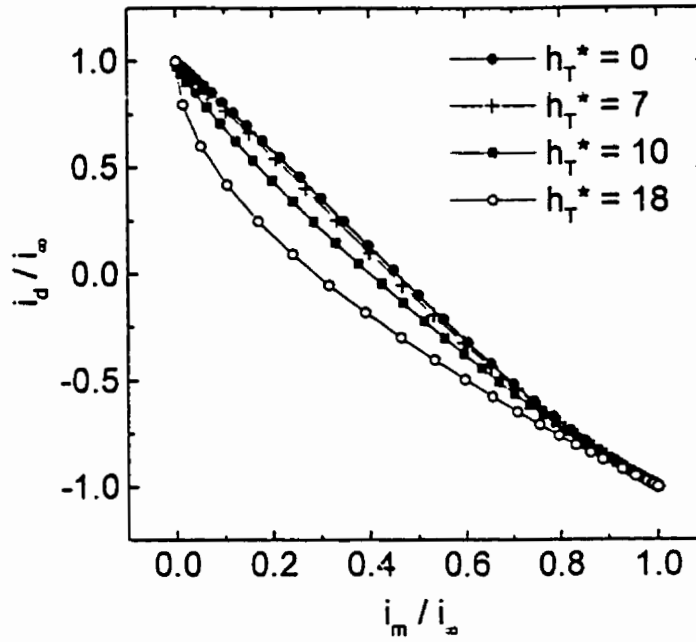


Figure 3.14 . A sequence of Henkel plots for an ac demagnetized system with  $k = +1$  and distribution parameters as in Figure 3.13. The Henkel plot has less demagnetizing curvature than for  $k = 0$  when no relaxation is allowed, but the sequence converges to the same limit as  $h_T^*$  increases.

common relaxation rate for the magnetization, then the effective time constant for relaxation  $t_{\text{eff}}$  may vary from branch to branch of the cycle, as will  $h_T^*$ . Furthermore, the Henkel plots will exhibit anomalous structure. Field cooled spin glasses are a particularly good demonstration of this “temporal asymmetry”. If a spin glass is cooled from above to below its ordering temperature in the presence of a field it attains its equilibrium magnetization essentially instantaneously (Souletie, 1983), independent of the actual measuring time  $t_{\text{exp}}$ , as if the effective time constant  $t_{\text{eff}}$  for relaxation were infinite. However, all subsequent field reversals, such as those required to reach the remanent state or the demagnetization branch, are governed by a necessarily much shorter time constant  $t'_{\text{eff}}$ , close to the actual, finite experimental one  $t_{\text{exp}}$ . This behaviour was replicated in the finite temperature Preisach model by assigning a very large value to the thermal field parameter  $h_{T1}^*$  along the initial magnetization curve, and another smaller value  $h_{T2}^*$  to the remanence (corresponding to the thermoremanent magnetization (TRM), discussed in Section 3.7), the descending branch of the major loop, and the demagnetizing remanence (Mitchler, Dalhberg, Wesseling & Roshko, 1996a).

Figure 3.15 shows a sequence of Henkel plots generated for a thermally demagnetized system with a Preisach distribution with parameters  $\bar{h}_c = 12$ ,  $\sigma_c = 4$ ,  $\sigma_i = 1$ ,  $k = 0$ , for thermal fields  $h_{T1}^* = 100$  and  $h_{T2}^* = 0, 15, 20, 25, 35$ . All Henkel plots show magnetizing-like curvature, which for thermally demagnetized systems would be unambiguous evidence for positive mean field interactions  $k > 0$  (Section 3.2), but this is actually an artificial consequence of the variation in time constants related to the experimental procedure of field cooling (Section 3.7). In real spin

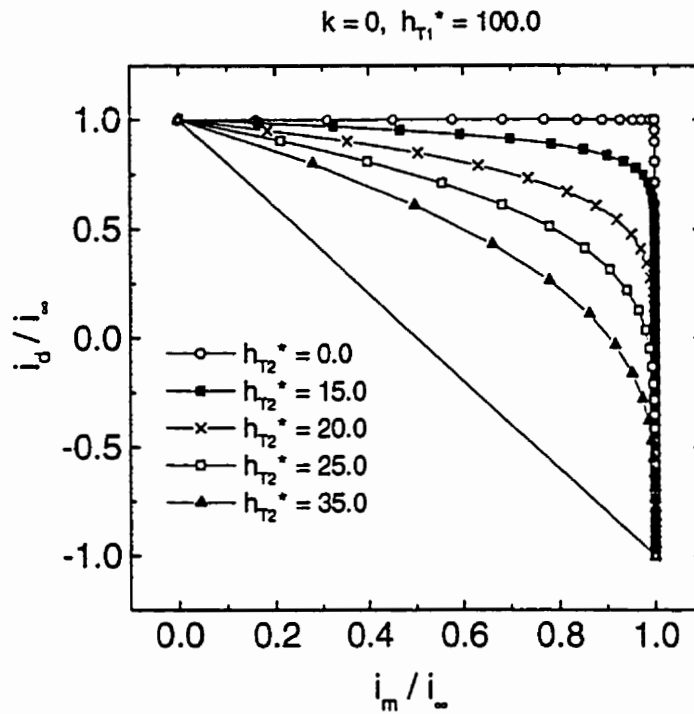


Figure 3.15 . The effect of two different relaxation rates,  $h_{T1}^* > h_{T2}^*$ , on Henkel plots for an initial thermally demagnetized (random) state. The magnetizing-like curvature of each plot is a consequence of the “experimental” procedure of field cooling, since  $k = 0$  for these calculations. The distribution parameters are  $\bar{h}_c = 12$ ,  $\sigma_c = 4$ , and  $\sigma_i = 1$ .

glasses, the situation is further complicated by the existence of a peak in the field dependence of the TRM, which is difficult to accommodate within the usual Henkel analysis, but can be reproduced using a modified version of the Preisach Model (Section 3.7).

The inverse configuration of time constants yields anomalous structure of a different kind, and may also be physically relevant to spin glasses. If we assume that the relaxation time constant is shorter along the initial magnetization curve than it is for the rest of the cycle, corresponding to  $h_{T1}^* < h_{T2}^*$ , then, in the absence of mean field effects, Henkel plots will always show demagnetizing-like curvature, as illustrated in Figure 3.16 for an ac demagnetized system with Preisach distribution parameters  $\bar{h}_c = 10$ ,  $\sigma_c = 3$ ,  $\sigma_i = 1$ , and  $k = 0$  and thermal parameters  $h_{T1}^* = 2.0, 2.5, 3.0, 3.5, 4.0, 4.5, 5.0$  and  $h_{T2}^* = 5.0$ . Moreover, if the difference between the two thermal fields is sufficiently large, the Henkel plots will actually cross the nominal  $T = 0$  lower boundary  $i_d = -i_m$ , as observed in canonical spin glass systems like AgMn (Wesseling, 1996) and CuMn (Jacobs & Schmitt, 1959) at low reduced temperatures  $T/T_{SG}$ , when they have been zero field cooled through their glass temperature. As  $h_{T1}^* \rightarrow h_{T2}^*$  this effect becomes weaker and eventually disappears. This is also observed experimentally with increasing temperature. If theoretical and experimental behaviours are indeed related, then it would mean that zero field cooling has essentially the opposite effect of field cooling, and “traps” the system in a region of its complicated configuration space, which requires relatively long times and high reduced temperatures for “escape.”

When  $T \neq 0$ , the effective time in which the magnetization relaxes becomes an

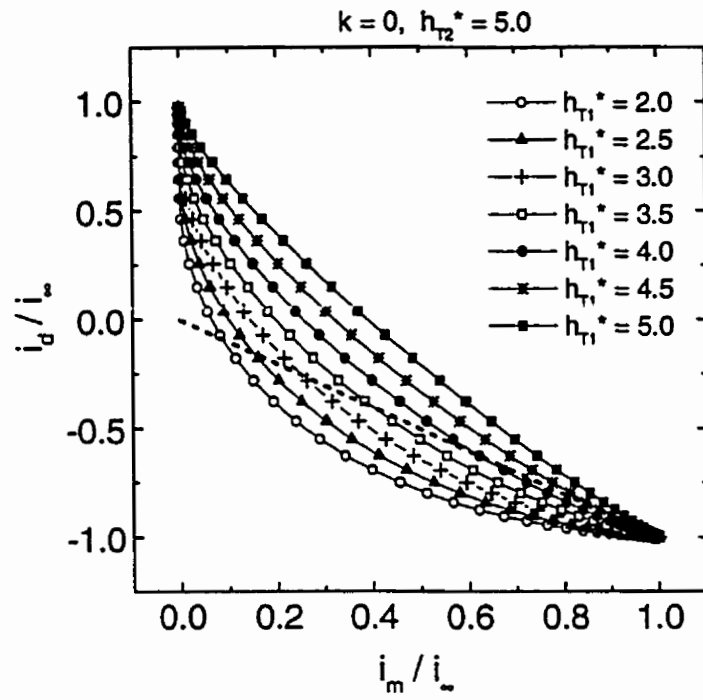


Figure 3.16 . The effect of two different relaxation rates,  $h_{T1}^* < h_{T2}^*$ , on Henkel plots for an initial ac demagnetized state and distribution parameters

$\bar{h}_c = 10$ ,  $\sigma_c = 3$ , and  $\sigma_i = 1$ . The Henkel plot violates the nominal  $T = 0$  lower boundary (dashed line) for  $h_{T2}^*$  sufficiently larger than  $h_{T1}^*$ .

important factor in shaping Henkel plots, and may lead to anomalous curvature that imitates mean field effects, or that violates nominal zero temperature boundaries.

### 3.6 Reversibility in the Preisach Model <sup>5</sup>

There are two sources of reversibility built into the modified Preisach Model as described. The pseudoparticles in the first and third quadrants of the Preisach plane, where  $\alpha$  and  $\beta$  are both positive or both negative, contribute to the total moment when the interaction field distribution is nonzero,  $\sigma_i \neq 0$ . These contributions are *reversible*. The second source of reversibility is a consequence of the thermal relaxation parameter,  $h_T^*$ , manifested in overbarrier relaxation effects. In practice, these two reversibility mechanisms are not sufficient to replicate either the field dependence of the total moment or the degree of recoil from the magnetized state to the remanent state in real systems. However, there are *physical* sources of reversibility that are not accommodated by the SPM: reversible rotation due to imperfect particle alignment, and field induced growth of the pseudoparticle moment over the spontaneous value, which results from increased atomic spin alignment. Hence, an additional reversibility term is usually required to supplement the Preisach calculation. Rather sophisticated procedures have been proposed for incorporating reversible nonlinearities directly into elementary Preisach loops, which effectively decompose each cycle into the superposition of two reversible functions of the form  $\pm(1-S)\exp(\mp\Gamma h_i) [1 - \exp(\mp\Gamma h_a)]$  and a vertically shifted rectangular loop with normalized outputs  $\pm[-(1-S)\exp(\mp\Gamma h_i) + 1]$ , where  $S$  is the squareness ratio and  $\Gamma$  is a constant (Vajda & Della Torre, 1992). For computational simplicity, a less elaborate

decomposition is implemented in the Preisach analysis of real systems presented in Chapter 5. Each rectangular Preisach cycle is supplemented by a single reversible nonlinearity  $\pm[1 - \exp(\mp\Gamma h_a)]$ , with upper (lower) signs for  $h_a > 0$  ( $h_a < 0$ ), which is identical for all pseudoparticles, independent of their individual characteristic parameters  $(h_c, h_f)$ . Moreover, the total response function of a pseudoparticle is a weighted superposition of reversible and Preisach components:

$f$  (reversible response) +  $(1 - f)$  (Preisach response), with  $0 \leq f \leq 1$ . This procedure is equivalent to replacing the two field-independent outputs of the scalar Preisach cycles ( $\pm 1$ ) by two nonlinear field-dependent outputs consisting of an upper branch  $+(1 - f) \pm f [1 - \exp(\mp\Gamma h_a)]$  and a lower branch  $-(1 - f) \pm f [1 - \exp(\mp\Gamma h_a)]$  (Figure 3.17), thus effectively creating Stoner-Wohlfarth-like cycles. However, unlike SW cycles, which specifically describe rotation processes in uniaxial single domain particles, these cycles are entirely phenomenological constructs, aimed at improving the predictive capabilities of the Preisach model while retaining both the simplicity and physical transparency of the thermally activated two-energy-level scheme.

### 3.7 Moving Coercive Field Distribution: The Preisach Model and Spin Glasses<sup>6</sup>

Magnetizing remanences can be measured in two different ways. One technique involves field cooling (FC); a sample is heated above its ordering temperature, and then cooled in an applied field. For a spin glass, the resulting magnetization is regarded to be the equilibrium one (Souletie, 1983). Upon removing the field, the residual magnetization, or the field cooled remanence, is named the *thermoremanent*

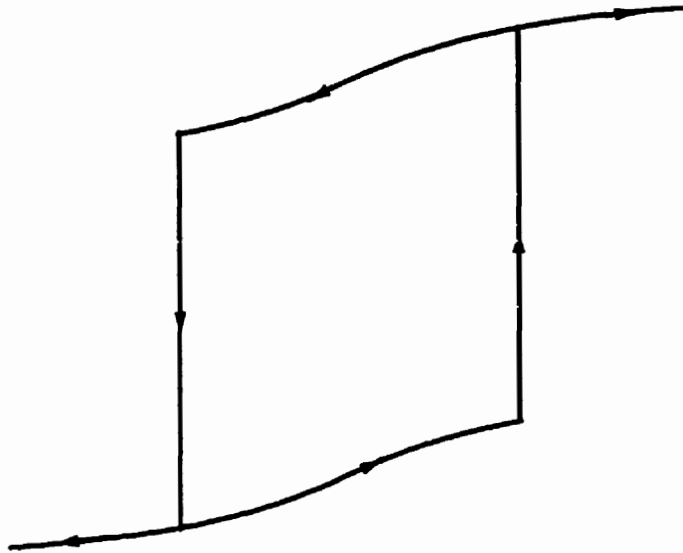


Figure 3.17 . An example of a phenomenological hysteresis loop constructed by a weighted superposition of reversible and Preisach components. This procedure replaces the field-independent outputs of the scalar Preisach cycles by nonlinear field-dependent outputs, consisting of an upper branch  $+(1 - f) \pm f [1 - \exp(\mp \Gamma h_a)]$  and a lower branch  $-(1 - f) \pm f [1 - \exp(\mp \Gamma h_a)]$  .

*magnetization* (TRM). The other measurement technique is known as zero field cooling (ZFC) where the temperature of a sample is reduced below its ordering temperature in the *absence* of an external field, and then a field is applied for a time,  $t_{exp}$ , prior to turning off the field and measuring the remanence. The magnetization is dependent on the field duration, and consequently, so is the remanence, in this case called the *isothermal remanent magnetization* (IRM).

Spin glasses exhibit an unusual remanence structure. While most materials exhibit a monotonically increasing remanence as a function of increasing applied field, spin glass remanence curves show a maximum. Data for the spin glass  $\text{Eu}_{0.4}\text{Sr}_{0.6}\text{S}$ , which exhibits this structure, is given in Figure 3.18. The TRM is measured by cooling in an applied field, removing the field and waiting for a time,  $t_{exp}$  before measuring the magnetization. This TRM shows a peak that moves left, toward lower applied fields as the experimental wait time increases. Figure 3.19 shows data for a AgMn spin glass, indicating that the isothermal remanence, obtained by ZFC, is smaller than the TRM and peaks at larger fields.

In an attempt to replicate numerically the spin glass behaviour using the scalar Preisach model, the extended version of the model that treats finite time and temperature relaxation effects was implemented. To calculate the IRM, the effective thermal parameter used in magnetization and remanence calculations is identical ( $h_{T1}^* = h_{T2}^*$ ); however, for the TRM we seek the equilibrium magnetization obtained by field cooling, and so, the effective thermal parameter is infinite in the magnetization calculation. In a practical calculation, an infinite  $h_{T1}^* \rightarrow \infty$  can be replicated by choosing a value of the

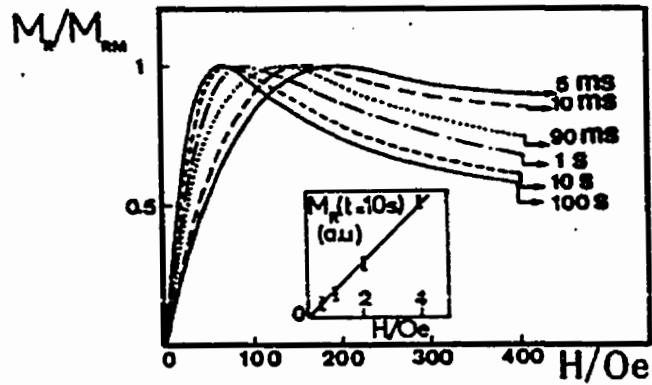


Figure 3.18 . Experimental data for the normalized thermoremanent magnetization at 1.32 K for  $\text{Eu}_{0.4}\text{Sr}_{0.6}\text{S}$  showing an obvious peak which moves toward lower applied fields with increasing experimental wait time. (from Fig. 7, Ferré, Rajchenbach & Maletta, 1981)

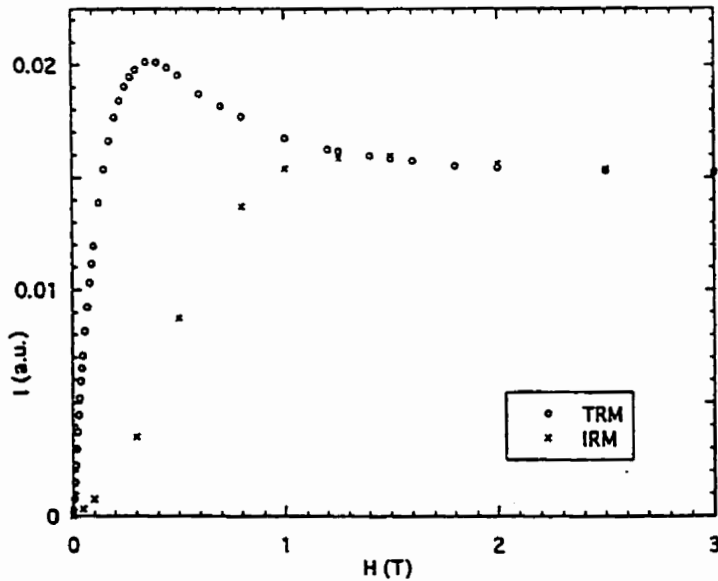


Figure 3.19 . The isothermal remanence (x), normalized to the maximum in the TRM for a Ag-7.8 at. % Mn spin glass at  $T=7$  K is smaller than the TRM (o) and peaks at larger fields (from Figure 28, Wesseling, 1996).

effective thermal parameter that is several standard deviations larger than the means of the interaction and coercive field distributions.

Figure 3.12 shows the Preisach plane that results from magnetizing from an initially demagnetized state in a field  $h_a$  with a finite effective thermal parameter  $h_T^*$ . The diagrammatic representation of the remanence, shown in Figure 3.20, is actualized by reducing the applied field to zero and sliding along the coercive field axis to  $h_T^*$ . The resulting shaded region is the remanence. For increasing fields, the square gets larger and the integration in the Preisach model calculations covers more of both the coercive and interaction field distributions, thus including a greater proportion of pseudoparticles. The result is a monotonic increase in the remanence. However, for spin glasses, a peak in the remanence is observed and the remanence tends to zero for larger values of the applied field. From the Figures 3.12 and 3.20, relaxation is complete and equilibrium, defined by the maximum magnetization possible and zero remanence, is reached only if  $h_T^*$  exceeds the maximum coercive (or anisotropy) field of the clusters. However,  $h_T^*$  is usually fixed by the experimental conditions,  $T$  and  $t_{exp}$ . To generate the peaks observed experimentally in the remanence curves of spin glass samples, the Preisach model must be modified such that application of a field seemingly changes the value of the effective thermal viscosity parameter  $h_T^*$ .

We have used the finite temperature Preisach model to replicate the peaks observed in spin glass remanence curves, by making the Preisach distribution dependent on magnetization, after a suggestion by Pr ejean and Souletie (1980). The authors proposed a coercive field distribution that has an upper cutoff  $h_{c,max}$ , which decreases in

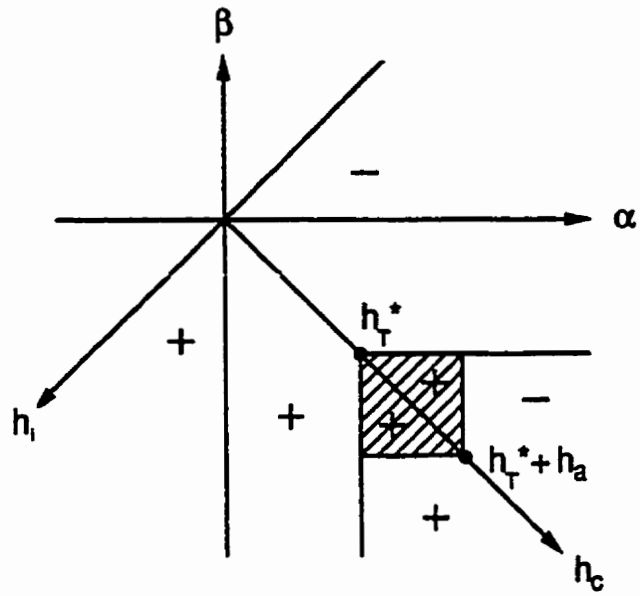


Figure 3.20 . The Preisach plane representation of remanence for a finite value of the effective thermal parameter  $h_T^*$  .

proportion to the magnetization  $m$  of the system

$$h_{c,\max} = h_{c,\max}^{(0)} - \gamma m$$

where  $h_{c,\max}^{(0)}$  is the zero field cutoff and  $\gamma$  is a positive proportionality constant. These changes are assumed to be irreversible, so that recoiling to zero field after application a field has no effect on the distribution established during the magnetization process. Then, the effective time available for relaxation toward equilibrium (zero remanence) will increase monotonically with  $m$ , and the remanence may exhibit a peak as a function of the applied field. The mechanism implies that the intrinsic coercive field of the magnetic pseudoparticle *evolves* during the magnetization process. The notion of a “moving” Preisach distribution was first introduced by Della Torre (1966) to address “instability” associated with random fluctuations in local *interaction* fields during the magnetization process. Here, we have implemented a similar procedure for the coercive fields, although for entirely different physical reasons. Since the only essential requirement of the physical mechanism suggested by Préjean and Souletie is that the coercive field distribution have a finite width, the Preisach distribution selected for model calculations (Mitchler, Roshko, Dahlberg & Wesseling, 1997) is a product of continuous Gaussian coercive and interaction field distributions

$$p(h_c, h_s, m) = \frac{1}{2\pi\sigma_c\sigma_s} \exp\left[-\frac{h_s^2}{2\sigma_s^2}\right] \exp\left[-\frac{(h_c - \bar{h}_c)^2}{2\sigma_c^2}\right],$$

where the magnetization dependence is incorporated into the mean value  $\bar{h}_c$  and width  $\sigma_c$  as follows:

$$\bar{h}_c = \bar{h}_{c0} - \gamma m$$

$$\sigma_c^2 = \frac{1}{4} \bar{h}_c = \frac{1}{4} (\bar{h}_{c0} - \gamma m).$$

The dispersion  $\sigma_c^2$  has been made an arbitrary fixed fraction of  $\bar{h}_c$ , so as to preserve the normalization as  $\bar{h}_c$  varies. The cutoff parameter is not explicit, but the finite value of  $\sigma_c$  guarantees that equilibrium is effectively reached when  $h_T^* \geq \bar{h}_c + 3\sigma_c$  since over 99% of the area of a Gaussian is included within three standard deviations from the mean. The magnetization is calculated self-consistently, by Newton's method of repeated substitution, from the Preisach integral. As the moment increases it pushes the distribution closer to the origin and integration is performed over less and less of the distribution. This can generate a peak in the remanence. An evolving coercive field distribution, shown in Figure 3.21, is tantamount to effectively increasing  $h_T^*$ , or waiting for a longer time  $t_{exp}$  at fixed temperature  $T$ . Experimentally, however, the time  $t_{exp}$  is fixed, so the *intrinsic* properties of the particles must change in response to a magnetization.

Calculating remanences with these ingredients built into the Preisach model, we find that for increasing  $h_T^*$  the peak moves toward the left (Figure 3.22) as was shown by Ferré, Rajchenbach and Maletta (1981), Figure 3.18. The IRM has the same systematics as the TRM. The maximum in the field dependence of the remanence becomes sharper and shifts  $h_T^*$  toward lower fields with increasing values of the effective thermal viscosity parameter. This maximum occurs because the reduction in the anisotropy barriers of the pseudoparticles allows the system to relax toward the zero remanence equilibrium state as the field and the magnetization increase, eventually overcoming the

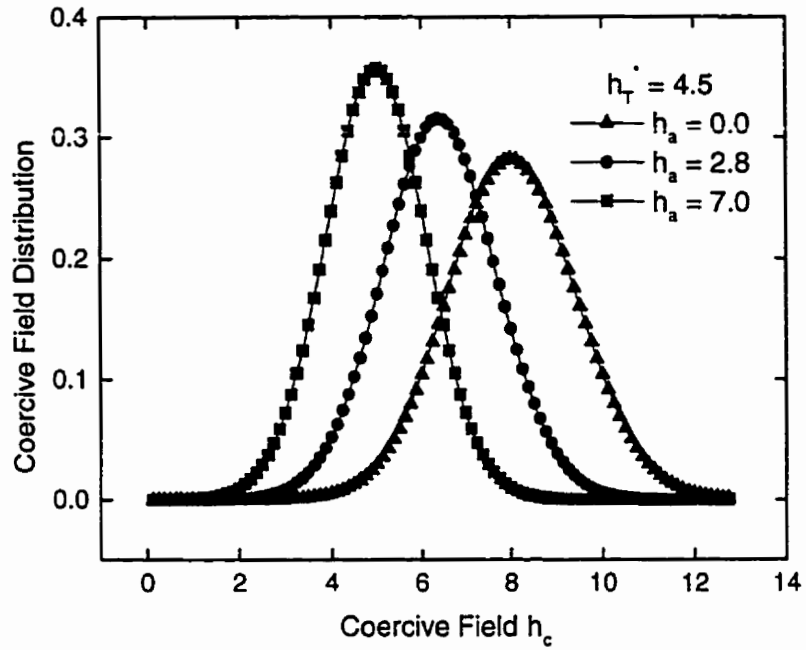


Figure 3.21 . The evolution of the coercive field distribution between zero applied field and saturation for  $h_T^* = 4.5$ . As  $h_a$  increases the distribution becomes narrower and more sharply peaked.

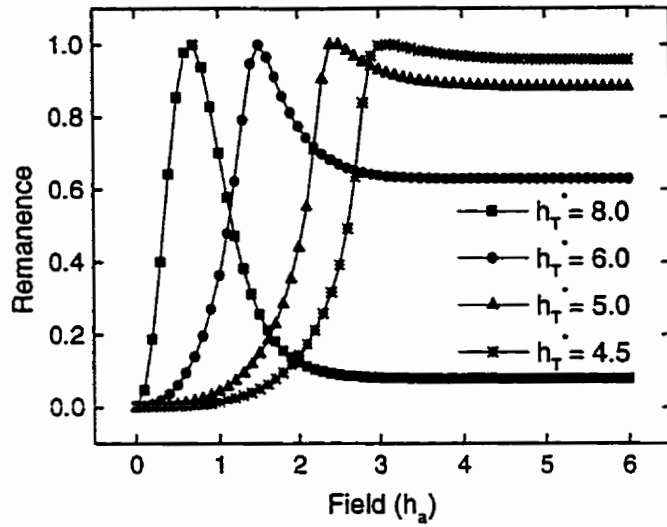


Figure 3.22 . The field dependence of the IRM for several values of the effective thermal parameter  $h_T^*$  and for Preisach distribution parameters  $\sigma_i = 1$ ,  $\bar{h}_{c0} = 8$ , and  $\gamma = 3$ .

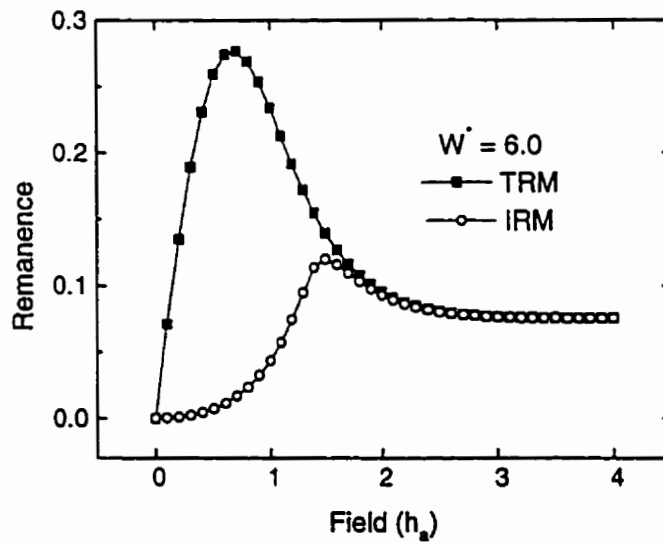


Figure 3.23 . A comparison of the TRM, for  $h_{T1}^* = 100$  on the magnetizing branch and  $h_{T2}^* = 6.0$  on the remanence branch, with the IRM, where  $h_{T1}^* = h_{T2}^* = 6.0$  . The IRM peak is smaller and occurs at higher fields.

tendency for the remanence to increase with field (Mitchler, Roshko & Dahlberg, 1997). These calculations also produce thermoremanent peaks that are larger and that occur at lower applied fields, than isothermal remanent peaks for the same remanence measurement time  $t_{exp}$ , (Figure 3.23) as was found experimentally by the Norblad, Lundgren and Sandlund (1987) and Wesseling (1996), shown in Figure 3.19. By using the finite temperature version of the Preisach model with an evolving coercive field distribution, the anomalous behaviour of spin glass remanences can be numerically replicated.

The physical mechanism for generating remanence maxima, as described, requires first that glassy spin structures with frustrated interactions can be decomposed into small localized groups of spins that behave like pseudoparticles or “clusters,” in order to be compatible with the Preisach formalism. Second the magnetic “clusters” constituting the system undergo some form of field-induced “growth” or reconfiguration that lowers their intrinsic anisotropies. Although a precise definition for the quasi-particles invoked in this theoretical picture has not been formulated (Préjean and Souletie, 1980), there is good experimental evidence that frustrated systems like spin glasses, prepared in either thermally or ac demagnetized states, have “dynamic” state dependent coercive field distributions that evolve continuously and permanently towards lower values as they are magnetized to saturation. Specifically, if a thermally demagnetized spin glass is saturated and then dc demagnetized and remagnetized, the magnetizing curve generated from the dc demagnetized state lies *above* the originally thermally demagnetized initial magnetization curve and saturates at *lower* fields (Wesseling, 1996). Thus, the system

becomes magnetically *softer* after it has been exposed to a saturating magnetic field. These changes cannot be attributed to differences in the structure of the two demagnetized states, since this would yield precisely the opposite effect, with the dc demagnetized initial curve below the thermally demagnetized virgin curve (Vajda, Della Torre & McMichael, 1994). Furthermore, the descending branch in the second and third quadrants of the major hysteresis loop of a thermally demagnetized spin glass reaches *negative* saturation in *lower* absolute fields than those require to saturate the initial magnetizing curve, from the demagnetized state (Wesseling, 1996 & Jacobs and Schmitt, 1959). This means that the descending branch would actually cross the initial magnetization curve if it were inverted through the origin. Thus, once the softer coercive field distribution has been established, memory of this deformation is preserved all the way to *negative* saturation.

There are also *theoretical* reasons to expect a state-dependent reduction in the potential energy barriers in a spin glass. Both infinite range mean field models (Sherrington & Kirkpatrick, 1975) and short range droplet scaling theories (Fisher & Huse, 1988) predict that the ordered spin glass state is destroyed by the application of a sufficiently large magnetic field so that the system actually becomes paramagnetic if the field exceeds a certain temperature-dependent “critical” value, given by the de Almeida-Thouless stability line (de Almeida & Thouless, 1980) for infinite range models, or by an equivalent dynamic freezing line (Huse & Fisher, 1987 & Fisher & Huse, 1988) for droplet theories. In either case, hysteresis vanishes on laboratory time scales above the instability field, and this implies that the potential barriers  $h_c$  become too small to

prevent the system from equilibrating. Accordingly, a state-dependent distribution of coercive fields is a simple and elegant way to incorporate field-induced instability into the Preisach formalism.

**Notes:**

1. The discussion in Section 3.4.4 appears modified in Mitchler, Dahlberg, Engle & Roshko, 1995 p. 2500-2501.
2. The discussion in Section 3.4.5 appears modified in Mitchler, Dahlberg, Engle & Roshko, 1995 p. 2502-2503.
3. Some portions of the discussion in Section 3.5.1 appear in Mitchler, Roshko, Dahlberg & Moskowitz, 1999, p. 2032.
4. Portions of the discussion in Section 3.5.2 appear in Mitchler, Dahlberg, Wesseling & Roshko, 1996a, p. 5760 & 1996b, p. 3188-3192.
5. Portions of the discussion in Section 3.6 appear in Mitchler, Roshko, Dahlberg & Moskowitz, 1999, p. 2032-2033.
6. Some portions of the discussion in Section 3.7 appear in Mitchler, Roshko, Dahlberg & Wesseling, 1997, p. 5883-5885.

## **Chapter 4**

# **Equipment, Experimental Protocols, and Magnetic Systems**

### **4.1 Magnetic Measurement Equipment**

#### **4.1.1 SQUID Magnetometer**

The Quantum Design SQUID-based magnetometer (Model MPMS 5S) was one of two magnetometers used to measure the properties of the magnetic systems investigated in this thesis (Figure 4.1). A SQUID (Superconducting Quantum Interference Device) magnetometer is the most sensitive of all commercially available magnetometers, including the Vibrating Sample Magnetometer (Section 4.1.2). The operating principle of a SQUID magnetometer is based on the detection of magnetic flux originating from a sample. The SQUID does not directly measure the magnetic moment of the sample, rather the sample moves through a system of superconducting coils that are connected to the SQUID with superconducting wires. When a sample is passing through these sensing

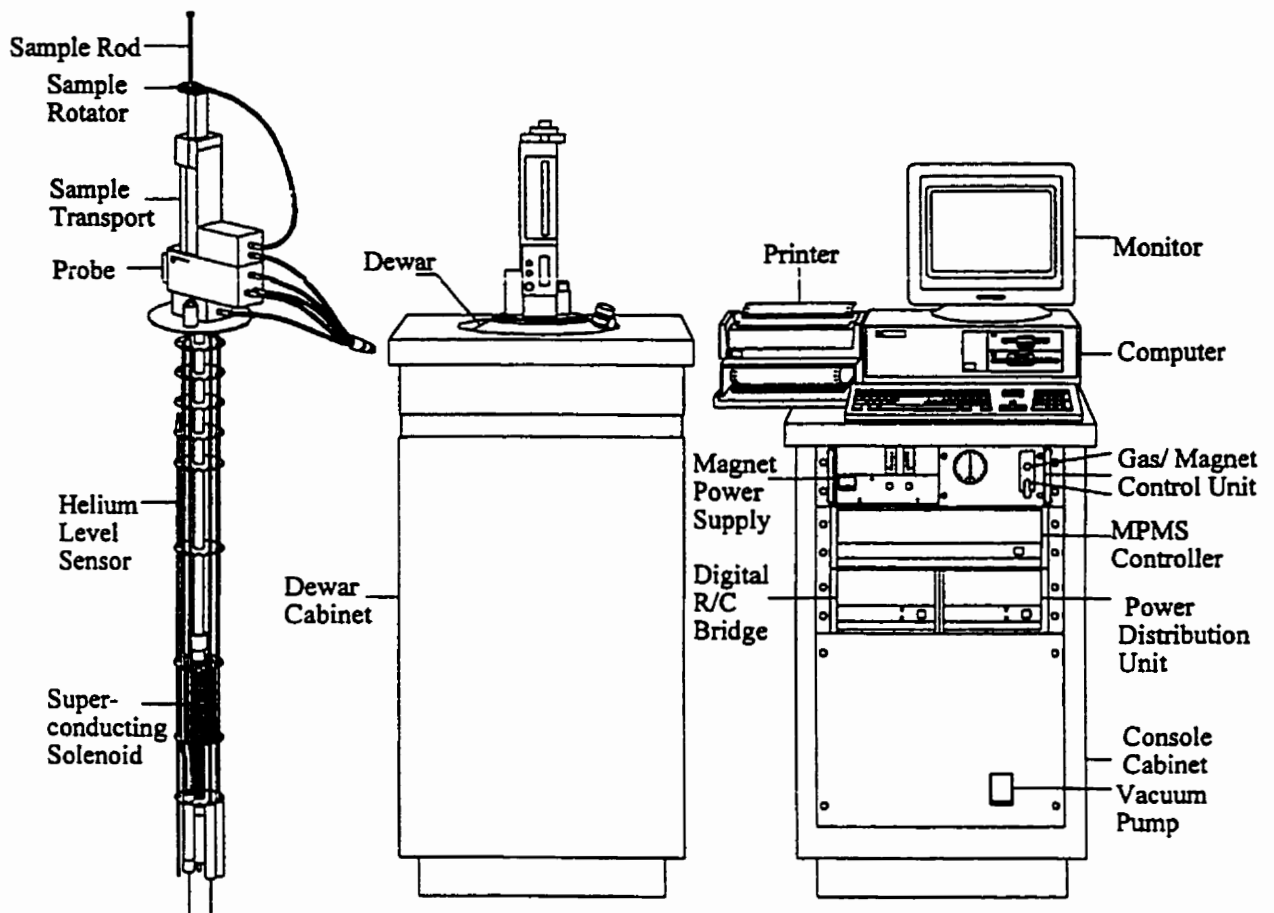


Figure 4.1 . Quantum Design MPMS System Components (after Quantum Design MPMS: Hardware Reference Manual, Fig. 1-1, 1996).

coils, a change in the magnetic flux produces a change in the current in the coil by an amount proportional to the change in flux. This change is inversely proportional to the inductance of the SQUID and is detected by an rf circuit, which is inductively coupled to the superconducting ring comprising the SQUID. The voltage of the rf signal is amplified and converted to units of magnetic moment after calibration. The SQUID is essentially a Josephson junction, a strongly coupled superconducting ring device. The current in the superconducting ring is modulated by the amount of flux passing through the ring with a period equal to one flux quantum. The sensing or detection coil is actually a single piece of superconducting wire wound into a three coil configuration called a second-order gradiometer. In this configuration, the upper coil is a single turn wound clockwise, the centre coil comprises two turns wound counterclockwise and the bottom coil is a single turn wound clockwise. The coils are positioned outside the sample chamber and at the centre of the superconducting magnet, such that the magnetization from the sample couples inductively to the coils as the sample is moved through them. This gradiometer configuration is used to reduce noise in the detection circuit caused by fluctuations in the large magnetic field of the superconducting magnet. Figure 4.2 schematically locates the detector assembly within the SQUID system.

The currents induced in the detection coil are associated with the movement of a point source magnetic dipole through the gradiometer (see Figure 4.3). Observing this type of signal requires the sample to be much smaller than the detection coil and it must be uniformly magnetized. A very long sample, extending beyond the measurement coils will produce no change in flux in the detection coil as it moves, whereas the current in the

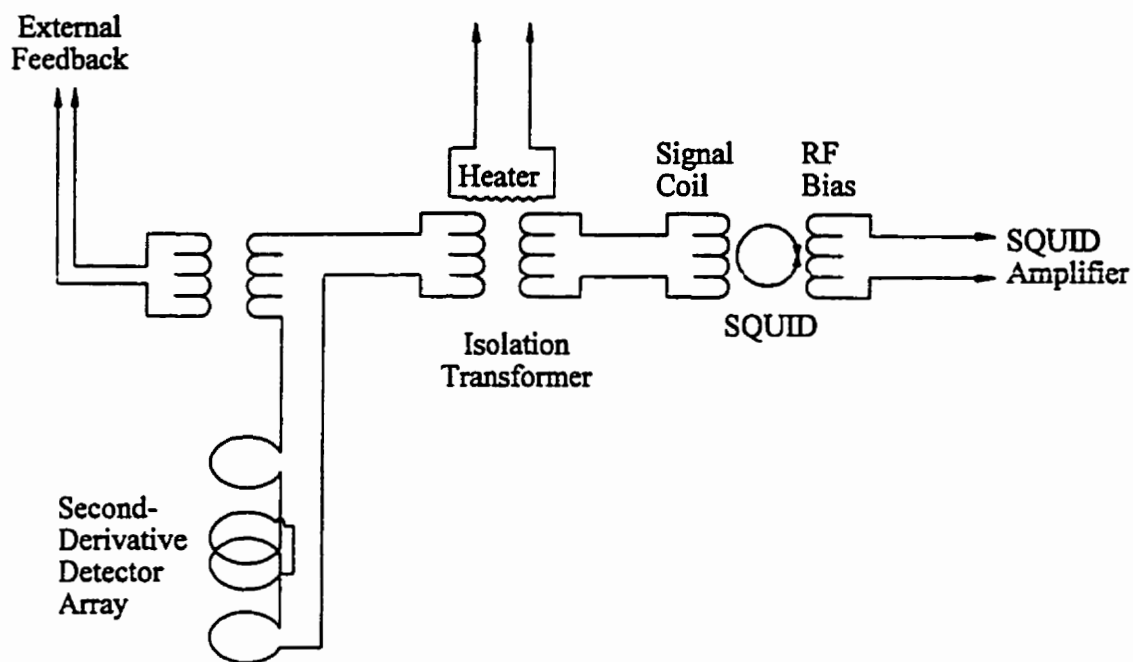


Figure 4.2 . SQUID System showing the second derivative detector array (second-order gradiometer) from Quantum Design MPMS: Hardware Reference Manual, Fig. 8-1, 1996.

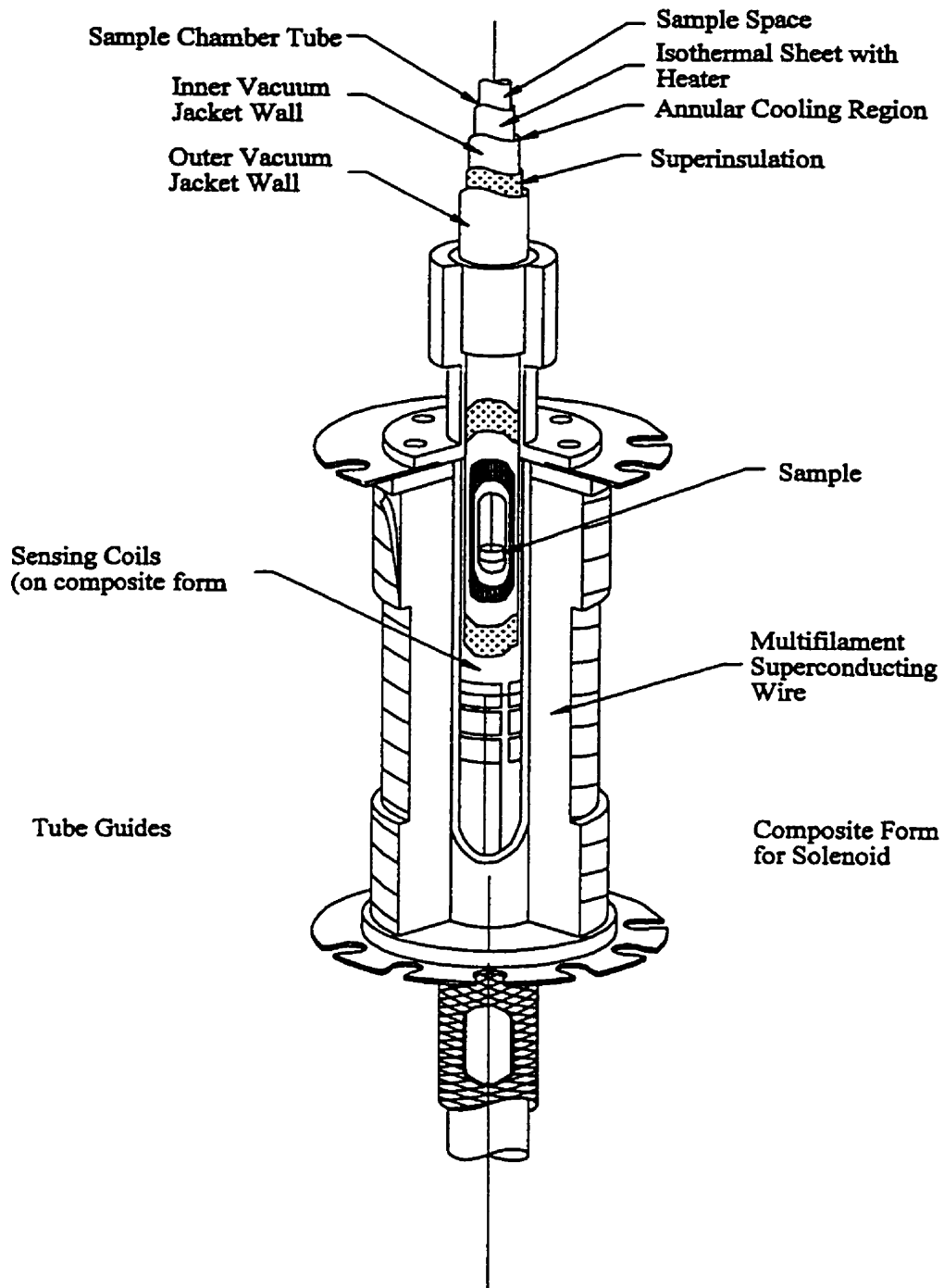


Figure 4.3 . Quantum Design MPMS magnet and sample chamber (after Quantum Design MPMS: Hardware Reference Manual, Fig. 1-3, 1996).

detection coil will change with sample position for a short sample.

For the SQUID magnetometer to operate, the Nb<sub>3</sub>Sn superconducting ring must be cooled below its superconducting transition temperature  $T_c = 12$  K, therefore requiring the use of liquid helium. The liquid He also cools the superconducting magnet, which has a magnetic field of  $\pm 50$  kOe (Quantum Design, 1992). The standard field resolution is 1.0 Oe in a  $\pm 10$  kOe field. The Quantum Design MPMS employs high resolution control for accurate manual compensation of the remanent field, allowing zero field setting to a resolution of 0.1 Oe at  $\pm 5$  kOe. Uniformity of the field within the measuring coils is 0.03%. Although the magnet can operate in an oscillating mode, only the no overshoot mode was used in the experiments since hysteresis measurements are affected by field history.

The liquid He also serves to regulate the temperature of the sample between 1.9 K and 400 K with the use of a heater and a feedback temperature controller. The temperature calibration at the sample space is typically  $\pm 0.5\%$ . The stability of the temperature is less than 0.05 K at 300 K and less than 0.01 K at 5 K. The spatial variation of temperature within the sample chamber is  $\pm 0.1$  K over 8 cm and  $\pm 1.0$  K over 15 cm. The temperature slew rate between 5 K and 300 K is 30 minutes.

The minimum detectable moment on the magnetometer is  $\pm 10^{-7}$  emu up to fields of 10 kOe and  $\pm 5 \times 10^{-7}$  emu for higher fields. The minimum resolvable change in magnetic moment is  $\pm 10^{-8}$  emu for fields up to 10 kOe while for higher fields this differential sensitivity drops to  $\pm 5 \times 10^{-7}$  emu.

Calibration is performed using a palladium (Pd) sample. Pd is paramagnetic. Due

to the remanence in the superconducting magnets and the absence of a Hall probe in the system, zero field must be found in an alternative fashion. The sample is removed from the chamber and the Pd standard is substituted into the holder. Because Pd is superparamagnetic, the plot of the moment against the applied field should be linear for small fields, and in a true zero field condition, the moment is also expected to be zero, that is, the line passes through the origin. If the field is not exactly zero, the intersection with the applied field axis,  $h_{\text{cross}}$  defines the value to which the field must be set in order to obtain the true zero field,  $h_{\text{zero}}$  via  $h_{\text{zero}} = -h_{\text{cross}}$ . Hence, zero field cooling is done in a field  $h_{\text{zero}}$ . The values of the applied field are set relative to this field.

The samples are contained in gelatin capsules, packed with asbestos wool to maintain verticality of the sample, and thus, to ensure alignment with the applied field. The sample is mounted by pushing the capsule into a plastic drinking straw of 6 mm diameter.

#### **4.1.2 Vibrating Sample Magnetometer (VSM)**

Many of the experimental magnetic measurements were made using a Princeton Measurements Corporation Model 3900 MicroMag™ Vibrating Sample Magnetometer (Princeton Measurements Corporation, 1995), which is a highly sensitive computer-controlled magnetic measurement system, capable of measuring magnetic properties of a wide range of sample materials. Since the field around a magnetized body varies as a function of position, the field existing at any particular point in space can be changed by moving the magnetized body. The magnetometer works by vibrating a sample vertically at the midpoint of the field produced by a magnet. When a magnetized sample is vibrated,

an electric current, proportional to the magnetic moment is induced in the pickup coils placed near the vibrating sample. The induced current has the same frequency as the vibration frequency of the sample. Thus, the flux change caused by the moving magnetic sample,  $\phi(t)$  induces a time-varying voltage across the terminals of the pickup coils that is  $V(t) \propto \frac{d\phi(t)}{dt}$  where  $\phi(t)$  is proportional to the field exerted by the sample. Special signal processing techniques ensure that the resulting measurement will only depend on the amplitude of the moment and will be independent of the drive amplitude. A calibration of the absolute moment and the sensitivity of the pickup coils can be made using a sample of known magnetization.

The mechanical transducer assembly, which in the Micromag™ VSM vibrates the sample at a frequency of 83.0 Hz, also permits precision three dimensional translation, as well as vibration isolation and continuous rotation about a vertical axis via computer control. Figure 4.4 shows a schematic diagram of the VSM.

The magnetometer has a sensitivity of 5  $\mu$ emu, defined as the standard deviation at room temperature operation at 1 second averaging time per point. The range of magnetic moments that can be measured on this system is between 50  $\mu$ emu and 10 emu. The accuracy of the moments measured is specified to be 2% as compared to calibration with a pure nickel standard. As the measured magnetic quantity is the total moment of the sample (Section 2.1) and not the magnetization, the volume of the sample becomes important in comparing absolute values of the measurements. Furthermore the shape of the sample determines the degree of demagnetization effects. Thus, calibration with a standard is only informative in comparing absolute measurements when the sample is the

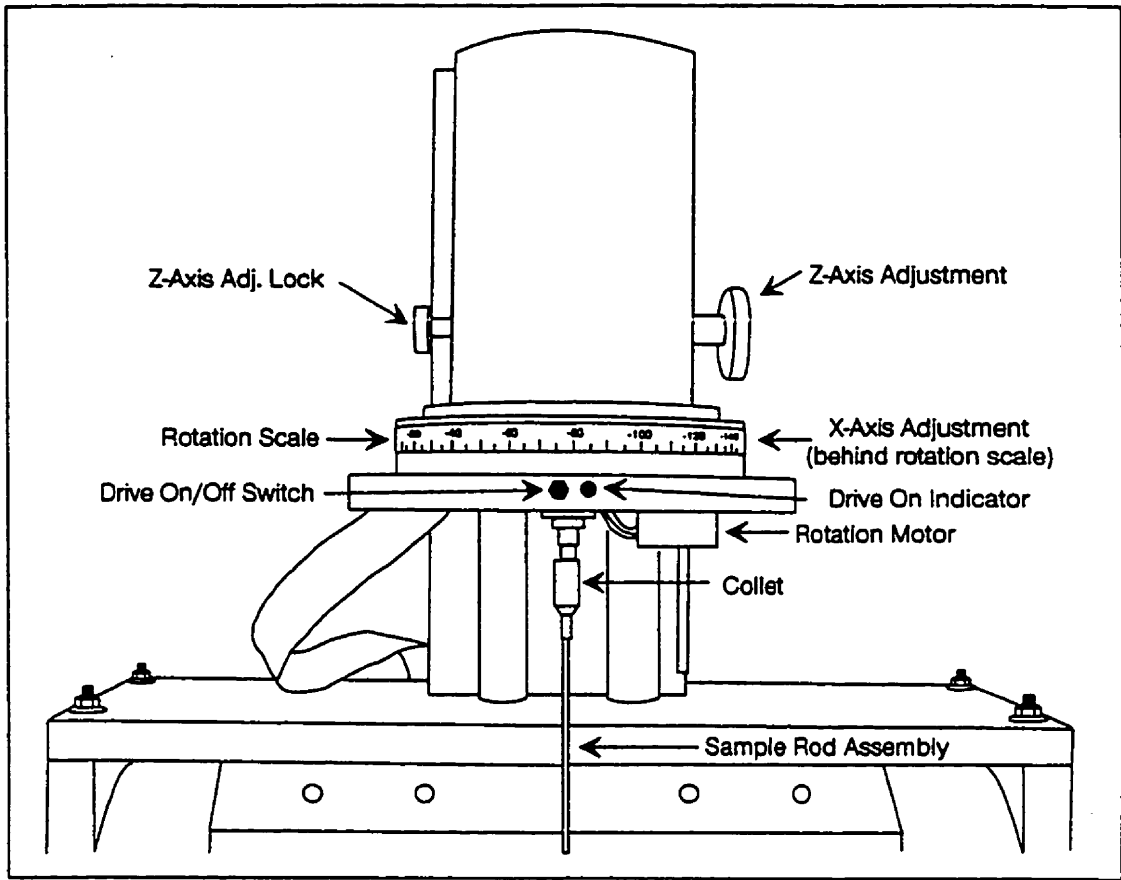


Figure 4.4 . Vibrating sample magnetometer: front view of the translation stage (from Princeton Measurements Corporation, Fig. 2-4, 1995).

same shape and volume as the standard. In these experiments, the absolute values of the measured moments are not critical to interpretation or comparison of data and are merely considered as scaling factors. Although the values are somewhat irrelevant on an absolute scale, the relative values of the measured moments are expected to be highly accurate, based on the sensitivity of the VSM. Nonetheless, the data processing capabilities of this VSM include some correction for the demagnetizing factor and normalization for sample mass or volume.

The field applied to the sample is generated by high-performance laboratory electromagnets with a 4 inch pole face diameter with pole caps tapering to 2 inches. The maximum field range for this system is  $\pm 18$  kOe. The applied field is continuously monitored with a built-in hall-effect gaussmeter and is accurate to within 2%  $\pm 1$  Oe. This feature ensures an accurate determination of a null field in the sample chamber. The magnet power supply is a bipolar, wideband pulse-width modulated power amplifier that regulates the field by a feedback signal, allowing precise servo control under field sweeping or static conditions. The maximum magnet slew rate is 20 kOe/s with an optional pause to achieve magnetic field stability before beginning a measurement. The electromagnet allows for quick setting of the field, making it an ideal instrument for hysteresis measurements.

The pick up coils are mounted on the ends of the pole pieces and the sample is mounted at the end of a glass rod, which is suspended in the electromagnet gap. The sample chamber is fused silica and the sample holder is made from high purity boron nitride, which can withstand high temperatures. The sample holder used in these

experiments allowed vertical mounting of the sample in the chamber, as shown in Figure 4.5.

This VSM system also includes a high-temperature oven (see Figure 4.6) that uses a continuous flow of He gas, employed for its superior heat-transfer characteristics, at a rate of 2 to 4 litres per minute to stabilize at temperatures above the ambient temperature, up to 750 °C to an accuracy of  $0.75\% \pm 2.2$  K. The flow rate is monitored and set. A thermocouple of designation type K, which is a chromel/alumel construction that is reliable from -200 °C to 1250 °C (Dunlap, 1988) is mounted about ¼ inch above the heater to monitor and control the temperature. The sample zone is directly above the thermocouple. Hot exhaust gas is removed via an extraction pump. A vacuum jacket offers the oven assembly additional thermal isolation and is pumped continuously during operation. The temperature controller is fully integrated into the system and the full range temperature change can be accomplished in 8 to 10 minutes.

The applications software package includes numerous automatic procedures to assist in positioning, demagnetizing and determining various sample characteristics. The measured sample parameters of interest in these experiments are magnetization curves, magnetization versus time, and isothermal remanence. The system also allows for measurement of minor loops and several other magnetic parameters. The saturation magnetization and remanence, coercivity, and remanence coercivity can also be extracted from raw data. The menu driven software is written in BASIC and is simple to use.

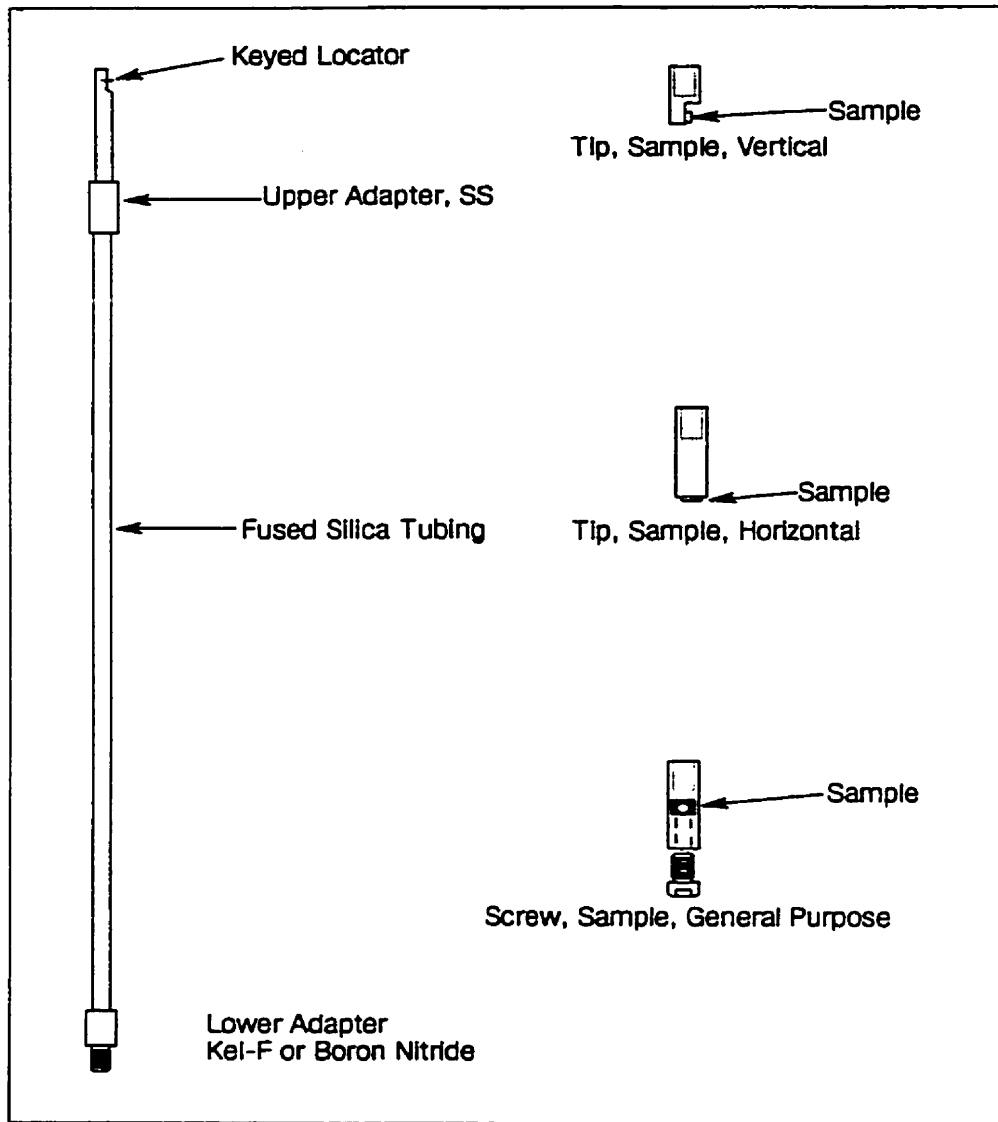


Figure 4.5 . The sample rod assembly and sample holders for the VSM (from Princeton Measurements Corporation, Fig. 3-4, 1995). Samples were mounted on the vertical holder (top right).

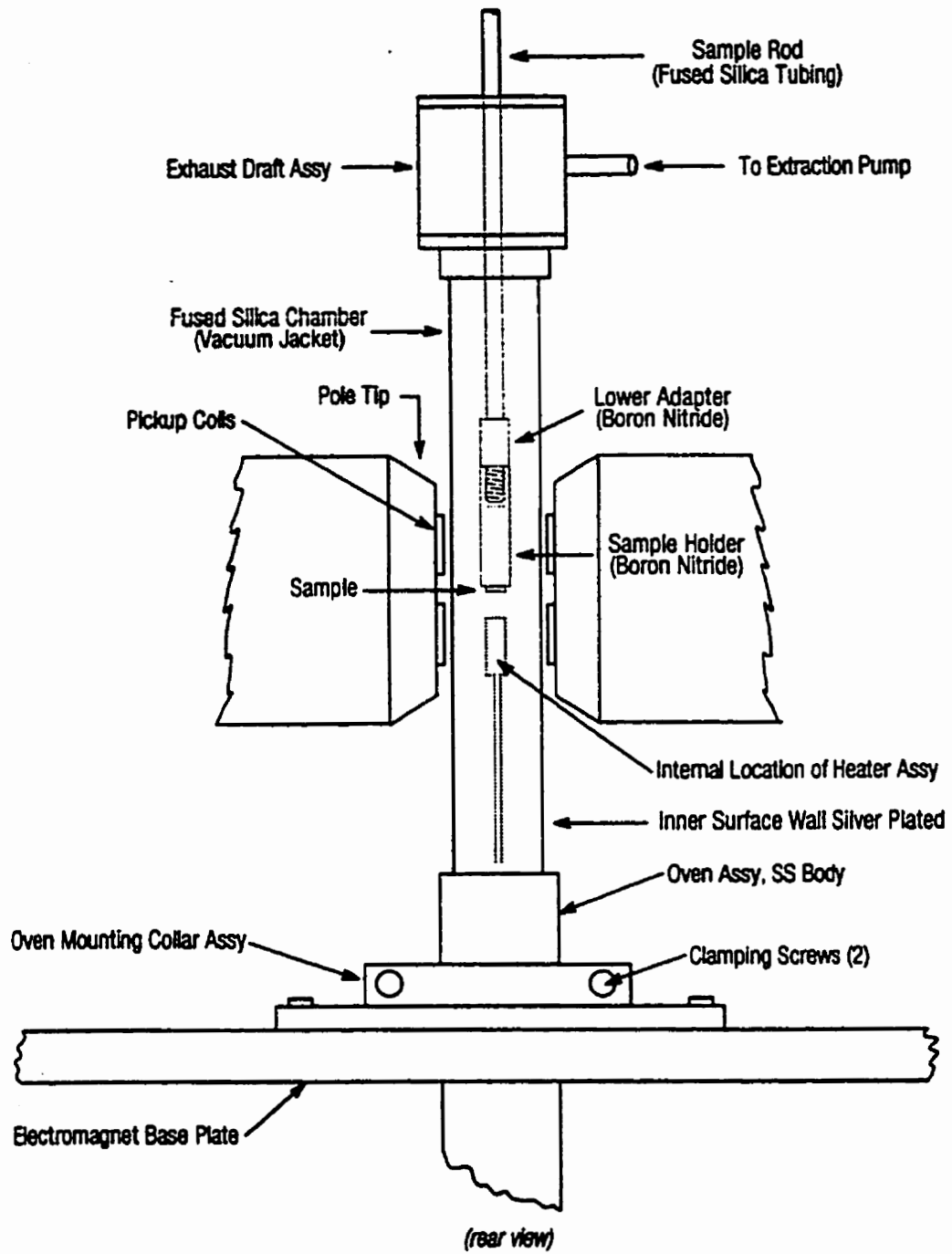


Figure 4.6 . The oven assembly that extends the operating range of the VSM to as high as 750 °C (from Princeton Measurements Corporation, Fig. A-2, 1995).

## 4.2 Experimental Protocols

### 4.2.1 Generating Magnetization Curves as a Function of Temperature

To obtain the magnetization curve as a function of temperature two techniques can be used: zero field cooling and field cooling. Zero field cooling (ZFC) entails cooling the sample in zero applied field from a reference temperature above either the ordering temperature  $T_C$ , or the highest blocking temperature  $T_{B,max}$ , to the lowest measuring temperature required. Then, a small dc field  $h_0$  is applied, and the moment is measured upon warming. To acquire the corresponding field cooled (FC) curve, the sample is cooled from the reference temperature to below the ordering temperature in the same dc field  $h_0$  as that applied in the ZFC procedure and the moment is once again measured upon warming. To get the points on the curve, it is necessary to increment and stabilize the temperature at each desired measurement temperature until the highest temperature required is reached.

Measurement of the field cooled and zero field cooled moments are typically characterized by a *bifurcation temperature* above which the two sets are identical and below which they are different, with the FC moment always lying above the ZFC curve, as will be seen in Chapter 5. When the applied field  $h_0$  is much less than the zero temperature coercive field, this bifurcation point indicates the onset of irreversibility and hysteresis.

The length of time required to cool to the desired measuring temperature depends

greatly on whether measurements were performed using the VSM or the QD system. The cooling rate of the VSM is very fast, on the order of 1 K/s and stability at each temperature is achieved in 15-20 seconds, whereas cooling is a very slow process for the QD magnetometer and 1-2 hours are required to cool and stabilize at the desired temperature, depending upon the difference between the reference temperature and the lowest desired measuring temperature. The range of temperatures and the number of measurements made depend on the particular magnetic system under investigation. When the VSM was used to acquire FC and ZFC data, the wait time for the moment to become zero at the reference temperature was about 15-20 seconds, and the moment could be monitored continuously, whereas for measurements performed on the QD magnetometer, a wait time on the order of minutes, which is essentially the time required to achieve thermal stability at the reference temperature, was implemented.

#### **4.2.2 Demagnetization**

*Ac demagnetization* on the VSM was performed in situ by dc cyclic erasure starting from a field sufficiently large to saturate the material and decrementing the upper limit of each successive cycle by 1% of its previous value. This was the smallest relative change in field between cycles available on the equipment. The typical time for this procedure was 5-10 minutes depending upon the required saturation field. The VSM's electromagnet enables very quick field reversals. By contrast, field changes on the QD SQUID based system can only be achieved very slowly, and it is impossible to perform the ac demagnetization procedure in situ. Thus, ac demagnetization was realized by employing a handheld Radio Shack Bulk Tape Eraser. The tape eraser, which produces a

60 Hz oscillating magnetic field, is similar in appearance to a small household iron. It was held very closely over the sample and then moved slowly away from the sample, essentially providing the necessary oscillating field of ever-decreasing amplitude, as the magnetic field falls off with distance.

*Thermal demagnetization* could be performed in situ in both the VSM and the QD magnetometer. Since the VSM has an internal furnace, thermal demagnetization was achieved by heating a sample above its magnetic ordering temperature for approximately 15 seconds and then cooling in zero field to the measurement temperature. The QD magnetometer can only measure the properties of magnetic systems whose ordering temperatures are below room temperature. However, for magnetic systems whose ordering temperatures are above 400 K, but whose range of investigation involved temperatures below 300 K, it was necessary to thermally demagnetize the samples in zero field, outside the QD magnetometer in an external furnace built especially for this purpose.

#### **4.2.3 Magnetization and Remanence Measurements: Generating a Henkel Plot**

The procedure for initial moment and remanence measurements and demagnetization and demagnetizing remanence curves is similar for both the VSM and the SQUID magnetometer, except for the time required to obtain a single isotherm. On the VSM, acquisition only requires 1-2 hours since only about 20 seconds are needed to stabilize the magnetic field between value adjustments; whereas on the SQUID system the field changes are much slower and 5-10 minutes may be required to stabilize the field,

so acquisition of magnetizing and demagnetizing characteristics may take about 10 hours. Waiting between field changes is necessary so that transients can be eliminated. Although eddy currents generated by these changes diminish rapidly, relaxation effects associated with thermal activation processes within the sample must also be considered.

Measurements are made only after the moment has reached a temporal plateau. In general, a field  $h_a$  is applied and before a moment measurement  $m(h_a)$  is made, the system is allowed to stabilize, then the field is reduced to zero in order to acquire the corresponding remanence  $i_m(h_a)$  after an equivalent wait time. This procedure is repeated for increasing values of  $h_a$  until saturation is reached. Similarly, data for the demagnetizing curve is accumulated by measuring the moment  $m_d(-h_a)$  and returning the field to zero to find the demagnetizing remanence  $i_d(-h_a)$ . In order to generate a Henkel plot (Section 3.3) from the data, measurements of the demagnetizing remanences must be taken with reverse applied fields of the same magnitude as those applied to obtain the magnetizing remanence data, that is, the points plotted on the Henkel plot are  $i_d(-h_a)$  versus  $i_m(+h_a)$ .

#### 4.2.4 Magnetization as a Function of Time

To determine how the moment of a sample changes when a field is applied, a time dependent measurement must be made. The sample was zero field cooled from a reference temperature  $T_{ref}$  larger than its Curie temperature  $T_c$  or its highest blocking temperature  $T_{B,max}$  to a temperature  $T < T_c$  or  $T_{B,max}$ . A step function field excitation was applied and the moment was observed. The moment was measured frequently to plot the magnetization characteristic as a function of time. The sampling rate and the time

period, over which measurements were made, were determined by the time required to ramp the field from zero to  $h_a$ , and by the dynamics of the magnetic system. The purpose of these measurements was to determine the relative importance of the thermal viscosity parameter  $h_T^*$ , since the peak in the temperature dependence of the ZFC moment has contributions from two sources: thermally activated overbarrier relaxation and the collapse of the coercive field distribution which is expected to occur as  $T \sim T_c$  from below.

## 4.3 Magnetic Systems

Experiments were conducted to investigate the nature of magnetization and the hysteretic properties of several magnetic systems of both technological and fundamental interest, as well as to determine the suitability of the Preisach model to describe and gain insight into the magnetic processes involved in these systems. Measurements were performed on chromium dioxide audio tape (Section 4.3.1), magnetoferritin, which is a contrast agent used for magnetic resonance imaging (Section 4.3.2), a neodymium iron boron permanent magnet (Section 4.3.3), floppy disk (Section 4.3.4), and cobalt chromium hard disk in both longitudinal (Section 4.3.5) and perpendicular (Section 4.3.6) magnetic particle configurations.

### 4.3.1 Chromium Dioxide Audio Tape

Chromium dioxide audio tape, a particulate magnetic medium, approximates an ideal scalar Preisach system, due to the regularity of particle size and shape and their well-aligned uniaxial anisotropy axes.  $\text{CrO}_2$  is a ferromagnetic oxide. It has a tetragonal

structure with lattice constants  $a = 4.423 \text{ \AA}$  and  $c = 2.917 \text{ \AA}$  and Cr ions are found at the corners and body centre, for a total of two Cr ions per tetragonal unit cell.  $\text{CrO}_2$  is not a naturally occurring compound. For magnetic recording applications, additives are added to reduce heat and pressure required in its preparation from chromyl chloride  $\text{CrO}_2\text{Cl}_2$  and  $\text{CrO}_3$ , and to provide nucleation sites on which particles can grow. Furthermore, additives are used to modify magnetic or physical properties such as the Curie temperature, coercivity and abrasiveness. Commonly used additives are Sb, Te and Fe. One advantage of  $\text{CrO}_2$  is the high recording density afforded by its small-sized acicular particles, which are about  $0.4 \mu\text{m} \times 0.05 \mu\text{m}$ . These particles are small enough to be single domain as determined by Darnell (1961, as cited in Bate, 1980, p. 472). Considering magnetostatic energy and wall energy, his calculations showed that for diameters less than  $0.4 \mu\text{m}$  single domain particles are expected, while his experimental study showed that particles having length to diameter ratio of 5 and diameters less than  $0.2 \mu\text{m}$  exhibited single domain behaviour. The crystalline anisotropy constant of  $\text{CrO}_2$  is  $K_1 = 2.5 \times 10^5 \text{ ergs/cm}^3$ . For the particles used in recording media, the principle source of anisotropy is particle shape, and these elongated particles possess an easy axis coincident with their long axes. The particle magnetization is about  $500 \text{ emu/cm}^3$ . The Curie temperature of  $\text{CrO}_2$  is quite low,  $T_c \approx 127 \text{ }^\circ\text{C}$ , which makes it more temperature sensitive than iron oxide tapes.

$\text{CrO}_2$  audio tape is prepared by coating a flexible non-magnetic plastic substrate with a solution of fine magnetic particles. The particles are aligned by applying a magnetic field along the length of the tape before the solution evaporates. The tape is then

heated and rolled, increasing the density of particles. The result is a particulate medium, consisting of magnetic particles with well-aligned easy axes.

The sample measured here consisted of two layers of CrO<sub>2</sub> audio tape (BASF Chrome Maxima II) cut to the tape width, yielding a 4 mm square sample. The two thicknesses, used to ensure a sufficiently strong signal, were stacked, while preserving the orientation of the particle alignment direction. The tape was placed on a Stycast 1266 epoxy base and sealed with the same.

The sample was prepared in two different demagnetized states using thermal and ac demagnetizing procedures. Two temperature ranges were considered  $10 \text{ K} \leq T \leq 300 \text{ K}$  and  $25 \text{ }^\circ\text{C} \leq T \leq 120 \text{ }^\circ\text{C}$ . The low temperature data was acquired on the Quantum Design SQUID-based magnetic property measurement system (MPMS), while the VSM was used for high temperature range data acquisition. A range of fields  $-3000 \text{ Oe} \leq h_a \leq +3000 \text{ Oe}$  was used to achieve saturation for low temperature data while the fields required at the highest temperatures were such that  $-500 \text{ Oe} \leq h_a \leq +500 \text{ Oe}$ . At each temperature of interest, the following measurements were performed: the initial magnetizing curve and the magnetizing remanence to positive saturation, and the demagnetizing curve and demagnetizing remanence to negative saturation.

The prepared sample was first subjected to a sequence of measurements under ac demagnetized initial conditions in the VSM at a number of temperatures between 25 °C and 120°C, during which the sample was *never heated above its ferromagnetic Curie temperature*,  $T_c \approx 127^\circ\text{C}$ . This was a crucial precaution since it was subsequently discovered that thermal annealing at 150°C produced a measurable irreversible loss of

magnetic moment, presumably due to chemical alterations within the  $\text{CrO}_2$  particles themselves. Since  $\text{CrO}_2$  is not a naturally occurring compound, the particles tend to react chemically with the atmosphere or binder resins (Bate, 1980). In our measurements, these changes took the form of a reduction in the amplitude of the hysteresis loop, with essentially no change in the shape or coercive field. Comparisons between ac and thermally demagnetized data at a particular temperature were performed by first thermally demagnetizing the sample at  $150^\circ\text{C}$ , quenching to the measurement temperature, completing a hysteresis cycle, then ac demagnetizing the sample *without altering the temperature* and repeating the cycle, so that the system was *chemically identical* under both sets of initial conditions.

The FC data were obtained using the VSM by cooling the sample in 100 Oe from a reference temperature  $T_{\text{ref}} = 150^\circ\text{C}$  in the paramagnetic region, through the Curie temperature to  $25^\circ\text{C}$ , and then measuring the moment on warming, while ZFC data were obtained by cooling in zero field from  $150^\circ\text{C}$  to  $25^\circ\text{C}$  then applying 100 Oe at  $25^\circ\text{C}$  and warming. The moment was measured as a function of temperature in one degree intervals up to  $150^\circ\text{C}$ . The time dependence of the moment was measured for  $0 \leq t \leq 20$  s after zero field cooling from  $150^\circ\text{C}$  to  $120^\circ\text{C}$  and applying a step field excitation  $h_a = 100$  Oe. The ramping time for the field is about 0.5 s.

### **4.3.2 Magnetoferritin**

Magnetoferritin is a biosynthetic material which consists of nanodimensional particles of maghemite, a ferrimagnetic iron oxide ( $\gamma\text{-Fe}_2\text{O}_3$ ) encaged in a roughly spherical protein shell, and derived from the biologically ubiquitous protein, ferritin.

Ferritin serves to stabilize and store colloidal iron oxide as ferrihydrite ( $5\text{Fe}_2\text{O}_3 \cdot 9\text{H}_2\text{O}$ ). The protein's constituent units assemble into a rather symmetrical shell, 120 Å in diameter, enclosing a central cavity about 80 Å in diameter and intersected by ion transport channels (Douglas, et al., 1994). Synthesis of magnetoferritin requires removal of the native hydrated mineral core by dialysis, leaving the shell intact, and remineralization of the central cavity with ferrimagnetic maghemite. Although the maghemite core exists in the face centred cubic (FCC) mineral phase ( $a = 8.4 \text{ \AA}$ ) and the shell is roughly spherical, the particle possesses shape or possibly stress induced *uniaxial* anisotropy,  $K = 10^5 \text{ ergs/cm}^3$  (Moskowitz, et al., 1997). This uniaxial anisotropy can develop as a consequence of irregularities in shape as shown by transmission electron microscopy (TEM) or residual stresses from cation vacancy disorder in maghemite. In addition, surface anisotropy due to the high fraction of surface atoms and heterogeneity of Fe sites at the core-shell interface can lower the symmetry of the intrinsic cubic anisotropy of the core.

A transmission electron micrograph of a magnetoferritin sample shows both discrete mineral cores and small aggregates of nanoparticles (Figure 4.7a). The discrete cores are 6 nm in diameter ( $\sigma = 1 \text{ nm}$ ), and particles in aggregated clusters, which possess greater variability in size and shape, are about 10 nm ( $\sigma = 2.6 \text{ nm}$ ). Being larger than the protein shell, these aggregate member particles probably outgrow the shell through the iron transport channels or through sites of shell damage, procured during synthesis. The precipitation of maghemite into particles of this size is unlikely, since control experiments without ferritin yield much larger, micrometre sized crystals. The particle

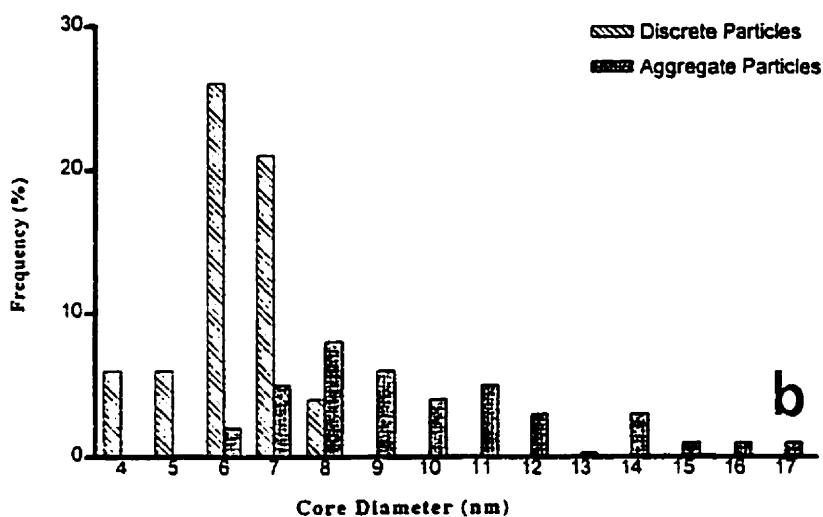
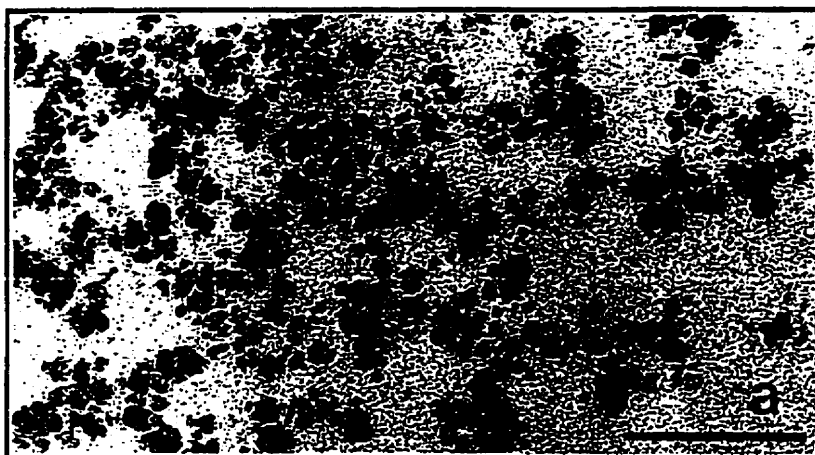


Figure 4.7 . (a) A transmission electron micrograph of unstained magnetoferritin showing discrete nanoparticles and larger aggregates. The scale bar represents 100 nm. (b) The particle size distribution plotted as a histogram showing core sizes for both the discrete cores and particles associated with the aggregated clusters. (Moskowitz, Frenkel, Walton, Dickson, Wong, Douglas, et al., Fig. 1, 1997)

size distribution histogram shows a broad asymmetric distribution of core diameters (Figure 4.7b).

Magnetoferritin behaves superparamagnetically, having a mean magnetic moment of about 22 000 Bohr magnetons per magnetoferritin molecule at 300 K (Moskowitz, et al., 1997). The mean blocking temperature, defined as the temperature at which one half the saturation remanence present at 5 K is lost, is 18 K (Moskowitz, et al).

The sample used in our measurements was a 30  $\mu\text{l}$  aqueous suspension of magnetoferritin particles, containing 0.16% magnetoferritin by volume. The sample was contained in an epoxy cylinder that was held in a gelatin capsule, which allowed easy mounting of the sample in a cylindrical holder. The low blocking temperature of magnetoferritin required use of the Quantum Design SQUID system to perform measurements at temperatures where the sample ceases to be superparamagnetic. The magnetoferritin sample was subjected only to thermal demagnetization, since ac demagnetization cannot be performed in situ on the QD magnetometer. (Since the ac demagnetization procedure is accomplished at room temperature for samples measured on this equipment, the magnetoferritin would remain thermally demagnetized despite being exposed to an oscillating field of ever-decreasing magnitude.) For  $T = 5, 6, 8, 10$  and 50 K, major hysteresis loops were measured for magnetoferritin, as were the magnetizing and demagnetizing remanences. The field range employed in this acquisition was from -3000 Oe to +3000 Oe. The reference temperature for thermal demagnetization of magnetoferritin was chosen to be  $T_{\text{ref}} = 200$  K, which is below the solidification temperature of the aqueous suspension, but well above its mean blocking

temperature. The FC and ZFC curves were obtained for magnetoferritin, by cooling from 200 K and by applying a dc field  $h_a = 15$  Oe. The moment was measured every five degrees over a range of temperatures  $10 \text{ K} \leq T \leq 150 \text{ K}$ . The time dependence of the moment was measured for  $0 \leq t \leq 100 \text{ s}$  after zero field cooling from 200 K to 50 K and applying a “step function” field excitation  $h_a = 20$  Oe. The time taken to ramp the field to this value was approximately 10 s.

### 4.3.3 Neodymium Iron Boron: A Permanent Magnet

Neodymium iron boron magnets comprise the strongest permanent magnets to date. While they possess the characteristic high remanent magnetization, high coercivities and a high magnetic energy product, their commercial advantage lies in their ease of production and a high performance-cost ratio. NdFeB magnets are widely implemented where space and weight are limited (Xinhuan Company, literature).

The permanent magnet was prepared by the Xinhuan Company (part of the Chinese Academy of Science) in Beijing, China. The sample of  $\text{Nd}_2\text{Fe}_{14}\text{B}$ , was produced by first melting the nominal composition of neodymium, iron, and boron together under an argon gas atmosphere to form an ingot. The ingots were crushed to  $\sim 1$  mm by a jaw crusher, to  $\sim 100 \mu\text{m}$  using a disk mill, and finally, pulverized to  $\sim 3 \mu\text{m}$  by a ball mill. The microparticles were aligned in an applied field, pressed perpendicular to the field direction under high pressure, and then sintered at high temperature ( $\sim 1400 \text{ K}$ ) for an hour. Following sintering the NdFeB compacts are rapidly cooled, heat treated and quenched (Sagawa, Fujimura, Togawa, Yamamoto & Matsuura, 1984).

The main phase of  $\text{Nd}_2\text{Fe}_{14}\text{B}$  is tetragonal  $a = 0.88 \text{ nm}$  and  $c = 1.22 \text{ nm}$ . Minor

phases present at grain boundaries and corners are tetragonal  $\text{Nd}_2\text{Fe}_7\text{B}_6$  and FCC Nd rich (95 at. %) (Sagawa, et al, 1984, as cited in Li & Strnat, 1985). The magnet has uniaxial anisotropy parallel to the c axis,  $K_1 \approx 3.5 \times 10^7$  ergs/cm<sup>3</sup> and its Curie temperature is about 312 °C (Xinhuan Company, specifications).

The sample used was cut with a diamond saw to be 3 mm long, 1 mm wide and to a thickness of less than 0.5 mm with the long dimension along the direction of easy axis alignment. The sample was mounted on the holder with cement to withstand the high temperatures required for thermal demagnetization. Only thermal demagnetization was used to produce the initial demagnetized state, since insufficient fields were available on the VSM to saturate the permanent magnet, as required for an ac demagnetization procedure. All measurements were acquired with the VSM. Prior to each magnetization sequence, the sample was thermally demagnetized at  $T = 400^\circ\text{C}$  and cooled in zero applied field to the measurement temperature. Measurements including the initial magnetization, magnetizing remanence, demagnetization, and demagnetizing remanence curves were performed on the sample of sintered aligned  $\text{Nd}_2\text{Fe}_{14}\text{B}$ , over an applied field range  $-12 \text{ kOe} \leq h_a \leq +12 \text{ kOe}$  and at eight temperatures in the range  $25^\circ\text{C} \leq T \leq 220^\circ\text{C}$ , selected to illustrate the thermal characteristics of the magnet. The magnetic field was applied parallel to the alignment direction, which being the longer dimension, also corresponds to the minimum demagnetizing factor.

The FC and ZFC curves were obtained using a reference temperature  $T_{\text{ref}} = 400^\circ\text{C}$  and a dc field  $h_a = 100 \text{ Oe}$ . The moment was measured every degree in the range  $25^\circ\text{C} \leq T \leq 380^\circ\text{C}$ . Measurements of the time dependence of the moment after

zero field cooling from 400 °C to 25 °C were made for  $0 \leq t \leq 75$  s after the application of a “step function” excitation  $h_a = 100$  Oe for which the ramping time was about 0.5 s.

#### 4.3.4 Commercial Floppy Disk

Floppy disks made for commercial use are prepared similarly to audio tape. Particulate coatings of magnetic particles are held in a polymer binder on a substrate of polyethylene terephthalate (PET) (Yaskawa & Heath, 1990, p. 796). The most widely used magnetic particle is gamma ferric oxide,  $\gamma\text{-Fe}_2\text{O}_3$ . The acicular particles are oriented randomly in the plane of the disk. For high density media, like the common 3.5 inch, 2 megabyte floppy disks, the magnetic coating is a cobalt modified  $\gamma\text{-Fe}_2\text{O}_3$  of thickness 0.9  $\mu\text{m}$ . Introducing cobalt ions into  $\gamma\text{-Fe}_2\text{O}_3$  increases the coercivity and this modification changes the coercivity of this medium from 300 Oe to about 630 Oe (Yaskawa & Heath, p. 795). The Curie temperature of the magnetic layer of floppy disks is about 675 °C (Sugaya & Yokoyama, 1990, p. 951).

The sample was taken from a standard commercial high density floppy disk removed from its plastic encasement. It was cut with scissors into a rectangle 4 mm by 1 mm. Only a single thickness of the floppy disk was required since the Quantum Design magnetometer was sufficiently sensitive. Measurements of magnetization and remanence were only performed at room temperature (300 K). Only the ac demagnetization procedure was used to produce the original demagnetized state. A thermal procedure was not used since very high temperatures are required to exceed the Curie temperature of  $\gamma\text{-Fe}_2\text{O}_3$  and the plastic binder deteriorates before the magnetic material can be demagnetized. Magnetization and remanence data for the initial curve as well as the

demagnetization and the corresponding demagnetization remanence data were acquired to generate a Henkel plot. The fields applied to the sample ranged between -3000 Oe and +3000 Oe.

#### **4.3.5 Commercial Hard Disk: Cobalt Chromium Based**

The memory storage unit most common in computers is the hard disk. It consists of an aluminum-magnesium substrate coated with several layers: a paramagnetic layer of nickel-phosphorus, a thin layer of magnetic recording medium, such as cobalt-nickel-chromium or cobalt-chromium-tantalum, and a nonmagnetic overlayer of carbon. A layer of Cr may be grown between the paramagnetic and magnetic layers. The Cr grows as columns and the sputtered Co-alloy will nucleate on the “domes” of these columns, which determine the magnetic grain size (Köster & Arnoldussen, p. 218). Grains are randomly oriented and their magnetic moments lie in the plane of the layer. The typical coercivity characteristics of hard disks range between 750 and 1250 Oe with a saturation magnetization of about 1000 emu/cm<sup>3</sup>.

The hard disk sample was acquired from the IBM Corporation (by D. Dahlberg, University of Minnesota) and consists of a cobalt chromium based magnetic alloy with some additives to improve recording characteristics. (The details of the composition are a trade secret and were unavailable to this author.) The disk was double-sided, meaning that both sides of the disk were coated with magnetic layers.

The disk was scored in concentric circles to assist with tracking of the read/write head. The sample was cut parallel to these striations, into 4 mm by 1 mm rectangle with a diamond saw, and was the thickness of the hard disk, ≈2 mm (although the actual film

thickness was only a few microns). When measurements were made along these directions, there was evidence of chain-like relaxation along these striations as observed using magnetic force microscopy. Observations of the relaxation behaviour of a saturated sample subjected to a reversing field shows that there is coupling in chains parallel to striations, but no coupling between these chains (private communication, Dan Dalhberg, 1997).

The sample was prepared in an ac demagnetized initial state. Thermal demagnetization was not possible. In fact, attempts to measure the Curie temperature of the sample failed because the substrate melted before the magnetic moment disappeared. The measurements of the initial magnetizing curve and remanence as well as the demagnetizing curve and its corresponding remanence were obtained on the QD magnetometer at 300 K. The field  $-1500 \text{ Oe} \leq h_a \leq +1500 \text{ Oe}$  was applied along the direction of the striations.

#### **4.3.6 Perpendicular Hard Disk: Cobalt Chromium**

Most commercially available recording media are longitudinal, that is, the easy axes of their constituent magnetic particles lie in the plane of the medium. This is true for audio and video tapes, as well as for flexible and hard disks. Perpendicular magnetic films are of interest as magnetic recording media due to the higher recording density offered by the perpendicular orientation of particles. Perpendicular films exploit the long axis alignment of rod-shaped grains normal to the plane.

The Curie temperature of these films is not well documented. In alloys, the addition of nonmagnetic constituents, like Cr in Co, actually reduces the ordering temperature. Bulk Co-Cr alloys containing 20% Cr have  $T_c \approx 150^\circ\text{C}$  (Bozorth, 1951, as cited by Köster & Arnoldussen, 1990, p. 236); however, the properties of the films differ

greatly from those of the bulk material. For example,  $\text{Co}_{84}\text{Cr}_{16}$  has  $T_c \approx 700^\circ\text{C}$  as a deposited film while in the bulk alloy, the Curie temperature is only  $355^\circ\text{C}$  (Ishizuka et al, 1983, as cited by Köster & Arnoldussen, p. 236).

The perpendicular film used in this experiment is a sputtered Co-Cr film with the particles' easy magnetization axes perpendicular to the film plane. The structure of the Co-Cr grains is hexagonal closed packed with the  $c$  (or long) axis normal to the plane. The sample, obtained from the School of Physics and Astronomy, University of Minnesota, was prepared by rf sputtering films of the alloy  $\text{Co}_{80}\text{Cr}_{20}$  onto an aluminum alloy substrate. The film thickness is between about 0.5 and 1.5  $\mu\text{m}$  (Lottis, Dahlberg, Christner, Lee, Peterson & White, 1988). Grain volumes are measured microscopically to be on the order of  $10^{-15} \text{ cm}^3$  (Khan et al, 1988, as cited by Lottis, White & Dahlberg, 1990).

The sample, punched out of the magnetic film, was a thin circular disk about 4 mm in diameter. This "foil" was mounted on a solid cylindrical epoxy base and coated with Stycast 1266 epoxy. Measurements were performed using the VSM magnetometer at 300 K and the sample was only prepared in the ac demagnetized state. Thermal demagnetization was not attempted since the sample base, the epoxy disk, would not withstand the high temperatures required. The sample was mounted such that a magnetic field  $-15 \text{ kOe} \leq h_a \leq +15 \text{ kOe}$  could be applied normal to its surface, that is along the easy direction. The initial magnetization curve and corresponding remanence as well as the demagnetizing curve of the major hysteresis loop and its associated remanence were measured.

## Chapter 5

# A Preisach-based Analysis and Discussion of the Hysteretic Properties of Magnetic Systems

### 5.1 Parameter Selection and Fitting

Generally, all of the calculations with the Preisach model presented here required specification of the following eight fitting parameters: the mean field parameter  $k$ , the mean (or most probable) or median coercive field  $\tilde{h}_c$ , the saturation magnetization  $m_\infty$ , the effective thermal viscosity parameter,  $h_T^*$ , the width of the interaction field distribution  $\sigma_i$ , the width of the coercive field distribution  $\sigma_c$ , the fraction of the moment due to reversible processes  $f$ , and the reversibility parameter  $\Gamma$ . Some of these parameters may be fixed by physical constraints imposed by the microstructure of the system or by

the experimental conditions. Initial values for many of the parameters were selected using information extracted from the magnetization and remanence measurements, as well as from Henkel plots of the remanence data. Analysis of  $\text{Nd}_2\text{Fe}_{14}\text{B}$  data required modification of the Preisach formalism introduced in Chapter 3 and is discussed separately in Section 5.7.

### 5.1.1 Initial Parameter Values

For many of the magnetic systems investigated, the particles, or pseudoparticles, are assumed to have no long range interactions, thus fixing the parameter  $k$  at  $k = 0$  for these systems. A positive value of  $k$  is selected where Henkel plots lie above the Wohlfarth line, while a negative value is employed where Henkel plots for *thermally demagnetized* samples lie below this line, or where strong curvature exists in the Henkel plot of ac demagnetized samples. Figure 5.1 shows the effect of the sign of  $k$  on Henkel plots for both ac and thermally demagnetized Preisach planes, and on the magnetization curves for these two initial states. The default values for parameters used in the following calculations are  $k = 0$ ,  $\tilde{h}_c = 1000$ ,  $\sigma_c = 0.5$ ,  $\sigma_i = 0.25$ ,  $h_T^* = 0$ ,  $m_\infty = 1.0$ ,  $f = 0$ , and  $\Gamma = 0.5$  unless otherwise indicated.

Since a positive slope is present in the magnetization curves even at high fields, the initial value for the saturation moment,  $m_\infty$  is estimated to be slightly higher than the moment measured at the highest field applied to the sample. For the purposes of calculation,  $m_\infty$  is treated simply as a temperature-dependent scaling factor. The effect of the saturation moment on the magnetizing curve is presented in Figure 5.2. Naturally, the saturation moment has no effect on normalized Henkel plots.

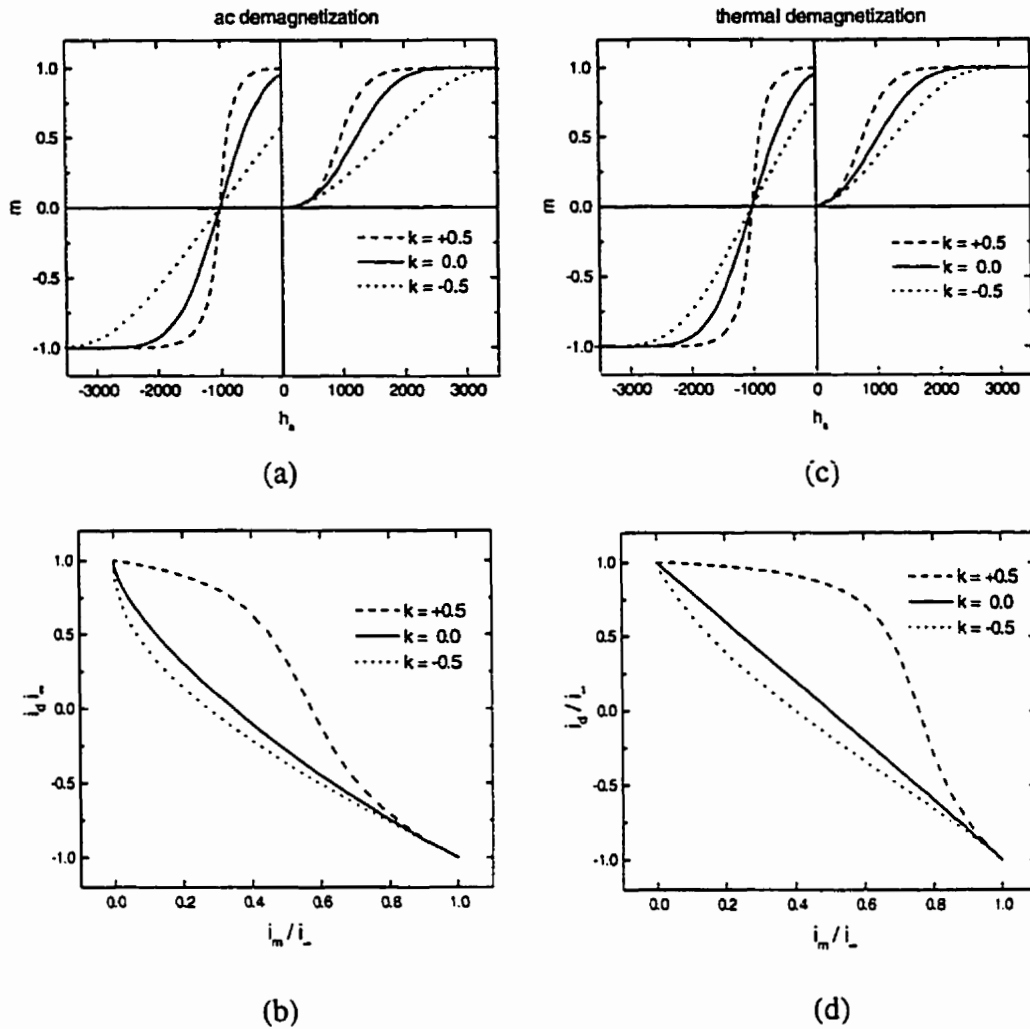


Figure 5.1 . The effect of the mean field parameter  $k$  on the initial magnetization curve, and the descending branch of the major loop, and on Henkel plots for both ac demagnetized ((a) and (b)) and thermally demagnetized ((c) and (d)) initial states. The rate of magnetization with respect to field increases with increasing  $k$  ((a) and (c)), and the curvature of the Henkel plot changes from negative (or zero) to positive with increasing  $k$  ((b) and (d)). Henkel plot curvature is unambiguously defined by the sign of the mean field parameter for thermally demagnetized initial states (d).

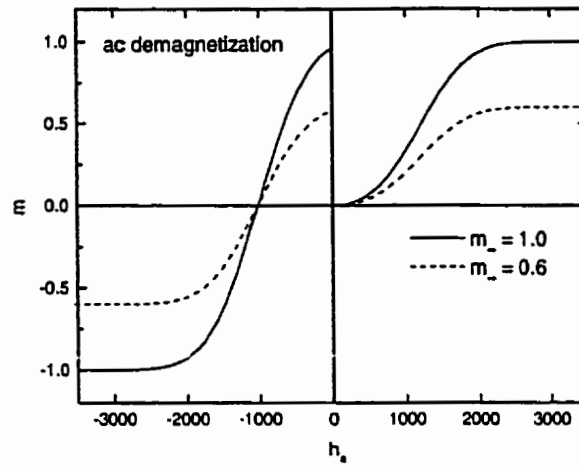


Figure 5.2 . The parameter  $m_{\infty}$  is simply a scaling factor.

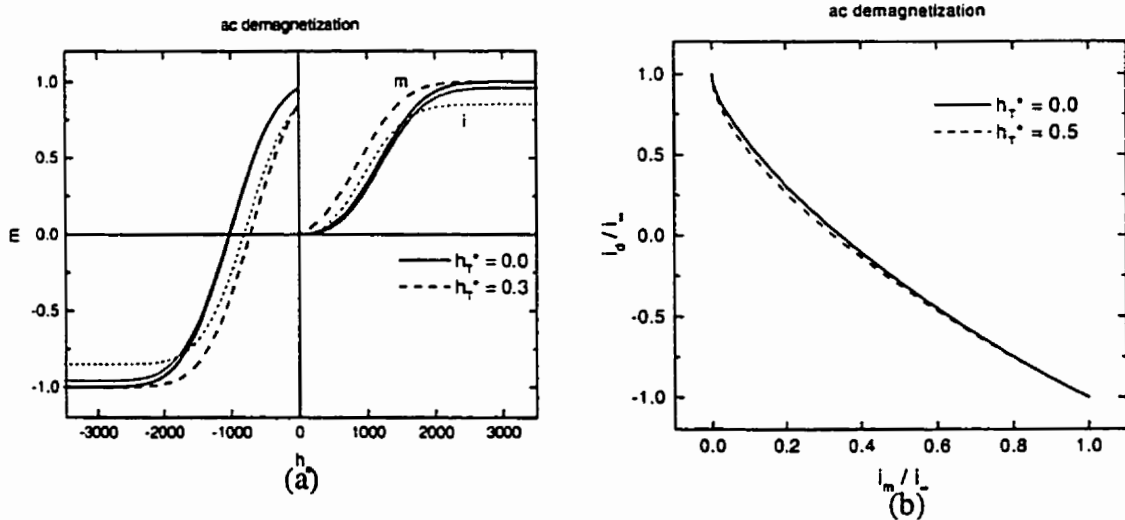


Figure 5.3 . (a) A finite thermal viscosity parameter  $h_T^*$  increases the reversibility of the magnetic response and (b) slightly increases the curvature of the ac demagnetized Henkel plot.  $h_T^*$  has no effect on Henkel plots generated for thermally demagnetized initial states with  $k = 0$ . The bold lines in (a) indicate the magnetization curves while the finer lines represent remanence curves.

The effective thermal field parameter,  $h_T^*$ , is estimated to be zero at temperatures far below the ordering temperature, and is increased with increasing temperature, as necessary, to account for the thermal dynamics of a system. Higher values of  $h_T^*$  increase the initial slope of the magnetization curve and reduce both the saturation remanence and coercivity (Figure 5.3a). Furthermore, larger values of  $h_T^*$  increase the negative curvature of the Henkel plot for ac demagnetized systems with  $k = 0$  (Figure 5.3b), assuming the distributions themselves are independent of temperature, which is only true far below the below the critical ordering temperature  $T_c$  of the material.

### 5.1.2 The Preisach Distribution

The Preisach distribution can be written as the product of coercive and local interaction field distributions  $p(h_c, h_i) = f(h_c)g(h_i)$ , as described in Section 3.1. The Preisach distribution was selected based on macroscopic symmetry properties of the data. Since hysteresis loops are symmetric, the interaction field distribution must reflect that symmetry. All calculations performed in the analysis of experimental data throughout this chapter, have employed an interaction distribution that is a Gaussian centred at zero,

$$g(h_i)dh_i = \frac{1}{\sqrt{2\pi\sigma_i^2}} \exp\left[-\frac{h_i^2}{2\sigma_i^2}\right]dh_i$$

where  $h_i$  and the dispersion  $\sigma_i$  are dimensionless. The scaling factor for these parameters is the mean coercive field,  $\tilde{h}_c$ . The actual centre of the interaction distribution is  $\bar{h}_i = km$ , but as discussed in Section 3.2, mean field effects can be treated by employing an effective field  $h = h_a + km$  rather than shifting the interaction distribution itself. The

width of the Gaussian interaction field distribution,  $\sigma_i$  was selected with reference to the rate of magnetization with respect to the field. A slower magnetization corresponds to a larger width parameter (Figure 5.4a). The effect of larger values of  $\sigma_i$  on the Henkel plot of an ac demagnetized Preisach plane with  $k \leq 0$ , is to increase its curvature, moving it further from the Wohlfarth line (Figure 5.4b). The width of the interaction distribution has no effect on the Henkel plots for thermally demagnetized (random) initial states.

The coercive field distribution was chosen such that it reflected the symmetry of the initial magnetizing curve. Two different functional forms were used to describe the distribution of coercive fields. If the curvature of the magnetization as the specimen begins to exhibit a moment is equal but opposite to that of the curvature as the magnetization flattens in its approach to saturation, then the distribution of coercive fields that best reflects the pseudoparticle distribution is a symmetric distribution that was chosen to be a Gaussian. The Gaussian distribution was used for analyzing data from  $\text{CrO}_2$  audio tape,  $\text{Nd}_2\text{Fe}_{14}\text{B}$ , floppy disk, and longitudinal hard disk media. Calculations were performed in reduced variables, with the mean value of the coercive field normalized to unity in the calculations, but the quoted value of  $\tilde{h}_c$  represents the true mean value of the coercive field, that was used as a scaling factor. A preliminary estimate for the scaling factor  $\tilde{h}_c$  is determined from the intersection of the demagnetization curve with the applied field axis. However, this is strictly the real value of  $\tilde{h}_c$  only at zero temperature. For the Gaussian coercive field distribution

$$f(h_c) dh_c = \frac{1}{\sqrt{2\pi\sigma_c^2}} \exp\left[-\frac{(h_c - \tilde{h}_c)^2}{2\sigma_c^2}\right] dh_c ,$$

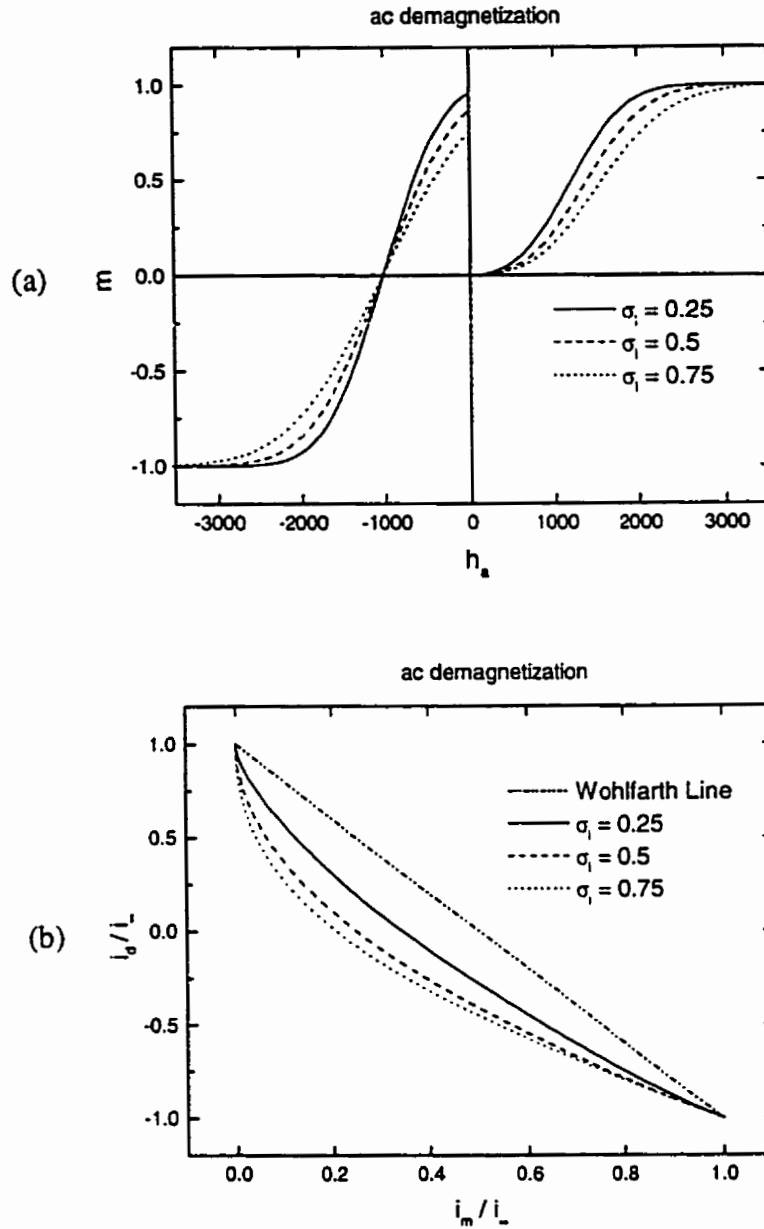


Figure 5.4 . (a) A larger interaction width parameter  $\sigma_i$  stretches out the hysteresis loop, yielding a decreased saturation remanence while the coercive field remains fixed. (b) The Henkel plot moves further from the Wohlfarth line as  $\sigma_i$  increases. Calculations were for  $k = 0$ .

the width parameter  $\sigma_c$  is also dimensionless, and quoted values of both interaction field and coercive field distribution widths have been scaled by  $\tilde{h}_c$ . The width of the coercive field distribution affects the steepness of the magnetization curve. Smaller values of  $\sigma_c$  delay the onset of magnetization and increase the maximum slope of the curve (Figure 5.5a). The effect of larger values of  $\sigma_c$  on the Henkel plot, for an ac demagnetized Preisach plane with  $k \leq 0$ , is to decrease the curvature, moving it closer to the Wohlfarth line (Figure 5.5b). The width parameter has no effect on the Henkel plots of thermally demagnetized systems.

If the curvature is weaker at the approach to saturation than the low field curvature, then a log-normal distribution was used to represent the pseudoparticle coercive field distribution. This coercive field distribution function was used in the analysis of magnetoferritin, floppy disk, and perpendicular hard disk media. The functional form of this distribution is given by:

$$f(h_c) dh_c = \frac{1}{h_c \sqrt{2\pi\sigma_c^2}} \exp\left[-\frac{(\ln h_c)^2}{2\sigma_c^2}\right] dh_c$$

where  $h_c = H_c/\tilde{H}_c$  is dimensionless and the true field  $H_c$  is found by scaling this reduced field by the *median* value  $\tilde{H}_c$ . For the log-normal distribution, the parameter  $\tilde{H}_c$  is typically *close* to the measured  $T = 0$  coercivity of a magnetic sample, but is not exactly equal. The width parameter  $\sigma_c$  in the log-normal distribution, is a measure of the dispersion in  $\ln H_c$ , which is easily seen by rewriting the distribution as a function of  $\ln H_c$

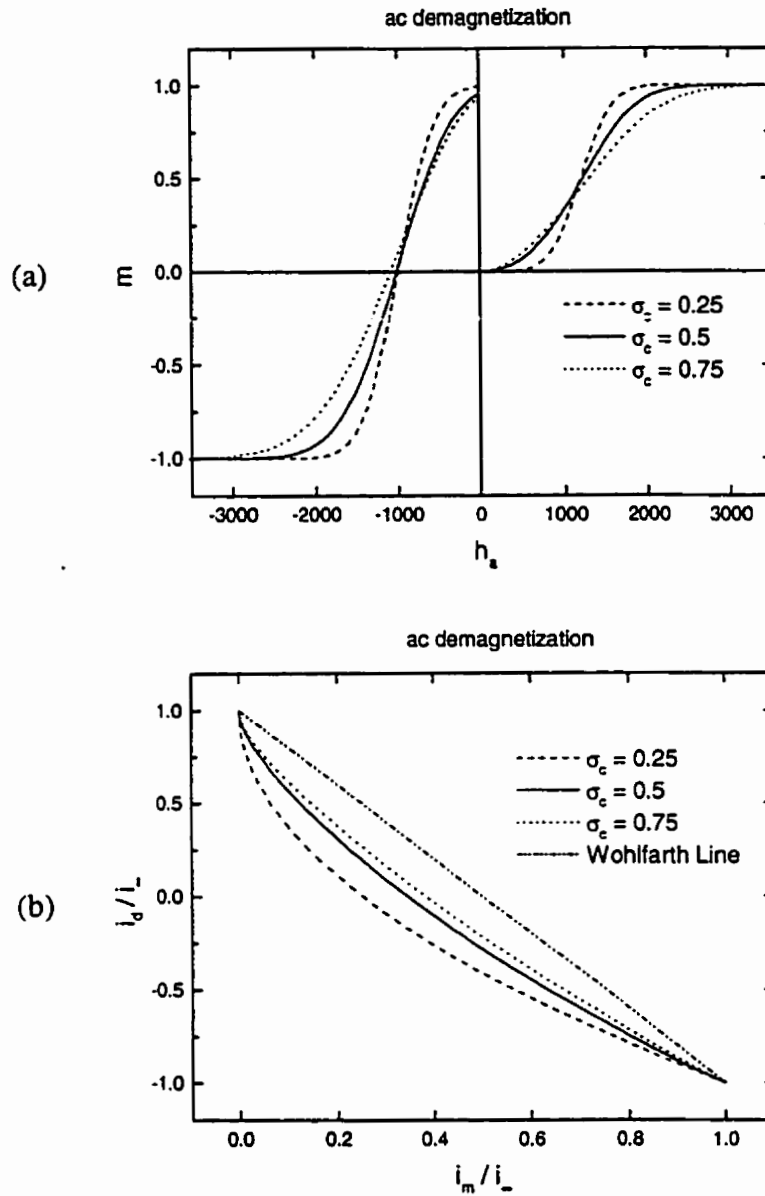


Figure 5.5 . (a) The initial magnetization begins more slowly but rises more steeply with an increasing coercive field distribution width parameter  $\sigma_c$ , while the coercive field and the saturation remanence show slight decreases. The Henkel plot moves toward the Wohlfarth line as  $\sigma_c$  increases, in direct contrast to the behaviour of the Henkel plot with increasing  $\sigma_i$ . Calculations were for  $k = 0$ .

$$f(h_c) dh_c = f'(\ln H_c) d(\ln H_c) = \frac{1}{\sqrt{2\pi\sigma_c^2}} \exp\left[-\frac{(\ln H_c - \ln \tilde{H}_c)^2}{2\sigma_c^2}\right] d(\ln H_c).$$

This Gaussian in  $\ln H_c$  drops to 0.6 of its maximum value when  $\sigma_c = \ln H_c - \ln \tilde{H}_c$ .

Rewriting this as  $e^{\sigma_c} - 1 = \frac{H_c - \tilde{H}_c}{\tilde{H}_c}$  and expanding the exponential for  $\sigma_c \ll 1$ , we obtain

$\sigma_c = \frac{H_c - \tilde{H}_c}{\tilde{H}_c}$ , so the width parameter roughly measures the *relative* spread in  $H_c$  about

$\tilde{H}_c$ . Figure 5.6 compares the Gaussian and log-normal distributions for  $\sigma_c = 0.45$ . The

initial values for all the coercive field distribution widths were chosen using the

information provided by Figures 5.5a and 5.5b and were adjusted to replicate the

character of the data.

### 5.1.3 The Reversible Component

The parameters of the phenomenological reversible component of the model that treats elastic distortions of domain walls, large populations of small energy barriers which behave quasi-reversibly, misalignment of the particles' easy axes with respect to the applied field, and field-induced moment growth are  $f$ , the reversible fraction, and  $\Gamma$ . The fraction  $f$  is estimated from high field ( $hf$ ) values of the moment and remanence,

$f \approx 1 - \frac{i_{hf}}{m_{hf}}$  and adjusted as required. Figure 5.7 shows the effect of  $f$  on magnetization

and remanence curves. The value for the reversibility parameter  $\Gamma$  is estimated. Lower

values of  $\Gamma$  correspond to smaller slopes of the magnetization curve at high fields (Figure 5.8) and weaker curvature.

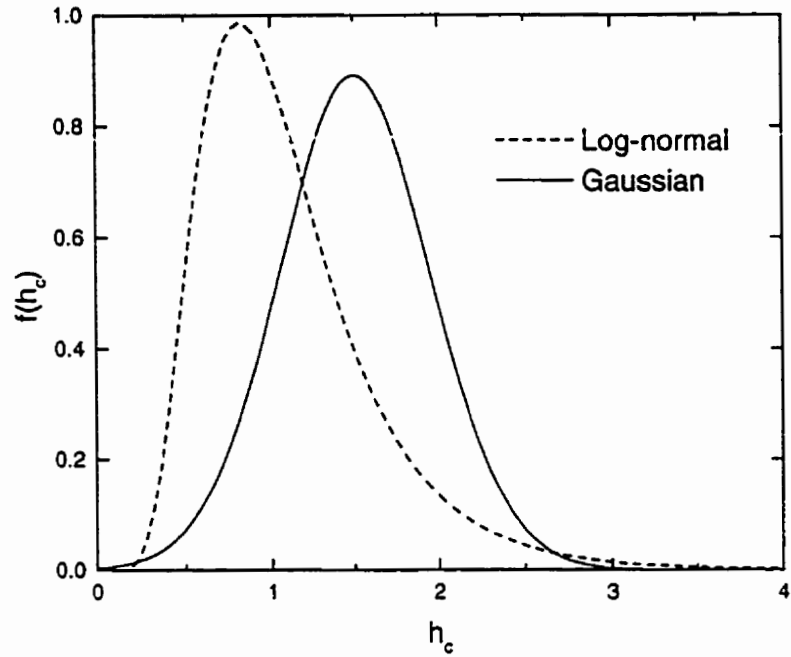


Figure 5.6 . A comparison of two coercive field distributions functions, showing the symmetry of the Gaussian ( $\tilde{h}_c = 1.5$ ) and the inherent asymmetry of the log-normal function, which approaches a Gaussian for sufficiently narrow widths.

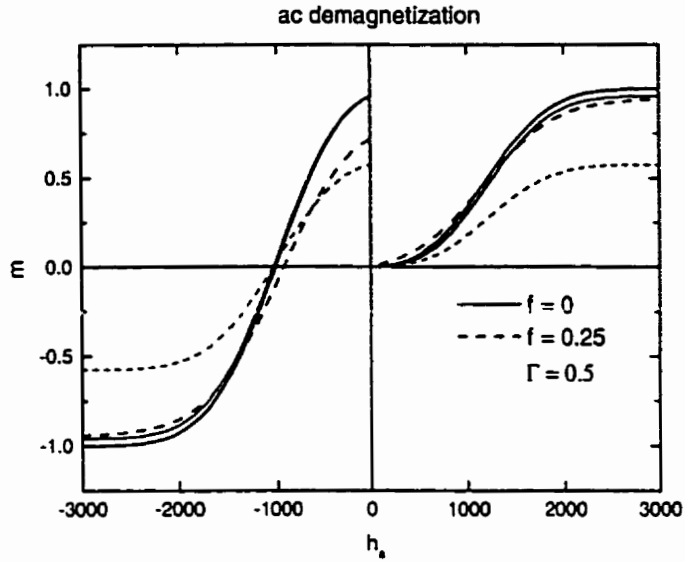


Figure 5.7 . The magnetic response becomes more reversible when a finite reversible contribution, a finite value of  $f$  is incorporated. The relative increase in reversibility is easily seen by comparing the bold (magnetization) and fine (remanence) curves.

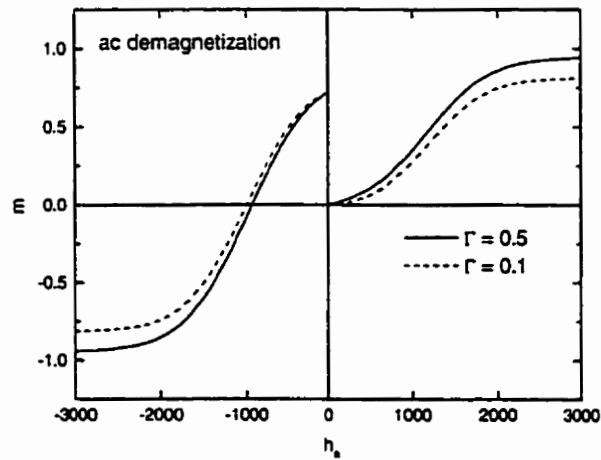


Figure 5.8 . The parameter  $\Gamma$  in the phenomenological reversibility expression controls the slope and curvature of the magnetization curves.

### 5.1.4 The “Fitting” Procedure

Once the starting values for the parameters were selected, the first Preisach calculations were made and the resulting magnetization and remanence curves and the Henkel plots were compared with the data. From the known trends, occurring with variation of a particular parameter, as discussed above, one parameter was changed at a time to improve agreement between the calculated curves and the experimental data. For much of the analysis of this experimental data, once the best possible fit, as judged by eye, was obtained, a rough numerical determination of the agreement was found by calculating a sum of the squares of the deviations at each data point (divided by the number of data points minus the number of fitting parameters) for each of three different curves: the magnetic moment as a function of applied field, the remanence as a function of field, and the Henkel plot. Then, each unfixed parameter was varied about its value to refine the agreement. Often a compromise was required to fit all three curves simultaneously. A set of parameters, which provides seemingly excellent agreement with the moment and remanence data, may yield a Henkel curve with little resemblance to that obtained experimentally. Small deviations from the data of the  $i_m(h_a)$  and  $i_d(h_a)$  curves can result in very large departures of the calculated Henkel plot from the measured data points, indicating the sensitivity of the Henkel plot. Likewise, a set of parameters which yields good agreement with Henkel data, may not provide a good description of the magnetization and remanence curves. Furthermore, parameters that mimic the shape of the magnetization curve may not follow the remanence data. To achieve the best possible compromise, the sum of the squares of the deviations of the calculated curves from the

data for *all three curves* were added to generate a total that represents the “overall goodness of fit.”

No *formal* numerical procedures were employed to optimize the individual fits or to characterize the quality of the agreement. Instead, the priority was to identify and replicate *systematic trends* that were associated with changes in temperature and, if possible, to correlate individual trends with specific model parameters so as to isolate the dominant physical mechanism responsible for each. Accordingly, uncertainties associated with particular model parameters are not stated. Figures 5.1 to 5.8 serve as a guide to understanding the effects of model parameters, demonstrating how the variation of a parameter can change magnetization, remanence, and Henkel curves. Moreover, the numerical results from these rough fitting procedures are not quoted in this discussion, although some references are made to the relative agreement between different parameter sets used to describe experimental data.

However, to *quantify* the effects of varying parameter values in an attempt to fit a typical data set, Table 5.1 provides a summary of the fitting parameters with their associated estimated uncertainties for magnetization, remanence, and Henkel plot data obtained from a commercial sample of CoCr-based hard disk (Section 5.3). The uncertainties represent the finest determination of the parameter, i.e. the smallest change from the “best” parameter values actually utilized in the Preisach calculations, and which resulted in an increase of the sum of the squares of deviations from the experimental data. The resulting changes in the agreement between the calculated curves and experimental data cannot be discriminated by eye. The agreement between calculated curves and

Table 5.1 . An example of uncertainties in the fitting parameters for Preisach calculations used for data analysis.

Parameter	k	$\tilde{h}_c$ (Oe)	$\sigma_c$	$\sigma_i$	$h_T^*$ (Oe)	$m_\infty$ ( $10^{-3}$ emu)	f	$\Gamma$
Value	0.110	1080	0.150	0.015	0.155	4.40	0.253	0.52
Uncertainty ( $\pm$ )	0.005	3	0.005	0.001	0.005	0.05	0.001	0.01
% Uncertainty	5	< 1	3	7	3	1	< 1	2

experimental data is more sensitive to change in some parameters than in others. In particular, scaling parameters like  $\tilde{h}_c$  and  $m_\infty$  can be very well defined, as can the reversible fraction,  $f$ .

Sections 5.2 through 5.4, which treat computer memory media at room temperature give greater insight into how parameters and Preisach distributions are selected, while the remaining sections of this chapter provide a detailed analysis of  $\text{CrO}_2$  audio tape, magnetoferritin and a Nd-Fe-B permanent magnet, and explore the power and limitations of the Preisach analysis as it relates to reproducing systematic temperature effects and investigating magnetization mechanisms.

## 5.2 Commercial Floppy Disk

Floppy or flexible disk is a particulate medium that consists of ferrimagnetic Co-modified  $\gamma\text{-Fe}_2\text{O}_3$ , whose easy axes are randomly oriented in the plane of the disk. The initial values for the Preisach model parameters selected to describe the data for this sample were based on observed characteristics of magnetization and remanence curves as well as the Henkel plot. The value of the mean field parameter was chosen to be  $k = 0$ , since the Henkel plot, although exhibiting a slight curvature beneath the Wohlfarth line, as expected for an ac demagnetized sample, showed no strong demagnetizing character. The value of the coercive field was selected as the modulus of the intersection of the demagnetization curve and the field axis at room temperature. The interaction field distribution was taken to be a Gaussian. Two different coercive field distributions, Gaussian and log-normal, were selected and compared in this Preisach analysis.

Figures 5.9 and 5.10 show the calculated magnetization and remanence curves for Gaussian and log-normal coercive distributions respectively. The corresponding Henkel plots are shown in Figure 5.11. The results from the fitting procedure indicate excellent agreement with the Henkel plots regardless of which functional form is chosen to represent the coercive field distribution. The differences in the effect of the coercive field distribution's functional form were more evident in the magnetization and remanence curves. Although the calculated magnetization and demagnetization curves that best correspond to the magnetization data were generated with a Gaussian distribution, the agreement with the magnetizing and demagnetizing remanences was not particularly close. The disagreement is especially noticeable for the demagnetizing remanence, where the calculated curve does not follow the data points except near the remanent coercive field. The log-normal coercive field distribution allowed a better fit to the remanence data, but did not describe the magnetic moment data as well, particularly at low fields on both magnetization and demagnetization curves. The quality of these fits may seem difficult to judge by simply looking at the curves; however, very little additional information is gleaned from a more in-depth analysis of the "goodness of fit." The procedure used to compare these data sets was to evaluate the sum of the squares of the deviations of the calculated curves and the measured data points after the best parameter values for each data set were separately determined. The result of this comparison showed that the agreement between the two calculated Henkel curves and the experimental plots were within 5% of each other, with the log-normal curve having a slight advantage. However, the magnetization curve generated with the Gaussian distribution was 13 times

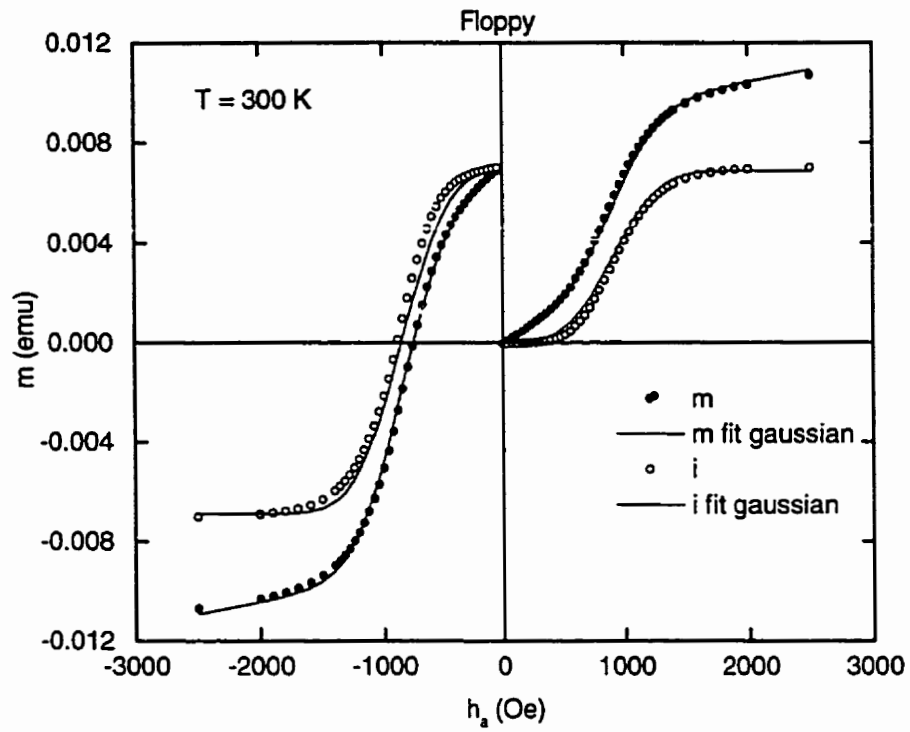


Figure 5.9 . Magnetization (solid dots) and remanence (open dots) data for a sample of commercial floppy disk shown with calculated magnetization and remanence curves (solid lines) using a *Gaussian* coercive field distribution.

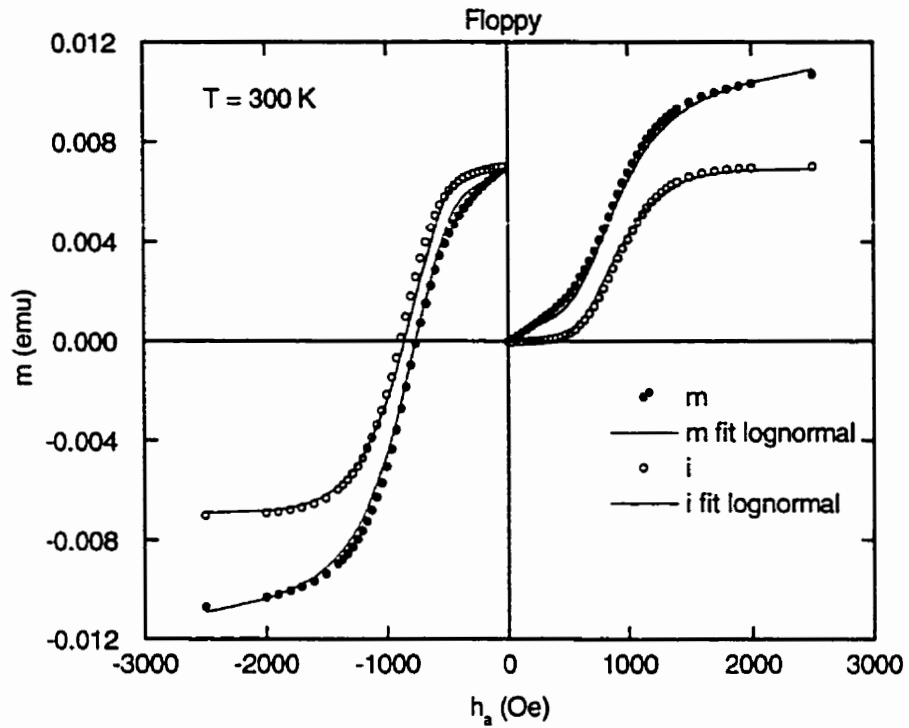
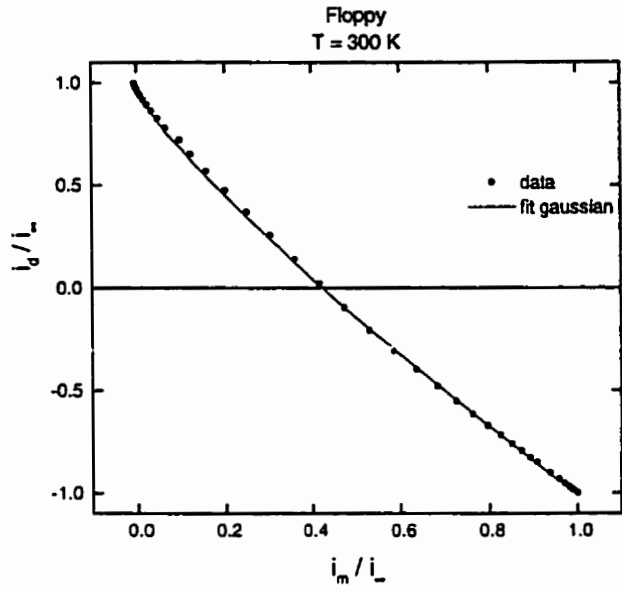
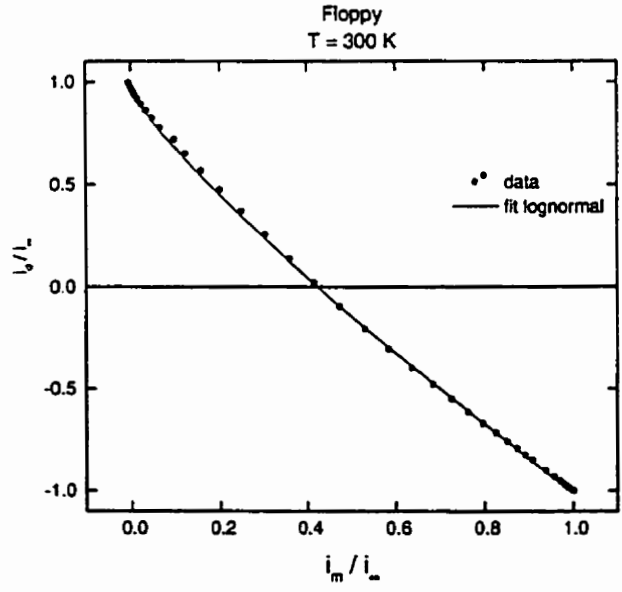


Figure 5.10 . Magnetization (solid dots) and remanence (open dots) data for a sample of commercial floppy disk shown with calculated magnetization and remanence curves (solid lines) using a *log-normal* coercive field distribution.



(a)



(b)

Figure 5.11 . The Henkel data for commercial floppy disk and the calculated Henkel curves for (a) a *Gaussian* and (b) a *log-normal* coercive field distribution.

better, while the remanence curves calculated using this distribution were nearly twice as bad as those of the remanence produced with a log-normal distribution. The total sum of the squares of the deviations for the three plots, magnetization, remanence, and the Henkel plots differ very slightly. Overall, the log-normal coercive field distribution seems to describe the data better by only 4%. Thus, choosing which of these two functional forms is a better description of the real distribution of the coercive fields of the particles is a difficult task. Nonetheless, this examination shows that visual judgements as to the goodness of fit are quite reliable when performing a Preisach analysis.

However, the Preisach calculations performed are expected to be somewhat more accurate for the remanence curves, as the reversible term employed to describe physical sources of reversibility not included in the Preisach model affects the magnetization curves and is merely phenomenological. As such, the log-normal distribution may be the more justifiable choice for the coercive field distribution, since it describes the remanence data better than the Gaussian distribution. Changing the functional form of this reversible contribution in calculations that implement the log-normal distribution may generate theoretical magnetization curves that better describe the magnetization data. Nevertheless, it is noteworthy that the magnetization curves calculated with the Gaussian coercive field distribution are 20 times better in agreement relative to the remanences generated by the log-normal function.

A comparison of the final parameter values selected for both of the functional forms are presented in Table 5.2. Both sets of parameters were equal. Since the specimen was ac demagnetized, the ac demagnetized Preisach plane was used in the calculations.

Table 5.2 . Best fit parameters for a sample of commercial floppy disk.

Distribution	$\tilde{h}_c$ (Oe)	$\sigma_c$	$\sigma_i$ (Oe)	$m_\infty$ (emu)	$h_T^*$ (Oe)
Gaussian	900	0.33	67.5	0.0129	49.5
Log-normal	900	0.33	67.5	0.0129	49.5

The mean field parameter was  $k = 0$  for these calculations, performed on an initially ac demagnetized plane. The reversible component is described by  $f = 0.465$  and  $\Gamma = 0.4$ .

The mean field parameter which best described the data was  $k = 0$ , which is expected for an ac demagnetized sample whose Henkel plot does not show strong curvature. Since  $k = 0$ , there appears to be no long-range interactions between particles. The mean coercive field value for the Gaussian distribution and the median coercive field value for the log-normal distribution were both  $\tilde{h}_c = 900$  Oe, in agreement with the relatively high values of coercivity required for magnetic memory media. Of course, the coercive field width parameter has a different meaning for the two distributions as explained in Section 5.1.2, and the log-normal distribution width is always dimensionless. The coercive distribution was a significant fraction of  $\tilde{h}_c$ ,  $\sigma_c = 300$  (Oe)  $\approx \frac{1}{3}\tilde{h}_c$ . The interaction field distribution was Gaussian and the width for both calculations was quite narrow, only  $\sigma_i = 67.5$  Oe. The effective thermal viscosity parameter  $h_T^* = 49.5$  Oe is only 5% of the mean coercivity of the floppy disk. This is a reflection of the fact that the measurement was performed at room temperature, far below the Curie temperature of the floppy disk material  $T_c \approx 675$  °C. The reversible fraction of the moment is 46%. This is not unexpected given the degree of randomness in the alignment of the easy axes of the magnetic particles fixed during fabrication (Section 4.3.4). Such randomness also may indicate that the log-normal distribution is a better choice of function to describe the coercive field distribution, for reasons which will be discussed in Section 5.6.

### **5.3 Commercial Cobalt-Chromium-Based Hard Disk**

This hard disk material is comprised of Co-rich ferromagnetic grains whose easy axes are aligned along striations in the plane of the disk. The measurements of the

magnetization and remanence characteristics of the cobalt-chromium-based hard disk, performed at 300 K on the QD magnetometer are shown in Figure 5.12. The most interesting feature of this CoCr-based longitudinal hard disk medium was the *positive curvature* of its Henkel plot above the Wohlfarth line (Figure 5.13). This positive curvature suggests the presence of magnetizing-like interactions within the material. Hence, the Preisach analysis was begun using a positive initial value for the mean field parameter,  $k > 0$ . The coercive field distribution that best described the data was a Gaussian, centred at  $\tilde{h}_c = 1080$  Oe with a width of  $\sigma_c = 160$  Oe. The interaction field distribution was also chosen as a Gaussian with a very narrow width parameter  $\sigma_i \approx 16$  Oe, so that the distribution resembles a delta function. As discussed in Section 3.4.1, the Wohlfarth relation holds for a  $\delta$ -function distribution of local interaction fields, and a unique relationship exists between the sign of the mean field parameter  $k$ , and the curvature of the Henkel plot. As mentioned in Section 4.3.5, evidence for ferromagnetic interactions, in the propagation of magnetization reversal along chains of particles, has been observed with magnetic force microscopy and the character of the Henkel plot is consistent with this observation. The Preisach analysis also yields  $k > 0$ , supporting the notion that magnetizing-like interactions are present within this material. In this case, the positive curvature of the Henkel plot is linked to a small positive mean field parameter  $k = 0.11$ . The thermal parameter,  $h_T^*$  was about 170 Oe, which is only about 16% of the coercivity of the material. This is consistent with expected values for measurements taken at room temperature far below the medium's Curie temperature, which is expected to be quite high as it is Co-based. The reversible fraction was 25%, which may reflect the more

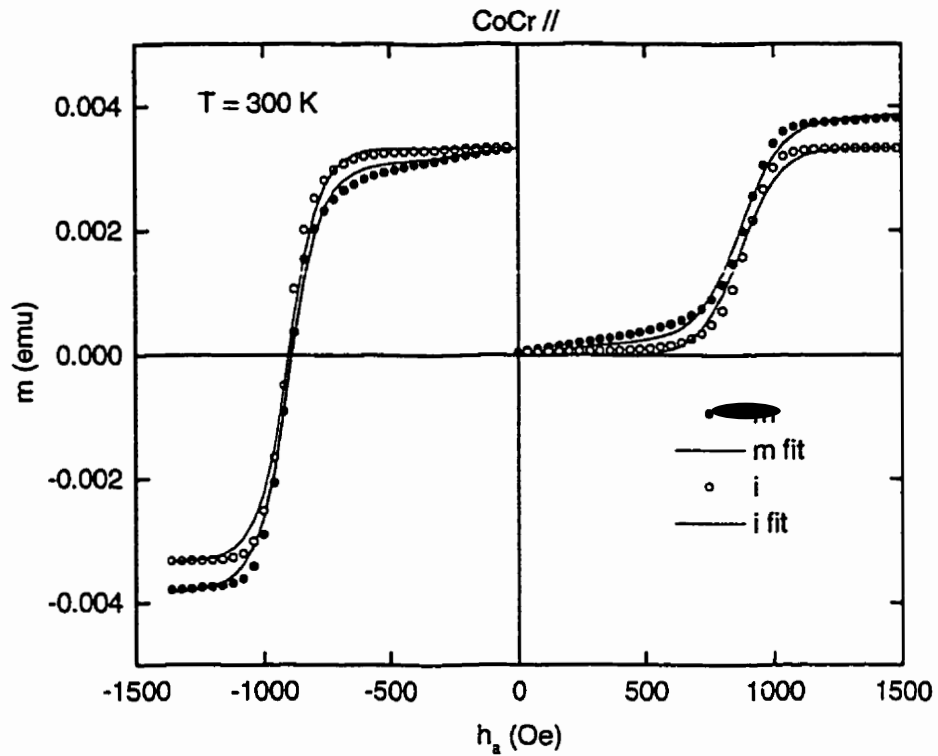


Figure 5.12 . Magnetization (solid dots) and remanence (open dots) data for cobalt-chromium-based hard disk and the corresponding calculated curves (solid lines) generated using a Gaussian coercive field distribution, with  $\tilde{h}_c = 1080$  Oe and  $\sigma_c = 160$  Oe,  $k = 0.11$ ,  $\sigma_i = 16$  Oe,  $h_T^* = 170$  Oe,  $m_\infty = 0.0044$  emu,  $f = 0.253$ , and  $\Gamma = 0.52$ .

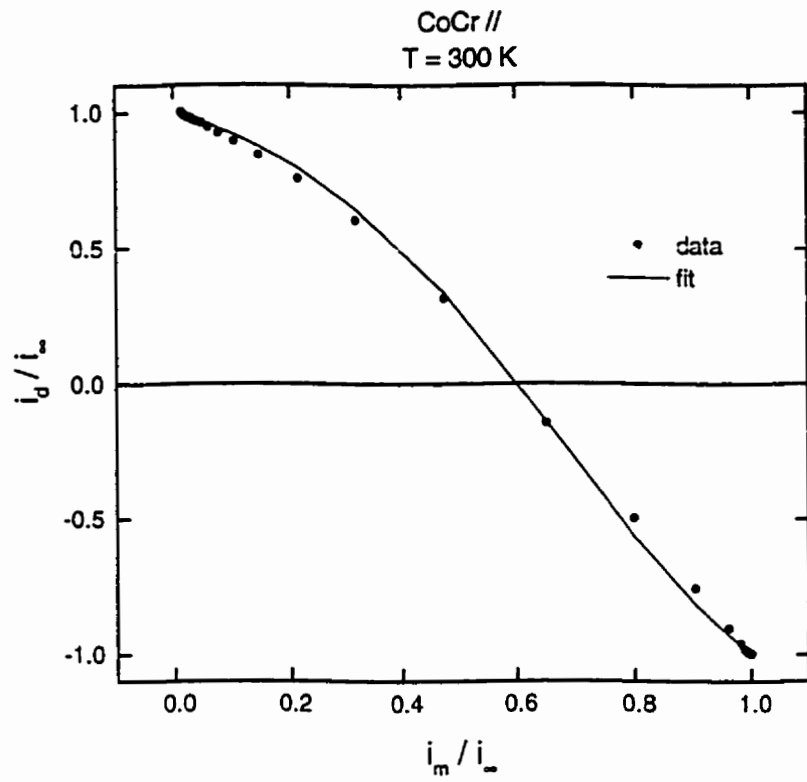


Figure 5.13 . Henkel data (solid dots) for cobalt-chromium-based hard disk and the calculated Henkel curve (solid line) generated using a positive value of the mean field parameter,  $k = 0.11$ .

ordered structure of this hard disk material, since particles are apparently aligned along striations in the material (Section 4.3.5).

## 5.4 Perpendicular $\text{Co}_{80}\text{Cr}_{20}$ Hard Disk

Columnar grains of  $\text{Co}_{80}\text{Cr}_{20}$ , whose easy axes are aligned perpendicular to the plane of the disk, comprise the magnetic system of this hard disk medium. The magnetization and remanence curves for  $\text{Co}_{80}\text{Cr}_{20}$ , measured at  $T = 300$  K with the VSM, are shown in Figure 5.14. The hysteresis loop for this perpendicular recording film is strongly sheared, as seen from the finite slope of the demagnetizing curve, due to the orientation of the field perpendicular to the film plane, and very large fields of  $\pm 10$  kOe are required to saturate the ac demagnetized sample. The saturation remanence is only 20% of the saturation moment; however, for recording purposes, the medium needs only to possess a high absolute remanence, rendering its relative value unimportant. This reversibility is due to the large demagnetization field for this perpendicular specimen, which increases as the magnetization increases. For the  $\text{Co}_{80}\text{Cr}_{20}$  sample, the expected demagnetization field is  $H_D \approx -4\pi M_s$  since it is a very thin disk (Cullity, 1975, p. 57).

The Henkel plot of the remanence data displays strong negative curvature, and points to negative mean field effects (Figure 5.15). However, this effect cannot be decoupled from the curvature inherent in the ac demagnetization procedure, as was possible in the analysis of the longitudinal hard disk medium, where the interaction field distribution was so narrow as to be considered a delta function. In fact, the width of the Gaussian interaction field distribution required to fit the  $\text{Co}_{80}\text{Cr}_{20}$  data was of the same

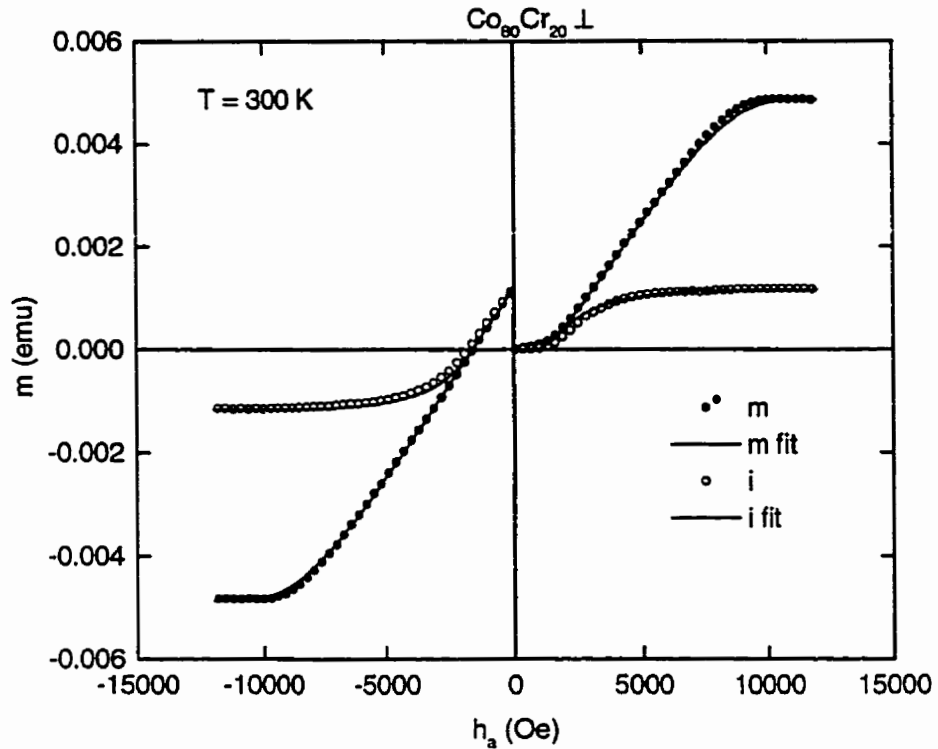


Figure 5.14 . Magnetization (solid dots) and remanence (open dots) data for  $\text{Co}_{80}\text{Cr}_{20}$ .

The shear hysteresis loop of this perpendicular medium is indicated by the demagnetization curve corresponding to the demagnetizing branch of the major hysteresis loop. The calculated curves (solid lines) were generated using a log-normal coercive field distribution, with  $\tilde{H}_c = 1512 \text{ Oe}$  and  $\sigma_c = 0.29$ ,  $k = -3.05$ ,  $\sigma_i = 1482 \text{ Oe}$ ,  $h_T^* = 0 \text{ Oe}$ ,  $m_\infty = 0.0044 \text{ emu}$ , and  $f = 0$ .

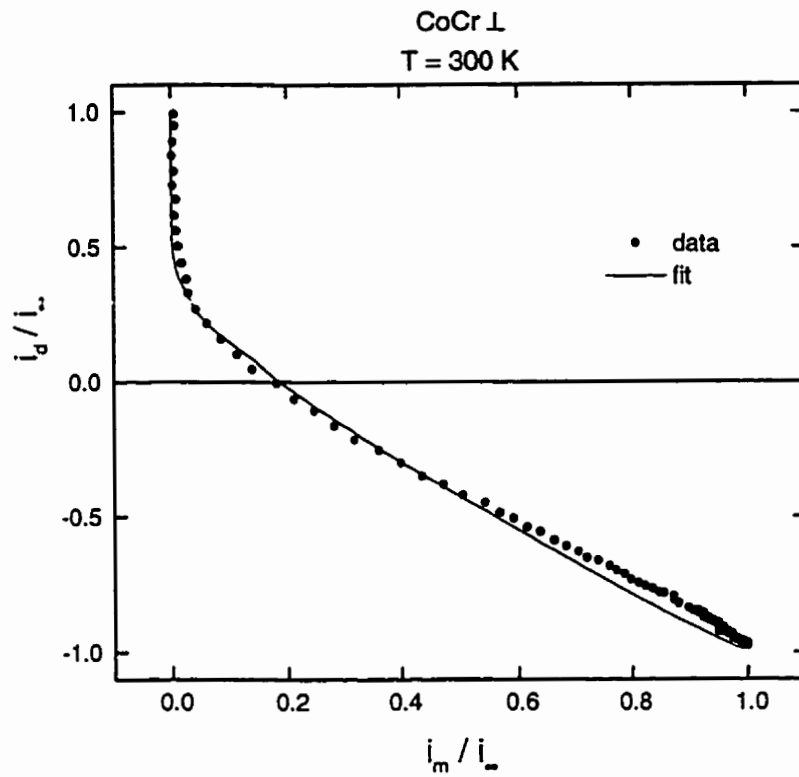


Figure 5.15 . Henkel data (solid dots) for cobalt-chromium-based hard disk, which shows strong demagnetizing-like curvature and the calculated Henkel curve (solid line) generated using a negative value of the mean field parameter,  $k = -3.05$ .

order as the coercive field. Furthermore, because the sample could not be thermally demagnetized (Section 4.3.6), this technique could not be used to separate mean field effects from the curvature in the Henkel plot of the ac demagnetized sample due to disorder, which is reflected in the finite width of the local interaction distribution (Section 3.4.4). Within the Preisach analysis, real demagnetizing interactions within the material cannot be discriminated from the demagnetizing factor, as both are simultaneously treated by the parameter  $k$  (Section 3.2). To generate calculated curves that describe the data, a negative value of  $k$  is required, in conjunction with the ac demagnetized Preisach plane. The value  $k \approx -3$  was used in the calculated curves shown in Figures 5.14 and 5.15. This is physically justifiable since a sizeable demagnetization factor is expected due to the perpendicular orientation of the particles.

An estimate of the contribution of the demagnetization factor to the mean field parameter can be made directly from the data and the sample volume  $V$ . The demagnetizing field can be rewritten as  $H_D = -DM_s = -\alpha m_s$ , where  $\alpha = \frac{D}{V}$ , and  $m_s$  is the spontaneous moment. The sample volume is simply the volume of a cylinder, and using a thickness  $t \approx 1.5 \mu\text{m}$ , which is the upper limit given in the specifications for this thin film (Section 4.3.6), and a radius  $r \approx 1.5 \text{ mm}$ , it is  $V \approx 1.1 \times 10^{-5} \text{ cm}^3$ . An estimate of the demagnetizing factor corresponding to the Preisach fit can be made by including mean field effects within the interaction distribution itself (Section 3.2), such that

$$g(h_i) \propto \exp \left[ -\frac{(h_i + \alpha M)^2}{2\sigma_i^2} \right],$$

where  $\alpha$  represents a mean field parameter, and where  $h_i$ ,  $M$ , and  $\sigma_i$  are in real units.

Rewriting this Gaussian in terms of the reduced parameters that are used in the fits, the dimensionless mean field parameter  $k$  can be expressed as  $k \equiv \alpha \frac{m_\infty}{\bar{H}_c}$ . Using  $k = -3.05$  yields  $\alpha \approx 1.0 \times 10^6 \text{ cm}^{-3}$ , which yields  $D = 11.3$ . The demagnetizing factor is very sensitive to the volume, and the thickness was only estimated. Nevertheless, the value of  $k$  given by the Preisach analysis is very reasonable, since physically, the largest demagnetizing factor possible,  $D = 4\pi \approx 13$ , corresponds to an infinite disk, and the  $\text{Co}_{80}\text{Cr}_{20}$  sample approximates this shape. So, shape demagnetization effects dominate in this perpendicular medium and this suggests that particles do not experience long-range interactions, but only local interaction effects.

The shape of the hysteresis loop can also provide insight into the microscopic nature of perpendicular media. The shearing effect, evident in the sloping parallelogram loop shape, rather than a rectangular hysteresis loop, is directly related to the microscopic structure. In the absence of demagnetization, a perpendicular film has a uniaxial anisotropy constant  $K$ , and a magnetocrystalline energy of the form  $K \sin^2 \theta$  (Section 2.7.1). The coercivity is described by  $H_c = \frac{2K}{M_s}$ . Such coercivity calculations for CoCr films yield very large values of  $H_c$  and perfectly square hysteresis loops. Some rounding of the loop can be induced if grain variations are treated using a finite width coercive or switching-field distribution. If demagnetizing effects are considered, the coercivity is lowered by  $-4\pi M_s$ , the demagnetizing field of a disk of infinite area. Again, the hysteresis loop would be square, except for rounding due to distribution effects. These

coercive fields, calculated under the assumption of uniform rotation are still nearly always higher than measured values. Consequently, a mode of reversal other than coherent rotation is expected to be the true mechanism. Calculations with models employing different reversal modes also yield square hysteresis loops, when intrinsic coercivities exceed demagnetizing effects, or no remanence at all, when demagnetizing fields dominate. These calculations assume that during switching a grain only sees its local self-demagnetizing field and *not* demagnetizing fields from neighbouring grains. Shearing of the type indicated by the demagnetizing curve in Figure 5.14 can be explained by a “variable aggregate demagnetization field” (Köster & Arnoldussen, 1970, p. 202). An aggregate demagnetization field is treated under the assumption that a single particle in the film, containing many small, *semi-independent* particles, may be influenced by demagnetization fields due to near neighbours, in addition to its own self-demagnetization field. At saturation, all particles have their magnetization aligned in the direction of the applied field. The aggregate magnetization is therefore  $M_s$ , and the demagnetizing field is  $-4\pi M_s$ . If the applied field is lowered sufficiently the particles with the lowest coercive fields reverse, which in turn lowers the average magnetization and the aggregate magnetization by  $\Delta M$ , and the demagnetizing field falls by  $4\pi\Delta M$ . Thus, the external field required to maintain this state is changed by  $+4\pi\Delta M$ . As the applied field is further reduced, what would be a nearly vertical side of a hysteresis loop without aggregate variable demagnetization, is mapped onto a sloped side with

$$\frac{dM}{dH_a} \approx \frac{1}{4\pi} \approx 0.08.$$

To compare this theoretical value with that of the demagnetization moment data in Figure 5.14, the slope of the curve must be divided by the volume of the

sample,  $\alpha^{-1}/V \approx 7.3 \times 10^{-7} \text{ cm}^3 / 1.1 \times 10^{-5} \text{ cm}^3 \approx 0.07$ . Considering the uncertainty in the volume of the sample, this coincides with the value predicted by the aggregate demagnetization field. This model implies that the particles or columnar grains comprising a perpendicular recording medium must be either non-interacting or weakly interacting, with diameters sufficiently small that an aggregate demagnetization field from surrounding grains dominates an individual grain's self-demagnetization field. Preisach calculations suggest that local interaction fields are quite high with  $\sigma_i \approx 1500$  (Oe), but interactions are confined to short-ranges, since the mean field parameter is seemingly dominated by shape demagnetization effects.

The Preisach distribution used in this analysis was the product of a Gaussian interaction distribution and a log-normal coercive field distribution, with a width parameter  $\sigma_c \approx 0.3$ . Due to its symmetry about the mean, a Gaussian distribution of coercive fields was unable to follow both the curvature of the primary magnetization curve as saturation was approached and the somewhat steeper curvature at low fields. Since the log-normal function possesses a similar asymmetry in its structure, it was better able to describe the data.

No thermal relaxation effects were found at the measurement temperature,  $T = 300$  K, as indicated by the value of the effective thermal viscosity parameter,  $h_T^* = 0$ . As for the other computer disk media, the Curie temperature is very high (Section 4.3.6), and the thermal effects are expected to be very small at ambient temperatures.

The phenomenological reversibility term, introduced in Section 3.6 as a modification to the Preisach model to account for physical sources of reversibility such as

field induced moment growth and reversible rotation, was not employed in the analysis of the CoCr sample data. In fact, the magnetization data showed evidence of a diamagnetic contribution, most likely from the sample holder, in the negative slope of the magnetization at high fields. To treat this data in the usual way, linear regression was used to fit a line through these points and the diamagnetic contribution was subtracted from the data.

## 5.5 Chromium Dioxide Audio Tape

### 5.5.1 General Features of the Magnetic Response<sup>1</sup>

$\text{CrO}_2$  audio tape consists of a collection of single domain, elongated, ferromagnetic particles whose long axes are roughly aligned with the direction of motion of the tape. Figure 5.16 shows the temperature dependence of the field cooled (FC) and zero field cooled (ZFC) moment of  $\text{CrO}_2$  audio tape measured in an applied field  $h_a = 100$  Oe. The FC and ZFC moments are identical above  $T_c \approx 127^\circ\text{C}$ , but below  $T_c$  the two sets of data bifurcate and the FC moment is greater than the ZFC value.

Measurements of the time dependence of the ZFC moment following a step function field excitation show that the evolution of the moment from the thermally demagnetized initial state towards its equilibrium value in 100 Oe proceeds in two stages, an essentially instantaneous initial response that follows the field change and is due to pseudoparticles with critical switching fields  $\alpha$  less than 100 Oe plus contributions from any reversible mechanisms, followed by a much slower viscous component likely due to thermally activated overbarrier relaxation of pseudoparticles with critical fields between  $100 \text{ Oe} \leq \alpha$

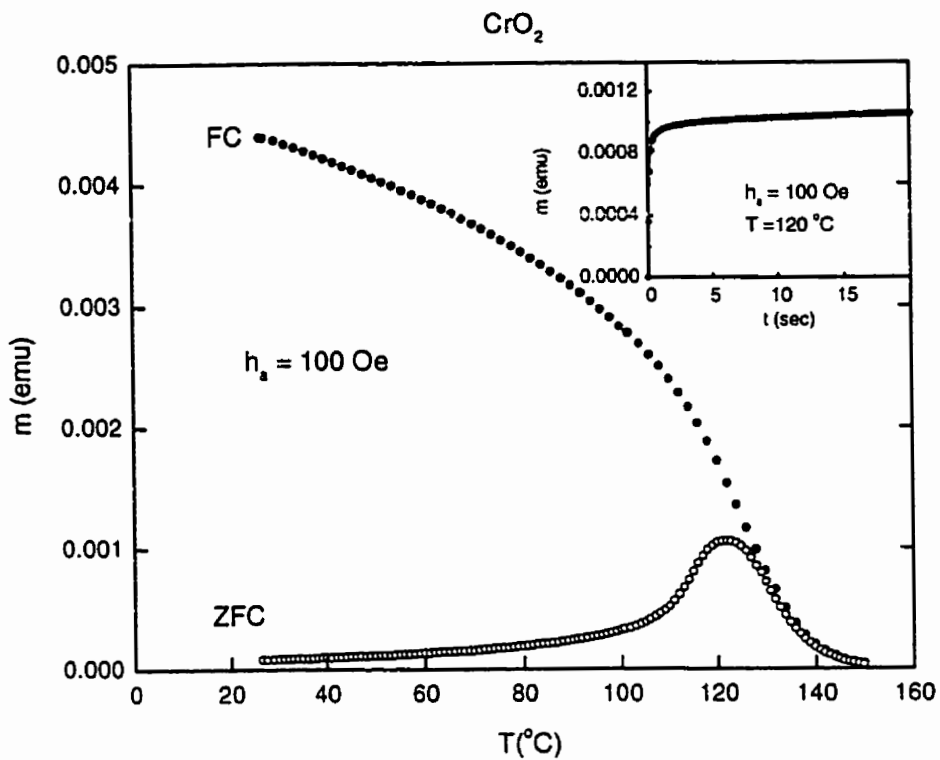


Figure 5.16 . The temperature dependence of the field cooled (FC) and zero field cooled (ZFC) moment of  $\text{CrO}_2$  audio tape measured in an applied field  $25^\circ\text{C}$  between  $25^\circ\text{C}$  and  $150^\circ\text{C}$ . The inset shows the time dependence of the moment for  $0 \leq t \leq 20$  s after zero field cooling from  $150^\circ\text{C}$  to  $120^\circ\text{C}$  and then applying a “step function” field excitation  $h_a = 100$  Oe. The field ramping time is  $\approx 0.5$  s, so the true viscous thermal relaxation corresponds to about 10% of the total response.

$\leq h_T^* + 100$  Oe. The inset in Figure 5.16 illustrates the time dependence of the ZFC response at  $T = 120^\circ\text{C}$ , measured in 100 Oe over a time interval  $0 \leq t \leq 20$  s. The field turn-on time is about 0.5 seconds, so the “true” viscous aftereffect corresponds to data points with  $m \geq 0.0009$  emu, that is, to about 10% of the total response under these conditions. Although our measurements show that thermal relaxation is present to some extent at all temperatures between  $25^\circ\text{C}$  and the Curie temperature, so that  $h_T^*$  is always finite, the amplitude of the ZFC moment in Figure 5.16 is dominated by the initial rapid response component. Thus, the peak in the ZFC moment in the vicinity of  $T_C$ , as well as any variations in the coercivity of  $\text{CrO}_2$  with temperature, are related primarily to changes in the *intrinsic anisotropy* of the pseudoparticles, with only a small contribution from thermally induced transitions. These transitions are characterized by a time required for activation, and blocking is said to occur when the moment of the particle is stable within the time scale of the experiment. Hence, the observed tracking of the moment with the field indicates that the particles are responding to the external field with only minor relaxation effects due to finite temperature, so most of the chromium dioxide particles are blocked at essentially all temperatures below  $T_C$ .

### 5.5.2 Analysis of AC Demagnetized Sample Data ( $25^\circ\text{C} \leq T \leq 120^\circ\text{C}$ )<sup>2</sup>

The magnetization curves (initial and demagnetizing branches) and the normalized Henkel plots of the remanence measured under ac demagnetized initial conditions at five temperatures  $T = 25^\circ\text{C}$ ,  $60^\circ\text{C}$ ,  $80^\circ\text{C}$ ,  $100^\circ\text{C}$ , and  $110^\circ\text{C}$ , are shown in Figures 5.17 and 5.18, respectively. The saturation moment, the saturation remanence, and the coercive field all fall with increasing temperature, while the Henkel

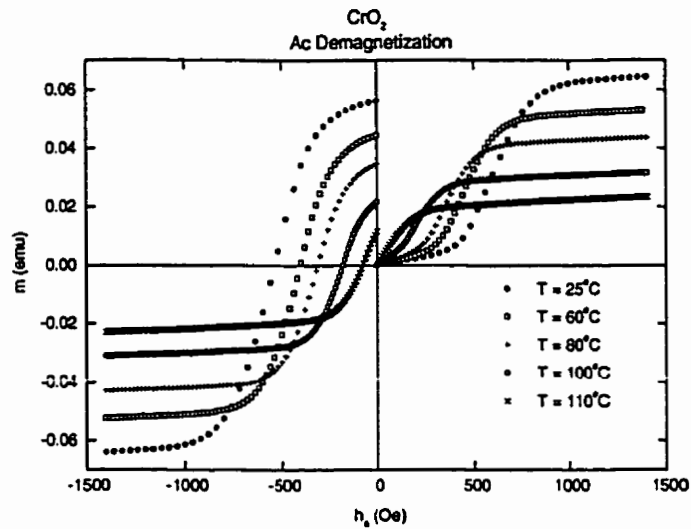


Figure 5.17 . Magnetization curves for CrO<sub>2</sub> audio tape measured under ac demagnetized initial conditions at five temperatures  $T = 25^{\circ}\text{C}$ ,  $60^{\circ}\text{C}$ ,  $80^{\circ}\text{C}$ ,  $100^{\circ}\text{C}$ , and  $110^{\circ}\text{C}$ .

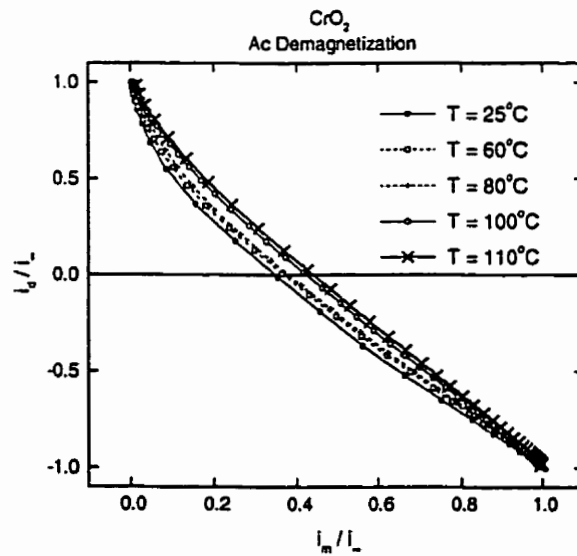


Figure 5.18 . Normalized Henkel curves for CrO<sub>2</sub> audio tape measured under ac demagnetized initial conditions at five temperatures  $T = 25^{\circ}\text{C}$ ,  $60^{\circ}\text{C}$ ,  $80^{\circ}\text{C}$ ,  $100^{\circ}\text{C}$ , and  $110^{\circ}\text{C}$ .

plots, which all lie below the Wohlfarth line, exhibit decreasing curvature with increasing temperature. Figures 5.19 through 5.21 show the initial magnetizing curve  $m(h_a > 0)$ , the magnetizing remanence  $i(h_a > 0) = i_m(h_a)$ , the descending branch of the major hysteresis loop  $m(h_a < 0)$ , and the demagnetizing remanence  $i(h_a < 0) = i_d(-|h_a|)$ , over a limited field range chosen so as to magnify the principal structural features of the data, at three representative temperatures  $T = 25^\circ\text{C}$ ,  $105^\circ\text{C}$ , and  $115^\circ\text{C}$ , under ac demagnetized initial conditions. Table 5.3 lists the “best fit” values of the model parameters,  $m_\infty$ ,  $f$ ,  $\Gamma$ ,  $\sigma_i$ ,  $\sigma_c$ ,  $\tilde{h}_c$ ,  $k$ ,  $h_T^*$ , for the ac demagnetized data in these figures. (Fits for other temperatures in the range  $25^\circ\text{C} \leq T \leq 120^\circ\text{C}$  can be found in Appendix 1, Figures A1.1 through A1.6.) The discrete symbols represent experimental data and the solid curves are numerical simulations based on the Preisach model. A comparison of the data in these figures shows that as the temperature increases there is a decrease in the apparent saturation moment, in the coercive field, and in the ratio of the saturation remanence to the saturation moment. This indicates that the response becomes progressively more reversible as  $T$  approaches  $T_c$ . Figure 5.22 shows the Henkel plots for the same three temperatures as in Figures 5.19 through 5.21. As explained in Section 3.4, these are parametric plots of the magnetizing remanence  $i_m(h_a)$  normalized to the saturation remanence  $i_\infty$ , as a function of the normalized demagnetizing remanence  $i_d(-|h_a|)/i_\infty$ , which match remanences corresponding to applied fields of common magnitude. Deviations from the linear Wohlfarth relation  $i_d/i_\infty = 1 - 2(i_m/i_\infty)$  (Section 3.4.1), indicate the presence of either random or mean field interactions between particles. The ac demagnetized data indicate that these interactions favour the demagnetizing process

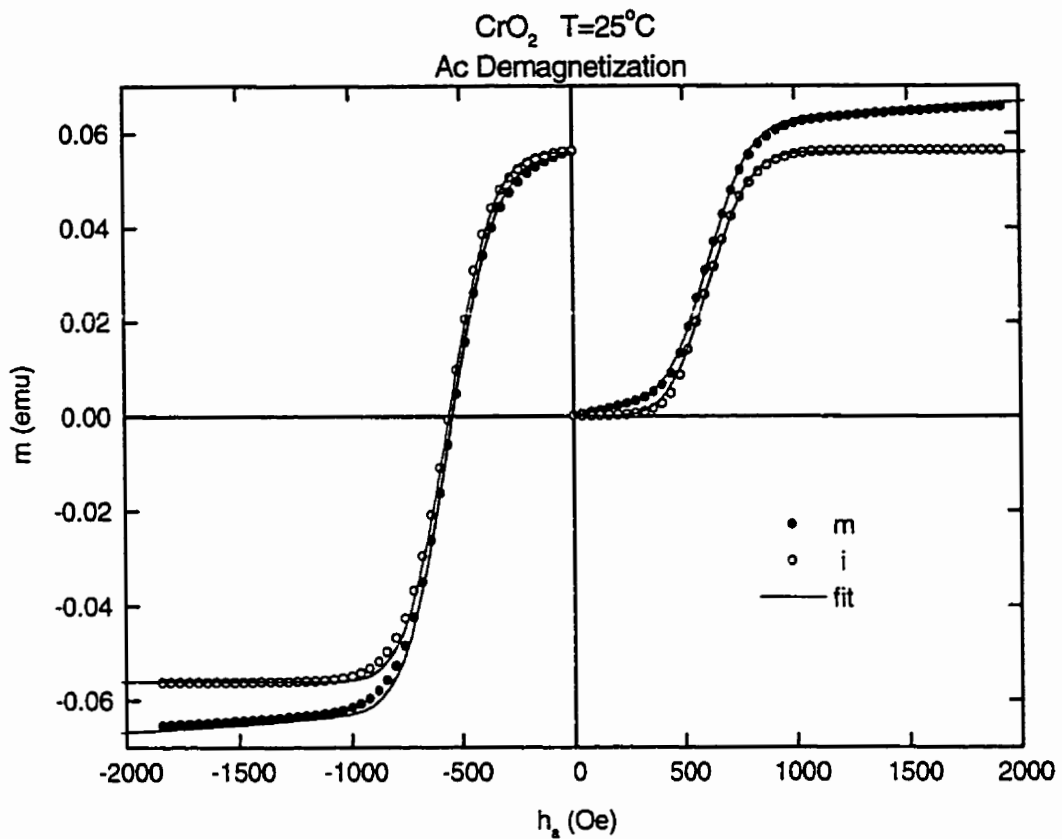


Figure 5.19 . The initial magnetizing curve ( $h_a > 0$ ) and the demagnetizing curve ( $h_a < 0$ )  $m$ , and the corresponding magnetizing and demagnetizing remanences  $i$  for ac demagnetized CrO<sub>2</sub> audio tape at  $T = 25^\circ\text{C}$ , plotted as a function of the applied field  $h_a$ . The discrete symbols denote experimental data while the continuous curves are Preisach model calculations.

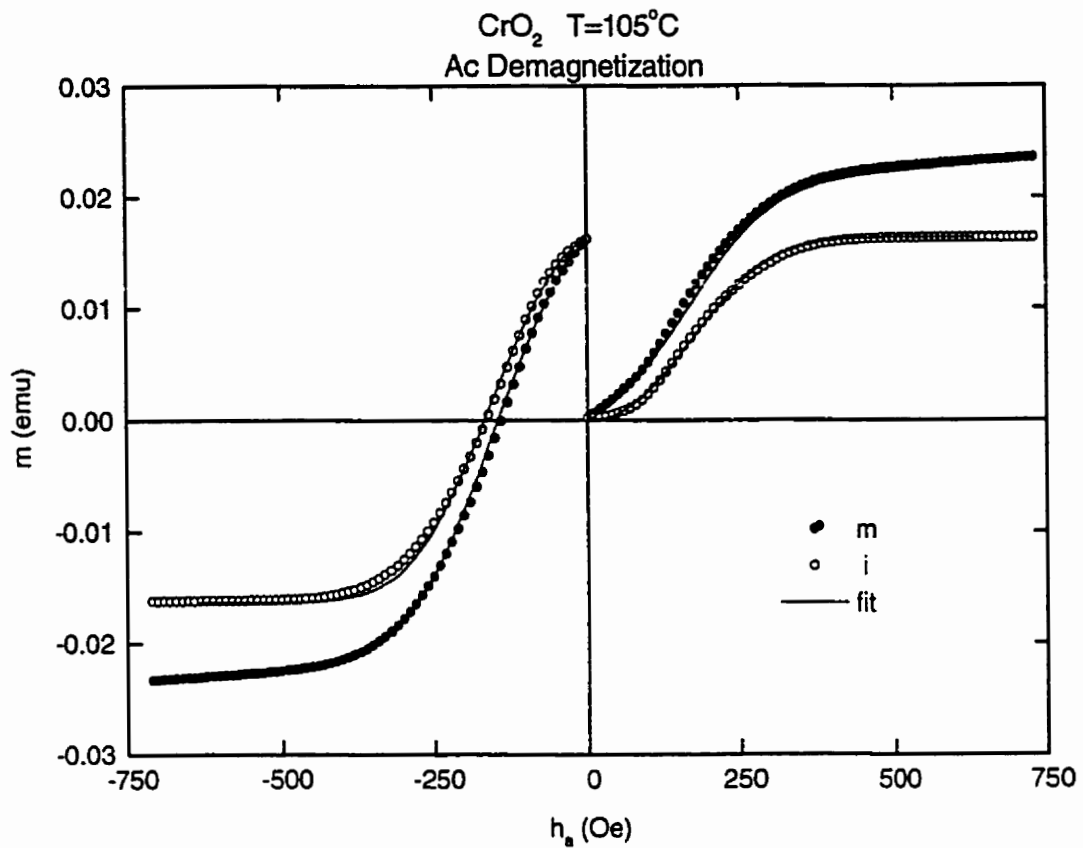


Figure 5.20 . The initial magnetizing curve ( $h_a > 0$ ) and the demagnetizing curve ( $h_a < 0$ )  $m$ , and the corresponding magnetizing and demagnetizing remanences  $i$  for ac demagnetized CrO<sub>2</sub> audio tape at  $T = 105^\circ\text{C}$ , plotted as a function of the applied field  $h_a$ . The discrete symbols denote experimental data while the continuous curves are Preisach model calculations.

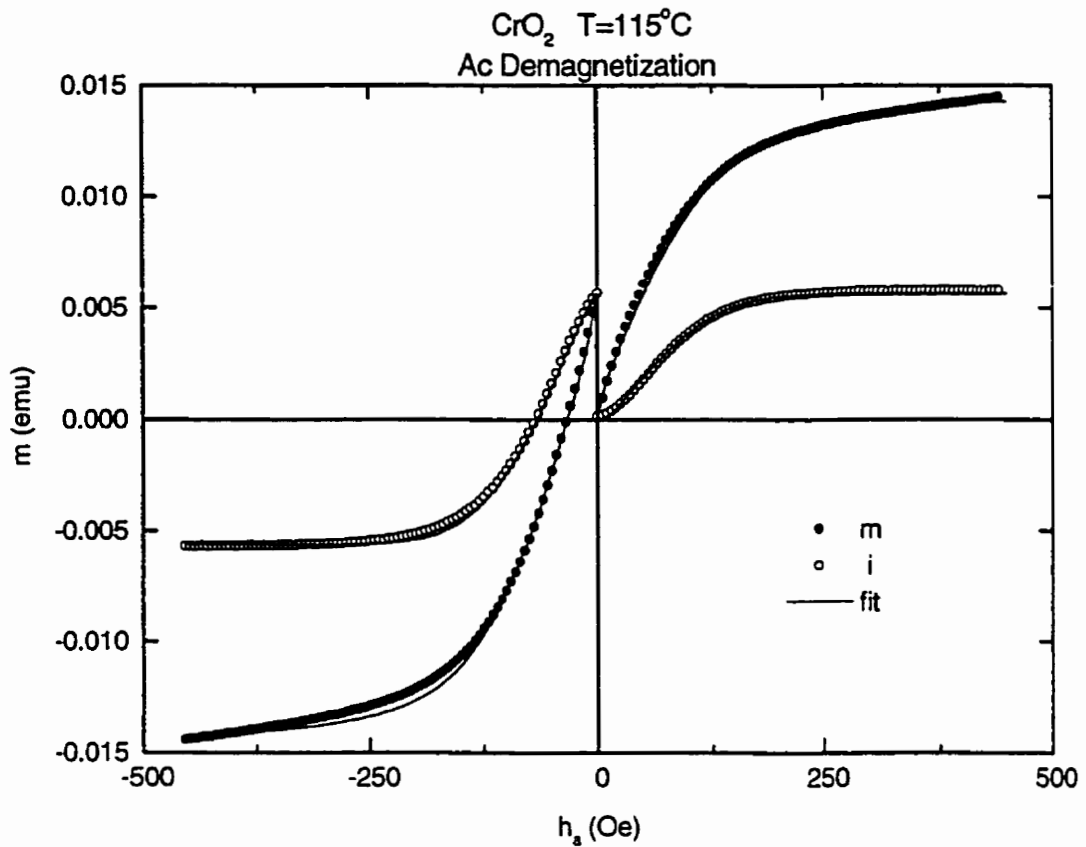


Figure 5.21 . The initial magnetizing curve ( $h_a > 0$ ) and the demagnetizing curve ( $h_a < 0$ )  $m$ , and the corresponding magnetizing and demagnetizing remanences  $i$  for ac demagnetized CrO<sub>2</sub> audio tape at  $T = 115^\circ\text{C}$ , plotted as a function of the applied field  $h_a$ . The discrete symbols denote experimental data while the continuous curves are Preisach model calculations.

Table 5.3 . Best fit Preisach parameters for CrO<sub>2</sub> (25 °C ≤ T ≤ 120 °C).

T (°C)	$\tilde{h}_c$ (Oe)	$\sigma_c$	$\sigma_i$	$h_T^*$ (Oe)	$m_\infty$ (emu)	f
25	560	0.25	0.14	5.6	0.070	0.20
40	495	0.27	0.13	7.4	0.063	0.20
60	428	0.305	0.135	8.6	0.056	0.20
80	340	0.33	0.14	10.2	0.0467	0.25
90	295	0.42	0.14	11.8	0.0366	0.27
100	205	0.505	0.14	13.5	0.0320	0.295
105	168	0.50	0.15	13.5	0.0245	0.30
110	90	1.1	0.12	13.5	0.0215	0.41
115	52	1.5	0.12	26.0	0.0145	0.52

The mean field parameter was  $k = 0$  for these calculations, performed on an initially *ac demagnetized* plane. The exponent parameter for the reversible component was  $\Gamma = 0.4$ .

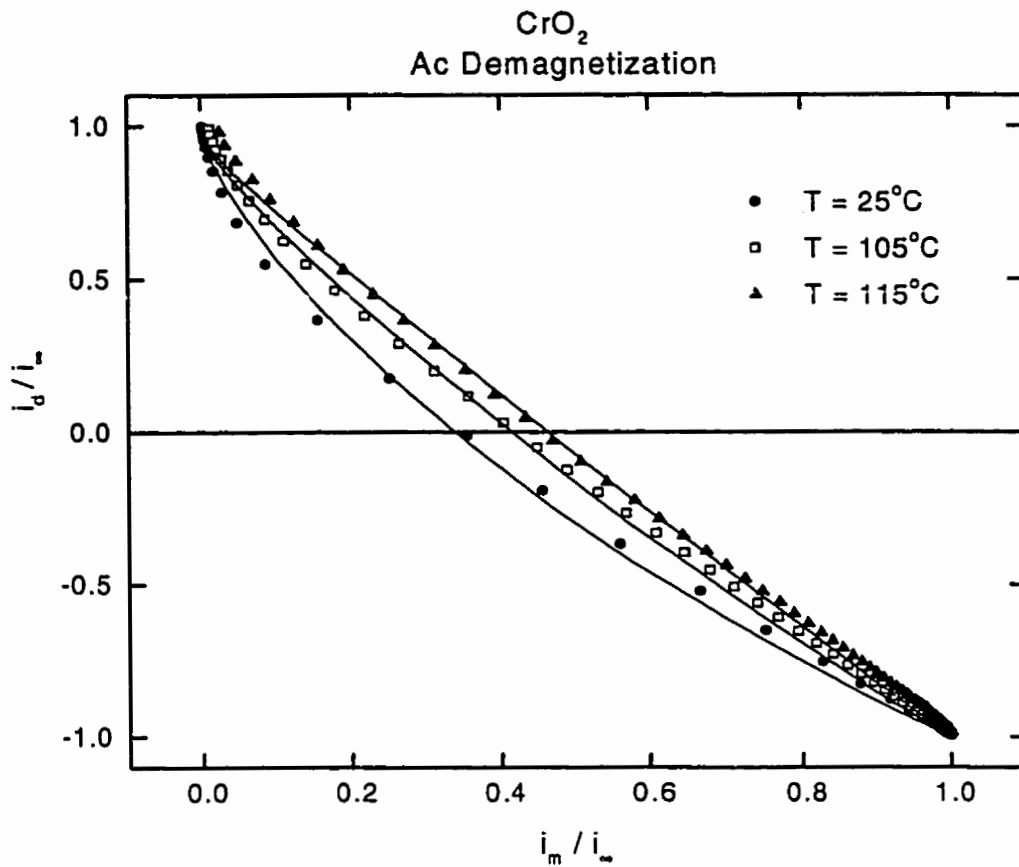


Figure 5.22 . The Henkel plots constructed from the ac demagnetized  $\text{CrO}_2$  remanences in Figures 5.19, 5.20, and 5.21. The discrete points are experimental data and the continuous curves are Preisach model calculations.

over the magnetizing process, since the curvature is always below the Wohlfarth line. Furthermore, they demonstrate that the interactions weaken and linearity is gradually restored with increasing temperature. By contrast, as will be presented in Section 5.5.3, the thermally demagnetized data shows minimal curvature, suggesting that interaction fields are nearly completely absent at all temperatures. Comparisons such as these enable separation of the contributions from interactions due to random local fields and those due to long range, mean field effects.

As mentioned earlier, the theoretical curves in Figures 5.19 through 5.21 were generated by superposing the individual, two-component responses of the Preisach pseudoparticles in the internal effective field,  $h$ :

$$m = m_{\infty} \left[ \int_{-\infty}^{\infty} dh_i \int_0^{\infty} dh_c p(h_c, h_i) \left\{ (1-f) \varphi(h_c, h_i, h, h_T^*) \pm f [1 - \exp(\mp \Gamma h)] \right\} \right] \quad (5.1)$$

$$= m_{\infty} \left[ (1-f) \int_{-\infty}^{\infty} dh_i \int_0^{\infty} dh_c p(h_c, h_i) \varphi(h_c, h_i, h, h_T^*) \pm f [1 - \exp(\mp \Gamma h)] \right] \quad (5.2)$$

and then employing the skew transformation  $h_a = h - km$  to convert the effective field  $h$  to an equivalent applied field  $h_a$  (Section 3.2). The first term in Equation 5.1 is the contribution from the rectangular portion of the Preisach cycles, and  $\varphi$  is the normalized, history-dependent output of each cycle, which is  $\varphi = +1$  if the pseudoparticle moment is up and  $\varphi = -1$  if the moment is down. The second term in Equation 5.1 represents contributions from reversible processes, like coherent rotation or reversible wall motion, or possibly from field-induced growth of the pseudoparticle moment, which cannot be

accommodated within the usual scalar Preisach formalism. With our choice of reversible function (Section 3.6), which is independent of the particle characteristic fields ( $h_c, h_i$ ), the second Preisach integral in Equation 5.1 can be performed analytically, yielding Equation 5.2.

The analysis began with data obtained with the VSM on an ac demagnetized  $\text{CrO}_2$  sample. The fit to the data set at  $T = 25^\circ\text{C}$  was the least flexible with respect to variations in the fitting parameters, and provided an essentially unambiguous characterization of the  $\text{CrO}_2$  system in the limit where thermal relaxation effects are negligible ( $h_T^* \ll \tilde{h}_c$ ). This fit was also used to define “constraints” on certain combinations of fitting parameters, based on physical considerations. These constraints guided the choice of the initial parameter values at higher temperatures. Specifically: (i) Since coercive fields  $h_c$  of individual  $\text{CrO}_2$  grains with anisotropy constant  $K$ , volume  $V$ , and spontaneous moment  $\tilde{\mu}$  are on the order of  $h_c \sim KV/\tilde{\mu}$ , and since the single particle anisotropy is likely to be dominated by *shape* effects, due to the extreme elongation of the  $\text{CrO}_2$  grains, it follows that  $K$  will vary as  $\tilde{\mu}^2$  (Section 2.7.1), and the particle coercivity  $h_c$  will be proportional to the spontaneous moment  $\tilde{\mu}$ . Thus, the ratio  $\tilde{h}_c/m_\infty$  should be a constant on the order of  $8 \times 10^3$  Oe/emu, which is its value at  $25^\circ\text{C}$ . (ii) The factor  $\ln(t_{\text{exp}}/\tau_0)$ , that appears in the definition of the thermal viscosity field  $h_T^* = (k_B T/\tilde{\mu}) \ln(t_{\text{exp}}/\tau_0)$ , is expected to be relatively insensitive to changes in  $\tau_0$  induced by changes in temperature. Consequently, the ratio  $h_T^* m_\infty/T$  (with  $T$  in degrees Kelvin) was not allowed to deviate appreciably from its value of  $1.3 \times 10^{-3}$  erg/K at  $T = 25^\circ\text{C}$ . (iii) Lastly, variations in  $\sigma_c$  and  $m_\infty$  were required to satisfy the condition

$\sigma_i/m_\infty \approx 1.0 \times 10^3$  Oe/emu in order to preserve a linear relationship  $h_i \propto \bar{\mu}$  between the local interaction fields  $h_i$  and the spontaneous moment  $\bar{\mu}$  of the interacting particles. The best fits were indeed consistent with these “constraints” at all temperatures up to and including  $T = 105^\circ\text{C}$ . Above this (that is for reduced temperatures  $T/T_C > 0.95$ ), it was necessary to allow some deviation from these conditions to optimize the fits.

The following interpretations emerged from our analysis: (i) The ac demagnetized data at all temperatures are quite consistent with a mean field parameter  $k = 0$ , so that there is little evidence for long range correlations between the  $\text{CrO}_2$  pseudoparticles, but only local, near neighbour couplings are present, with a dispersion  $\sigma_i$  due to random fluctuations in their local environments. This conclusion is strikingly confirmed by comparisons of ac and thermally demagnetized data (Section 5.5.3). (ii) The magnetization curves at different temperatures are all essentially parallel at high fields and show no signs of convergence, so that the *apparent* saturation moment  $m_\infty$  (and hence the spontaneous moment) decreases monotonically with increasing temperature. This type of behaviour is typical of strongly exchange coupled systems like ferromagnets (or ferrimagnets) where enormous applied fields are required below  $T_C$  in order to overcome the randomizing effects of thermal fluctuations on the populations of the *atomic* spin states and hence to improve the *intraparticle* spin alignment appreciably over its spontaneous value produced by the internal molecular field. However, such field-induced growth of the particle moment is eventually expected to become a consideration close to  $T_C$ , where the internal molecular field is itself collapsing rapidly, and may be at least partially responsible for the tendency of the calculated moment to saturate *below* the

measured moment at temperatures above 105°C. (iii) The shape of each model Henkel plot in Figure 5.22 is determined *jointly* by the *relative dispersions*  $\sigma_c/\bar{h}_c$  and  $\sigma_i/\bar{h}_c$  of the coercive and interaction field distributions. However, according to our fits, the systematic loss of curvature and the approach to linearity observed in the measured Henkel plots with increasing temperature is determined almost exclusively by the increase in the *relative width* of the *coercive* field distribution  $\sigma_c/\bar{h}_c$ , and *not* by changes in the local interaction field distribution, which has a constant relative width  $\sigma_i/\bar{h}_c \approx 0.13$ , nor by thermal viscosity effects. In fact, numerical calculations show that increases in the thermal viscosity field  $h_T^*$  *alone*, keeping all other distribution parameters fixed, will induce precisely the opposite trend, actually *increasing* the curvature of the model Henkel plots for ac demagnetized systems with  $k = 0$  (Roshko, Mitchler & Dahlberg, 1997). (iv) The increase in the *relative width*  $\sigma_c/\bar{h}_c$  of the coercive field distribution with temperature is also responsible for the progressive “smearing” or broadening of the field dependence of the moment and remanence isotherms in Figures 5.19 through 5.21, which characterizes the collapse of the hysteresis cycle with increasing temperature. As the particle coercivities become more widely dispersed about  $\bar{h}_c$ , the original Gaussian distribution extends progressively further into the unphysical, negative- $h_c$  region and must, of course, be truncated at  $h_c = 0$  and renormalized to compensate for the loss of area. Nevertheless, even in instances of severe truncation, where up to 25% of the original area is “lost”, the parameter  $\bar{h}_c$  retains its physical significance as the *system* coercive field in the *zero temperature* limit. (v) The systematic decrease in the measured coercivity with increasing temperature originates primarily in the explicit temperature dependence

of the parameter  $\tilde{h}_c$ , and hence, in the temperature dependence of the intrinsic anisotropy of the CrO<sub>2</sub> particles, although thermal relaxation  $h_T^*$  definitely plays a role, particularly at higher temperatures. For example, the measured coercivity at  $T = 115^\circ\text{C}$  is about 35 Oe, which is approximately 30% less than the intrinsic coercivity of the pseudoparticles  $\tilde{h}_c = 52$  Oe obtained from the fit at this temperature. (When  $f > 0.5$ , there may also be a minor contribution from the reversible branches of the elementary cycles, that distorts some of the loops sufficiently to reduce their coercive fields below the critical value  $h_c$  at which irreversible reorientation occurs. This is also a feature of Stoner-Wohlfarth cycles when particle misalignment is appreciable (Stoner & Wohlfarth, 1948).)

### 5.5.3 Comparison of AC and Thermally Demagnetized Sample Data <sup>3</sup> ( $25^\circ\text{C} \leq T \leq 120^\circ\text{C}$ )

Theoretical calculations based on the Preisach model show that the precise shape of a Henkel plot is a complicated function of the dispersion of random interaction fields  $\sigma_i$ , the mean field parameter  $k$ , and the structure of the initial demagnetized state, so that the interpretation of Henkel plots is far from trivial (Basso & Bertotti, 1994, Vajda, Della Torre & McMichael, 1994, Roshko, Mitchler & Dahlberg, 1997). However, we have shown that if the initial demagnetized state is *random*, so that pseudoparticles of type  $(h_c, h_i)$  have an *equal probability*  $p(h_c, h_i)/2$  of occupying each of their two energy levels  $\pm \mu h_i$  in zero field, then the Preisach model predicts that random local effects cannot curve a Henkel plot, and that any deviations from the linear Wohlfarth relation are thus a *direct* manifestation of a *nonzero mean field parameter*  $k$  (Mitchler, Dahlberg, Engle & Roshko, 1995). When  $k > 0$ , the curvature is uniquely magnetizing-like and the Henkel

plot is completely above the Wohlfarth line, while for  $k < 0$ , the opposite is true.

Furthermore, since this random state has the highest energy of all the possible demagnetized initial states, it follows that the response induced by the application of a field  $h_i$  to the random state will exceed the response from any other state. To achieve a random initial state experimentally, the sample must be quenched very rapidly in zero applied field *through its Curie temperature*  $T_C$ , and blocking must occur *before* the interaction fields  $h_i$  have developed sufficiently to produce an appreciable splitting of the two energy levels. Since the ratio of the population of the upper to the lower level at the blocking temperature  $T_B$  is  $\exp(-2\bar{\mu}h_i/k_B T_B)$ , this would require that  $-2\bar{\mu}h_i \ll k_B T_B \approx k_B T_C$ , assuming that blocking occurs within a relatively narrow temperature range just below  $T_C$  (which is consistent with the relative ineffectiveness of the thermal viscosity parameter  $h_T^*$  at temperatures below about 110°C for  $\text{CrO}_2$ ).

This suggests that the essential features of the Preisach-based interpretation of the ac demagnetized  $\text{CrO}_2$  data, and particularly the choice of the mean field parameter  $k$ , may be confirmed by comparing ac and thermally demagnetized data acquired at the same temperature (Mitchler, Roshko & Dahlberg, 1998), since both sets of data must be consistent with the same set of fitting parameters. A typical example of such a comparison is presented in Figures 5.23 and 5.24 at  $T = 60^\circ\text{C}$ , and the corresponding Preisach fitting parameters for all temperatures are listed in Table 5.4. Graphical comparisons at other temperatures in the range can be found in Appendix 1, Figures A1.7 through A1.9.

Data obtained under thermally demagnetized initial conditions differs from the ac

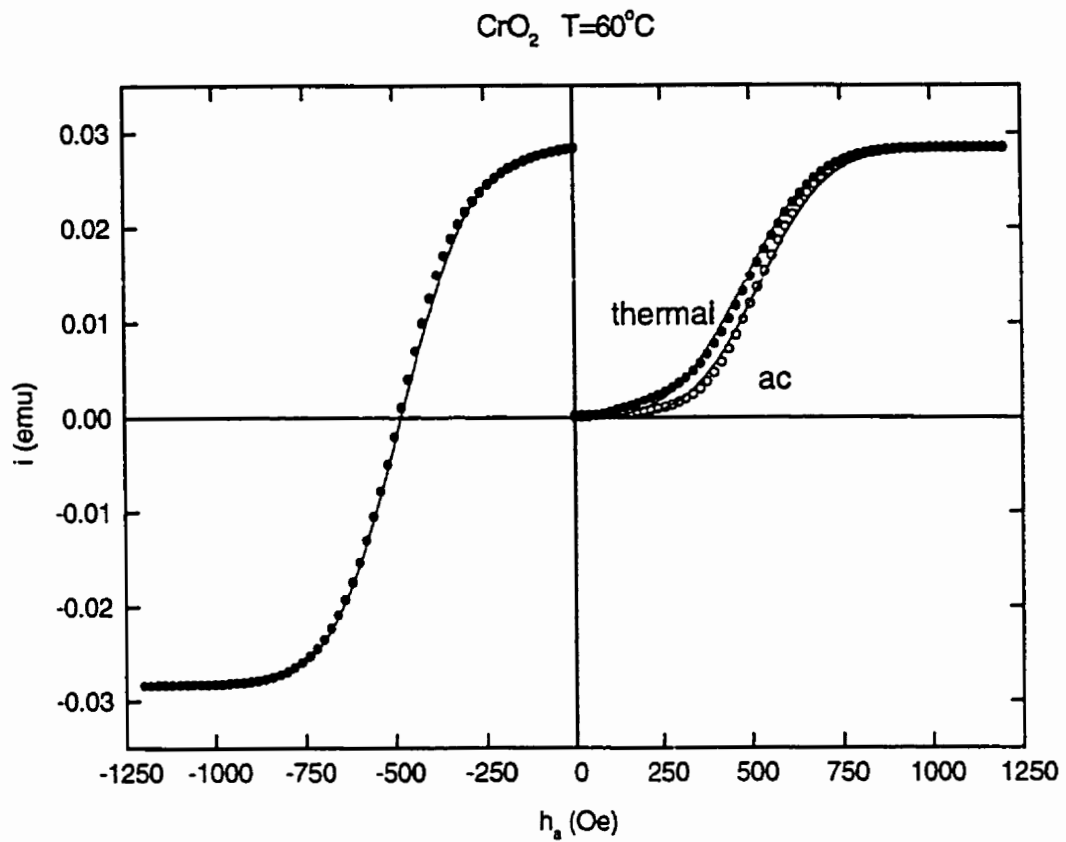


Figure 5.23 . A comparison of the magnetizing and demagnetizing remanences for thermally and ac demagnetized CrO<sub>2</sub> audio tape at T = 60 °C , plotted as a function of applied field h<sub>a</sub> . The discrete symbols are the measured remanences and the continuous curves are Preisach model calculations.

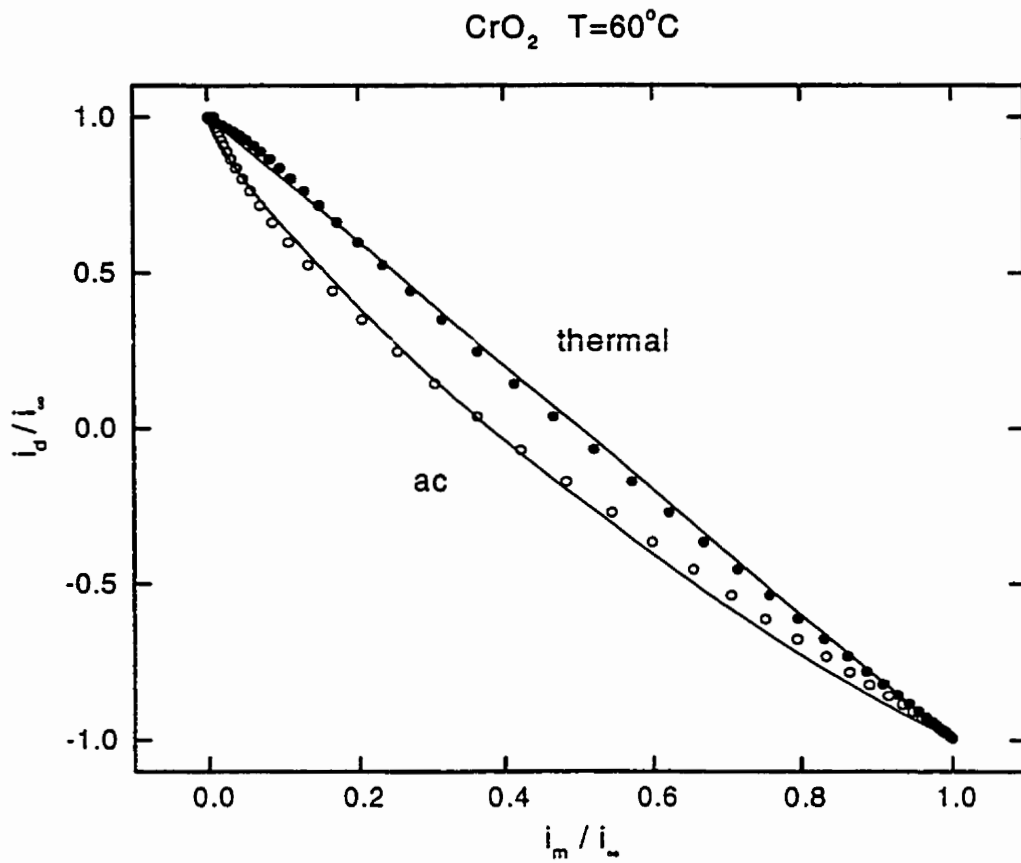


Figure 5.24 . The Henkel plots constructed from the ac and thermally demagnetized  $\text{CrO}_2$  remanences at  $T = 60^\circ\text{C}$ , in Fig. 5.21. The discrete symbols are the experimental data and the continuous curves are Preisach model calculations.

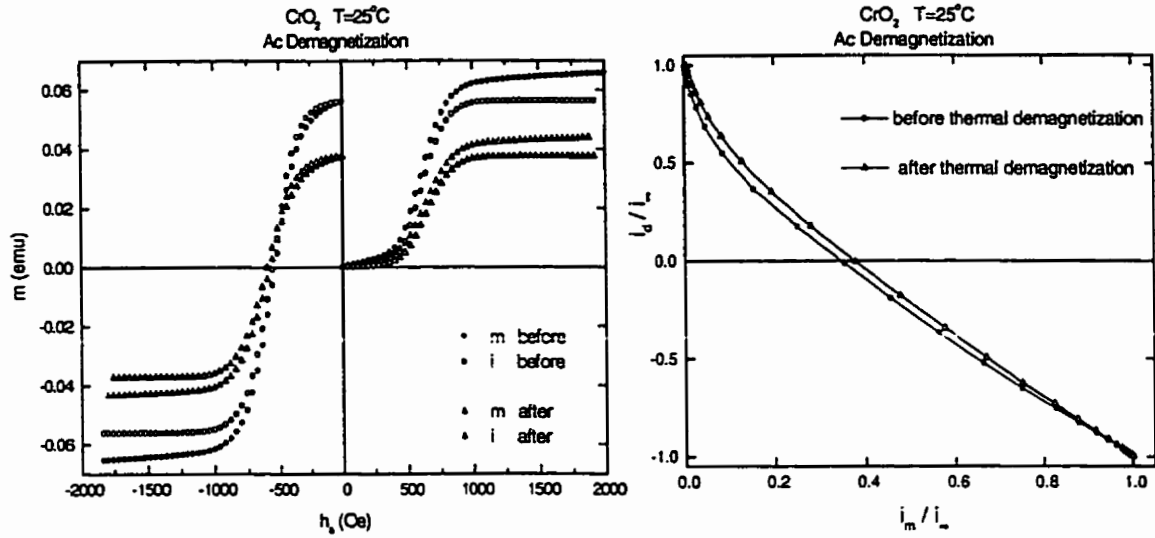
Table 5.4 . Best fit Preisach parameters for CrO<sub>2</sub> (25 °C ≤ T ≤ 120 °C) for comparison of initially ac and thermally demagnetized samples.

T (°C)	$\tilde{h}_c$ (Oe)	$\sigma_c$	$\sigma_i$	$h_T^*$ (Oe)	$m_\infty$ (emu)	f
30	595	0.27	0.11	6.0	0.041	0.20
60	480	0.30	0.12	6.0	0.037	0.24
80	380	0.32	0.12	7.6	0.035	0.24
100	240	0.47	0.13	14.4	0.0255	0.26

The mean field parameter was  $k = 0$  for these calculations, performed for *both* initially ac and *thermally demagnetized* (random) planes. The exponent parameter for the reversible component was  $\Gamma = 0.4$ .

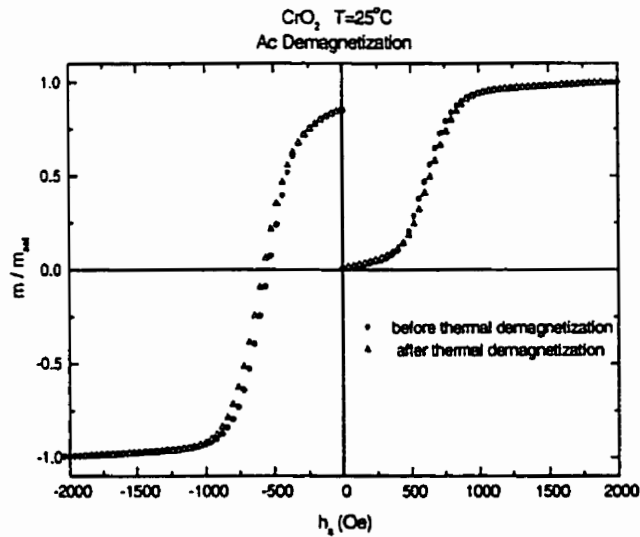
demagnetized data in two principal respects: (i) the initial low field slopes of the “thermal” magnetization and remanence data are both steeper than their ac counterparts, and (ii) as a consequence, the “thermal” Henkel plots have much weaker curvature than the corresponding “ac” Henkel plots. This latter behaviour is particularly strong evidence that mean field interactions are, in fact, essentially absent in CrO<sub>2</sub> audio tape (that is,  $k = 0$ ), as predicted by our analysis of the ac demagnetized data. This conclusion is indeed confirmed by the detailed fits in Figures 5.23 and 5.24, which clearly show that only *one* set of fitting parameters is necessary to describe *both* the ac and the thermally demagnetized data at any given temperature.

As mentioned in Section 4.3.1, in such comparisons of ac and thermally demagnetized data, the thermally demagnetized sequence was performed first, followed immediately by the ac demagnetized sequence, so that both sets of data at a common temperature refer to an identical geometrical configuration of chemically identical particles. The reason for performing the data acquisition in this particular order was that the thermal demagnetization procedure had a profound effect on the magnetic properties of the sample, as shown in Figure 5.25. This figure compares measurements performed under ac demagnetized initial conditions at  $T = 25\text{ }^{\circ}\text{C}$  both before and after heating the CrO<sub>2</sub> audio tape above its Curie temperature. The saturation moment drops quite dramatically, after thermally demagnetizing the sample (Figure 5.25a), resulting in a reduction of the amplitude of the hysteresis loop. The Henkel plot exhibits reduced curvature following thermal demagnetization (Figure 5.25b). The normalized magnetization curves plotted in Figure 5.25c indicate that although the magnetization is



(a)

(b)



(c)

Figure 5.25 . A comparison of (a) the magnetization and remanence curves, (b) Henkel plots, and (c) normalized magnetization curves for ac demagnetized  $\text{CrO}_2$  at  $T = 25^\circ\text{C}$  before and after thermal demagnetization at  $T = 150^\circ\text{C}$ .

similar for both conditions, they are not identical. The coercive field is slightly increased and the magnetization varies more slowly with field after heating. Thus, not unexpectedly, thermal demagnetization above  $T_C$  appears to change the chemical composition of the  $\text{CrO}_2$  particles (Bate, 1980).

#### 5.5.4 Alternative Parameter Selection ( $25^\circ\text{C} \leq T \leq 120^\circ\text{C}$ )

To further investigate the quality of the fits to the data for temperatures  $T = 25^\circ\text{C}$ ,  $60^\circ\text{C}$ ,  $80^\circ\text{C}$ , and  $110^\circ\text{C}$ , additional calculations were performed with *negative* values of  $k$ . For the ac demagnetized sample at  $T = 25^\circ\text{C}$ , the small negative value of the mean field parameter employed,  $k = -0.08$ , with the attendant adjustment of other parameters, including reduction in the distribution width parameters  $\sigma_c = 123$  Oe and  $\sigma_i = 50$  Oe, yielded very little difference in the calculated magnetization and remanence curves (Figure 5.26a); however, the Henkel plot with  $k = -0.08$ , which attains a slightly greater curvature for low values of the matching field, follows the Henkel data more precisely (Figure 5.26b). Similar improvements are shown for Henkel plots corresponding to ac demagnetized initial states at higher temperatures. (Fits with negative values of  $k$  for  $T = 60^\circ\text{C}$ ,  $80^\circ\text{C}$ , and  $110^\circ\text{C}$  are shown in Appendix 1, Figures A1.10 through A1.12.) Although this amelioration may be interpreted as evidence for the existence of small demagnetizing mean field effects in  $\text{CrO}_2$ , the high temperature ( $25^\circ\text{C} \leq T \leq 120^\circ\text{C}$ ) data corresponding to *thermally demagnetized* initial states of the  $\text{CrO}_2$  sample do *not* suggest this interpretation. The very slight curvature of the Henkel plots obtained under thermally demagnetized conditions ensures that long range interactions or other such mean field effects are highly unlikely in this system. In fact,

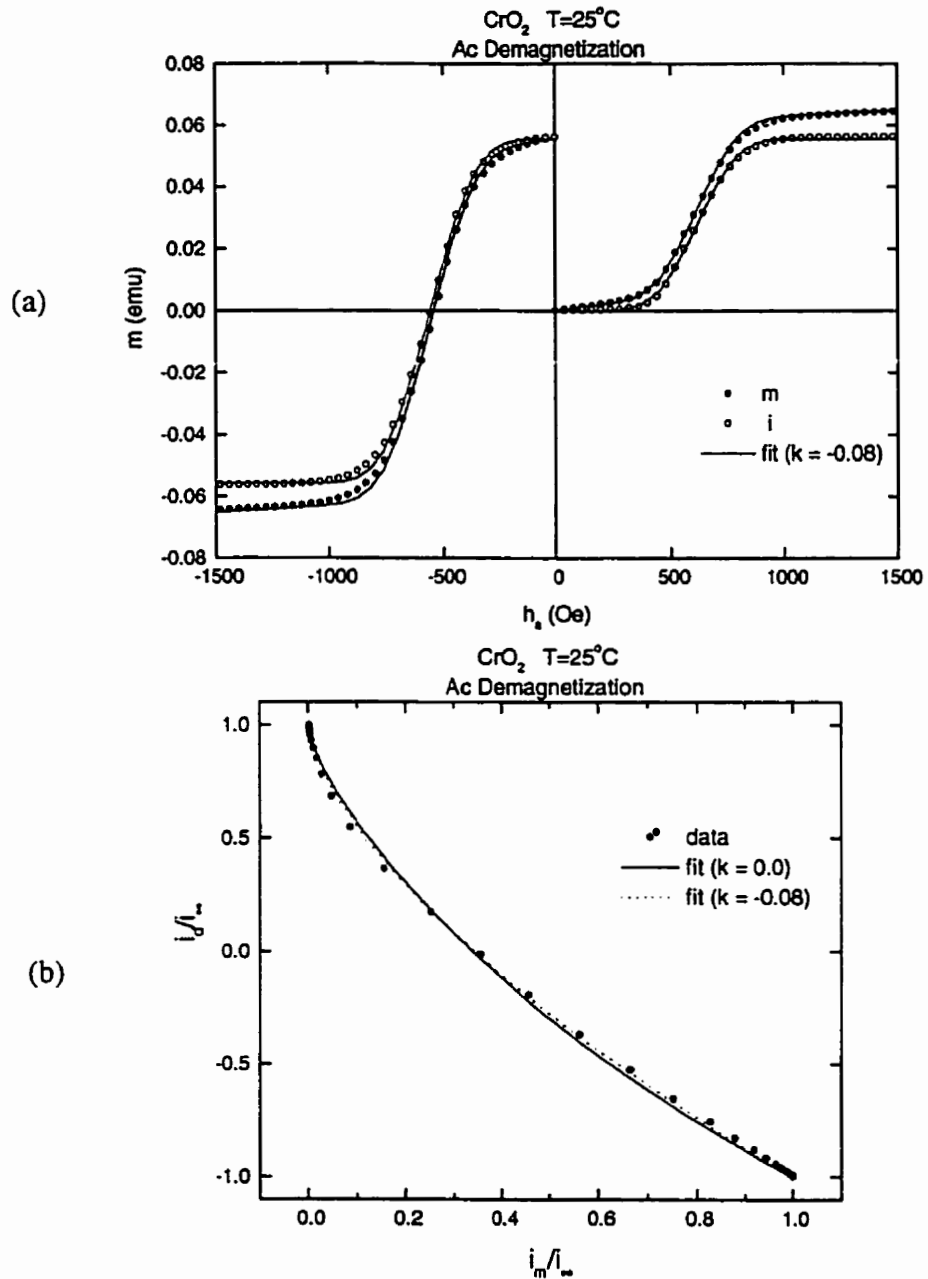


Figure 5.26 . (a) Comparison of experimental data (discrete points) and calculated magnetization and remanence curves (solid line) using  $k = -0.08$  with  $\sigma_c = 123$  Oe and  $\sigma_i = 50$  Oe. (b) Comparison of the experimental Henkel plot with calculated curves for  $k = 0$  (solid line) and  $k = -0.08$  (dashed line).

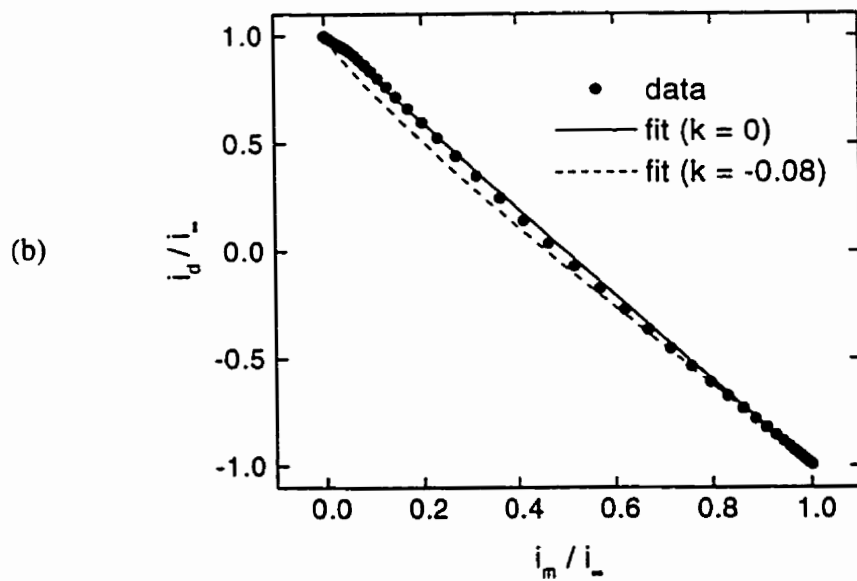
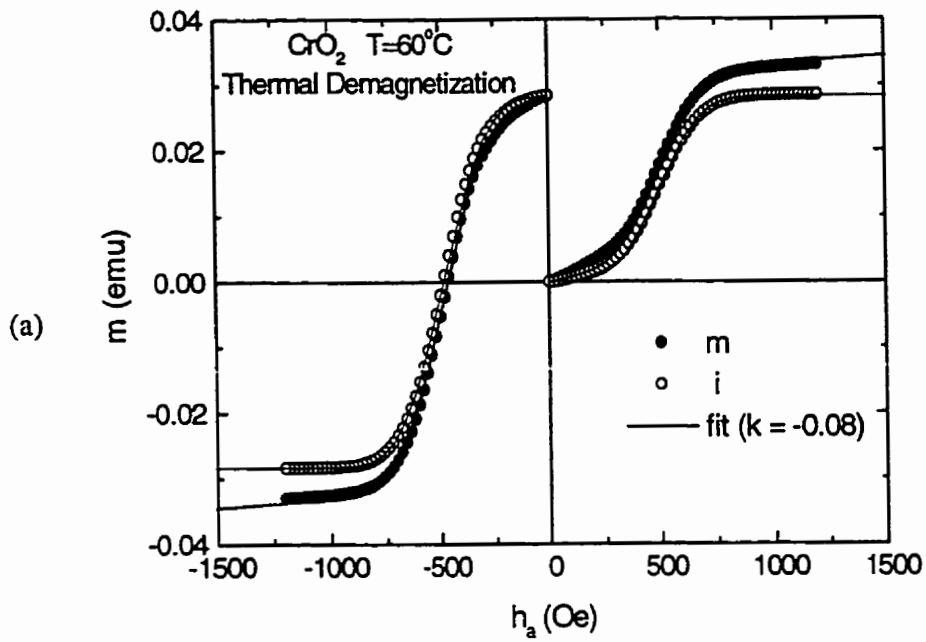


Figure 5.27 . (a) Comparison of experimental data (discrete points) at  $T = 60^\circ\text{C}$  under thermally demagnetized initial conditions and calculated magnetization and remanence curves (solid line) using  $k = -0.08$ . (b) Comparison of the experimental Henkel plot with calculated curves for  $k = 0$  (solid line) and  $k = -0.08$  (dashed line).

Figure 5.27a shows that the same small negative value of  $k$  used to fit ac demagnetized sample data actually leads to a significant discrepancy when applied to the analysis of the thermally demagnetized initial state. This is particularly apparent in the Henkel plots shown in Figure 5.27b.

The selection of an appropriate coercive field distribution is a very important aspect of Preisach analysis, since using distributions whose symmetries do not match those of the magnetizing and, especially, the remanence curves (Section 5.1.2), will not permit fitting of the data, despite parameter adjustment. Although the form of a log-normal distribution can sometimes mimic a Gaussian for sufficiently small widths, since the log-normal function becomes increasingly symmetric with a decreasing width parameter  $\sigma_c$ , a Gaussian can never be successfully employed where remanence curves show an obviously sharper curvature at low fields than at the approach to saturation. To test the selection of a Gaussian  $h_c$ -distribution to describe the  $\text{CrO}_2$  system, the data obtained at 25 °C was analyzed using a log-normal distribution with  $\sigma_c = 116$  Oe and  $\tilde{h}_c = 580$  Oe, while employing an interaction width  $\sigma_i = 58$  Oe and a larger value of the thermal parameter  $h_T^* = 29$  Oe. The results of the calculations are shown in Figure 5.28. Comparing this figure with the previous calculations, which employed a Gaussian distribution, displayed in Figure 5.26, the curves generated using the log-normal  $h_c$ -distribution show obvious deviations from the data, especially on the demagnetizing branches of both the magnetization and the remanence (Figure 5.28a). By contrast, if the Henkel plots are compared, the log-normal distribution yields better agreement for the ac demagnetized data (Figure 5.28b).

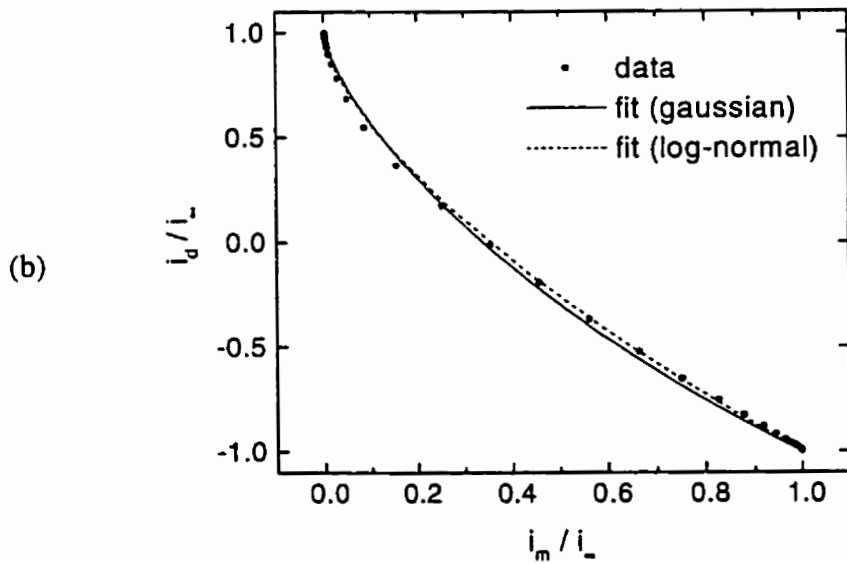
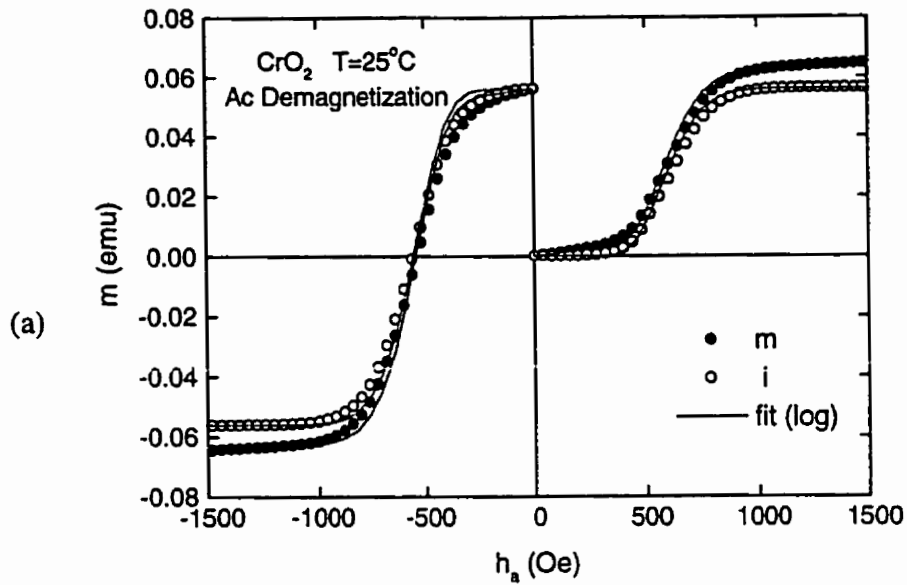


Figure 5.28 . (a) Comparison of experimental data (discrete points) at  $T = 25^\circ\text{C}$  under ac demagnetized initial conditions and calculated magnetization and remanence curves (solid line) using a log-normal distribution. (b) Comparison of the experimental Henkel plot with calculated curves for log-normal (dashed line) and Gaussian (solid line) coercive field distributions.

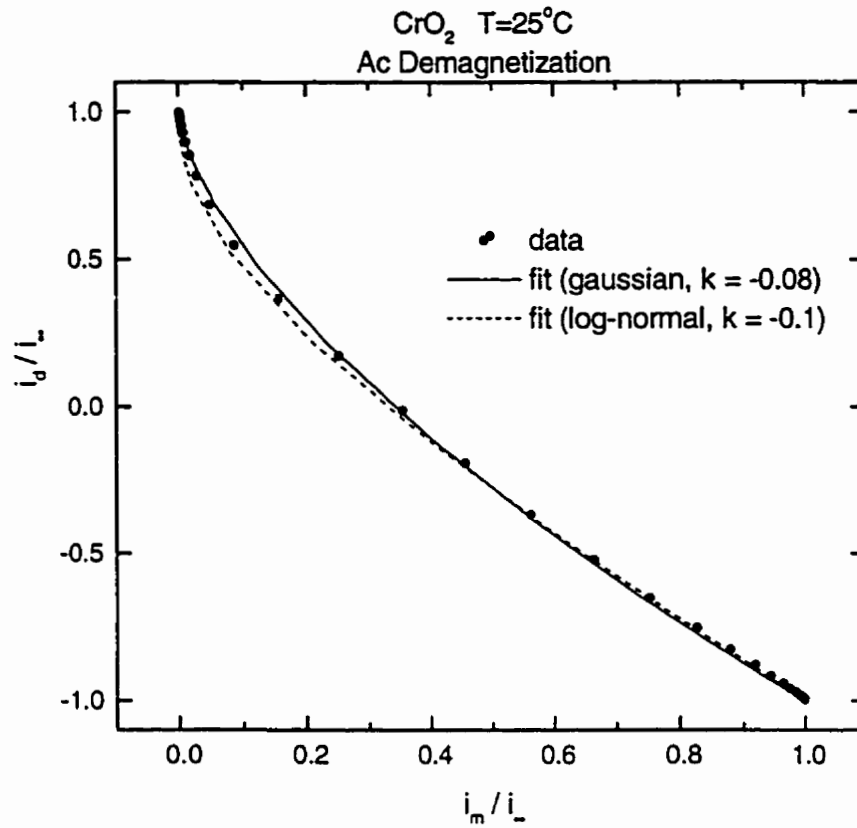


Figure 5.29 . Comparison of experimental data (discrete points) with best fit Henkel plots generated using a Gaussian distribution and  $k = -0.08$  (solid line) and a log-normal distribution with  $k = -0.1$  (dashed line). The distribution parameters for the log-normal fit were  $\tilde{h}_c = 560$  Oe,  $\sigma_c = 112$  Oe, and  $\sigma_i = 450$  Oe.

For  $T = 25\text{ }^{\circ}\text{C}$ , a log-normal distribution with a negative value of  $k = -0.1$  was compared to the best fit to the Henkel plot using the Gaussian distribution, which was also generated with  $k < 0$ . Figure 5.29 shows that Henkel data for an ac demagnetized initial state may be best represented by a log-normal distribution with a small negative value of the mean field parameter, although the distinction between the two is rather marginal.

Although greater success in fitting to Henkel data acquired under ac demagnetized initial conditions was achieved with small negative values of the mean field parameter  $k$ , and with a log-normal distribution, there is really no physical justification for assuming long range interactions between the  $\text{CrO}_2$  particles comprising the audio tape. Furthermore, the character of the *magnetization* and *remanence* curves are best described by a *Gaussian* coercive field distribution and a *zero* mean field parameter, and for initial states achieved by thermal demagnetization, the same negative values of  $k$  that improved agreement between measured and calculated Henkel plots for ac demagnetized initial conditions, actually worsened the fit to data.

### **5.5.5 Analysis of AC and Thermally Demagnetized Low Temperature Data ( $10\text{ K} \leq T \leq 300\text{ K}$ )**

The data, obtained with the QD MPMS, for ac demagnetized samples at low temperatures  $T = 10\text{ K}$ ,  $50\text{ K}$ ,  $100\text{ K}$ ,  $200\text{ K}$ , and  $300\text{ K}$ , are shown in Figure 5.30a. These curves exhibit the same systematic variations as the high temperature data acquired with the VSM. The normalized Henkel plots for these temperatures, shown in Figure 5.30b, demonstrate that there is very little difference between Henkel curves corresponding to

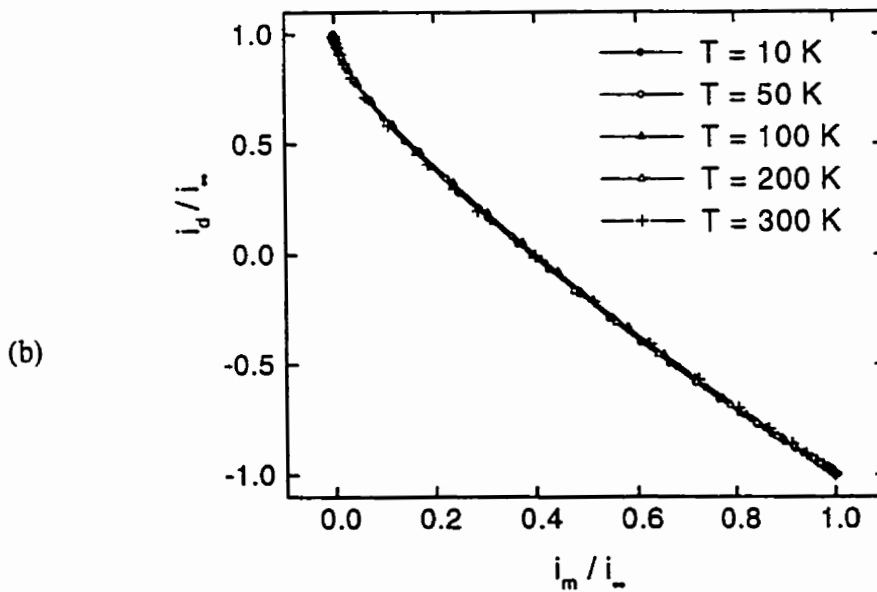
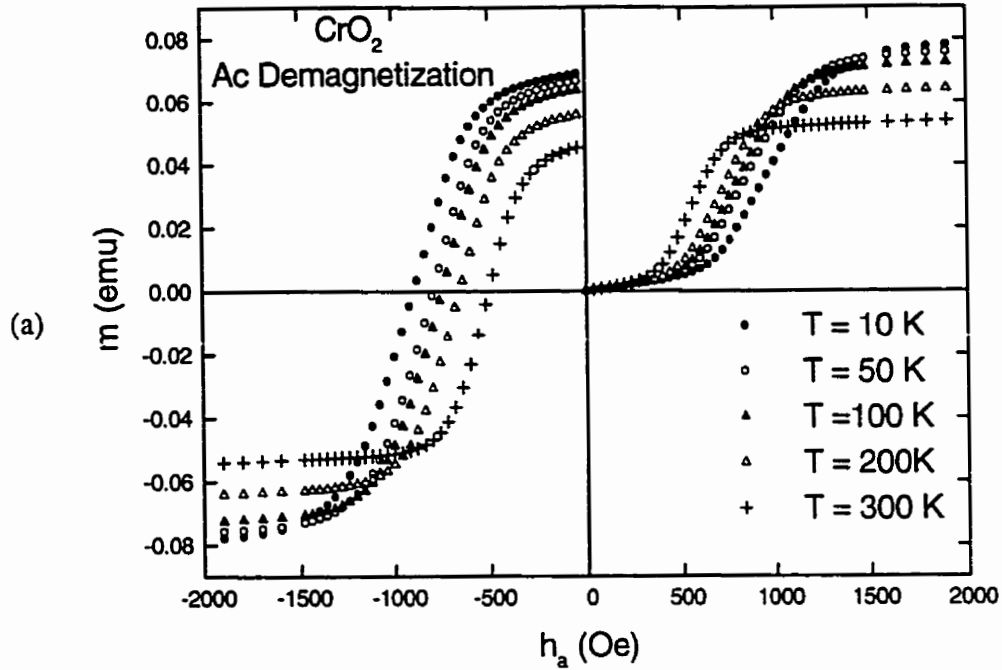


Figure 5.30 . (a) Magnetization curves and (b) Henkel plots of the remanence data measured at five temperatures  $T = 10$  K, 50 K, 100 K, 200 K, and 300 K under ac demagnetized initial conditions.

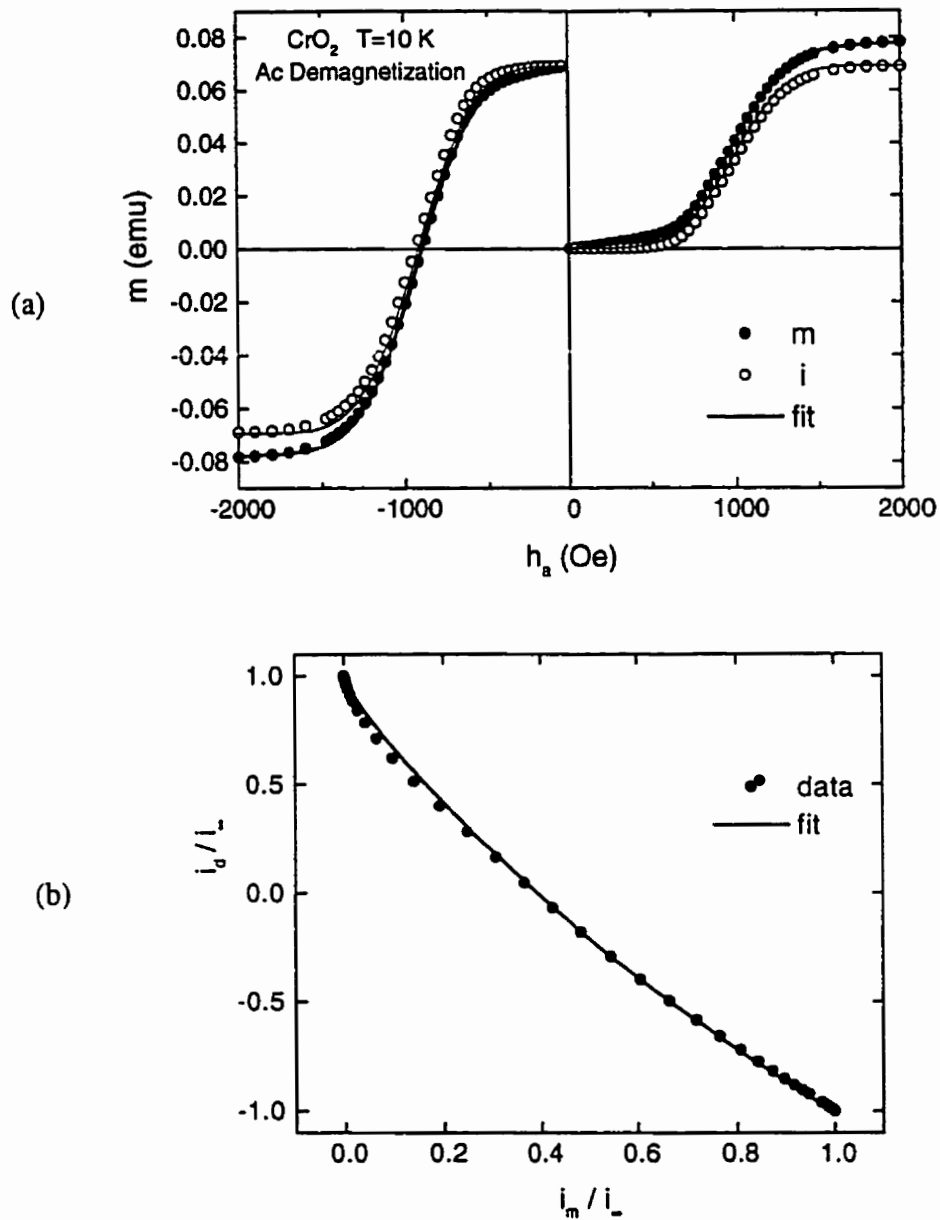


Figure 5.31 . (a) The initial magnetizing curve, magnetization remanences, the demagnetizing curve, and the demagnetizing remanences for ac demagnetized  $\text{CrO}_2$  audio tape at  $T = 10 \text{ K}$ , plotted as a function of applied field  $h_a$ . (b) The Henkel plot constructed from the remanence data in (a). The discrete points are experimental data and the continuous lines are Preisach model calculations.

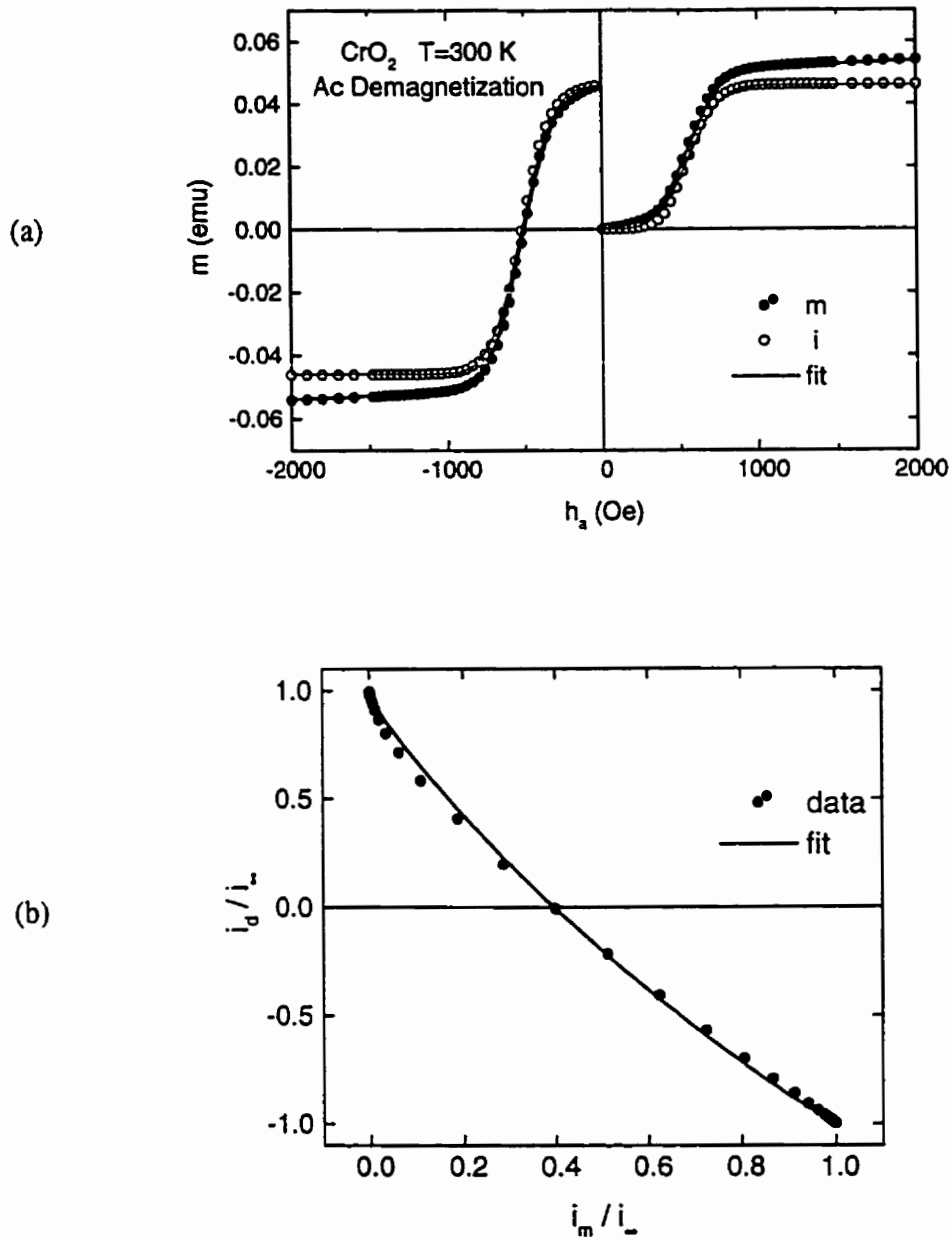


Figure 5.32 . (a) The initial magnetizing curve, magnetization remanences, the demagnetizing curve, and the demagnetizing remanences for ac demagnetized  $\text{CrO}_2$  audio tape at  $T = 300 \text{ K}$ , plotted as a function of applied field  $h_a$ . (b) The Henkel plot constructed from the remanence data in (a). The discrete points are experimental data and the continuous lines are Preisach model calculations.

different temperatures below  $T = 300$  K. This indicates that the systematic increase in the curvature of the high temperature plots with decreasing temperature saturates below room temperature. Figures 5.31 and 5.32 show the curves generated with an eight parameter Preisach analysis for  $T = 10$  K and  $T = 300$  K, respectively. (Fits at other temperatures are included in Appendix 1, Figures A1.13 through A1.15.) The values of the parameters used in these calculations, tabulated in Table 5.5, are consistent with the high temperature fits, particularly the value of the mean field parameter  $k = 0$ .

The data corresponding to thermally demagnetized initial states was obtained at the same temperatures as for ac initially demagnetized states and is shown in Figure 5.33. The data in Figure 5.33a clearly do not exhibit the same monotonic increase in the saturation moment with decreasing temperature as do the data for the ac demagnetized sample. In fact, with the exception of the 300 K data, the systematics are precisely the opposite. However, this is clearly a consequence of the *multiple thermal demagnetization* procedures, which have a cumulative degrading effect on the saturation moment due to the chemical alterations discussed earlier. The behaviour of the Henkel plots in Figure 5.33b is more problematic. While the 300 K data acquired on the MPMS are completely consistent with the 25 °C VSM data, both of which are characterized by an essentially linear Henkel plot indicative of the absence of mean field interaction effects, the lower temperature data in Figure 5.33b show a clear and systematic increase in the curvature of the Henkel plot with decreasing temperature. Obviously, Preisach fits assuming a random thermally demagnetized initial state and  $k = 0$  cannot provide a good description of the experimental data. This is illustrated in Figure 5.34 for one particular temperature  $T = 10$

Table 5.5 . Best fit Preisach parameters for an *ac* demagnetized sample of CrO<sub>2</sub> (10 K ≤ T ≤ 300 K).

T (K)	$\tilde{h}_c$ (Oe)	$\sigma_c$	$\sigma_i$	$h_T^*$ (Oe)	$m_\infty$ (emu)	f	$\Gamma$
10	930	0.28	0.103	0	0.084	0.180	0.45
50	825	0.28	0.100	0	0.081	0.175	0.40
100	774	0.28	0.095	0	0.079	0.175	0.40
200	680	0.30	0.105	0.004	0.068	0.170	0.43
300	526	0.30	0.100	0.015	0.056	0.180	0.4

The mean field parameter was  $k = 0$  for these calculations, performed on an initially *ac* demagnetized Preisach plane using occupation probabilities of (0,1).

Table 5.6 . Best fit Preisach parameters for a *thermally* demagnetized sample of CrO<sub>2</sub> (10 K ≤ T ≤ 300 K).

T (K)	$\tilde{h}_c$ (Oe)	$\sigma_c$	$\sigma_i$	$h_T^*$ (Oe)	$m_\infty$ (emu)	f	$\Gamma$
10	1110	0.29	0.105	0	0.050	0.185	0.4
50	875	0.28	0.100	0	0.056	0.170	0.4
100	790	0.28	0.110	0	0.060	0.180	0.4
200	670	0.29	0.109	0	0.060	0.170	0.4
300	550	0.29	0.130	0.015	0.035	0.185	0.4

The mean field parameter was  $k = 0$  for these calculations, performed on an initially *thermally demagnetized* Preisach plane, using occupation probabilities of (½, ½).

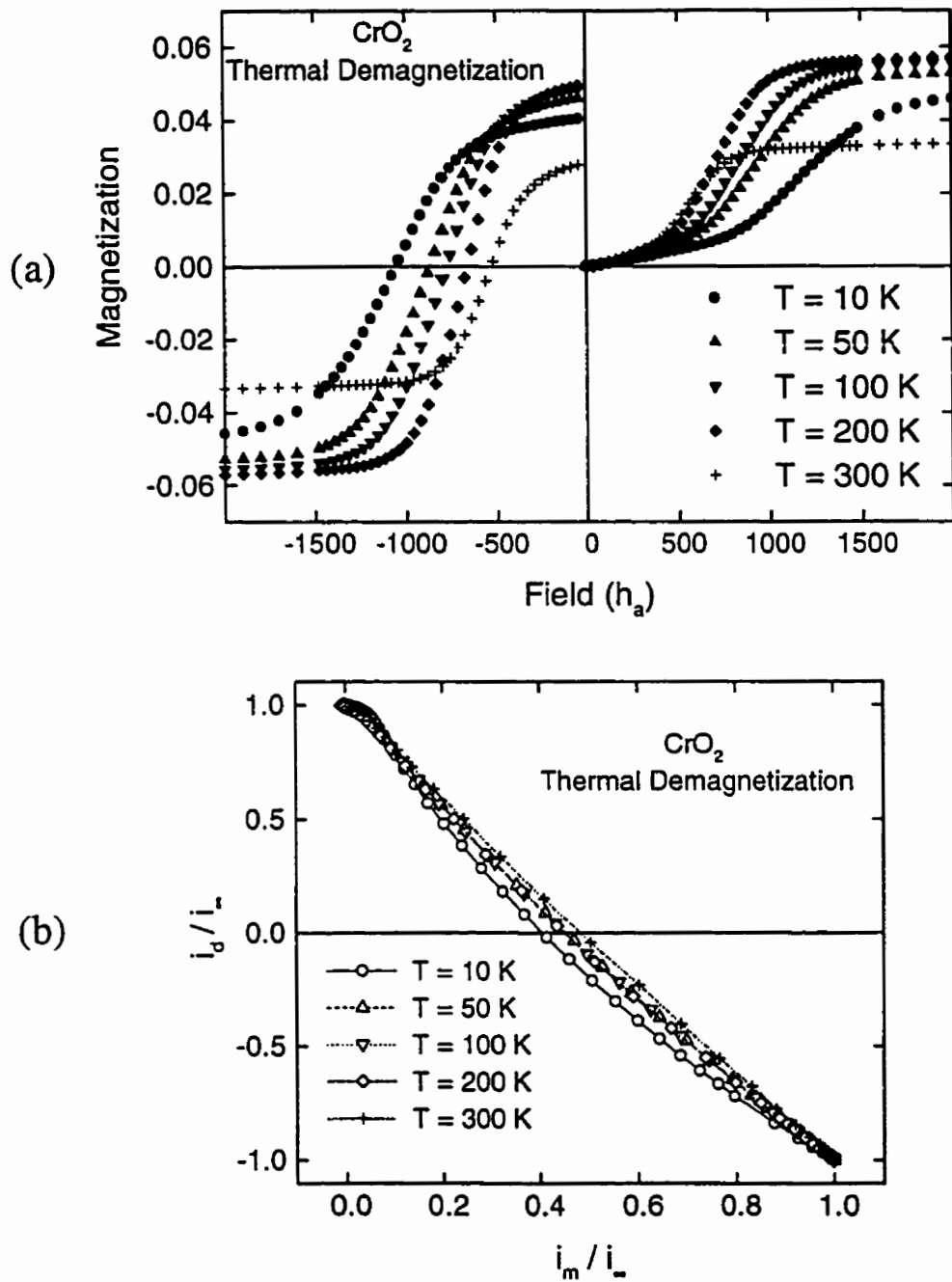


Figure 5.33 . (a) Magnetization curves and (b) Henkel plots of the remanence data for CrO<sub>2</sub> measured at five temperatures  $T = 10$  K, 50 K, 100 K, 200 K, and 300 K under thermally demagnetized initial conditions.

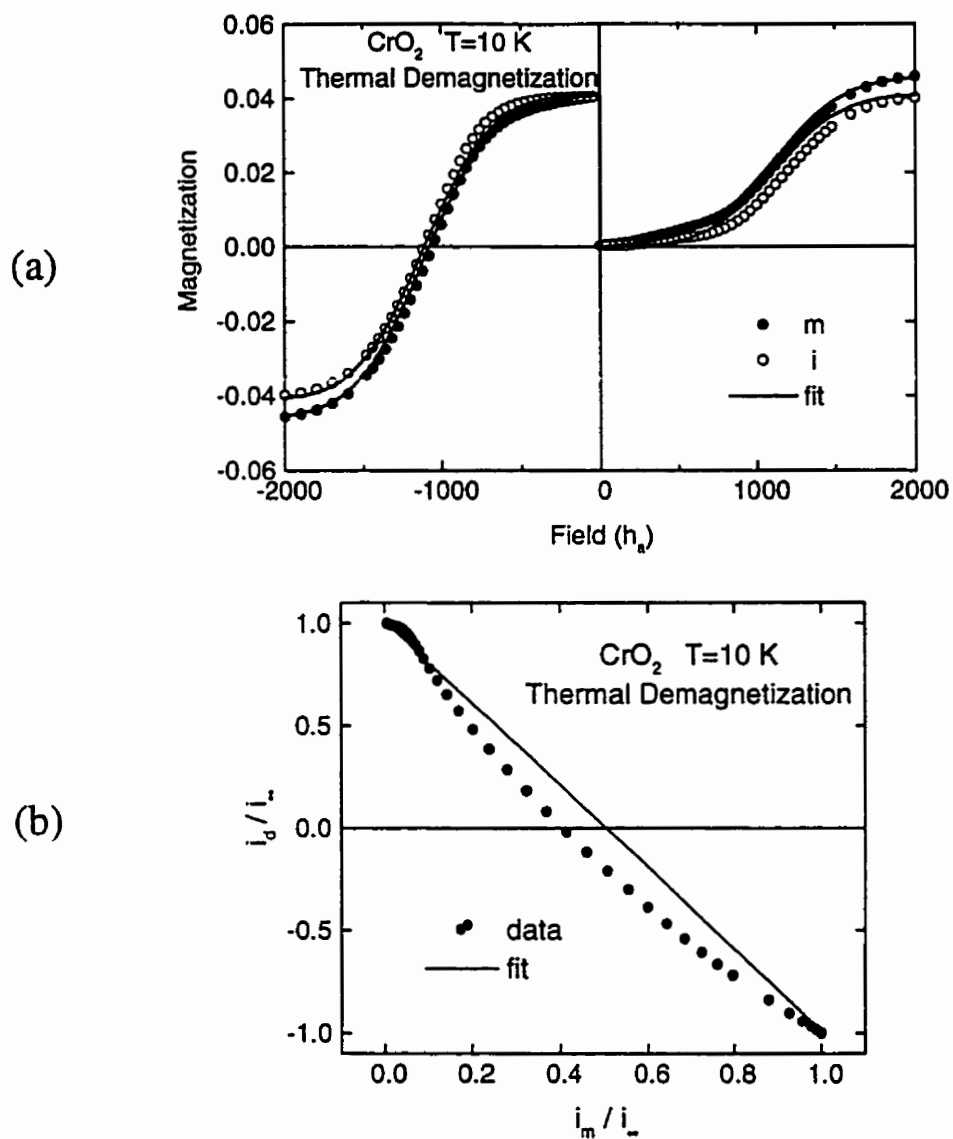


Figure 5.34 . Comparison of experimental data (discrete points) for thermally demagnetized  $\text{CrO}_2$  at  $T = 10\text{ K}$  and (a) calculated magnetization ( $m$ ) and remanence ( $i$ ) curves (solid lines) and (b) the normalized experimental Henkel plot with the calculated curve. Calculations assumed an initial random state with occupation probabilities of  $(\frac{1}{2}, \frac{1}{2})$ .

K, and the parameters for all the fits (shown in Figures A1.16 To A1.19) are listed in Table 5.6.

Since the curvature of these Henkel plots below the Wohlfarth line suggest that a negative value of  $k$  may be appropriate, such fits were attempted. Figure 5.35 illustrates the best fit for  $T = 200$  K. A small negative value of  $k$  greatly improves the agreement between the calculated curve and the experimental data in the Henkel plot. This amelioration of agreement for data was not observed for thermally demagnetized samples measured at higher temperatures on the VSM, as demonstrated in Figure 5.27. Furthermore, the introduction of the finite mean field parameter has little effect on the quality of the fit to magnetization and remanence data.

However, the mean field parameter  $k$  is not the sole determinant of Henkel plot curvature. An *ac demagnetized* sample will demonstrate curvature below the Wohlfarth line. As described in Section 3.3.2, the occupation probability for metastable and stable states respectively can be written as  $(0,1)$  for the *ac demagnetized* state, while for thermal demagnetization the occupation probabilities are equal for both energy states of a Preisach pseudoparticle. Freeing the initial state Preisach plane from the  $(\frac{1}{2},\frac{1}{2})$  constraint imposed by the thermal demagnetization procedure will thus affect the curvature of the Henkel plot and consequently, an attempt was made to fit the data using general occupation probabilities  $(w, 1-w)$  where  $w \leq \frac{1}{2}$ , in effect, introducing a ninth parameter,  $w$ , into the Preisach calculations. The results of these fits are tabulated in Table 5.7 and displayed graphically in Figures 5.36 and 5.37 as well as in Appendix 1, Figures A1.16 through A1.18.

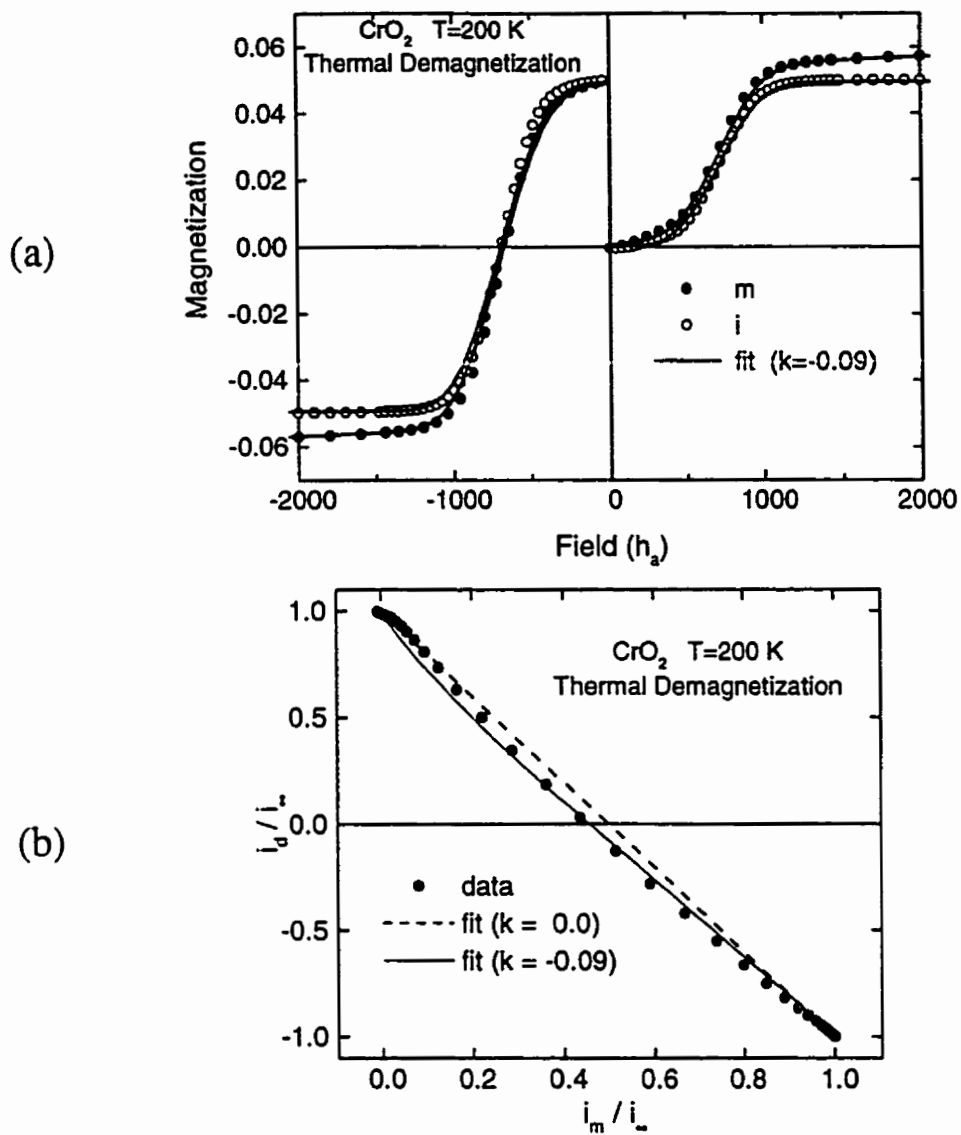


Figure 5.35 . Comparison of experimental data (discrete points) for thermally demagnetized CrO<sub>2</sub> at T = 200 K and (a) calculated magnetization (m) and remanence (i) curves (solid lines) and (b) the normalized experimental Henkel plot with the calculated curve. Calculations assumed an initial random state with occupation probabilities of (½, ½) and  $k < 0$ .

Table 5.7 . Best fit Preisach parameters for a *thermally* demagnetized sample of CrO<sub>2</sub> (10 K ≤ T ≤ 300 K) allowing initial occupation probabilities (w, 1-w) where w ≤ ½.

T (K)	w	$\tilde{h}_c$ (Oe)	$\sigma_c$	$\sigma_i$	$h_T^*$ (Oe)	$m_\infty$ (emu)	f	$\Gamma$
10	0.175	1110	0.28	0.103	0	0.050	0.183	0.58
50	0.28	895	0.28	0.100	0	0.059	0.175	0.55
100	0.31	815	0.285	0.100	0	0.060	0.188	0.50
200	0.30	690	0.29	0.109	0	0.060	0.170	0.43
300	0.49	563	0.31	0.100	0.025	0.035	0.189	0.44

The mean field parameter was set at  $k = 0$  for these calculations.

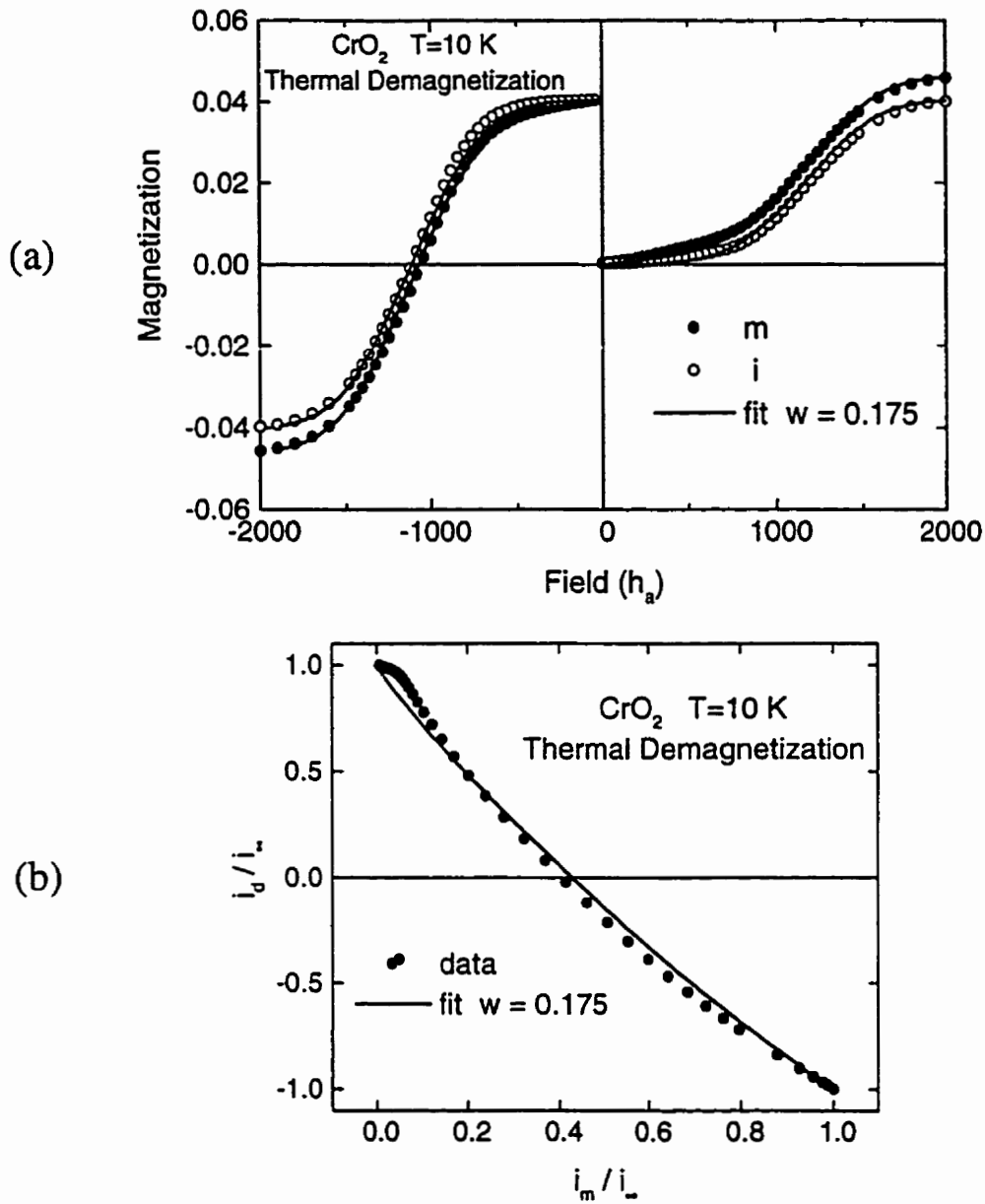


Figure 5.36 . Comparison of experimental data (discrete points) for thermally demagnetized  $\text{CrO}_2$  at  $T = 10 \text{ K}$  and (a) calculated magnetization ( $m$ ) and remanence ( $i$ ) curves (solid lines) and (b) the normalized experimental Henkel plot with the calculated curve. Calculations assumed initial *non*-random state with occupation probabilities ( $w, 1-w$ ) and  $w = 0.175$ .

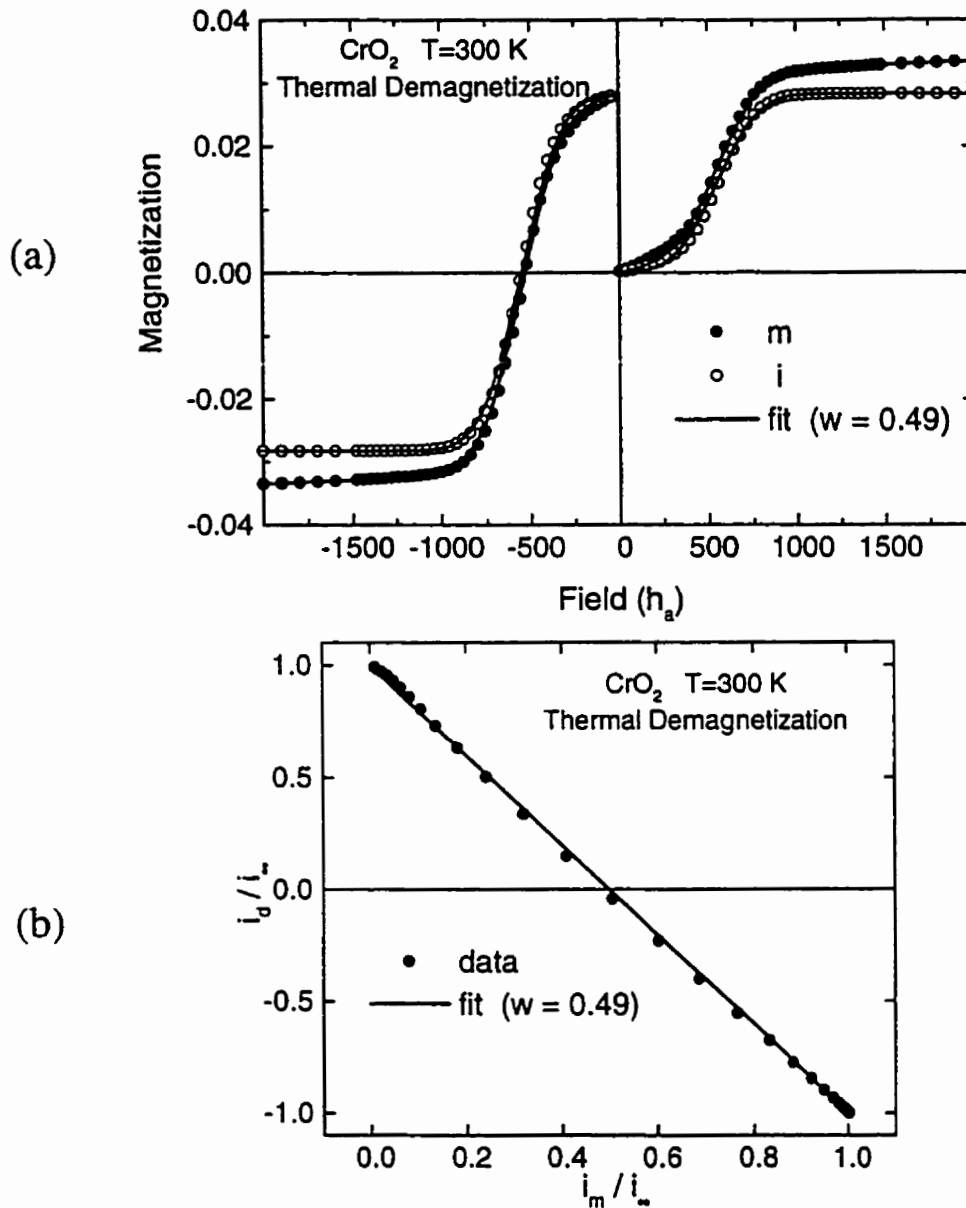


Figure 5.37 . Comparison of experimental data (discrete points) for thermally demagnetized  $\text{CrO}_2$  at  $T = 300 \text{ K}$  and (a) calculated magnetization ( $m$ ) and remanence ( $i$ ) curves (solid lines) and (b) the normalized experimental Henkel plot with the calculated curve. Calculations assumed initial *non-random* state with occupation probabilities ( $w$ ,  $1-w$ ) and  $w = 0.49$ .

The quality of the fit is improved substantially by allowing  $w$  to vary with temperature. For example, a quantitative measure of the improvement determined by the total of the sums of the squares of the deviations from the magnetization, remanence and Henkel plots, shows a 20% improvement at  $T = 10$  K. Except for the fitting parameter  $\Gamma$ , no other parameter changes appreciably with  $w$ . In particular, the Preisach distribution parameters remain essentially fixed. The fits indicate that  $w$  approaches its expected random thermal value of 0.5 as the temperature increases (Figure 5.37 and Table 5.7), and decreases monotonically to  $w \approx 0.175$  at  $T = 10$  K. One way to interpret values of  $w \neq 0.5$  under thermally demagnetized initial conditions is to say that the magnetic system reached thermal equilibrium too quickly to ensure equal populations in both energy levels; that is, interaction fields developed that split the degeneracy of the two levels and produce *unequal* Boltzmann factors *before* the particle response was blocked by the growth of the anisotropy barriers. Particles with high zero temperature energy barriers that grow very rapidly close to  $T_c$  may tend to block with random level populations ( $1/2, 1/2$ ), while particles with low zero temperature energy barriers, which grow slowly, are more susceptible to thermal activation and may block with highly asymmetric level populations (0,1), and the increased wait time imposed by the QD magnetometer (which often totals several hours before temperature stability is reached), may provide a means to effect these thermal transitions. Thus, an occupation probability  $w \neq 0.5$  for a thermally demagnetized initial state may be representative of the *average* of the random ( $1/2, 1/2$ ) and nonrandom (1,0) demagnetized portions of the plane. These explanations are difficult to justify physically for  $\text{CrO}_2$ , because they depend on the details of the barrier

growth close to  $T_c$  and on the growth of the interaction fields, neither of which are currently well understood. Thus, these suggestions must remain highly speculative at this stage, and more extensive measurements are required in order to resolve the apparent contradictory behaviour of the thermally demagnetized  $\text{CrO}_2$  data.

## 5.6 Magnetoferritin

### 5.6.1 General Features of the Magnetic Response<sup>4</sup>

Magnetoferritin is a collection of nanodimensional ferrimagnetic  $\gamma\text{-Fe}_2\text{O}_3$  particles with easy axes oriented randomly in a frozen aqueous suspension. Figure 5.38 shows the temperature dependence of the moment of the magnetoferritin sample measured in an applied field  $h_a = 15 \text{ Oe}$ , after field cooling (FC) and zero field cooling (ZFC) the sample from  $T = 200 \text{ K}$  to  $T = 5 \text{ K}$ . The inset in Figure 5.38 shows the time dependence of the ZFC response in  $h_a = 20 \text{ Oe}$  at  $T = 50 \text{ K}$ . Although the behaviour of the FC and ZFC moment of magnetoferritin bears a superficial resemblance to that observed in the  $\text{CrO}_2$  system in Figure 5.16, specifically, a bifurcation of the FC and ZFC branches and a peak in the ZFC moment, the physical origin of the structure is completely different in the two systems. The preceding analysis of  $\text{CrO}_2$ , showed that the evolution of the spontaneous moment with temperature, and the accompanying formation or dissolution of the free energy barriers, that is, changes in the intrinsic properties of the pseudoparticles themselves, are primarily responsible for the thermal profiles in Figure 5.16. In fact, the  $\text{CrO}_2$  pseudoparticles are all thermally blocked within a few degrees of the Curie temperature. Conversely, in magnetoferritin, the critical temperature  $T_c \approx 670 \text{ K}$  (Section

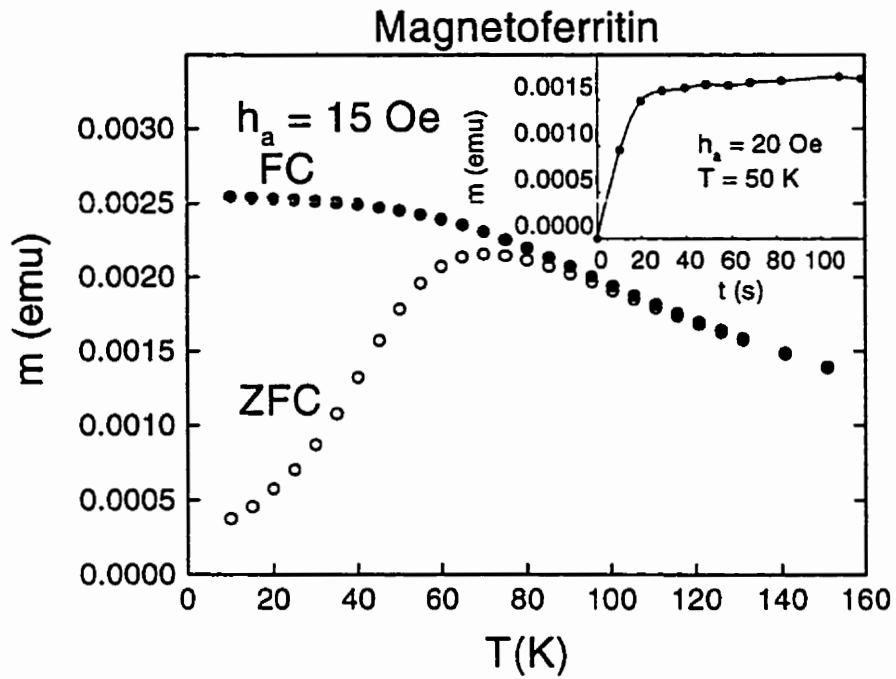


Figure 5.38 . The temperature dependence of the field cooled (FC) and zero field cooled (ZFC) moment of magnetoferritin measured in an applied field . The inset shows the time dependence of the moment after zero field cooling from  $T = 200$  K to 5 K and then applying a “step function” excitation. The field ramping is  $\approx 10$  s , so the true viscous thermal relaxation component corresponds to about 50% of the total response.

4.3.2) lies well above the experimental temperature range and the development of the spontaneous moment and the free energy landscape are essentially complete below 200 K, so that variations of the magnetic response with temperature are almost exclusively a consequence of changes in the dynamic relaxation response of the pseudoparticles. This is particularly apparent from the relaxation data in the inset to Figure 5.38 , which shows that at least 50% of the total signal at  $T = 50$  K is viscous aftereffect that occurs after the applied field  $h_a$  has been stabilized at 20 Oe, which requires slightly less than 10 s.

### 5.6.2 Analysis of Thermally Demagnetized Hysteresis Data <sup>5</sup>

The essential characteristics of hysteresis in magnetoferritin for  $5 \text{ K} \leq T \leq 50 \text{ K}$  are summarized in Figures 5.39 through 5.41. Figure 5.39 shows the field dependence of the major hysteresis loop at three representative temperatures  $T = 5 \text{ K}$ ,  $10 \text{ K}$  , and  $50 \text{ K}$ . Figure 5.40 also displays the field dependence of the principal magnetizing and demagnetizing remanences  $i_m(h_a)$  and  $i_d(-|h_a|)$  at  $T = 5, 6, \text{ and } 8 \text{ K}$ . A comparison of the field dependence of the remanence as well as the parametric Henkel plots of  $i_m(h_a)/i_\infty$  versus  $i_d(-|h_a|)/i_\infty$ , at two measurement temperatures  $T = 5 \text{ K}$  and  $T = 10 \text{ K}$ , is shown in Figure 5.41. The discrete points are experimental data and the solid curves are Preisach simulations, using a log-normal distribution of coercive fields and a Gaussian distribution of interaction fields, as described earlier. While the magnetoferritin data exhibits many of the same systematic trends as the  $\text{CrO}_2$  data, such as the bifurcation of the FC and ZFC data, the maximum in the temperature dependence of the ZFC moment, and the decrease in coercivity and in the ratio of the saturation remanence to the saturation moment with increasing temperature, there are several notable exceptions

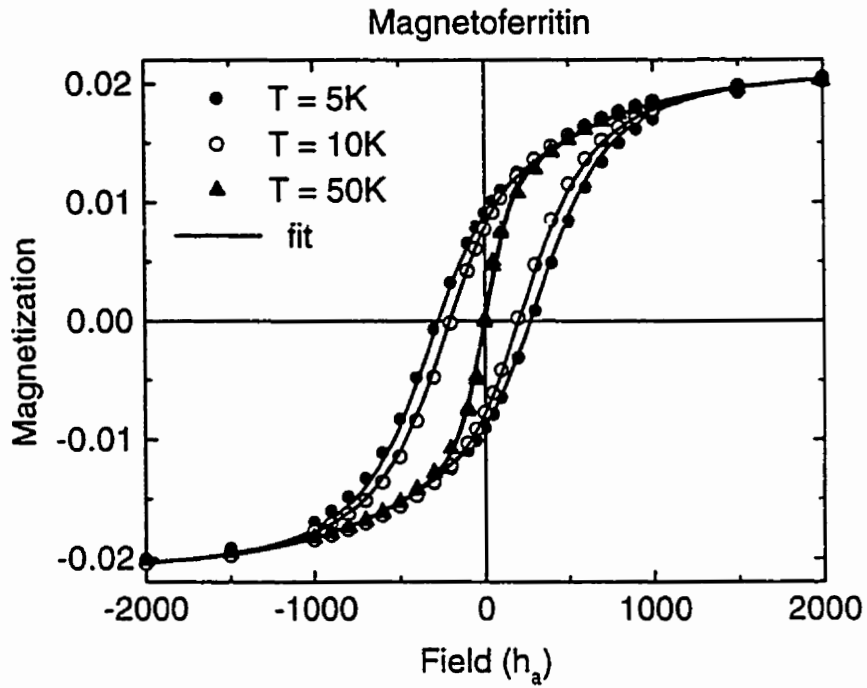
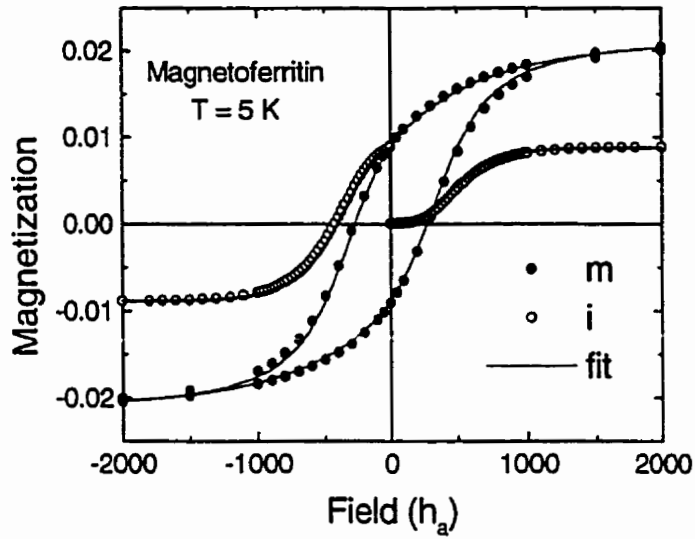
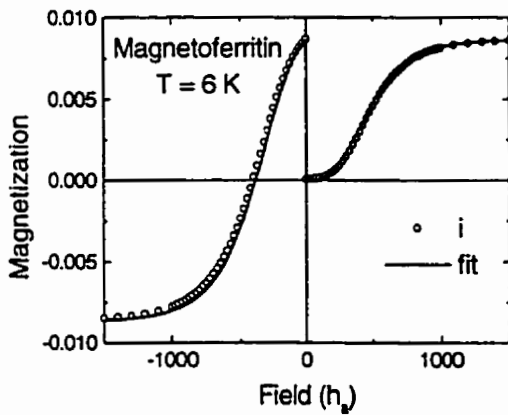


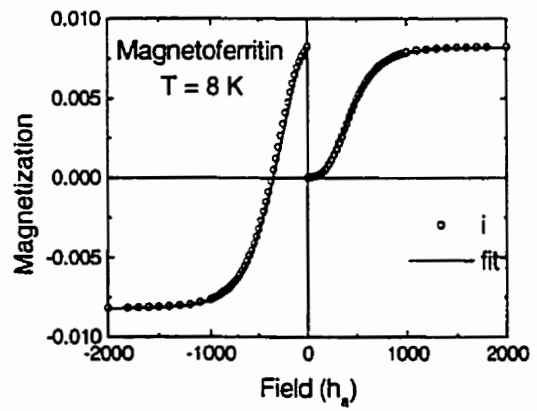
Figure 5.39 . Comparison of major hysteresis loops for magnetoferritin at three temperatures  $T = 5\text{ K}$ ,  $10\text{ K}$ , and  $50\text{ K}$ . The amplitude of the hysteresis loop is independent of temperature; however, there is a marked decrease in its width as temperature increases. The response of the magnetoferritin sample becomes more reversible as temperature increases.



(a)



(b)



(c)

Figure 5.40 . (a) A comparison of the major hysteresis loop (solid dots) and the magnetizing and demagnetizing remanences (open dots) at  $T = 5$  K, (b) remanence curves at  $T = 6$  K, and (c) remanence curves at  $T = 8$  K. The experimental data are shown as discrete points and the fits are solid lines.

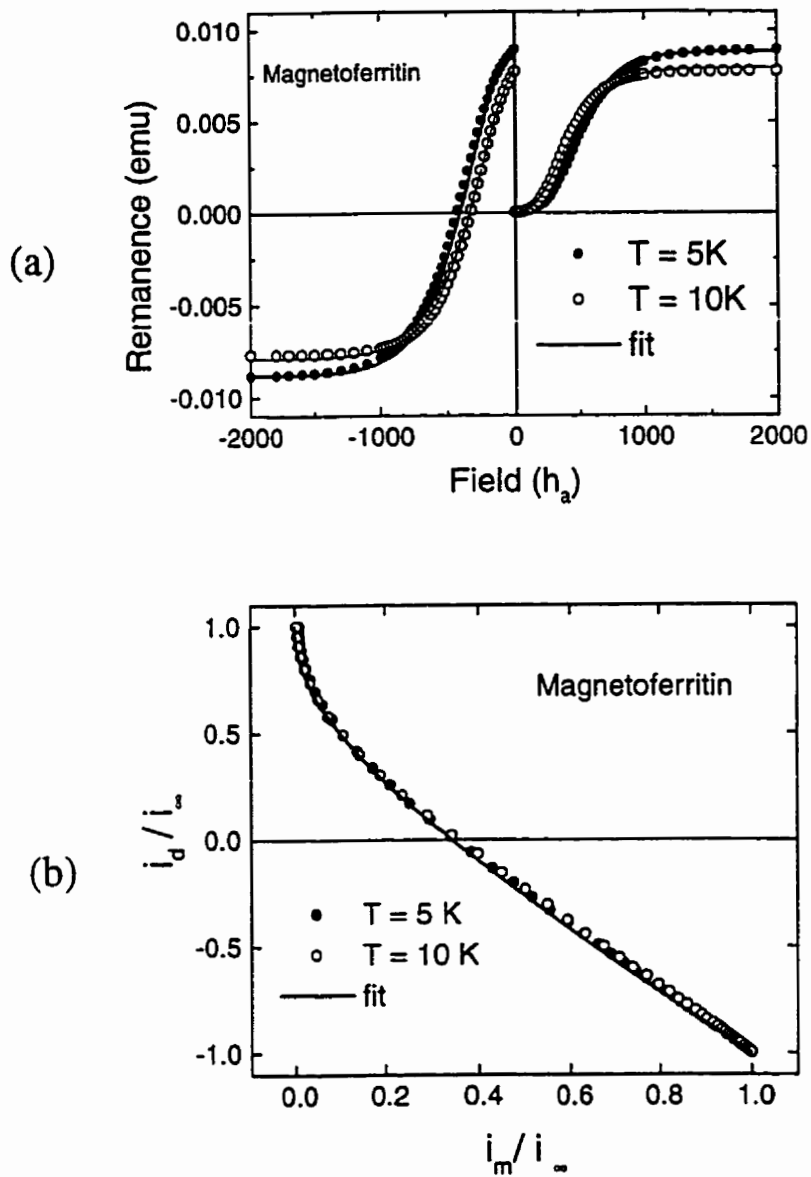


Figure 5.41 . Comparison of (a) magnetization and remanence data and (b) Henkel plots for magnetoferritin at  $T = 5$  K and  $T = 10$  K. Although the sample exhibits greater reversibility at higher temperatures, the normalized Henkel plots are practically identical.

(Mitchler, Roshko, Dahlberg & Moskowitz, 1999). First, there is a distinct “asymmetry” in the field dependence of the magnetoferritin remanences that is not present in the “low” temperature  $\text{CrO}_2$  data; the curvature of the data is much stronger at lower fields, during the initial stages of the magnetizing and demagnetizing processes, than it is at higher fields, where the system is approaching saturation. This is readily observed by plotting the derivative of the magnetizing remanence data in Figures 5.40a, for example, as a function of field; this derivative has a peak at the inflection point followed by a long tail, reflecting the gradual approach of the remanence,  $i_m$ , to saturation (Figure 5.42). This “asymmetry” *cannot* be replicated by a Gaussian distribution of coercive fields, and is the principal motivation underlying the choice of the log-normal distribution, which has a similar asymmetry. Next, at all temperatures below 50 K, where the magnetoferritin response is hysteretic, as seen in Figures 5.39, changes in temperature affect only the *width* of the major loop, but leave the amplitude of the loop unchanged. This implies that the spontaneous moment of the individual particles, as well as other *intrinsic* properties such as the single-particle anisotropy constant, are independent of temperature, while the measured coercivity is a *dynamic* property that measures a typical intrinsic  $T \rightarrow 0$  particle coercivity *reduced by thermal relaxation effects* (Mitchler, Dahlberg, Wesseling & Roshko, 1996b). By contrast, the collapse of the hysteresis cycle in  $\text{CrO}_2$  as  $T \rightarrow T_C$  involves simultaneous changes in both amplitude and width, and both are direct manifestations of changes in the *intrinsic* characteristics of the constituent particles. Lastly, the ratio of the saturation remanence to the saturation moment of the magnetoferritin sample at  $T = 5$  K is  $i_\infty/m_\infty \approx 0.5$ , which is characteristic of an

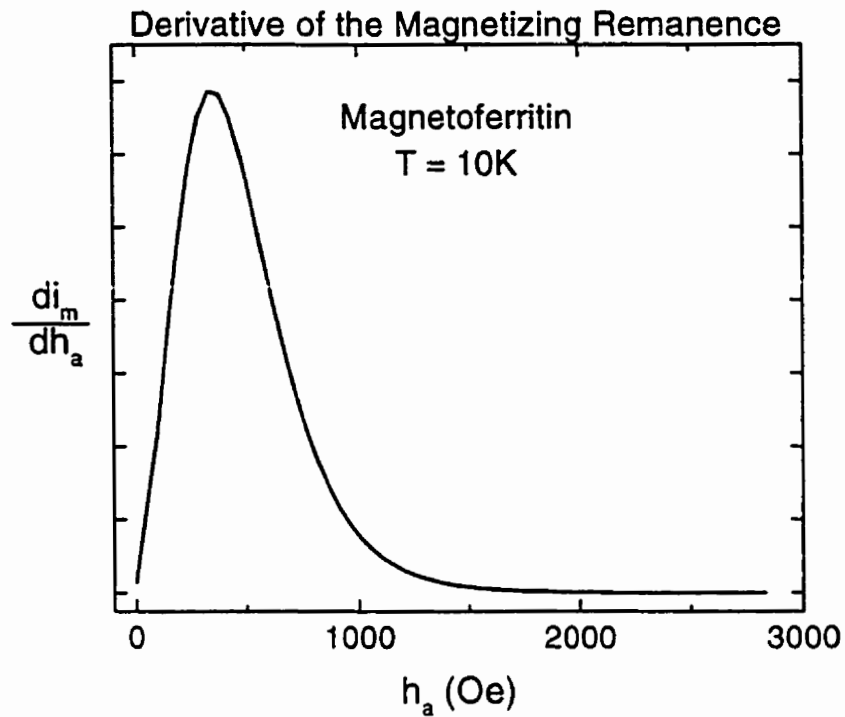


Figure 5.42 . The derivative of the magnetizing remanence of magnetoferitin as a function of applied field at  $T = 10$  K. The asymmetry of this curve is reminiscent of the log-normal function which was selected to describe the distribution of coercive fields utilized in the Preisach calculation for magnetoferitin data.

aggregation of single-domain particles with uniaxial anisotropy and a *spatially isotropic distribution of easy axes* (Stoner & Wohlfarth, 1948). In the CrO<sub>2</sub> audio tape, the value of this ratio  $T = 25^\circ\text{C}$  is  $i_\infty/m_\infty \approx 0.85$ , which is indicative of the high degree of easy axis alignment in this type of recording medium.

If thermal demagnetization of magnetoferritin at 200 K, followed by zero field cooling into the hysteretic region, produced a random initial state in which each of the two single-particle energy levels were occupied with an equal probability of  $\frac{1}{2}$ , as occurs in the CrO<sub>2</sub> system, then according to our Preisach simulations (Roshko, Mitchler & Dalhberg, 1997), the demagnetizing-like curvature of the Henkel plots in Figure 5.41b would be direct evidence for a negative mean field parameter  $k < 0$ , with  $k$  on the order of  $-5$  to supply the necessary curvature (Roshko et al, 1997). This would imply either a significant demagnetizing correction, which is inconsistent with both the shape of the sample, a long thin tube, and with its extremely dilute magnetoferritin content, or a reasonably strong “antiferromagnetic” coupling between particles, which is once again incompatible with the dilution (and possibly also with the mean field formalism (km) itself, which does not include the necessary two-sublattice structure (Section 2.8.3)). However, there is an important distinction between the CrO<sub>2</sub> and magnetoferritin systems. The magnetoferritin system must be cooled to temperatures  $T < 100$  K, *well below* its instability (“critical”) temperature  $T_C = 670$  K, before hysteresis is observed, while, in CrO<sub>2</sub>, irreversibility develops almost *immediately below* the ferromagnetic Curie temperature  $T_C$ . This means that on average the energy barriers in CrO<sub>2</sub> must be higher than those in magnetoferritin at the same temperature. However, it also has a more subtle

implication. The populations of the single-particle energy levels that are established during cooling ultimately depend on the *rate* at which the critical barrier  $W^* = k_B T \ln(t_{\text{exp}}/\tau_0)$  sweeps through the distribution of system energy barriers. This is controlled in part by the experimental cooling rate, which determines  $t_{\text{exp}}$ , but also in part by the temperature dependence  $W(T)$  of the barriers themselves. If this temperature dependence is sufficiently strong, then it may be possible to sweep through the entire distribution almost instantaneously and to block all the barriers almost simultaneously, even though the actual cooling rate may be quite modest. This is what happens in  $\text{CrO}_2$ , where the combination of rapid barrier growth *just below*  $T_C$  and relatively low thermal energy  $k_B T_C$  at the ordering temperature allow blocking to occur before the interaction fields  $h_i$  have had a chance to develop and lift the degeneracy of the levels, thus trapping equal Boltzmann populations ( $1/2, 1/2$ ) in each level. In magnetoferritin, this possibility is eliminated by the fact that there is too much thermal energy at  $T_C$  to permit any of the barriers  $W(T)$  to block, with the result that  $W(T) \ll W^* = k_B T \ln(t_{\text{exp}}/\tau_0)$  over a wide range of temperatures below  $T_C$ . When blocking eventually occurs in magnetoferritin at much lower temperatures, where the barriers have ceased to evolve, the level populations are determined primarily by the experimental cooling rate. This blocking process is potentially much slower than that in  $\text{CrO}_2$  since it lacks the advantage of barrier growth, and may yield very *asymmetric level distributions*, perhaps resembling those of an *ac demagnetized* state. These ideas are illustrated in Figures 5.43a and 5.43b, which show schematic representations of energy barrier distributions  $W(T)$  corresponding to a  $\text{CrO}_2$ -like system and a magnetoferritin-like system, respectively. Figure 5.44 compares the fits

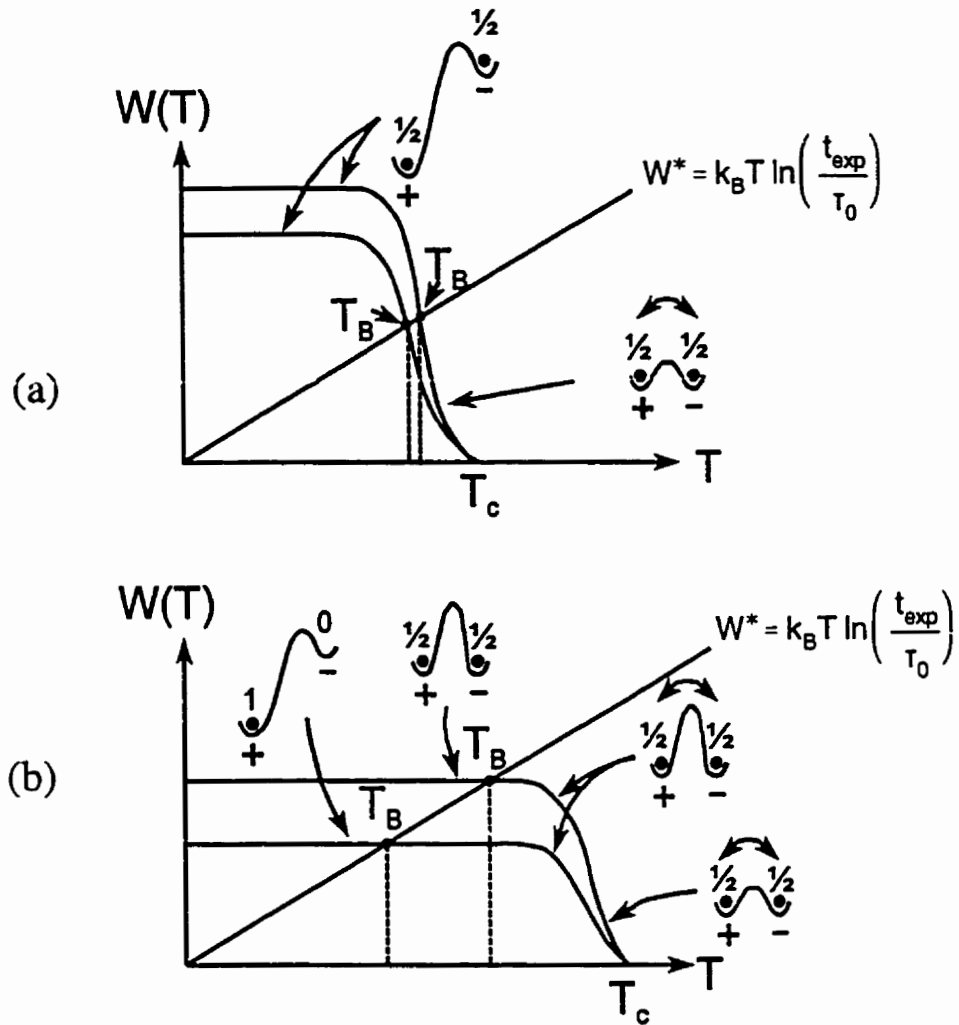


Figure 5.43 . A distribution of energy barriers  $W(T)$  means that some particles will block before others. The intersection of  $W^* = k_B T \ln(t_{\text{exp}}/\tau_0)$  with the distribution  $W(T)$  defines the range of blocking temperatures  $T_B$ . (a) If the distribution is *narrow* where  $W(T)$  meets  $W^*$ , and if barrier growth is rapid, then upon cooling, particles will block at nearly the same time, before inter-particle interaction fields develop, and random occupation probabilities ( $1/2, 1/2$ ) will result. (b) If the distribution is *sufficiently wide* where  $W(T)$  meets  $W^*$ , and if barrier growth is slow, then upon cooling, inter-particle interaction fields will develop before all particles are blocked. These interaction fields can lift the level degeneracy and freeze particle moments into a state bearing a much closer resemblance to that resulting from ac demagnetization with level occupation probabilities (0, 1) or (1, 0).

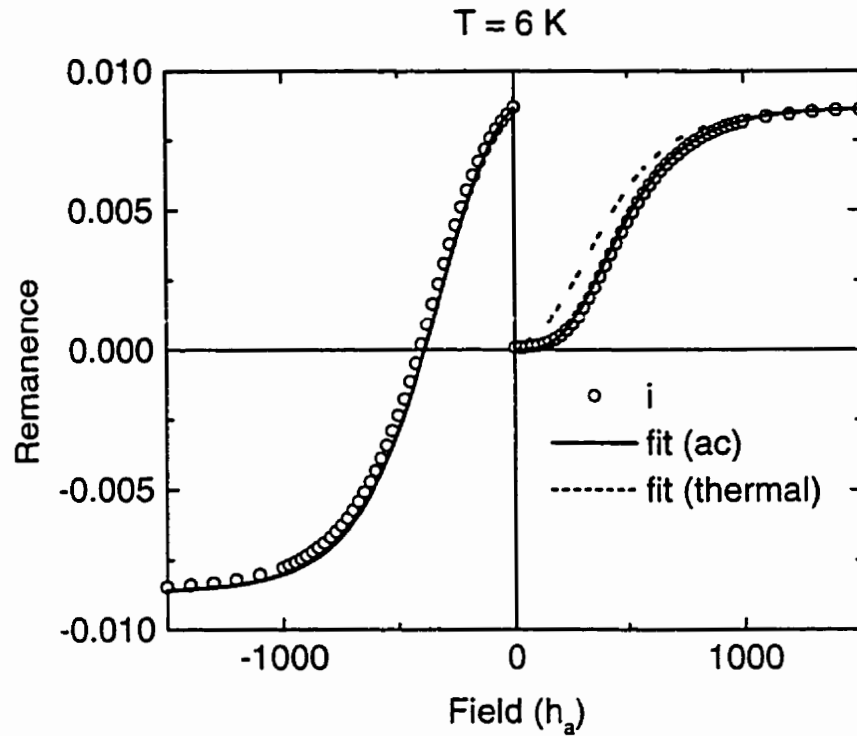


Figure 5.44 . A comparison of fits to the magnetizing and demagnetizing remanence curves (i) at  $T = 6$  K utilizing initial probabilities for the occupation of energy levels in the ac demagnetized state (solid line) where the high energy metastable state is completely unoccupied, and the random thermally demagnetized state (dotted line) where the stable and metastable states are equally populated.

obtained using ac and random populations for Preisach calculations of remanence. Even if a negative value of  $k$  were incorporated into the fit for a random initial state, the curvature generated by the model does not match the curvature of the experimental data, and the magnetizing remanence curve generated using ac demagnetized plane populations obviously provides a better description of the experimental data. Furthermore, the demagnetization and demagnetizing remanence curves generated with  $k = 0$  offer excellent descriptions of the data. The solid curves in Figures 5.39 through 5.41 were all generated assuming an ac demagnetized initial state ( $+\bar{\mu}$  for  $h_i > 0$ ,  $-\bar{\mu}$  for  $h_i < 0$ ), and a Preisach distribution of the form

$$p(h_c, h_i) = (2\pi\sigma_c^2 h_c^2)^{-1/2} \exp\left[-(\log(h_c/\bar{h}_c))^2/2\sigma_c^2\right] (2\pi\sigma_i^2)^{-1/2} \exp\left[-h_i^2/2\sigma_i^2\right],$$

where, as before, the mean field term is treated in terms of an effective field in the Preisach calculations and the skew transformation  $h_a = h - km$  is employed to convert the effective field  $h$  to an equivalent applied field  $h_a$  (Section 3.3). The rectangular Preisach cycles were supplemented by the same reversible nonlinearity,  $\pm[1 - \exp(\mp\Gamma h_a)]$ , used in the  $\text{CrO}_2$  analysis. Table 5.8 summarizes the best fit parameters for the magnetoferritin data.

The model clearly provides an excellent description of the experimental data, and the fits are consistent with the following physical picture of magnetoferritin (Mitchler, Roshko, Dahlberg & Moskowitz, 1999; Roshko & Moskowitz, 1998). First, the mean field parameter  $k = 0$ , so that the interparticle interactions are all short range, and the curvature of the Henkel plots is due exclusively to the dispersion  $\sigma_i$  in these local fields produced by random fluctuations in the local environment. Second, the best fit parameters

Table 5.8 . Best fit Preisach parameters for magnetoferritin.

T (K)	$\sigma_c$	$\sigma_i$ (Oe)	$\tilde{h}_c$ (Oe)	$m_\infty$ (emu)	$h_T^*$ (Oe)
5	0.45	120	480	0.009	96
6	0.45	120	480	0.009	120
8	0.45	120	480	0.009	168
10	0.45	120	480	0.009	192
50	0.45	120	480	0.009	1100

The calculations were performed using the initial state populations of an ac demagnetized system (1, 0). All parameters were independent of temperature except for the effective thermal parameter  $h_T^*$ . The reversible component parameters were  $f = 0.56$  and  $\Gamma = 0.7$ .

$\sigma_c$ ,  $\tilde{h}_c$ ,  $\sigma_i$ , and  $m_\infty$  are all temperature independent, so that the pseudoparticle moments and energy barriers are independent of temperature, at least below 10 K. Thus, temperature enters the analysis exclusively through the thermal viscosity field  $h_T^* = W^*/\bar{\mu} = [k_B \ln(t_{exp}/\tau_0)/\bar{\mu}]T$ , which controls the relative proportions of thermally blocked and unblocked pseudoparticles. Next, the mean coercive field of the particles is  $\bar{h}_c = \tilde{h}_c \exp(\sigma_c^2/2) \approx 530$  Oe, and together with  $t \approx 10$  m (typical of the measurements performed on the QD MPMS),  $\bar{\mu} = 2.2 \times 10^{-16}$  emu, and  $\tau_0 \approx 10^{-9}$  s, this yields a mean blocking temperature  $\bar{T}_B = \bar{\mu} \bar{h}_c / (k_B \ln(t/\tau_0)) \approx 30$  K. Also, the structure of the demagnetized state obtained after zero field cooling from 200 K is determined by the ratio of the populations of the energy levels of the pseudoparticles at their individual blocking temperatures,  $\exp(-2\bar{\mu}h_i/k_B T_B)$ . Taking  $T_B \approx \bar{T}_B = 30$  K and  $h_i \approx \frac{1}{4}\sigma_s \tilde{h}_c = 30$  Oe, which is the minimum interaction field experienced by ~80% of the pseudoparticles, then  $\exp(-2\bar{\mu}h_i/k_B T_B) \approx 0.03$ , which justifies the use of the ac demagnetized state. Finally, the current analysis shows that the magnetic response of magnetoferritin can be modeled using a system of equivalent Preisach *pseudoparticles* with a log-normal distribution of coercive fields, with median field  $\tilde{H}_c = 480$  Oe and dispersion  $\sigma_c = 0.45$ .

The pseudoparticle coercive fields  $h_c$  are *not* identical to the anisotropy fields  $h_K$  of the real particles, because the pseudoparticles are perfectly aligned while the real particles are not. In fact, the distribution of pseudoparticle coercive fields is actually a convolution of two *real* particle distributions, one for the anisotropy fields  $h_K$  and one for the orientations of the easy axes at angles  $\theta$  with respect to the applied field  $h_a$ . The latter

has the effect of reducing the critical (coercive) field of a particle *below* its perfect-alignment value  $h_K$ , and is expected to play an important role in magnetoferritin, where the easy axes are distributed isotropically. If we adopt the Stoner-Wohlfarth model of coherent rotation (Stoner & Wohlfarth, 1948), then  $h_c = h_K [(\sin \theta)^{2/3} + (\cos \theta)^{2/3}]^{3/2}$ , and the distribution  $f(h_c)$  of critical switching fields produced by a distribution  $g_1(\theta)$  of orientations and a distribution  $g_2(h_K)$  of anisotropy fields is given by

$$f(h_c) = \int_0^{\pi/2} g_1(\theta) g_2(h_K = h_c Z(\theta)) Z(\theta) d\theta$$

where  $Z(\theta) = dh_K/dh_c = [(\sin \theta)^{2/3} + (\cos \theta)^{2/3}]^{3/2}$  (Mitchler, Roshko, Dalhberg & Moskowitz, 1999). Figure 5.45 shows a comparison of the critical field distributions  $f(h_c)$  for a system of perfectly aligned particles  $g_1(\theta) = \delta(\theta)$ , and for a system of isotropically oriented particles  $g_1(\theta) = \sin \theta$ , both with the *same* Gaussian distribution of anisotropy fields  $g_2(h_K) = (2\pi\sigma_K^2)^{-1/2} \cdot \exp[-(h_K - \bar{h}_K)^2/2\sigma_K^2]$ , with  $\bar{h}_K = 1$  and  $\sigma_K = 0.1$ . The effect of randomness is twofold: (i) the most probable critical field  $\bar{h}_{cm}$  decreases from  $\bar{h}_{cm} = \bar{h}_K$  to approximately  $\bar{h}_{cm} = \bar{h}_K/2$  and (ii) the distribution  $f(h_c)$  develops an asymmetry about  $\bar{h}_{cm}$  that is reminiscent of the asymmetry characterizing the log-normal distribution of coercive fields used in Preisach analysis. Thus, the most probable anisotropy field of the *real* magnetoferritin particles  $\bar{h}_K = 2\bar{h}_{cm} = 2\bar{h}_c \exp(-\sigma_c^2) = 780$  Oe.

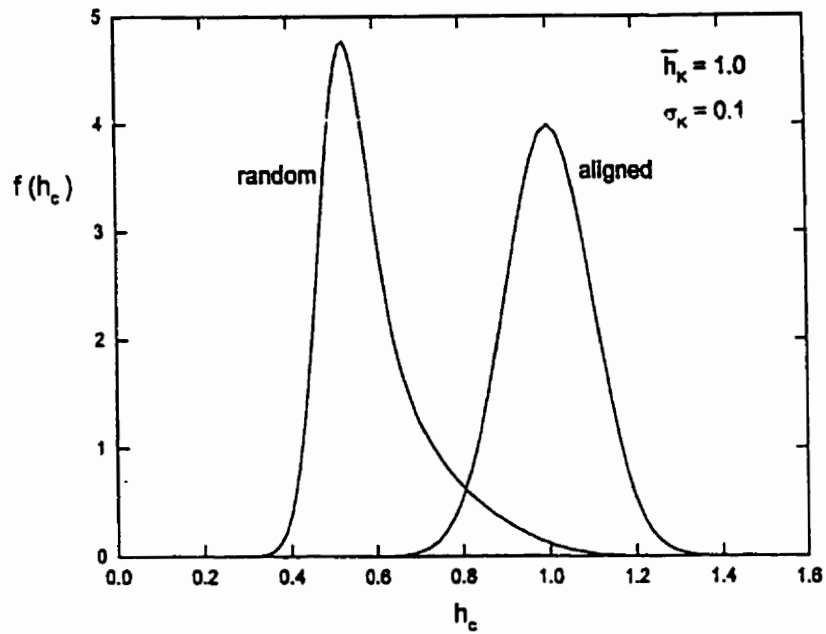


Figure 5.45 . Distributions of coercive fields  $h_c$  for a system of *aligned* particles, with a Gaussian distribution of anisotropy fields  $h_k$  with a mean  $\bar{h}_k = 1.0$  and a dispersion  $\sigma_k = 0.1$ , and for a system with *isotropically oriented* easy axes with the same parameters.

## 5.7 Neodymium Iron Boron

### 5.7.1 General Features of the Magnetic Response

Like  $\text{CrO}_2$ , this permanent magnet is a ferromagnet and it consists of a collection of ferromagnetic  $\text{Nd}_2\text{Fe}_{14}\text{B}$  particles with hexagonal easy axes aligned parallel to each other. Figure 5.46 shows the ZFC and FC curves for the  $\text{Nd}_2\text{Fe}_{14}\text{B}$  sample. The moment drops steeply at  $T_c \approx 312^\circ\text{C}$ , which is typical of a material with a well-defined paramagnetic-ferromagnetic phase transition. The ZFC moment of  $\text{Nd}_2\text{Fe}_{14}\text{B}$  differs from the  $\text{CrO}_2$  and magnetoferritin ZFC moments in that the ZFC peak is very broad and almost temperature independent. Furthermore, since the ZFC moment is a significant fraction of the FC moment and since the magnetic response to the application of a step-function field excitation, shown in the inset of Figure 5.46, is very rapid, indicating that thermal transitions are essentially absent (as in  $\text{CrO}_2$ ), we conclude that the initial magnetic response of  $\text{Nd}_2\text{Fe}_{14}\text{B}$  in low fields  $h_a \leq 100$  Oe has a significant reversible component.

### 5.7.2. Analysis of the Hysteresis Data: Modifying the Elementary Preisach Loop <sup>6</sup>

If a magnetic system is prepared in a thermally demagnetized initial state, the shape of the initial magnetization curve and its location within the major hysteresis loop can be used to identify the coercivity mechanism, as shown in Figure 2.13. A very soft initial response (Section 1.4) that saturates at fields well below the demagnetizing coercive field is typical of nucleation dominated reversal, in which small regions of reverse magnetization expand outward from a high density of defects localized on a

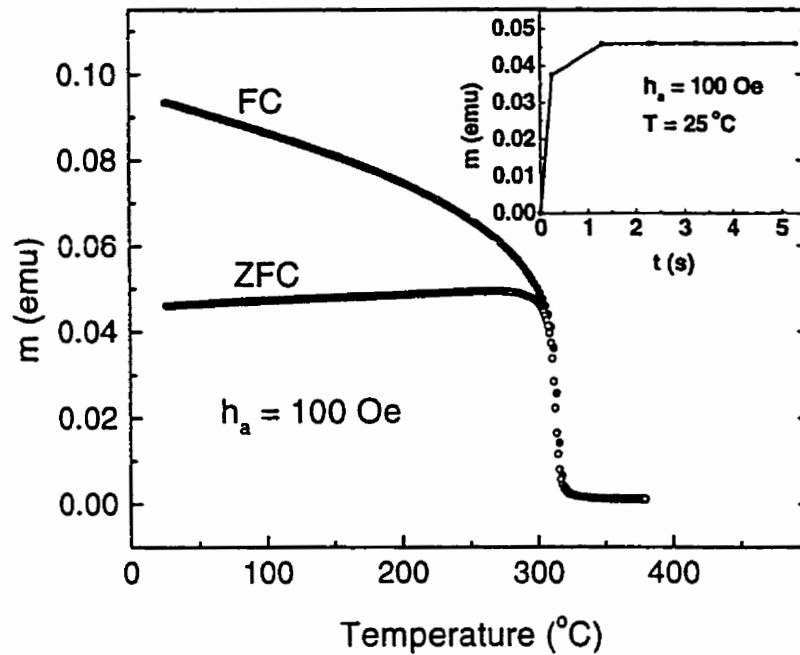


Figure 5.46 . The temperature dependence of the field cooled (FC) and zero field cooled (ZFC) moment of  $\text{Nd}_2\text{Fe}_{14}\text{B}$  measured in an applied field . The inset shows the time dependence of the moment for after zero field cooling from  $T = 380^\circ\text{C}$  to  $20^\circ\text{C}$  and then applying a “step function” excitation. The field ramping time was  $\approx 0.5\text{s}$ , so the true viscous thermal relaxation component corresponds to about 10% of the total response.

surface or grain boundary. A hard initial response with similar (forward) magnetizing and demagnetizing coercive fields, is characteristic of coherent rotation, as in  $\text{CrO}_2$  or of bulk wall pinning, in which moment reversal is accomplished by forcing the domain wall through a homogeneous dispersion of defects with a magnetic field. (The magnetizing, or forward, coercive field is defined as the positive field at which most of the particles have been flipped into the up-moment state.)

Figure 5.47 summarizes the essential features of the field and temperature dependence of the  $\text{Nd}_2\text{Fe}_{14}\text{B}$  sample. The figure shows one representative initial magnetization curve at  $T = 40^\circ\text{C}$ , and six complete sets of magnetizing and demagnetizing remanences for  $T = 40^\circ\text{C}$ ,  $60^\circ\text{C}$ ,  $80^\circ\text{C}$ ,  $100^\circ\text{C}$ ,  $140^\circ\text{C}$ , and  $180^\circ\text{C}$ . For this system, the initial response is almost ideally soft and saturation is virtually complete in applied fields of a few kOes, indicating the presence of domain walls which are nearly free to move within the grains. For applied fields in excess of about 4 kOe, the remanence increases significantly as the domain walls are pinned at the grain boundaries. This magnetizing process is characterized by a forward coercive field of about 6 kOe and by a distribution of “switching fields” (roughly given by the shape of the magnetizing remanence  $di_m/dh_a$  (Section 5.1.3)) that is only weakly temperature dependent. By contrast, changes in temperature have a dramatic affect on the field dependence of the demagnetizing isotherms in Figure 5.47. Near room temperature the remanent coercive field is much larger than the forward coercivity suggesting that reversal processes in  $\text{Nd}_2\text{Fe}_{14}\text{B}$  are dominated by wall nucleation, as discussed above. The remanent coercivity collapses rapidly, and the demagnetizing isotherms develop structure along the negative

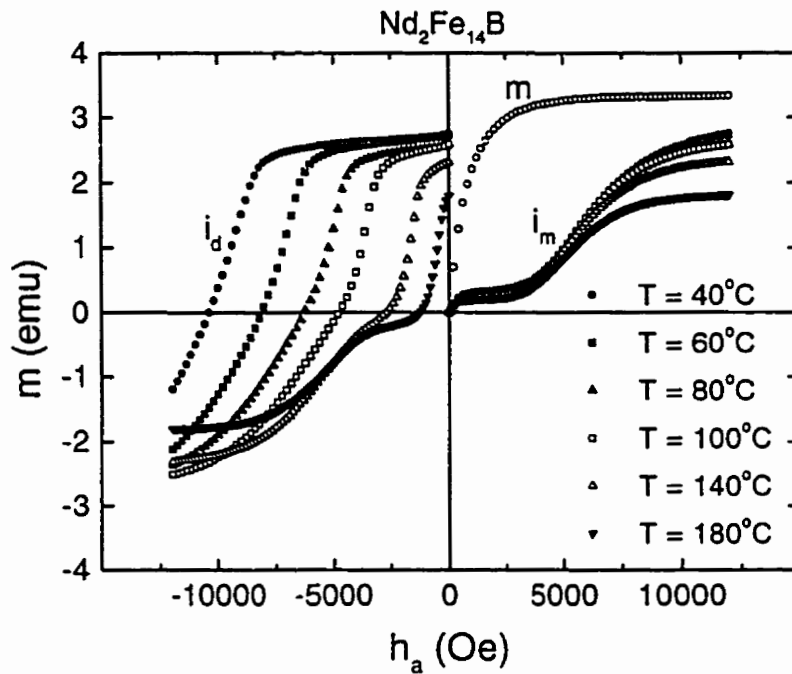


Figure 5.47 . Field and temperature dependence of  $\text{Nd}_2\text{Fe}_{14}\text{B}$ . One representative initial magnetization curve ( $m$ ) is given at  $T = 40^\circ\text{C}$  and six sets of magnetizing ( $i_m$ ) and demagnetizing ( $i_d$ ) remanences.

branch ( $i_d < 0$ ) that gradually assumes more and more of the characteristics of the initial magnetizing process, but inverted through the origin. This trend towards inversion symmetry is particularly clear for temperatures  $T \geq 140^\circ\text{C}$ . The curvature of the Henkel plots,  $i_d/i_\infty$  versus  $i_m/i_\infty$ , also changes systematically with temperature, from almost perfectly magnetizing-like behaviour at room temperature to almost perfectly demagnetizing-like character at temperatures above about  $140^\circ\text{C}$ , as shown in Figure 5.48.

Although conventional applications of the Preisach model to other permanent magnetic materials with similar characteristics postulate that long range, ferromagnetic interactions ( $k > 0$ ) between the particles are responsible for the magnetizing-like curvature of the Henkel plots at room temperature (Basso & Bertotti, 1994), this study of the temperature dependence of  $\text{Nd}_2\text{Fe}_{14}\text{B}$  suggests a very different mechanism. Figure 5.49 shows a proposed revision of the elementary Preisach loop that contains the essential elements needed to reproduce all of the experimental systematics described above.

Figures 5.50 and 5.51 illustrate the physical processes which are relevant to the various branches of the elementary loop, and their equivalent Preisach representations. Each grain of  $\text{Nd}_2\text{Fe}_{14}\text{B}$  is assumed to contain two equal and opposite magnetic domains in the thermally demagnetized state. In zero field ( $h_a = 0$ ), these two domains are represented by two Preisach pseudoparticles, one occupying the state  $\varphi = +1$  and the other occupying the state  $\varphi = -1$ , which are illustrated schematically in Figure 5.50a. During the magnetizing process ( $h_a > 0$ ), the initial wall motion is described by a reversible nonlinearity

$$\varphi_{\text{rev}} = 1 - \exp(-\Gamma h_a), \text{ which simulates the reversible rotation of the Preisach}$$

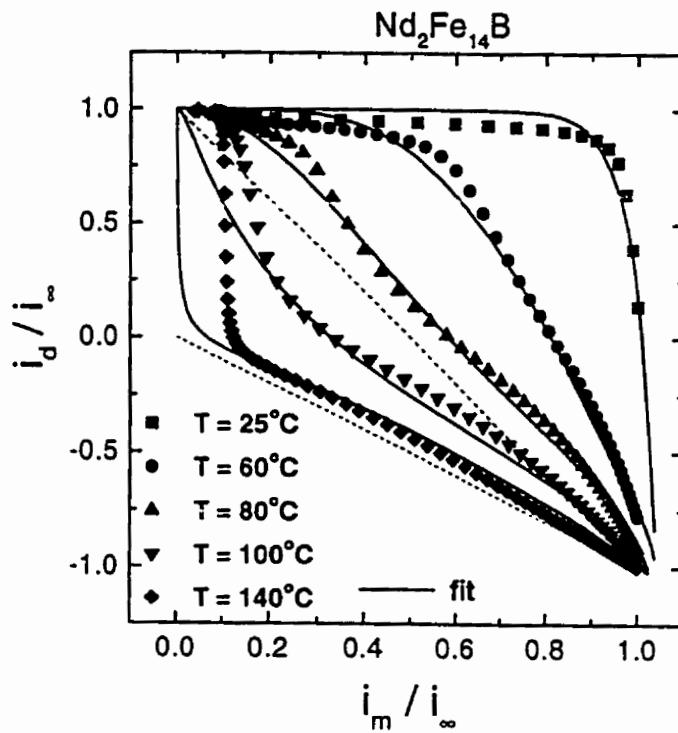


Figure 5.48 . Henkel plots for  $\text{Nd}_2\text{Fe}_{14}\text{B}$  which exhibit a systematic change of curvature with temperature from nearly perfectly magnetizing-like behaviour at  $T = 25^\circ\text{C}$  to almost perfectly demagnetizing-like character for  $T > 140^\circ\text{C}$ .

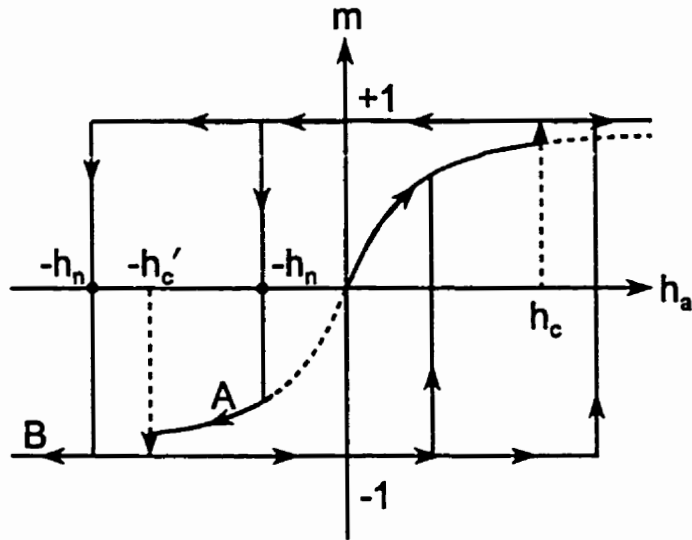
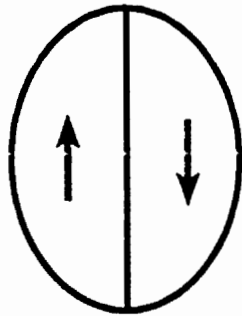


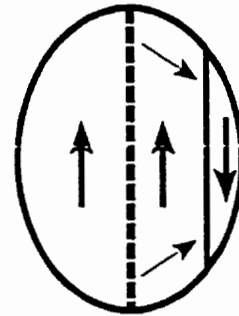
Figure 5.49 . Modified elementary Preisach loop. The relative magnitudes of the nucleation ( $h_n$ ) and demagnetizing coercive ( $h'_c$ ) fields determine the demagnetization path followed. If  $|h_n| < |h'_c|$  the particle will behave reversibly (path A) and if  $|h_n| > |h'_c|$  then irreversible switching occurs (path B). If the particle coercivity is zero, it behaves completely reversible.

**Nd<sub>2</sub>Fe<sub>14</sub>B PARTICLE  
DOMAIN STRUCTURE**



$h_a = 0$

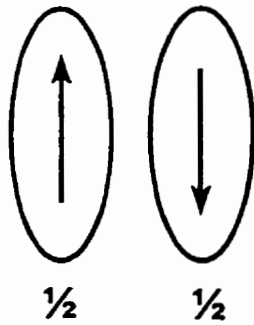
**THERMALLY DEMAGNETIZED**



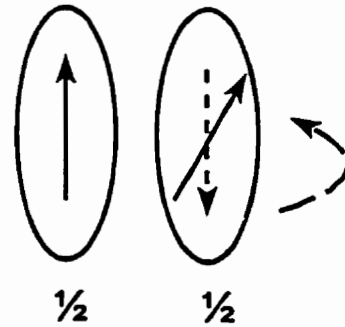
$h_a = h_c > 0$

**WALL PINNING**

**EQUIVALENT PREISACH  
PSEUDOPARTICLES**



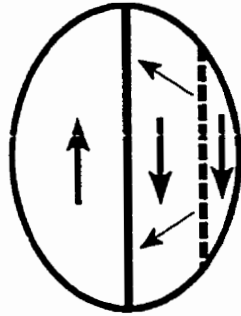
(a)



(b)

Figure 5.50 . The magnetizing process by wall motion described in terms of a pair of Preisach pseudoparticles. The curved arrow in (b) represents the reversible rotation of the Preisach pseudoparticle.

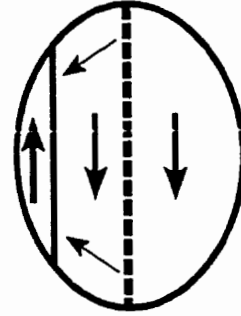
**Nd<sub>2</sub>Fe<sub>14</sub>B PARTICLE  
DOMAIN STRUCTURE**



**STAGE 1: WALL NUCLEATION**

$$h_a = -h_n < 0$$

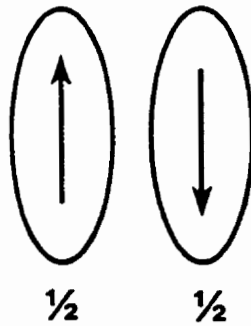
$$-h_c' < h_a < 0$$



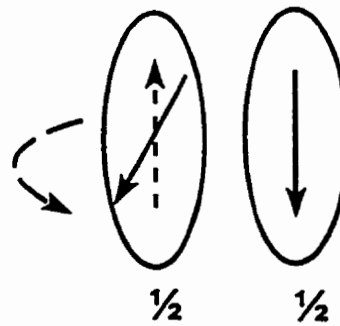
**STAGE 2: WALL PINNING**

$$h_a = -h_c' < 0$$

**EQUIVALENT PREISACH  
PSEUDOPARTICLES**



(a)



(b)

Figure 5.51 . The demagnetizing process by wall motion described in terms of a pair of Preisach pseudoparticles. The curved arrow in (b) represents the reversible rotation of the Preisach pseudoparticle.

pseudoparticle in the  $\varphi = -1$  state. Wall pinning occurs when the applied field  $h_a$  exceeds a forward coercive field  $h_c$ , and flips the  $\varphi = -1$  pseudoparticle up, thus creating a remanence, as shown in Figure 5.50b. In the modified Preisach loop (Figure 5.49) this process includes the initial magnetizing curve and the Barkhausen jump at  $h_c$ .

Demagnetization proceeds sequentially, in two stages, as shown in Figure 5.51. The first stage is characterized by a nucleation field  $h_n$ , which reintroduces the domain wall into the particle and reestablishes the original random configuration (Figure 5.51a). This corresponds to the vertical transition at  $h_a = -h_n$ , from  $m = +1$  to  $m = 0$ , in Figure 5.49.

The second stage is initiated when the magnitude of the reverse applied field  $|h_a|$  exceeds  $h_n$  (Figure 5.51a). The particle then retraces the initial magnetizing process, but in the negative sense and perhaps with a different pinning field  $-h_c'$ , and will behave either reversibly (path A in Figure 5.49) if  $h_n < h_c'$  or irreversibly (path B in Figure 5.49) if  $h_n > h_c'$ . If an interaction field  $h_i$  is also present, irreversible "switching" occurs at  $\alpha = h_c - h_i$  in the forward direction and  $\beta = -h_c' - h_i$  in the reverse direction.

This model has been used to calculate the magnetic response of an ensemble of interacting pseudoparticles (Mitchler, Roshko & Dahlberg, 1999). The Preisach distribution for the initial magnetizing process, starting from the thermal random state, was assumed to be

$$p(h_c, h_i) = (2\pi h_c \sigma_c \sigma_i)^{-1} \exp[-(\log(h_c/\tilde{h}_c))^2/2\sigma_c^2] \cdot \exp(-h_i^2/2\sigma_i^2).$$

Particles with  $\alpha \leq h_a$  are magnetized using the standard Preisach construction for a random initial state (Mitchler, Dahlberg, Engle & Roshko, 1995), while those with  $\alpha > h_a$  contribute a purely reversible response. Demagnetization was accomplished by assuming

a log-normal distribution of nucleation fields

$$g(h_n) = (2\pi h_n^2 \sigma_n^2)^{-1/2} \exp[-\log(h_n/\tilde{h}_n)^2/2\sigma_n^2],$$

and calculating the fraction of Preisach pseudoparticles  $f = \int_0^{|h_a|} g(h_n) dh_n$  that have nucleated a wall and have returned to their original random demagnetized state in a given negative applied field  $-h_a$ , and the fraction  $1 - f$  that remain “trapped” in their positive saturation remanence state. The fraction  $f$  of nucleation-demagnetized particles are then remagnetized using the standard Preisach construction for negative applied fields  $-h_a$ , assuming a random initial state and a Preisach distribution of the form

$$p'(h_c', h_i) = (2\pi h_c' \sigma_c' \sigma_i')^{-1} \exp[-\log(h_c'/\tilde{h}_c')^2/2\sigma_c'^2] \cdot \exp(-h_i'^2/2\sigma_i'^2).$$

Figure 5.52 shows a comparison of the measured response (discrete points) and the calculated response (solid curves) at  $T = 140^\circ\text{C}$ , where the two demagnetizing stages are reasonably well differentiated, and Figure 5.48 compares the measured and calculated Henkel plots over a wide range of temperatures. The best fit distribution parameters are listed in Table 5.9. (The calculated magnetization and remanence curves for other temperatures are included in Appendix 1, Figure A1.20.)

Aside from a systematic discrepancy at low positive fields, which is due to the neglect of homogeneous bulk wall pinning during the early stages of the magnetizing process, the model provides an excellent description of the experimental *systematics*. The fits show that the observed behaviour of  $\text{Nd}_2\text{Fe}_{14}\text{B}$  is indeed consistent with the two-stage demagnetizing process proposed above, and that the collapse of the coercivity and the systematic change in the curvature of the Henkel plots originate primarily from the *temperature dependence of the energy barriers  $h_n$  that block the nucleation or unpinning*

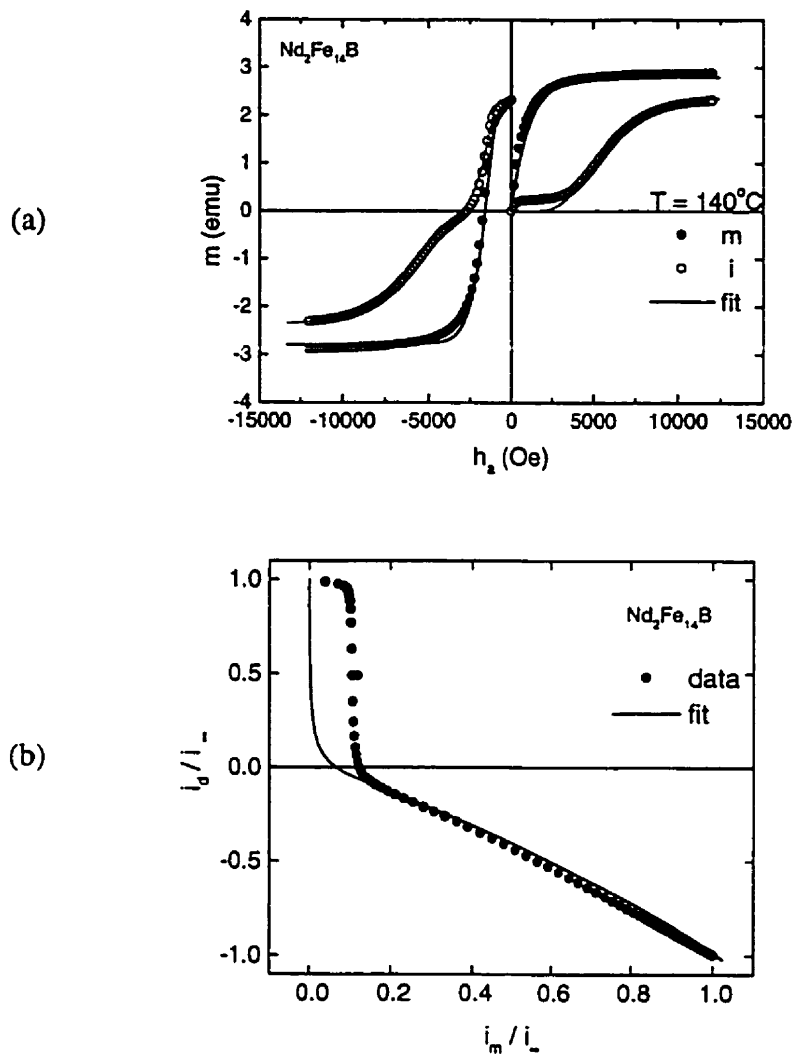


Figure 5.52 . (a) A comparison of the measured response (discrete points) of  $\text{Nd}_2\text{Fe}_{14}\text{B}$  and the calculated response (solid curves) at  $T = 140^\circ\text{C}$ .

Table 5.9 . Best fit Preisach distribution parameters for Nd<sub>2</sub>Fe<sub>14</sub>B.

T (°C)	$\tilde{h}_c$ (Oe)	$\sigma_c$	$\tilde{h}_n$ (Oe)	$\sigma_n$	$\tilde{h}'_c$ (Oe)	$\sigma'_c$	$\sigma_i$ (Oe)
25	6000	0.40	12000	0.18	10800	0.40	600
60	6000	0.40	7200	0.20	9600	0.40	600
80	6000	0.35	5400	0.22	8160	0.35	600
100	6000	0.35	3900	0.25	7170	0.35	600
140	5500	0.35	1650	0.35	5775	0.35	550

The magnetizing or forward coercive field distribution parameters are given by  $\tilde{h}_c$  and  $\sigma_c$  while the demagnetizing coercive field distribution parameters are given by the primed quantities. The nucleation field distribution is described by  $\tilde{h}_n$  and  $\sigma_n$ .

*of reverse domains*, with no detectable contribution from long range, mean field-like interactions, neither positive nor negative. At room temperature, these nucleation barriers are large enough to *mask* the presence of the pinning barriers  $h_c'$  along the demagnetizing branch, and the Henkel plot has the *apparent* characteristics of a Preisach system with a single coercive field distribution and with a ferromagnetic mean field coupling between the particles. However, as the temperature increases and the nucleation barriers collapse, the pinning barriers  $h_c'$  gradually emerge and begin to influence the character of the demagnetizing remanence and the shape of the Henkel plots. At higher temperatures, the two sets of pinning barriers  $h_c'$  and  $h_c$  converge, as shown in Table 5.9, producing Henkel plots with almost perfectly demagnetizing-like curvature.

**Notes:**

1. The discussion in Section 5.5.1 appears modified in Mitchler, Roshko, Dahlberg & Moskowitz, 1999, p. 2033-2034.
2. The discussion in Section 5.5.2 appears modified in Mitchler, Roshko, Dahlberg & Moskowitz, 1999, p. 2034-2036.
3. The discussion in Section 5.5.3 appears modified in Mitchler, Roshko, Dahlberg & Moskowitz, 1999, p. 2036-2037.
4. The discussion in Section 5.6.1 appears modified in Mitchler, Roshko, Dahlberg & Moskowitz, 1999, p. 2037.
5. The discussion in Section 5.6.2 appears in Mitchler, Roshko, Dahlberg & Moskowitz, 1999, p. 2037-2040.
6. Portions of the discussion in Section 5.7.2 appear in Mitchler, Roshko & Dahlberg, 1999, p. 4386-4387.

## Chapter 6

# A Critical Appraisal of the Preisach

## Approach

Magnetic hysteresis is ultimately a consequence of the multiplicity of long-lived metastable states available to magnetic systems in their free energy landscape. A *fundamental* description of hysteresis should thus invoke principles of non-equilibrium statistical mechanics and thermodynamics. At present, no such comprehensive theory exists, and consequently, phenomenological approaches, of which the Preisach model is one, are employed.

Any attempt to model hysteresis must clearly incorporate some description of the multi-valley structure of configuration space and some mechanism to drive the system from one local minimum to another. Such descriptions of hysteresis necessarily include approximations. If we restrict the treatment to zero temperature, then the system remains

fixed in its initial state, provided that no external influences act on it. The application of an external magnetic field will deform the zero-field landscape until the valley currently occupied by the system is obliterated, and the system abruptly drops into another accessible state. This sudden change of state is known as a Barkhausen jump. The Preisach model replicates this complex process by assuming that all magnetic systems can be decomposed into an ensemble of two-level subsystems, each of which satisfies the *minimum* requirements to exhibit hysteresis. Each subsystem is characterized by two metastable states and by two generally unequal energy barriers, which represent the excitation energies required to activate transitions between the states. Equivalently, each subsystem may be characterized by a coercive field, which is related to the average barrier, and an asymmetry (interaction) field, which is related to the difference between the two barriers. The application of an external field distorts the double well configuration by elevating one minimum and depressing the other, thus yielding an elementary rectangular response function with two Barkhausen instabilities. In general, the time required to complete a Barkhausen jump is assumed to be negligibly small, and such an approximation describes rate-independent hysteresis, since field variations on the time scale of the jump are ignored.

A generalized version of the scalar Preisach model, based on a physical picture of thermally activated two-level subsystems, eases the restrictions of the zero-temperature approximation. The actions of the external field and thermal fluctuations operate on the same free energy profile, and the barriers to transition are assumed to be the same as those in the zero-temperature approach. Including thermal activation over these energy

barriers means that hysteresis is rate-dependent, since the mechanism responsible for exciting over-barrier transitions is dependent on the time spent in a local energy minimum. In the generalized Preisach model, relaxation over barriers occurs at a rate of  $\tau_0^{-1} \exp\left[\frac{-W}{k_B T}\right]$  where  $W$  is the barrier height and  $\tau_0^{-1}$  is a microscopic attempt frequency.

Unlike many other approaches to hysteresis, the Preisach model includes an explicit treatment of interactions. Random local interactions, due to fluctuations in the local environments of the subsystems, are incorporated through a distribution of interaction fields, symmetric about zero field, which shift of the centres of the elementary loops away from  $h_a = 0$ . These non-zero local interactions produce an energy profile with two *non-degenerate* local energy minima. Long range interactions, or mean field effects, which describe the presence of long-range ordered magnetic structures, are replicated in the moving Preisach model, by the parameter  $k$ , which shifts the interaction field distribution  $g(h_i)$  in proportion to the instantaneous magnetization  $m$  of the system,

$$g(h_i) \rightarrow g(h_i - km).$$

The Preisach model is remarkably successful in its description of both particulate and continuous magnetic media. An impressive amount of very detailed information regarding the structure of the ground state, achieved by various demagnetization procedures, the nature of interactions within the material, and the physical origin of changes in the magnetic response as a function of temperature can be gleaned from a scalar Preisach treatment of experimental data.

With respect to the influences of the initial demagnetization procedure on the structure of the ground state, our analysis revealed that for superparamagnetic systems

like magnetoferritin, in which the response is dominated by thermal activation effects, thermal demagnetization yields *highly asymmetric* subsystem level populations, reminiscent of occupation probabilities associated with *ac* demagnetization. By contrast, for ferromagnetics like  $\text{CrO}_2$  and  $\text{Nd}_2\text{Fe}_{14}\text{B}$ , the same thermal demagnetization procedure produced a *random* initial state, with equal level populations.

Similarly, the role of thermal relaxation in the temperature dependence of a magnetic system's hysteretic properties, can be revealed through a Preisach analysis. Thus, the simulations performed in the study of the  $\text{CrO}_2$  recording medium showed that the explicit temperature dependence of the free energy landscape is primarily responsible for shaping the magnetic response. Thermal activation is essentially "frozen out" in the  $\text{CrO}_2$  system at virtually all temperatures below the ferromagnetic Curie temperature  $T_C$ , so that changes in hysteresis with temperature are due almost exclusively to *changes in the free energy landscape*, as reflected in the temperature dependence of  $\bar{\mu}$ ,  $h_c$ , and  $h_i$ . By contrast, the magnetoferritin data can be modeled by a temperature independent system of moments relaxing by thermal activation over a *temperature independent system of energy barriers*, so that changes in hysteresis with temperature are related almost exclusively to changes in the relative populations of blocked and unblocked pseudoparticles. As for  $\text{CrO}_2$ , the temperature dependence of hysteresis in  $\text{Nd}_2\text{Fe}_{14}\text{B}$  is almost entirely due to changes in the free energy landscape. In this case, it is the barriers for nucleation of reverse domains that collapse as temperature increases. Thermal relaxation processes in the hard disk and floppy disk media play a minimal role in shaping their hysteretic properties, as expected for media utilized in information storage

and retrieval applications at ambient temperatures.

Determining the nature of interaction effects in magnetic materials is of great importance, and considerable insight can be gained by applying a Preisach analysis to experimental remanence data, particularly over a range of temperatures. Comparison of the parameter values resulting from the analysis of  $\text{CrO}_2$  audio tape data for both thermal and ac initially demagnetized states, over a 400 degree temperature range, indicated an absence of long range mean field-like interactions in this particulate system. The origin of the strong temperature dependence of the Henkel plots of thermally demagnetized  $\text{Nd}_2\text{Fe}_{14}\text{B}$  would be impossible to interpret based on an examination of their curvature, which shows apparently strong magnetizing-like curvature at low temperatures and equally strong demagnetizing-like characteristics at high temperatures. Although a traditional Henkel plot analysis would explain these curvatures by long range interactions corresponding to positive and negative values of  $k$ , respectively, the modification of the elementary Preisach loop, to account for reversibility in domain wall motion and the possibility of a field-history dependent coercive field distribution, clearly demonstrates that for this permanent magnet, the radical changes in Henkel plot curvature can be described by a single mean field parameter,  $k = 0$ . Temperature does not change the nature of the long-range interactions, which are absent in this system, and only slightly affects random local interactions, but temperature strongly affects the nucleation field distribution. By contrast, the positive curvature in the Henkel plots of remanence data from the ac demagnetized sample of longitudinal CoCr-based hard disk is undeniably a consequence of positive mean field interactions ( $k > 0$ ), since under ac demagnetized

conditions negative curvature of the Henkel plot is expected both in the absence of long-range interactions, and of course, for negative interactions.

For experiments performed at a single temperature, conclusions based on a Preisach analysis are limited. However, the Preisach analyses performed on the computer memory media including floppy disk, and longitudinal and perpendicular CoCr-based hard disk materials demonstrate the significance of the mean field parameter in assessing interactions present in magnetic systems. For the sample of commercial floppy disk, better treated with a log-normal distribution of coercive fields, possibly due to the random orientation of the constituent magnetic particles in the film, the value of the mean field parameter was  $k = 0$ . There are no long range interactions. Only random local weak interactions between particles are present, as implied by the relatively narrow distribution of interaction fields. The best description of the data obtained from the CoCr-based hard disk whose magnetic particles were longitudinally oriented required  $k > 0$ , and this is interpreted as evidence of magnetizing-like, or “ferromagnetic” interactions in the initially ac demagnetized sample. This interpretation is supported by the observed propagation of magnetic reversal along chains of particles in the material. The CoCr-based perpendicular media exhibited strong demagnetizing-like interactions, in the Henkel plot of its remanence data and the negative value of  $k$  required to describe the data is mainly due to its shape demagnetization factor.

Although the Preisach analysis of real magnetic systems has proved to be remarkably fruitful, the current Preisach model has inherent limitations and the following discussion explores these issues and provides proposals for generalizing and improving

the formalism.

Reversible processes such as moment rotation and elastic distortion of domain structure are *not* well described within the Preisach formalism. In this discussion, reversibility is treated phenomenologically. The magnetic response is considered to be the superposition of two contributions, one being the irreversible Preisach component, and the other being a reversible function. Considered together these responses yield a distorted Preisach elementary loop unlike any derived from specific models, like the Stoner-Wohlfarth model (Figure 3.17). As suggested by Bertotti (1998), reversible processes can be modeled by adding a second integral over a distinct distribution localized along the  $h_c = 0$  axis and representing large populations of quasi-reversible particles with negligible coercive field barriers. Vajda and Della Torre (1991) offer a more realistic approach, by including reversible branches in the elementary loop itself, resulting in Stoner-Wohlfarth-like cycles. This approach is computationally intensive and although it provides a more physical description of orientational effects and reversibility, it lacks the simplicity inherent in the “additive” method employed here.

The role of temperature in thermally activated transitions is not explicit in the generalized Preisach model, as presented here, in the sense that temperature appears only indirectly through the effective thermal parameter  $h_T^* = \frac{k_B T \ln(t/\tau)}{\mu}$ . However, to treat temperature as an explicit input parameter it is necessary to know the particle moments and the temperature dependence of the spontaneous moment. In fact, a distribution of particle moments is required to describe an ensemble of particles which vary in size and/or composition. Incorporating yet another distribution into the model further

increases the computational challenge, since a distribution of particle moments implies the existence of a corresponding distribution of thermal parameters  $h_T^*$ . Each value of the particle moment yields a different set of thermal activation boundaries in the Preisach plane, and must be treated separately. Nevertheless, the generalization is currently being attempted (Roshko & Song, unpublished).

The Preisach calculations presented here do not treat thermal equilibrium properly. When thermal energy is sufficient to overcome both subsystem energy barriers, the moments  $\pm\mu$  of the pseudoparticles should be replaced by hyperbolic tangent functions  $\varphi = \mu \tanh[\mu(h_a + h_i)/k_B T]$ . These details are particularly essential for describing FC and ZFC response functions and are now being implemented in recent Preisach calculations (Song & Roshko, 2000a).

Critical effects, also absent from this theoretical treatment, are also being explored by Song and Roshko (2000b), in order to model not only the temperature dependence of the hysteresis loop, but also of the field cooled and the zero field cooled moments. This is an essential ingredient for the analysis of materials that have a critical temperature within the experimentally accessible range, since the moment of the system must go to zero at its Curie temperature. The temperature dependence of the spontaneous moment can be modeled approximately as  $\mu = \mu_0 \left(1 - \frac{T}{T_c}\right)^\Gamma$  where  $\Gamma$  is a power that represents a critical exponent (typically  $\Gamma \sim 1/3$  for magnets). The distributions of coercive fields and interaction fields also exhibit critical behaviour, and must collapse into delta functions  $T \rightarrow T_c$  since  $h_c$  and  $h_i$  both depend more or less directly on  $\mu$ . These parameters can be described by similar functional forms with respect to temperature, but they may require

different values of the critical exponent  $\Gamma$ .

Within the standard formulation of the Preisach model, the anisotropy barrier heights are considered fixed under the application of a magnetic field  $h_a$ . However, according to the Stoner-Wohlfarth theory of coherent rotation in uniaxial single domain particles, the intrinsic energy barrier  $E_A$  varies as  $E_A = \frac{h_c}{2} \left[ 1 + \left( \frac{h_a}{h_c} \right)^2 \right]$  and grows from  $\frac{h_c}{2}$  in zero applied field to a maximum of  $h_c$  at  $h_a = h_c$ . In the Preisach model, the barrier is fixed at this maximum value. So, our calculations actually underestimate the role of thermal fluctuations in producing transitions. Song and Roshko (2000a) have shown that in the absence of interactions ( $\sigma_i = 0$ ) the effect of field dependent anisotropy barriers is equivalent to replacing  $h_T^*$  by  $\tilde{h}_T^* = h_T^* + \sqrt{(h_a + h_T^*)^2 - h_a^2}$ . The field dependence of anisotropy barriers is considered explicitly in some Preisach-based approaches to superparamagnetism (Stancu & Spinu, 1998 and Spinu & Stancu, 1998).

The properties of the Preisach distribution are difficult to match to specific elements of the microstructures of magnetic systems, and for some investigators, this characteristic limits the appeal of the Preisach approach. The selection of the Preisach distribution in this investigation can be justified by the approach of Cornejo, Lo Bue, Basso, Bertotti and Missell (1997). They calculated the functional form of the distribution from experimental data, by measuring minor hysteresis loops. The Preisach distribution is then given by the *second derivative* of the response with respect to the effective field and the peak field attained in the minor loop. This approach is further complicated by the fact that the effective field and the applied field are not the same when mean field contributions are present. Furthermore, when such a procedure is performed

experimentally, the resulting distributions are rather noisy. The experimentally determined distributions are then replaced with smooth analytic functions of similar form. Cornejo et al employed a log-normal function for the coercive field distribution and a Gaussian interaction field distribution in the Preisach analysis. The analysis of the magnetic systems presented in this thesis concentrated on the determination of *general* relationships and experimental systematics, and thus the particular form of the Preisach distribution was selected based on the characteristics of the remanence data, and not explicitly determined by the procedure described above.

The Preisach distribution used to describe an ensemble of particles also obscures specific characteristics of the pseudoparticle population. The particle moments are fixed by the standard Preisach treatment and the number of particles described by the same elementary loop is given by the Preisach distribution. Particles with identical coercive and interaction fields  $(h_c, h_i)$ , but of different moment (loop height)  $\mu(h_c, h_i)$  are not distinguished by different distributions, but are instead all folded into a single Preisach distribution. Also, for non-aligned systems, the coercive distribution itself must consist of a convolution of an anisotropy distribution for the Preisach pseudoparticles and the angular distribution of their moments (Section 5.6.2). Separating these distributions is not straightforward.

The standard Preisach model is obviously limited by its scalar nature. Vector models exist to describe the angular dispersion of moments in a magnetic system and they can include a superposition of scalar models oriented along different directions or they may employ an astroid in place of the elementary loop adopted in scalar treatments.

Orientational effects have recently been incorporated into the scalar Preisach formalism (Stancu & Spinu, 1998), but these rely on specific models like the Stoner-Wohlfarth model of coherent rotation and, as such, lack the flexibility to describe real systems, where reversal mechanisms are seldom Stoner-Wohlfarth like.

# Appendix 1

## Additional Data and Fits

CrO <sub>2</sub> ac demagnetized data and fits ( $25^{\circ}\text{C} \leq T \leq 120^{\circ}\text{C}$ )	Figures A1.1 to A1.6
CrO <sub>2</sub> comparison of ac and thermally demagnetized data ( $25^{\circ}\text{C} \leq T \leq 120^{\circ}\text{C}$ )	Figures A1.7 to A1.9
CrO <sub>2</sub> ac demagnetized comparison of data with fits using $k = 0$ and $k < 0$ ( $25^{\circ}\text{C} \leq T \leq 120^{\circ}\text{C}$ )	Figures A1.10 to A1.12
CrO <sub>2</sub> ac demagnetized data and fits ( $10\text{ K} \leq T \leq 300\text{ K}$ )	Figures A1.13 to A1.15
CrO <sub>2</sub> thermally demagnetized data, comparison of fits with occupation probabilities $w = \frac{1}{2}$ and $w \neq \frac{1}{2}$ ( $10\text{ K} \leq T \leq 300\text{ K}$ )	Figures A1.16 to A1.19
Nd <sub>2</sub> Fe <sub>14</sub> B fits to magnetization and remanence data	Figure A1.20

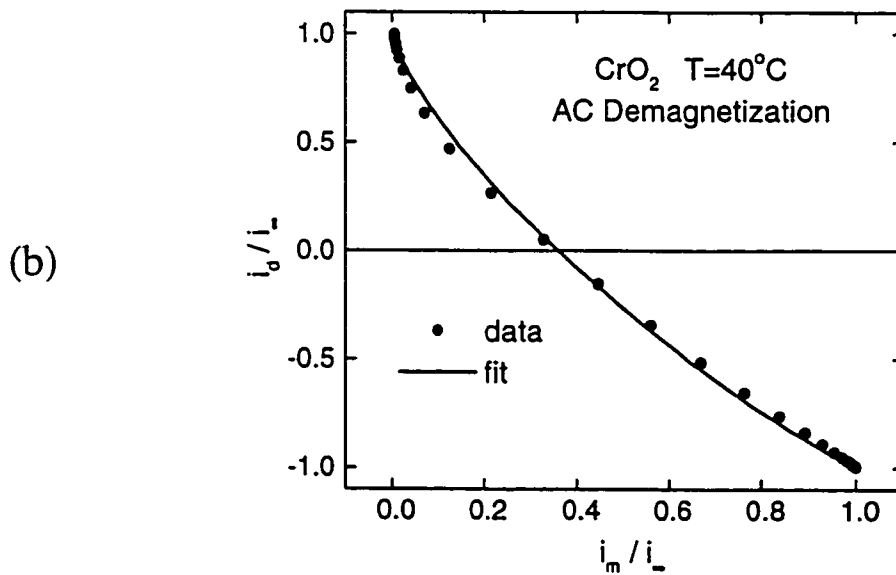
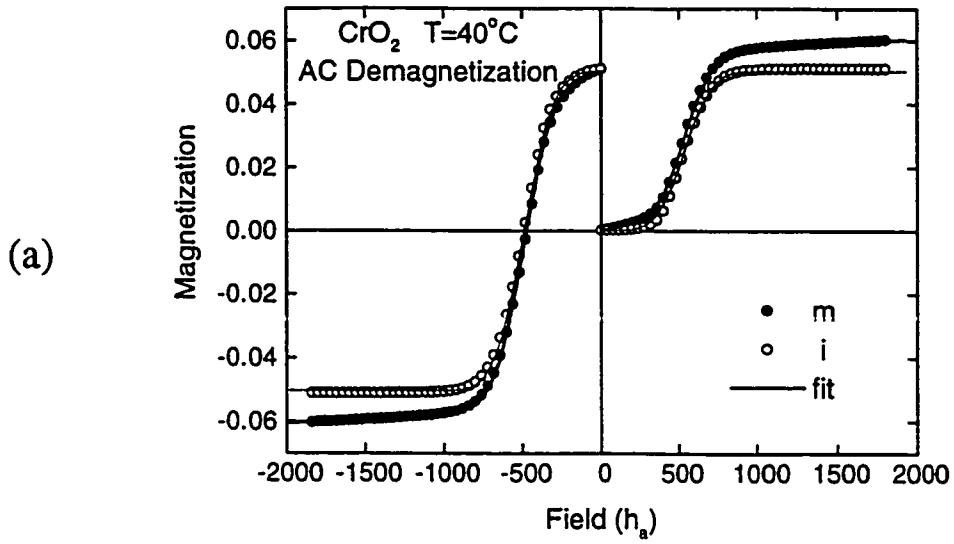


Figure A1.1 . Data and fits for CrO<sub>2</sub> audio tape at T = 40°C. (a) Magnetizing and demagnetizing curves, m, and the corresponding magnetizing and demagnetizing remanences, i. (b) Henkel plots constructed from remanences in (a).

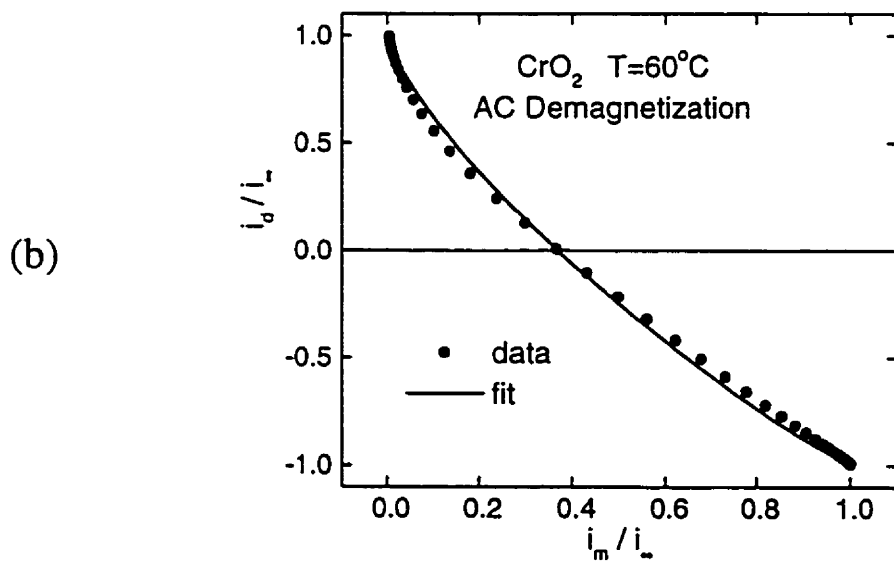
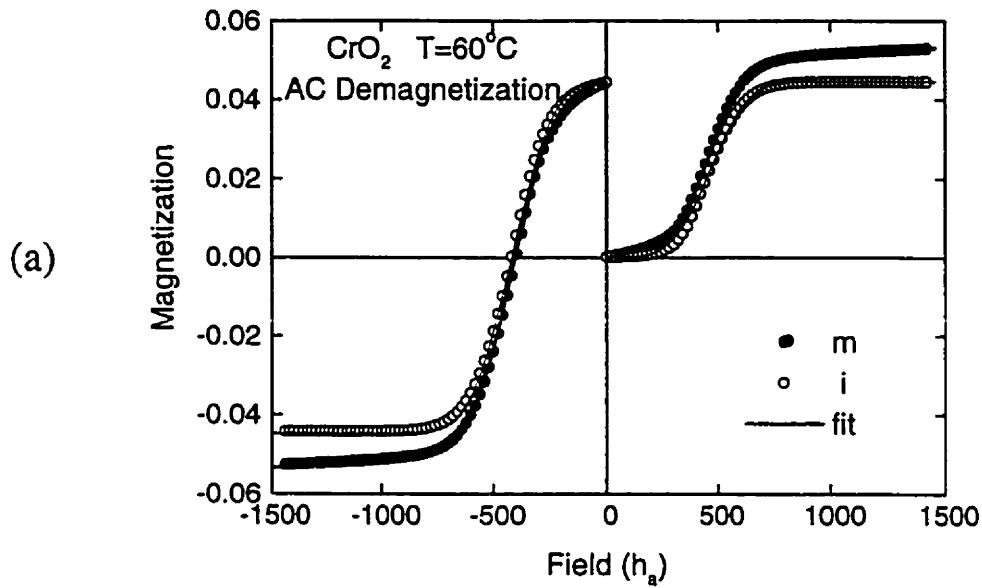


Figure A1.2 . Data and fits for CrO<sub>2</sub> audio tape at T = 60°C. (a) Magnetizing and demagnetizing curves, m, and the corresponding magnetizing and demagnetizing remanences, i. (b) Henkel plots constructed from remanences in (a).

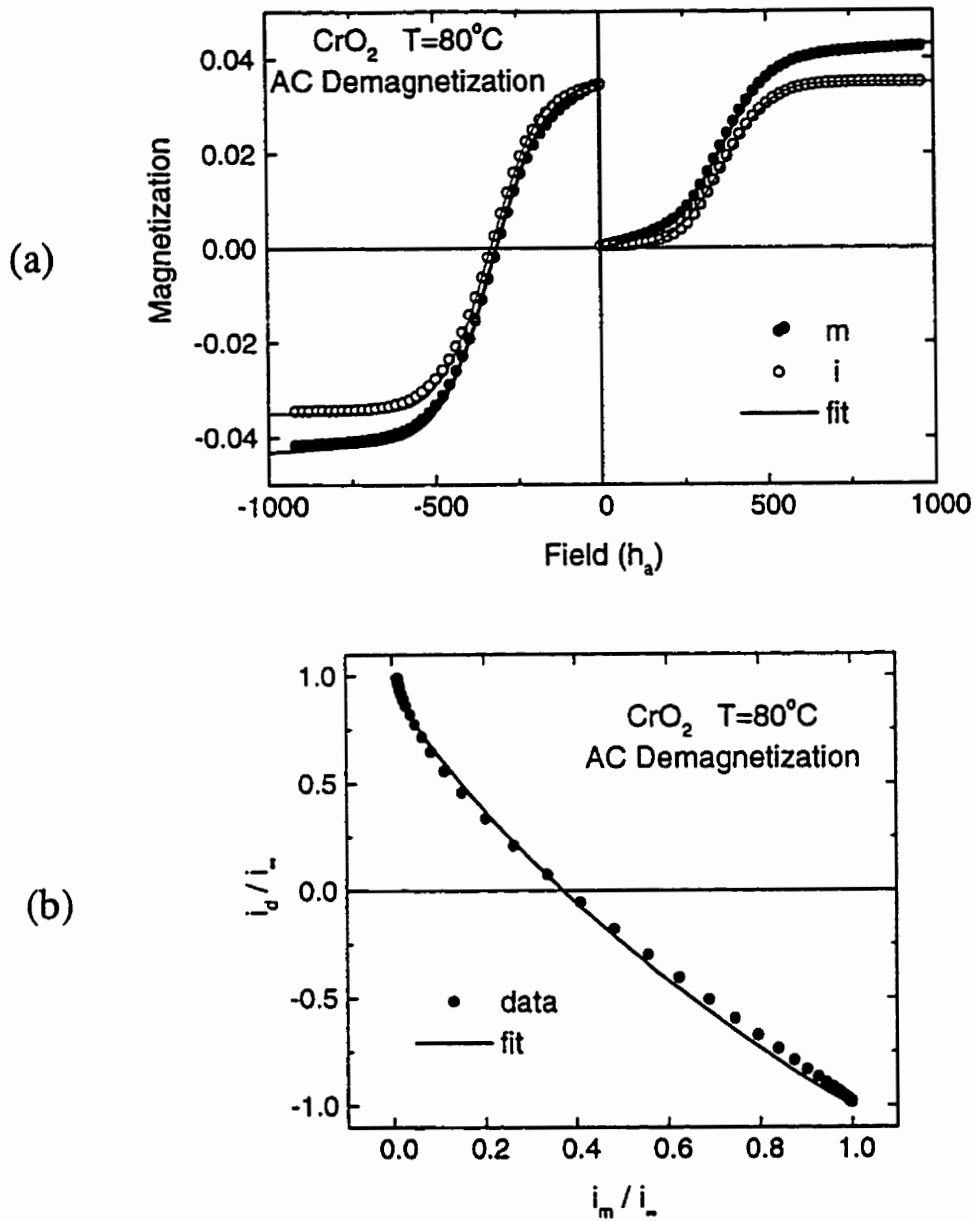


Figure A1.3 . Data and fits for CrO<sub>2</sub> audio tape at T = 80°C. (a) Magnetizing and demagnetizing curves, m, and the corresponding magnetizing and demagnetizing remanences, i. (b) Henkel plots constructed from remanences in (a).

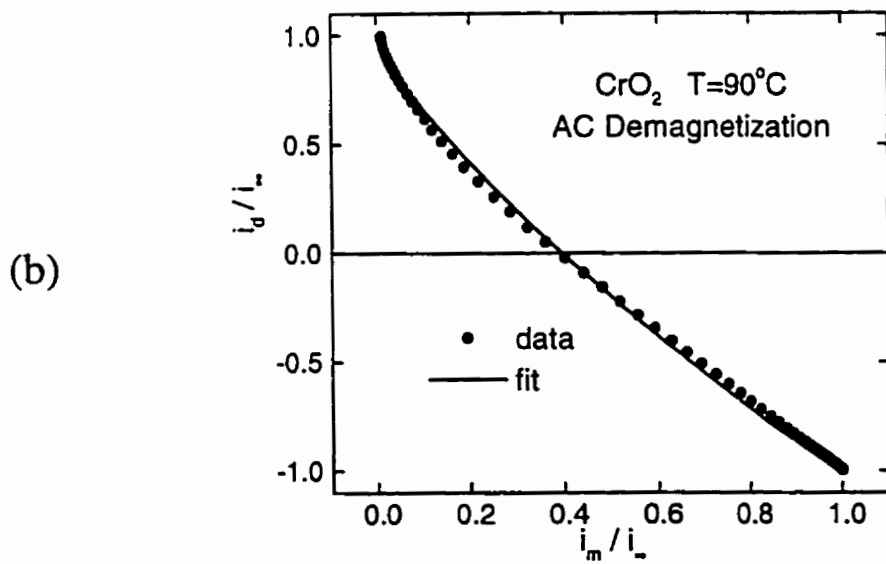
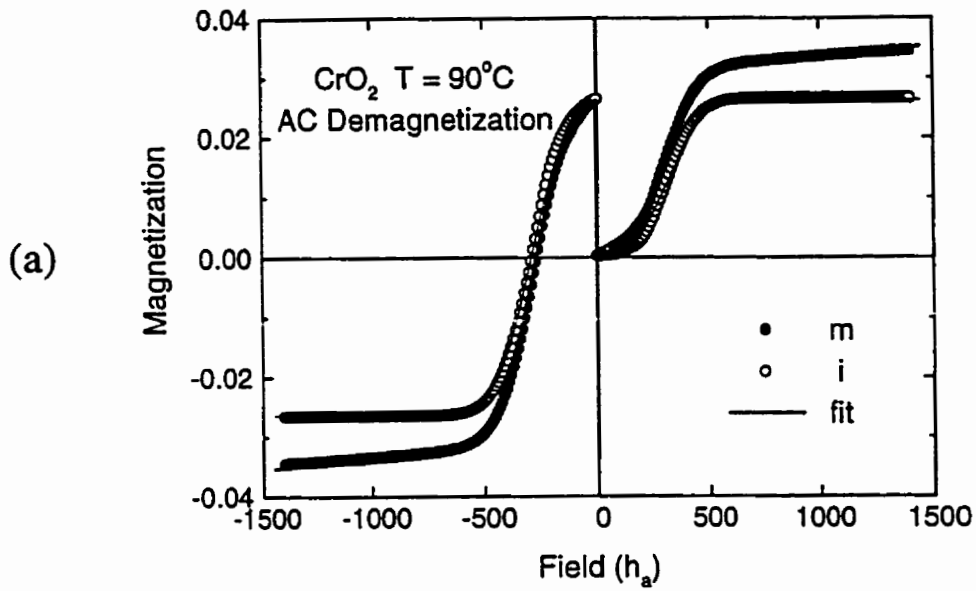


Figure A1.4 . Data and fits for CrO<sub>2</sub> audio tape at T = 90°C. (a) Magnetizing and demagnetizing curves, m, and the corresponding magnetizing and demagnetizing remanences, i. (b) Henkel plots constructed from remanences in (a).

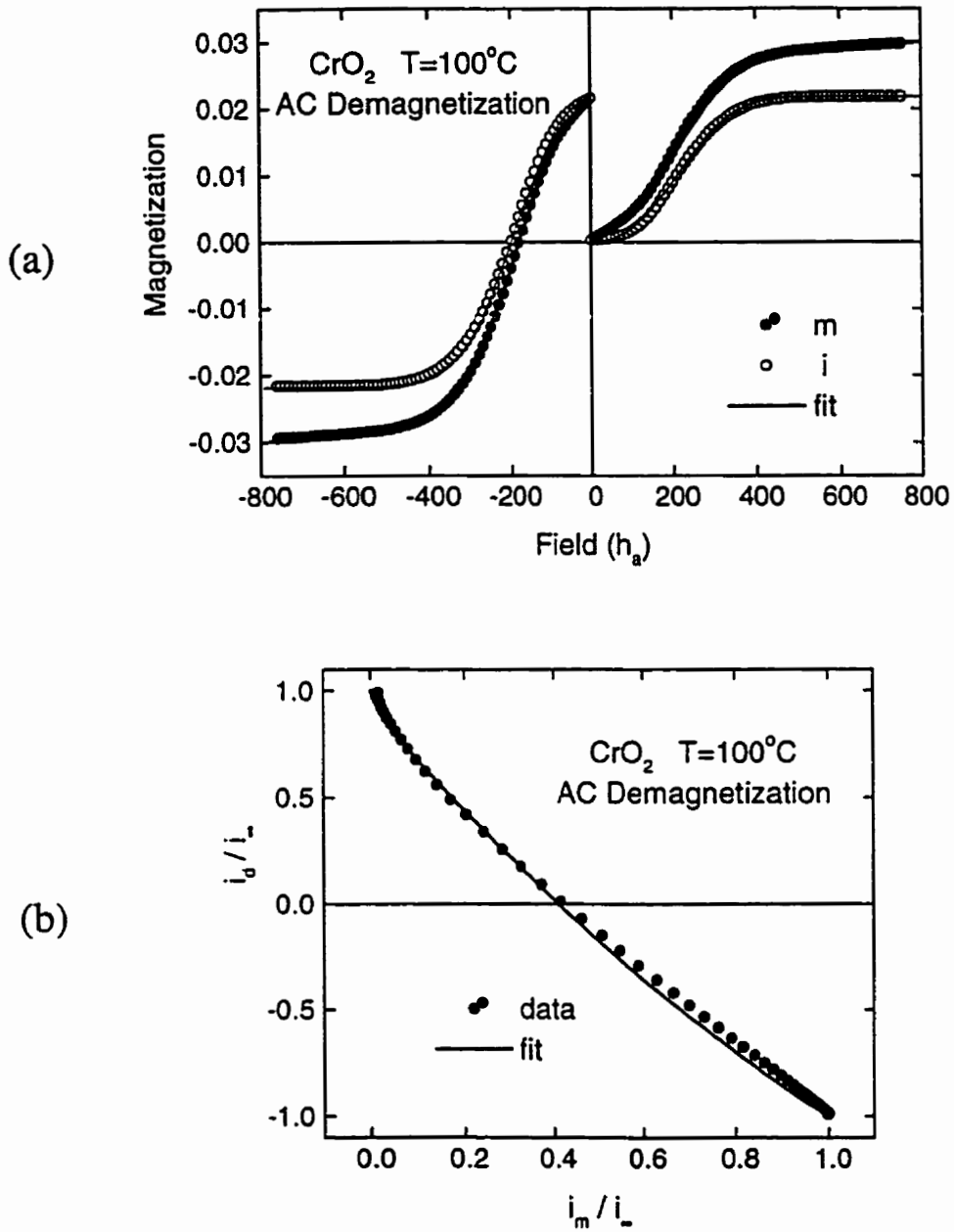


Figure A1.5 . Data and fits for  $\text{CrO}_2$  audio tape at  $T = 100^\circ\text{C}$ . (a) Magnetizing and demagnetizing curves,  $m$ , and the corresponding magnetizing and demagnetizing remanences,  $i$ . (b) Henkel plots constructed from remanences in (a).

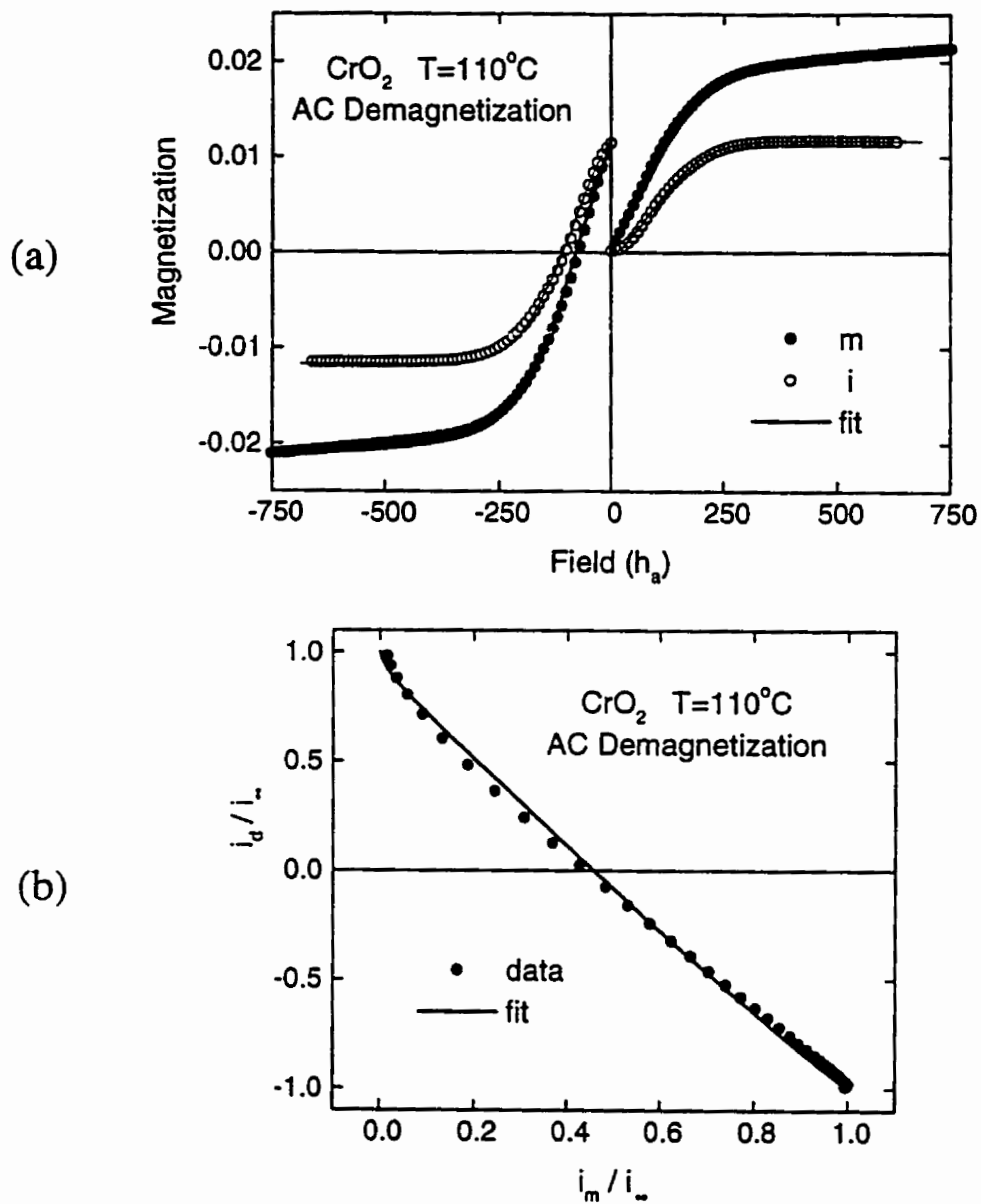


Figure A1.6 . Data and fits for CrO<sub>2</sub> audio tape at T = 110°C. (a) Magnetizing and demagnetizing curves, m, and the corresponding magnetizing and demagnetizing remanences, i. (b) Henkel plots constructed from remanences in (a).

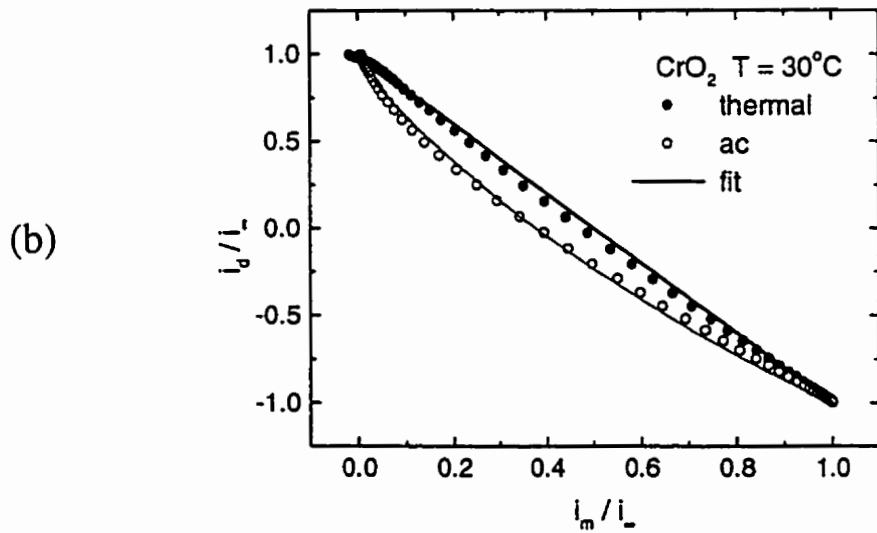
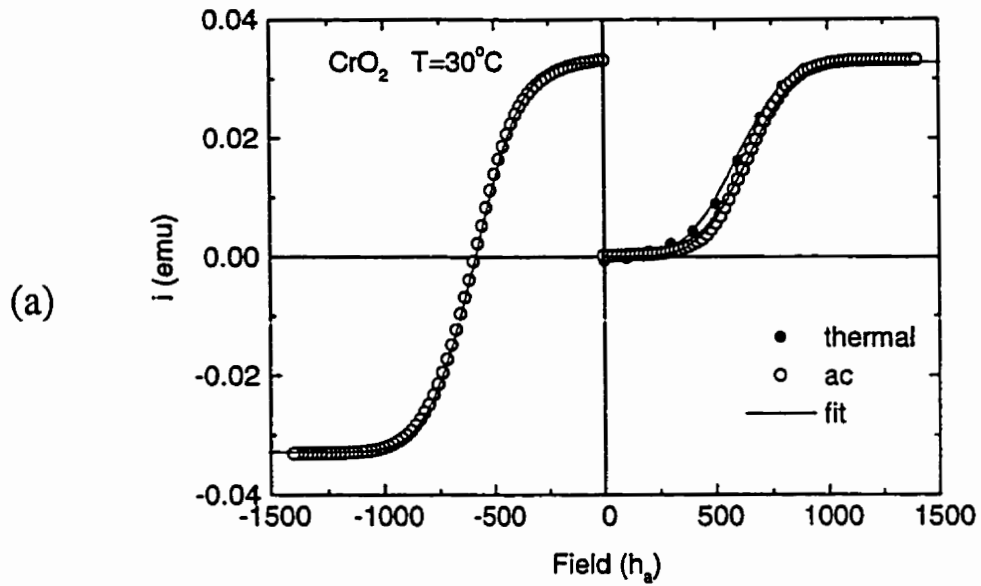


Figure A1.7 . Comparison of fits for ac and thermally demagnetized CrO<sub>2</sub> audio tape at T = 30°C. (a) Magnetizing and demagnetizing remanences,  $i$ . (b) Henkel plots constructed from remanences in (a).

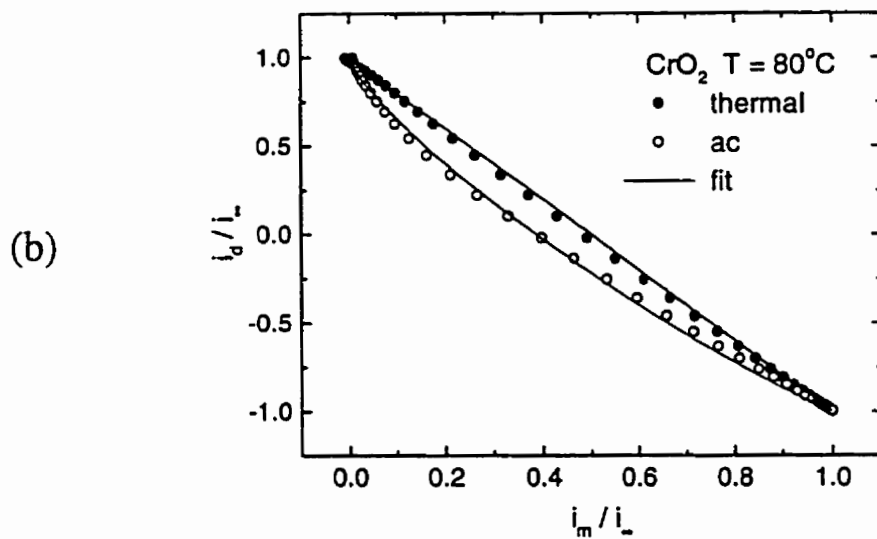
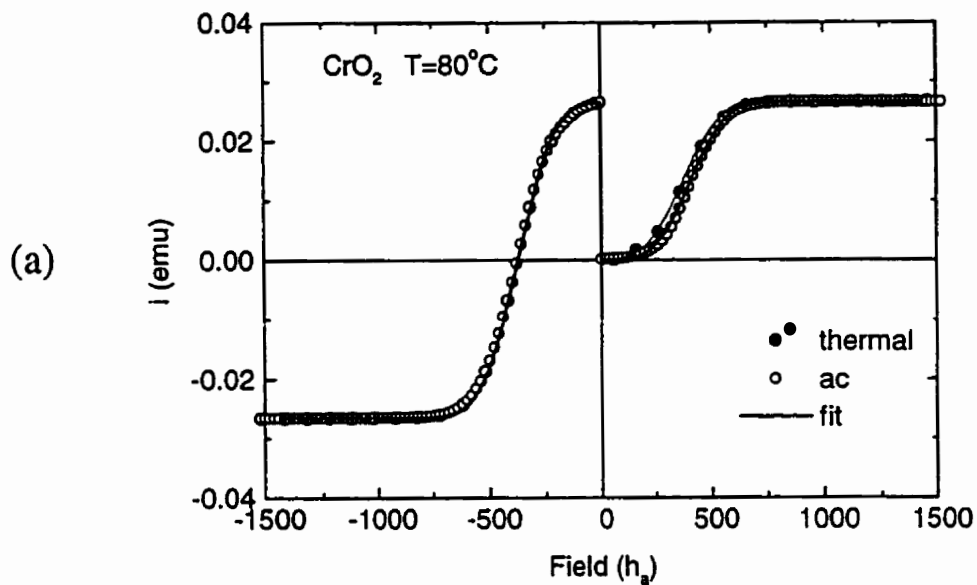


Figure A1.8 . Comparison of fits for ac and thermally demagnetized CrO<sub>2</sub> audio tape at T = 80°C. (a) Magnetizing and demagnetizing remanences,  $i$ . (b) Henkel plots constructed from remanences in (a).

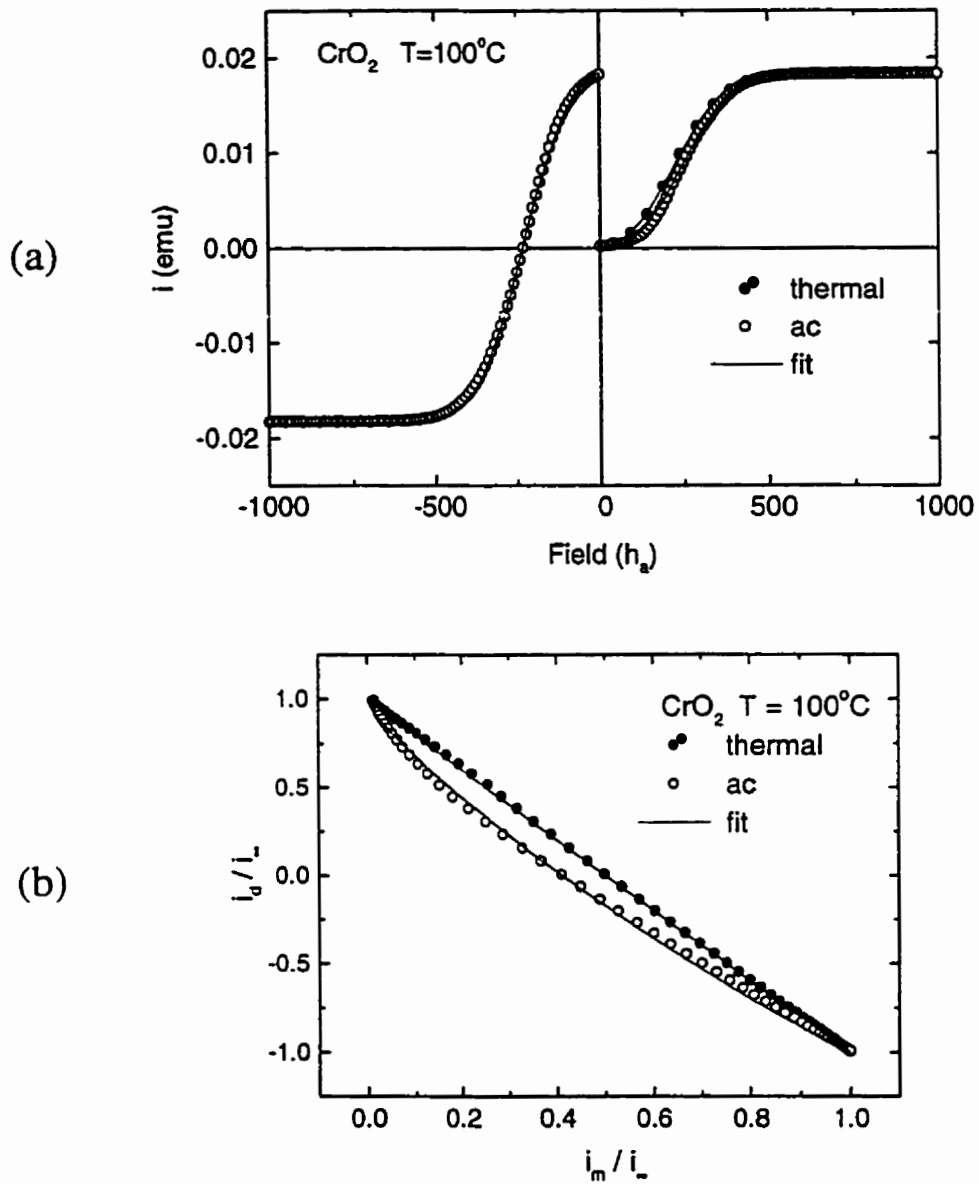


Figure A1.9 . Comparison of fits for ac and thermally demagnetized CrO<sub>2</sub> audio tape at T = 100°C. (a) Magnetizing and demagnetizing remanences,  $i$ . (b) Henkel plots constructed from remanences in (a).

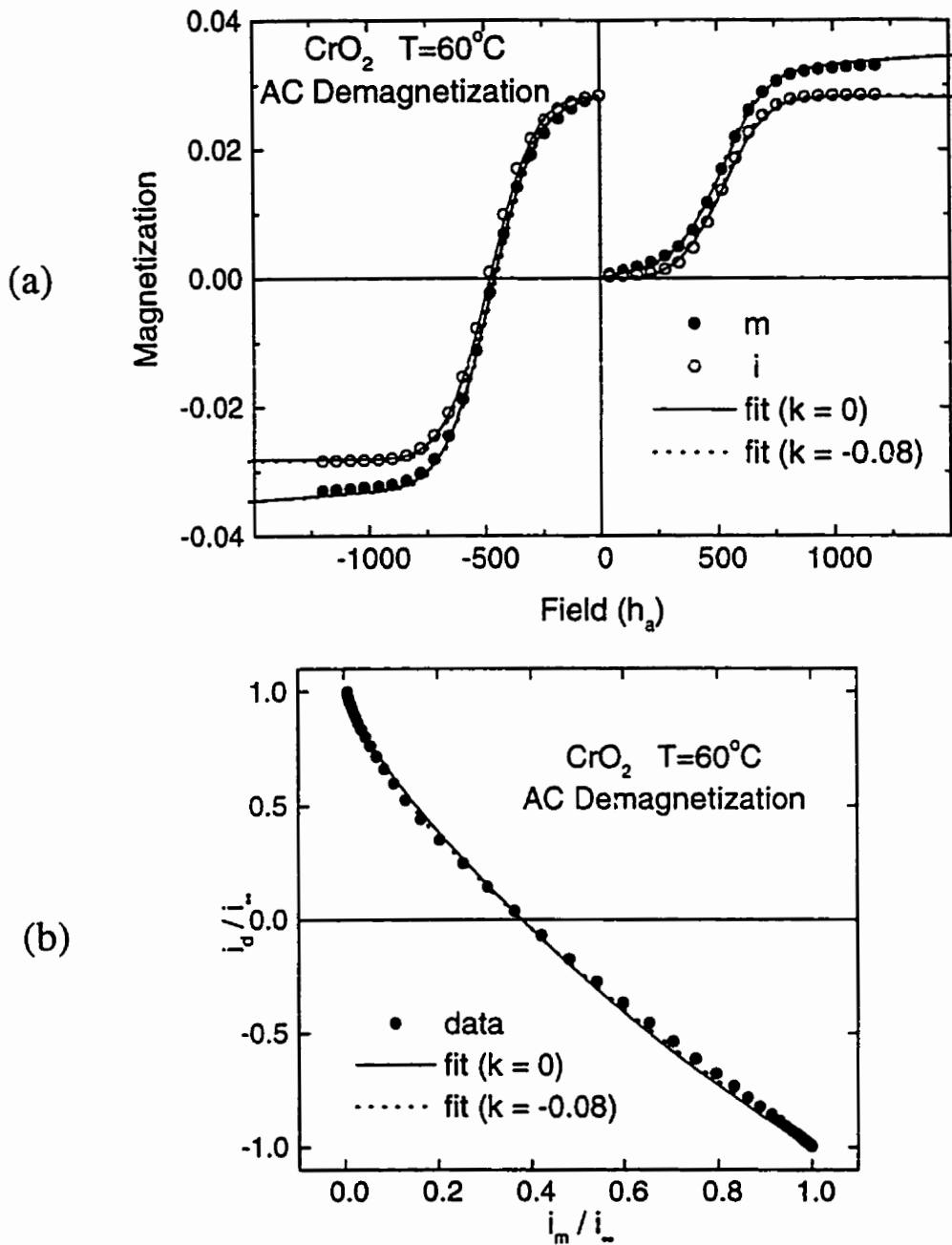


Figure A1.10 . Data for CrO<sub>2</sub> audio tape at T = 60°C and comparison of fits with  $k = 0$  and  $k < 0$ . (a) Magnetizing and demagnetizing curves,  $m$ , and the corresponding magnetizing and demagnetizing remanences,  $i$ . (b) Henkel plots constructed from remanences in (a).

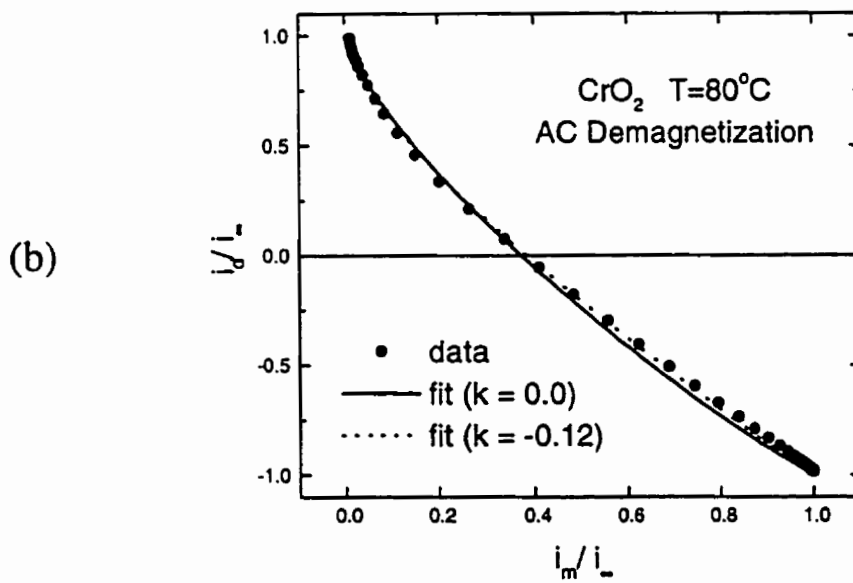
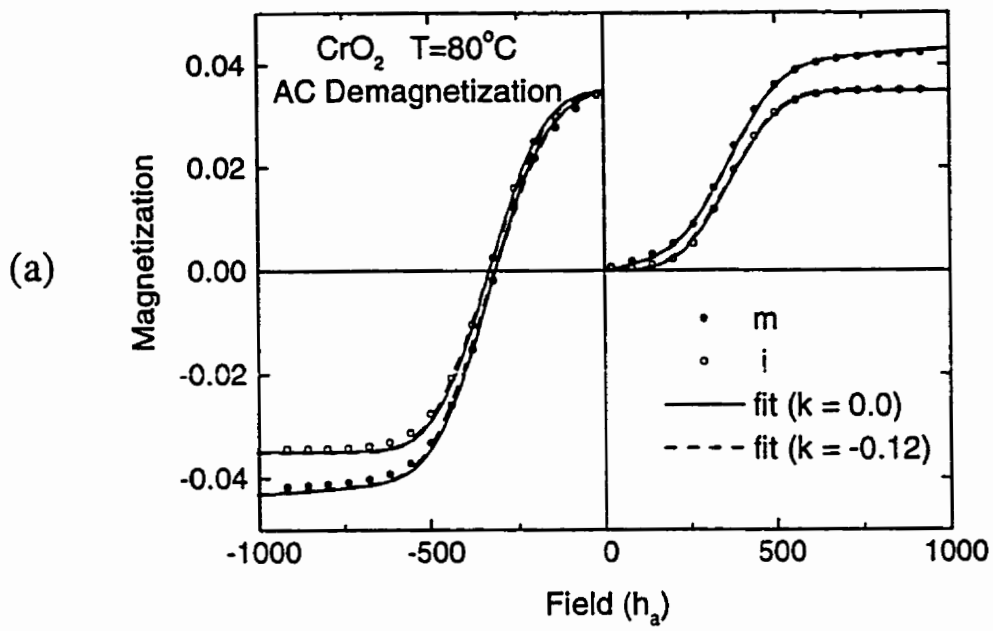


Figure A1.11 . Data for CrO<sub>2</sub> audio tape at  $T = 80^\circ\text{C}$  and a comparison of fits with  $k = 0$  and  $k < 0$ . (a) Magnetizing and demagnetizing curves,  $m$ , and the corresponding magnetizing and demagnetizing remanences,  $i$ . (b) Henkel plots constructed from remanences in (a).

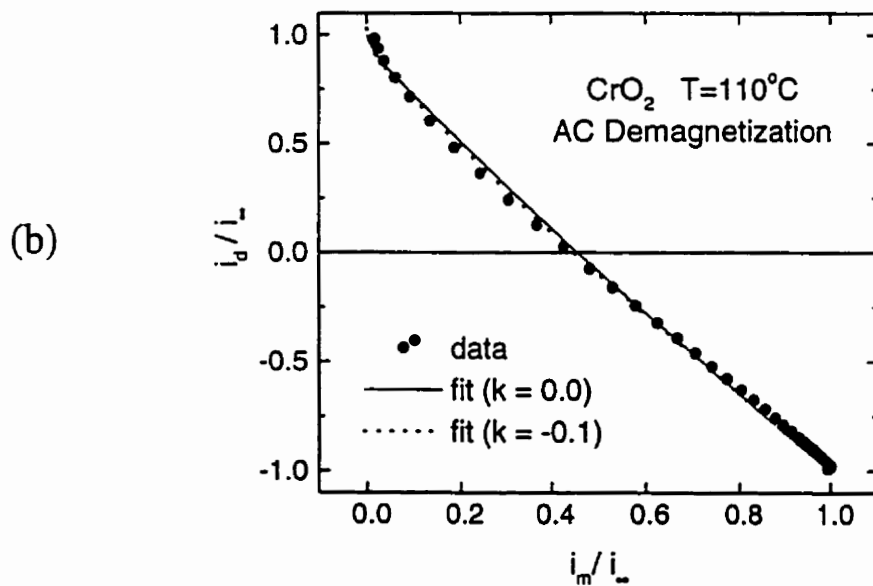
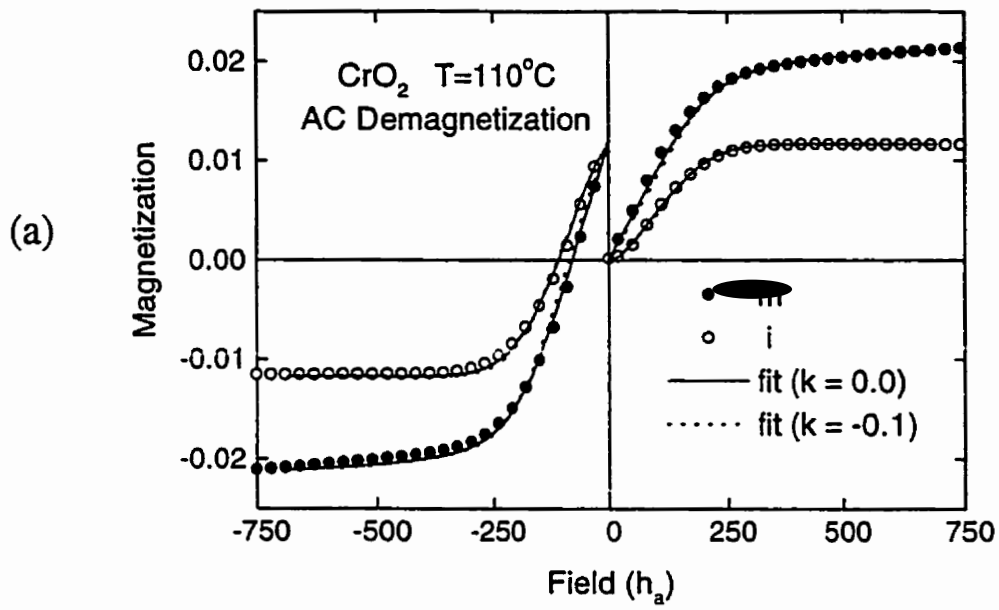


Figure A1.12 . Data for CrO<sub>2</sub> audio tape at  $T = 110^\circ\text{C}$  and a comparison of fits with  $k = 0$  and  $k < 0$ . (a) Magnetizing and demagnetizing curves,  $m$ , and the corresponding magnetizing and demagnetizing remanences,  $i$ . (b) Henkel plots constructed from remanences in (a).

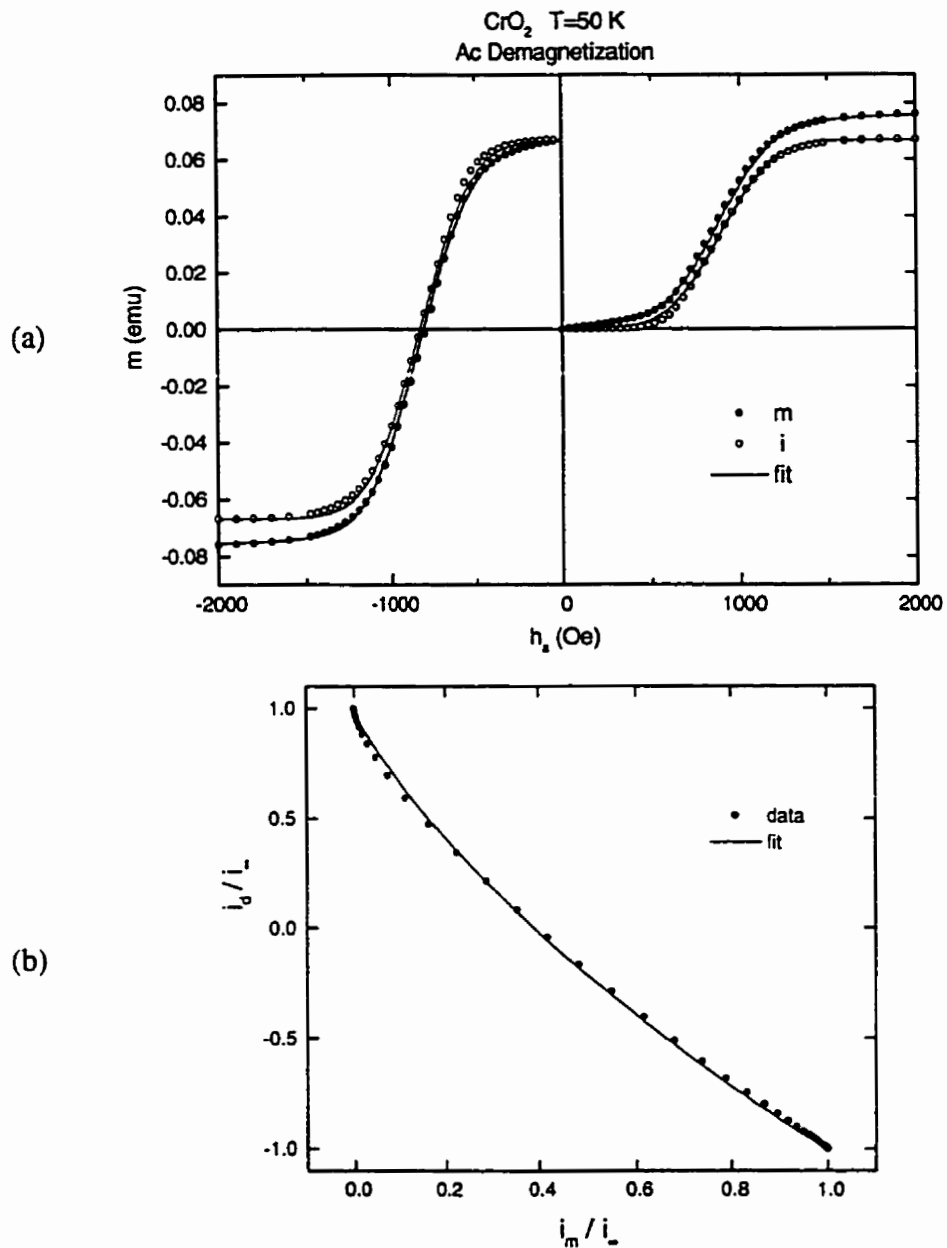


Figure A1.13 . (a) The initial magnetizing curve, magnetization remanences, the demagnetizing curve, and the demagnetizing remanences for ac demagnetized CrO<sub>2</sub> audio tape at T = 50 K, plotted as a function of applied field  $h_x$ . (b) The Henkel plot constructed from the remanence data in (a). The discrete points are experimental data and the continuous lines are Preisach model calculations.

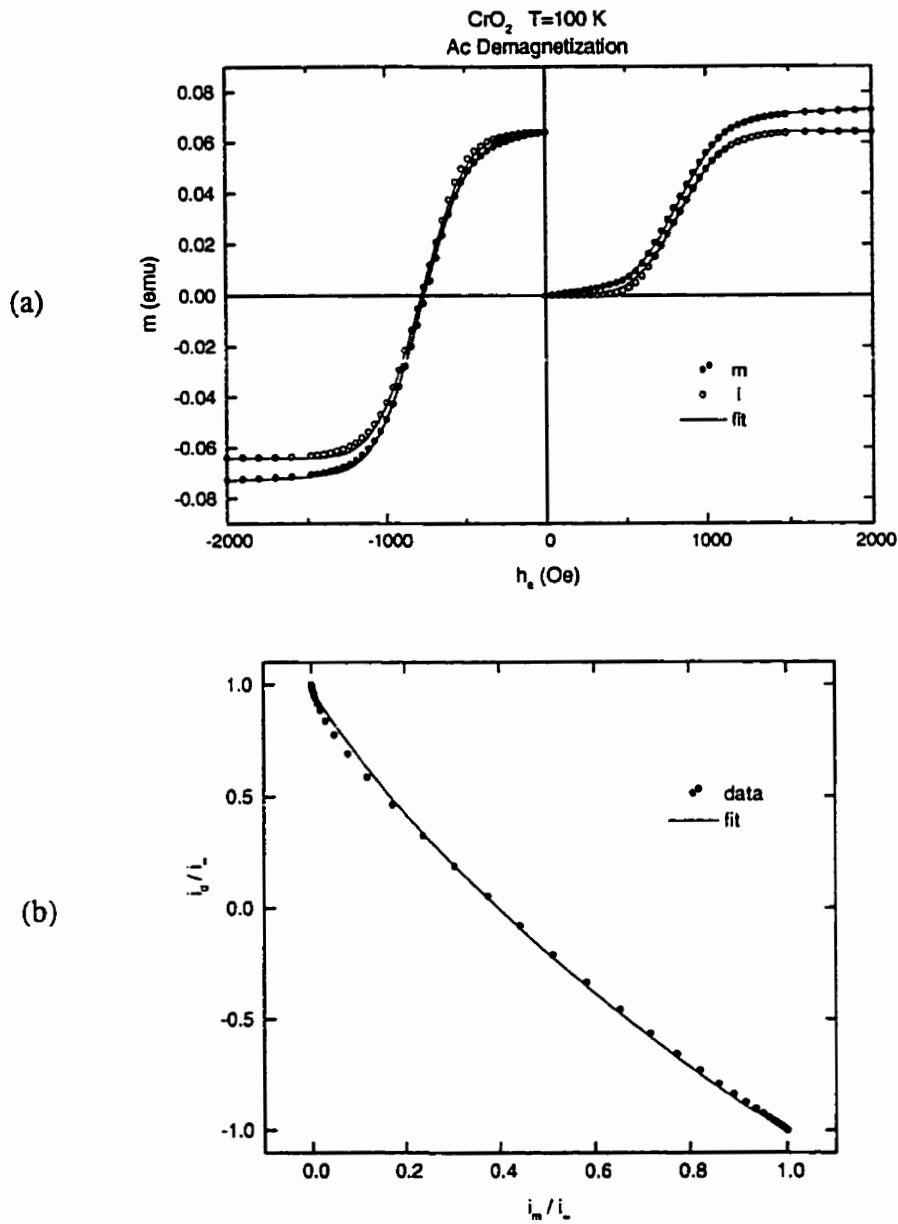


Figure A1.14 . (a) The initial magnetizing curve, magnetization remanences, the demagnetizing curve, and the demagnetizing remanences for ac demagnetized CrO<sub>2</sub> audio tape at T = 100 K, plotted as a function of applied field  $h_a$ . (b) The Henkel plot constructed from the remanence data in (a). The discrete points are experimental data and the continuous lines are Preisach model calculations.

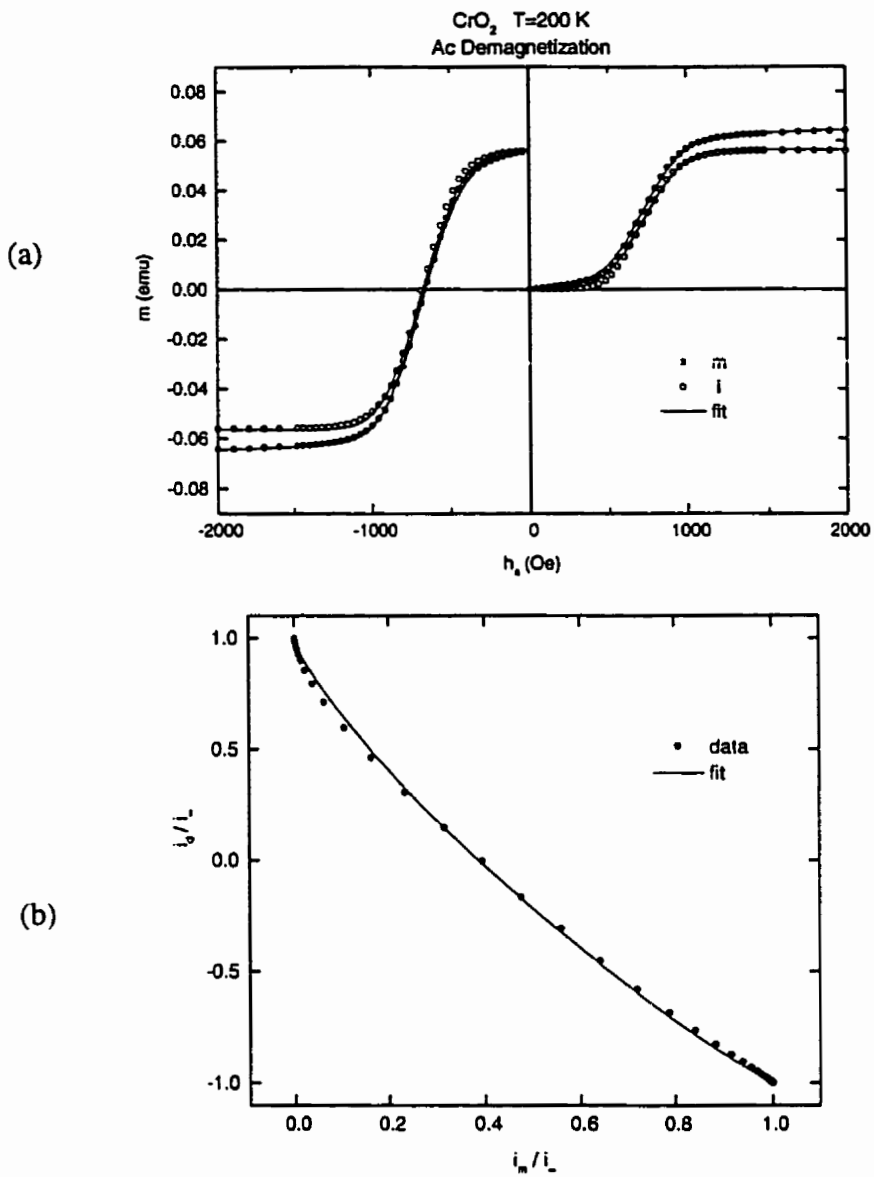


Figure A1.15 . (a) The initial magnetizing curve, magnetization remanences, the demagnetizing curve, and the demagnetizing remanences for ac demagnetized CrO<sub>2</sub> audio tape at T = 200 K, plotted as a function of applied field h<sub>a</sub>. (b) The Henkel plot constructed from the remanence data in (a). The discrete points are experimental data and the continuous lines are Preisach model calculations.

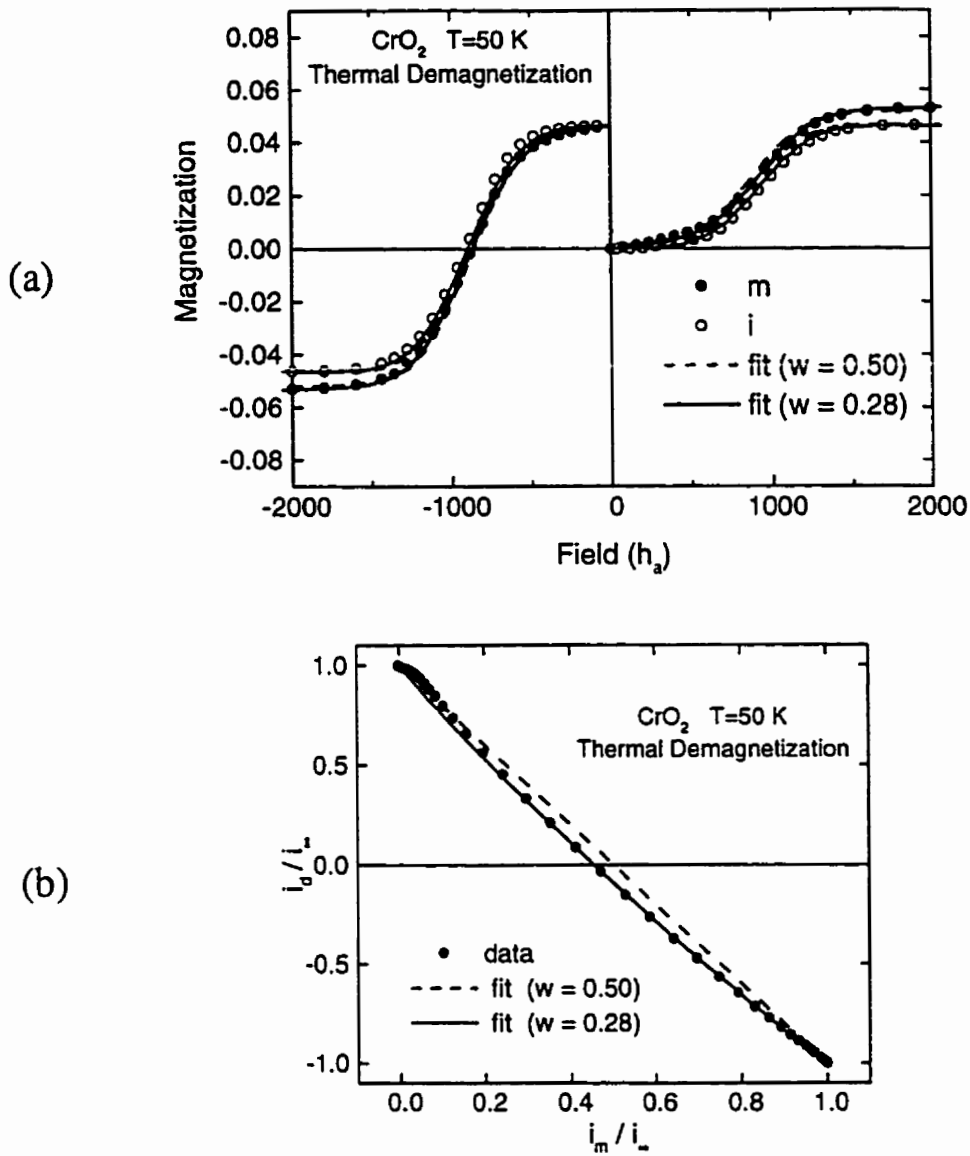


Figure A1.16 . (a) The initial magnetizing curve, magnetization remanences, the demagnetizing curve, and the demagnetizing remanences for ac demagnetized CrO<sub>2</sub> at T = 50 K, plotted as a function of applied field  $h_a$ . (b) The Henkel plot constructed from the remanence data in (a). The discrete points are experimental data while the dashed lines represent fits with random occupation probabilities ( $w = 0.5$ ) and the solid lines show the best fit when the parameter  $w$  is allowed to vary ( $0 \leq w \leq 0.5$ ).

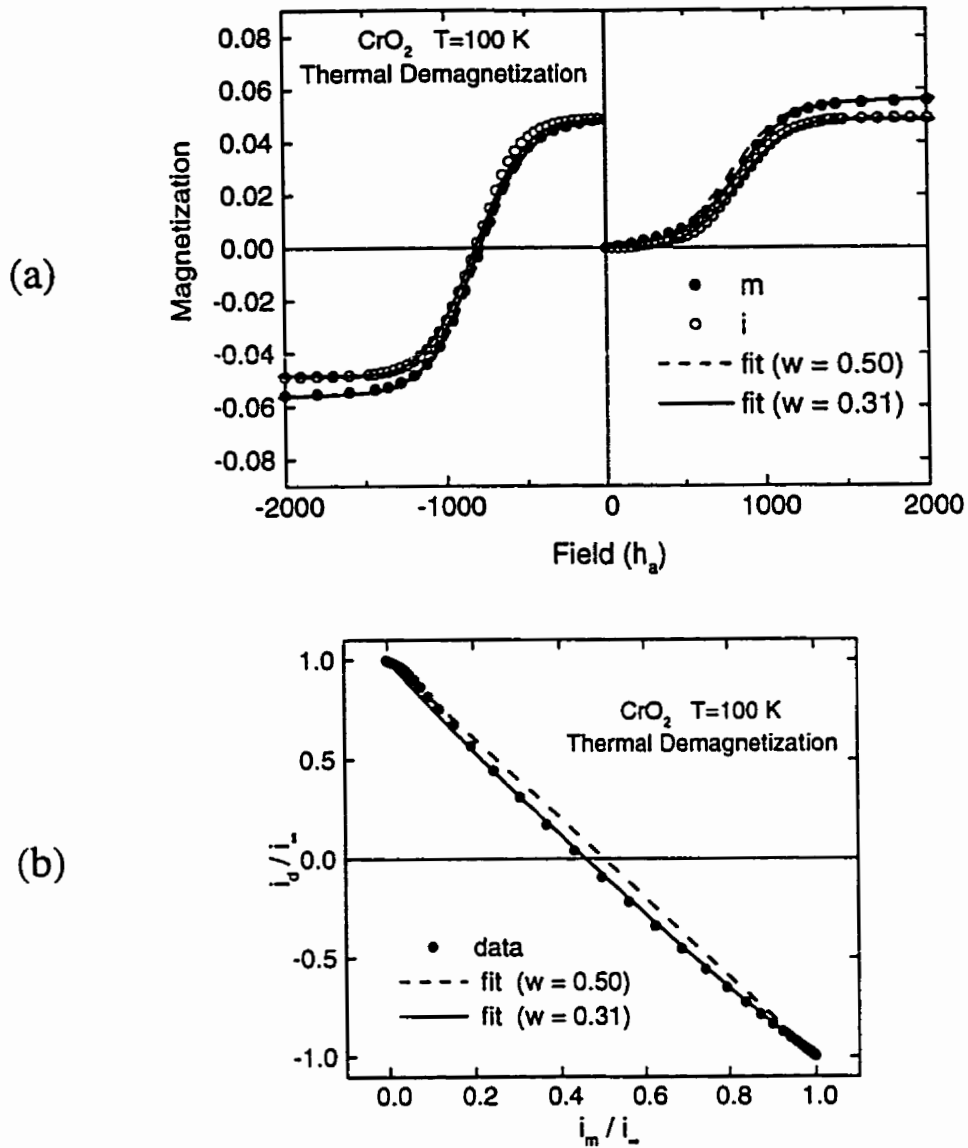


Figure A1.17 . (a) The initial magnetizing curve, magnetization remanences, the demagnetizing curve, and the demagnetizing remanences for ac demagnetized  $\text{CrO}_2$  at  $T = 100 \text{ K}$ , plotted as a function of applied field  $h_a$ . (b) The Henkel plot constructed from the remanence data in (a). The discrete points are experimental data while the dashed lines represent fits with random occupation probabilities ( $w = 0.5$ ) and the solid lines show the best fit when the parameter  $w$  is allowed to vary ( $0 \leq w \leq 0.5$ ).

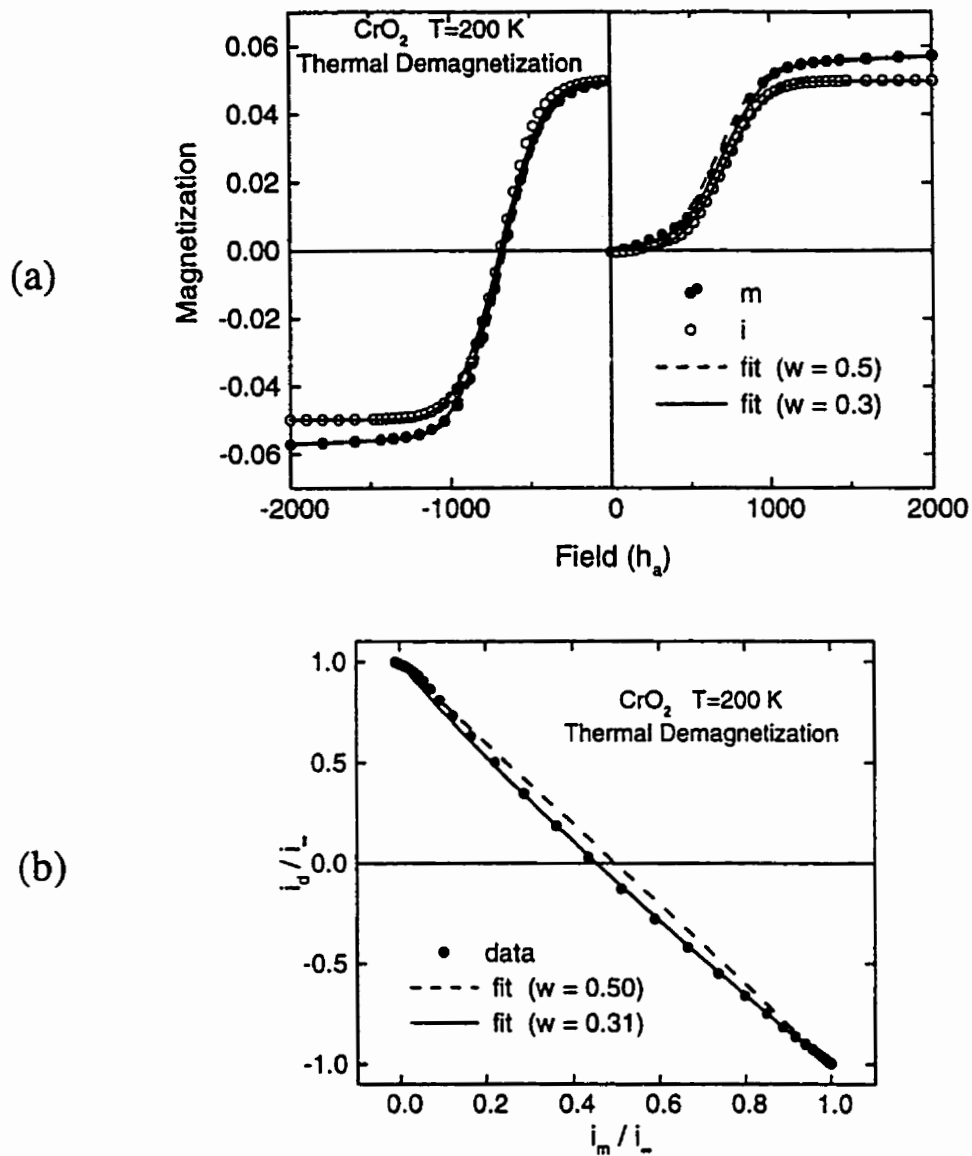


Figure A1.18 . (a) The initial magnetizing curve, magnetization remanences, the demagnetizing curve, and the demagnetizing remanences for ac demagnetized CrO<sub>2</sub> at T = 200 K, plotted as a function of applied field  $h_a$ . (b) The Henkel plot constructed from the remanence data in (a). The discrete points are experimental data while the dashed lines represent fits with random occupation probabilities ( $w = 0.5$ ) and the solid lines show the best fit when the parameter  $w$  is allowed to vary ( $0 \leq w \leq 0.5$ ).

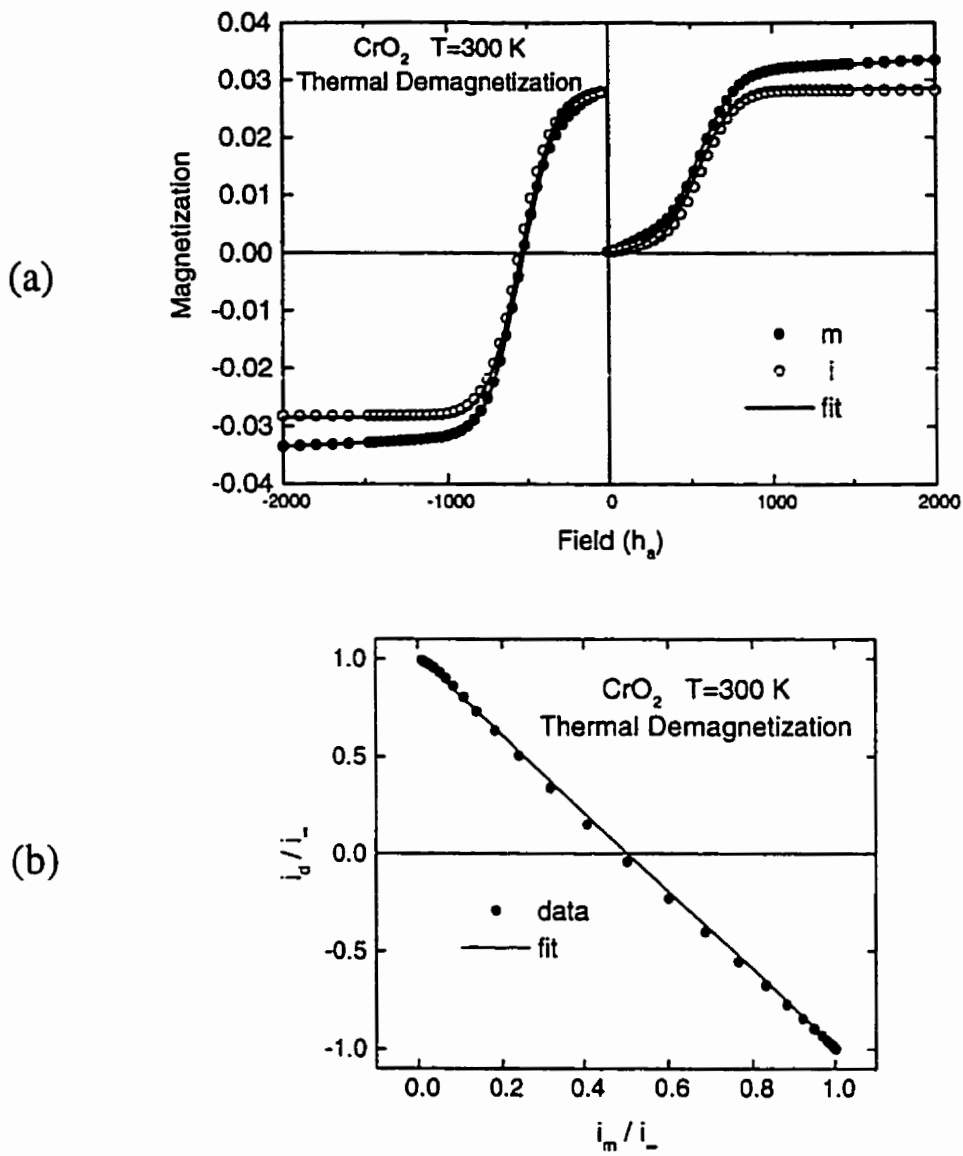


Figure A1.19 . (a) The initial magnetizing curve, magnetization remanences, the demagnetizing curve, and the demagnetizing remanences for ac demagnetized  $\text{CrO}_2$  at  $T = 300 \text{ K}$ , plotted as a function of applied field  $h_a$ . (b) The Henkel plot constructed from the remanence data in (a). The discrete points are experimental data while the solid lines represent fits with random occupation probabilities ( $w = 0.5$ ).

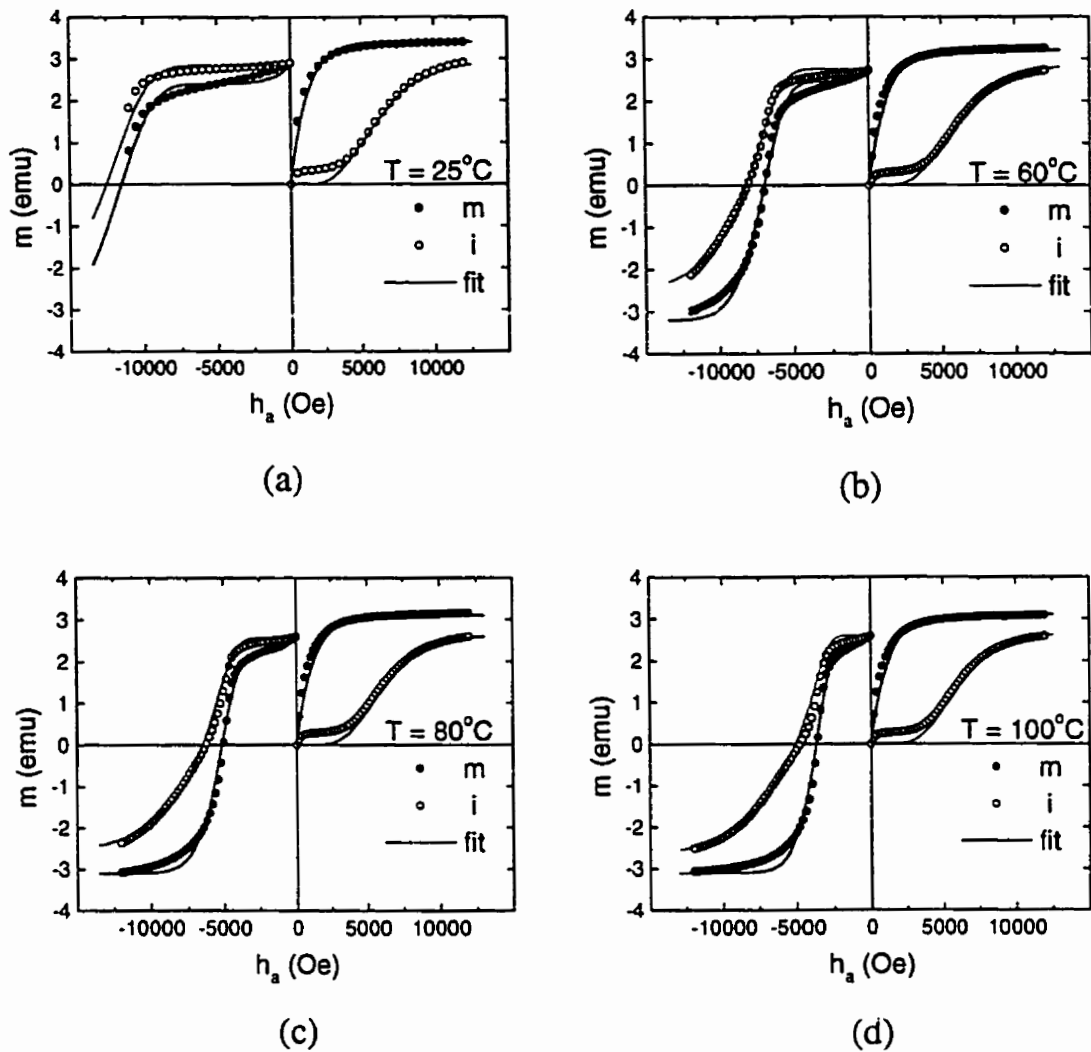


Figure A1.20 . Magnetization and remanence data for  $\text{Nd}_2\text{Fe}_{14}\text{B}$  at four different temperatures  $T =$  (a)  $25^\circ\text{C}$ , (b)  $60^\circ\text{C}$ , (c)  $80^\circ\text{C}$ , and (d)  $100^\circ\text{C}$ . The experimental magnetizing and demagnetizing curves,  $m$  are represented by the solid dots while the experimental magnetizing and demagnetizing remanences,  $i$  are given by the open dots. The solid lines are fits to the data.

## Appendix 2

### Fortran Programs for Preisach Calculations

**A2.1:** This program was used to calculate magnetizing and demagnetizing curves and the corresponding remanences and to construct Henkel plots. More than one set of fitting parameters could be read into the program, and the program performed calculation of the sum of squares of the deviations between calculated and experimental values. This type of program was used in generating all calculated curves in this thesis except those representing fits to  $\text{Nd}_2\text{Fe}_{14}\text{B}$  data.

**A2.2:** This program calculates curves corresponding to a Preisach plane with modified elementary loops as shown in Figure 5.49 to describe  $\text{Nd}_2\text{Fe}_{14}\text{B}$  data. It incorporates the nucleating field distribution, magnetizing and demagnetizing coercive field distribution, and the reversible branch of the hysteresis loop.

## A2.1 Fortran Program for Preisach Calculations (General)

```

C-----
C   PATRICIA MITCHLER, JULY 1998
C   Program for Preisach calculations with more than one parameter set.
C-----

      IMPLICIT NONE
      REAL*8 C,FIELD,C,MEANC0,MEANC(1000),WIDTHC(1000),MEANI,
      *      WIDTHI,HTSTAR,msat,f,gamma,ALPHA,WEIGHT,INFINITY,
      *      INFINITYI,shift

      COMMON
/FTPARAMETERS/C,FIELD,C,MEANC0,MEANC,WIDTC,MEANI,
      *      WIDTHI,HTSTAR,msat,f,gamma,ALPHA,WEIGHT,INFINITY,
      *      INFINITYI,shift

      INTEGER*4 COUNT,npts,chi,mpts,hnpts,npara,nparaMAX

      COMMON /NUM/COUNT
      COMMON /CHI1/npts,mpts,hnpts,chi

      OPEN (FILE='autokmw1.dat', UNIT=4, STATUS='OLD')
      READ (4,*) nparaMAX,npts,mpts,hnpts

      DO npara= 1,nparaMAX
        CALL CHIFIT
      ENDDO

      CLOSE (4)

      STOP
      END

C-----
SUBROUTINE CHIFIT
C-----
C   Magnetization and remanence (IRM) calculations using the Preisach Model.
C   Good for all values of k, mean field parameter.
C   Good for all thermal weightings of the demagnetized plane, including ac demag.
C   Generates files for Henkel plots.
C   DOES NOT CALCULATE k > 0 WHEN h > hstar AND hprime > hstar.
C   Want to do a CHI-SQUARED estimate.

```

```

C-----
      IMPLICIT NONE
      REAL*8 W(10),X(10)
      REAL*8 C,FIELD,C,MEANC0,MEANC(1000),WIDTHC(1000),MEANI,
      *      WIDTHI,HTSTAR,msat,f,gamma,ALPHA,WEIGHT,INFINITY,
      *      INFINITYI,shift

      COMMON /INTEGRATION/W,X
      COMMON
/FTPARAMETERS/C,FIELD,C,MEANC0,MEANC,WIDTC,MEANI,
      *      WIDTHI,HTSTAR,msat,f,gamma,ALPHA,WEIGHT,INFINITY,
      *      INFINITYI,shift

      INTEGER*4 COUNT,npts,chi,mpts,hnpts

      COMMON /NUM/COUNT
      COMMON /CHI1/npts,mpts,hnpts,chi

C-----
C   Get value for fitting parameters from a file.
C-----
      READ (4,*) C,MEANC0,FIELD,C,WIDTC(1),WIDTHI,HTSTAR,msat,f,gamma,
      *      ALPHA,WEIGHT,shift

C-----
C   X and W values for integration scheme.
C-----
      X(1) = -0.9739065285D0
      W(1) = 0.0666713443D0
      X(2) = -0.8650633667D0
      W(2) = 0.1494513492D0
      X(3) = -0.6794095683D0
      W(3) = 0.2190863625D0
      X(4) = -0.4333953941D0
      W(4) = 0.2692667193D0
      X(5) = -0.1488743390D0
      W(5) = 0.2955242247D0
      X(6) = -X(5)

```

## A2.1 Fortran Program for Preisach Calculations (General)

```

W(6) = W(5)
X(7) = -X(4)
W(7) = W(4)
X(8) = -X(3)
W(8) = W(3)
X(9) = -X(2)
W(9) = W(2)
X(10) = -X(1)
W(10) = W(1)

INFINITY = 10.D0*WIDTHC(1)+MEANC0
INFINITYI = 10.D0*WIDTHI
MEANI = 0.D0
COUNT = 60
chi = 0
-----
C-----
C Call subroutines to calculate magnetizations and remanences, and to tabulate results.
C-----
CALL NORMCCALC
CALL NORMICALC
CALL MAGCALC
CALL REMCALC
CALL DEMAGCALC
CALL DEMAGINTERPOL
CALL DEREMCALC
CALL FILE
CALL CHISQR(shift)

RETURN
END
-----
SUBROUTINE NORMCCALC
-----
C Coercive field normalization.
-----

IMPLICIT NONE
C REAL*8 W(10),X(10),XA,XB
REAL*8 XA,XB
-----
REAL*8 C,FIELDC,MEANC0,MEANC(1000),WIDTHC(1000),MEANI,
      WIDTHI,HTSTAR,msat,f,gamma,ALPHA,WEIGHT,INFINITY,
      INFINITYI,shift
C COMMON /INTEGRATION/W,X
COMMON
/FITPARAMETERS/C,FIELDC,MEANC0,MEANC,WIDTHC,MEANI,
      WIDTHI,HTSTAR,msat,f,gamma,ALPHA,WEIGHT,INFINITY,
      INFINITYI,shift

REAL*8 DELTAC,NORMC,GRIDC(1000),INTEG
COMMON /NORMC/NORMC,DELTAC

INTEGER*4 N,LG
C
NORMC = 1.D0
GRIDC(1) = 10.D0
N=IDINT(GRIDC(1))
IF (N.LT.1) N=1
XA = 0.D0
XB = INFINITY
DELTAC=(XB-XA)/DFLOAT(N)
LG = 0
CALL
INTEG1D(XA,XB,N,DELTAC,MEANC0,WIDTHC(1),NORMC,INTEG,LG)

NORMC = INTEG
C WRITE (6,*) NORMC
RETURN
END
-----
SUBROUTINE NORMICALC
-----
C Coercive field normalization.
-----

IMPLICIT NONE
C REAL*8 XA,XB
-----

```

## A2.1 Fortran Program for Preisach Calculations (General)

```

REAL*8 C,FIELD,MEANC0,MEANC(1000),WIDTHC(1000),MEANI,
*      WIDTHI,HTSTAR,msat,f,gamma,ALPHA,WEIGHT,INFINITY,
*      INFINITYI,shift

COMMON
/FITPARAMETERS/C,FIELD,MEANC0,MEANC,WIDTHC,MEANI,
*      WIDTHI,HTSTAR,msat,f,gamma,ALPHA,WEIGHT,INFINITY,
*      INFINITYI,shift

REAL*8 DELTAI,NORMI,GRIDI,INTEG
COMMON /NORMI/NORMI,DELTAI

INTEGER*4 N,LG

C
NORMI = 1.D0
GRIDI = 10.D0
N=IDINT(GRIDI)
IF (N.LT.1) N=1
XA=-INFINITYI
XB= INFINITYI
DELTAI=(XB-XA)/DFLOAT(N)
LG = 0

CALL INTEGID(XA,XB,N,DELTAI,MEANI,WIDTHI,NORMI,INTEG,LG)

NORMI = INTEG

C WRITE (6,*) NORMI
RETURN
END

C-----
SUBROUTINE MAGCALC
C-----
C This program calculates the magnetization i(h). (For any k.)
C-----

IMPLICIT NONE

REAL*8 C,FIELD,MEANC0,MEANC(1000),WIDTHC(1000),MEANI,
*      WIDTHI,HTSTAR,msat,f,gamma,ALPHA,WEIGHT,INFINITY,
*      INFINITYI,shift

COMMON
/FITPARAMETERS/C,FIELD,MEANC0,MEANC,WIDTHC,MEANI,
*      WIDTHI,HTSTAR,msat,f,gamma,ALPHA,WEIGHT,INFINITY,
*      INFINITYI,shift

REAL*8 DELTAC,NORMC
REAL*8 DELTAI,NORMI

COMMON /NORMC/NORMC,DELTAC
COMMON /NORMI/NORMI,DELTAI

REAL*8 FACTOR(20),XA(20),XB(20),XPRIM(20),XR(999),
*      YA(20),YB(20),INTEG,SUMK,H,HA(300),IHZ(300),NC

COMMON /MAG/HA,IHZ

INTEGER*4 COUNT,I,J,P,Q,Q2,TAG,LG
COMMON /NUM/COUNT

DO P=1,COUNT

IHZ(P) = 0.D0
INTEG = 0.D0

H =(P-1.D0)/13.D0
MEANC(P) = MEANC0 - ALPHA*IHZ(P)
WIDTHC(P) = WIDTHC(1)

IF (H.LE.HTSTAR) THEN
FACTOR(1)= 2.D0
FACTOR(2)= 2.D0*(1.D0-WEIGHT)
FACTOR(3)= 2.D0*(1.D0-WEIGHT)
FACTOR(4)= 2.D0*(1.D0-WEIGHT)
FACTOR(5)= 2.D0*(WEIGHT)
FACTOR(6)= 2.D0*(WEIGHT)
FACTOR(7)= -2.D0*(WEIGHT)
FACTOR(8)= -2.D0*(WEIGHT)

```

## A2.1 Fortran Program for Preisach Calculations (General)

```

XA(1)=0.D0
XA(2)=0.D0
XA(3)=H
XA(4)=HTSTAR
XA(5)=0.D0
XA(6)=H + HTSTAR
XA(7)=H
XA(8)=HTSTAR
XB(1)=H
XB(2)=H
XB(3)=HTSTAR
XB(4)=H + HTSTAR
XB(5)=H + HTSTAR
XB(6)=INFINITY
XB(7)=HTSTAR
XB(8)=INFINITY
Q2=8
  ELSE
    FACTOR(1)= 2.D0
    FACTOR(2)= 2.D0
    FACTOR(3)= 2.D0*(1.D0-WEIGHT)
    FACTOR(4)= 2.D0*(1.D0-WEIGHT)
    FACTOR(5)= 2.D0*(WEIGHT)
    FACTOR(6)= 2.D0*(WEIGHT)
XA(1)=0.D0
XA(2)=HTSTAR
XA(3)=0.D0
XA(4)=(H+HTSTAR)/2.D0
XA(5)=0.D0
XA(6)=H+HTSTAR
XB(1)=HTSTAR
XB(2)=(H+HTSTAR)/2.D0
XB(3)=(H+HTSTAR)/2.D0
XB(4)=H+HTSTAR
XB(5)=H+HTSTAR
XB(6)=INFINITY
Q2=6
  END IF

  DO Q=1,Q2
    SUMK = 0.D0
    J = 1
    I = 1
    TAG = 0
    LG = 0
    CALL INTEG2D(XA,XB,Q,P,J,I,TAG,&5,INTEG,XPRIM,XR,NC,
    YA,YB,SUMK,FACTOR,LG)
    TAG = 1
    LG = 0
    IF (H.LE.HTSTAR) THEN
      YA(1)=XPRIM(J)
      YA(2)=0.D0
      YA(3)=0.D0
      YA(4)=0.D0
      YA(5)=-XPRIM(J)
      YA(6)=-XPRIM(J)
      YA(7)=H
      YA(8)=XPRIM(J)+(H-HTSTAR)
      YB(1)=H
      YB(2)=XPRIM(J)
      YB(3)=H
      YB(4)=-XPRIM(J)+(H+HTSTAR)
      YB(5)=0.D0
      YB(6)=-XPRIM(J)+(H+HTSTAR)
      YB(7)=XPRIM(J)
      YB(8)=XPRIM(J)
    ELSE
      YA(1)=XPRIM(J)
      YA(2)=XPRIM(J)
      YA(3)=0.D0
      YA(4)=0.D0
      YA(5)=-XPRIM(J)
      YA(6)=-XPRIM(J)
      YB(1)=H
      YB(2)=-XPRIM(J)+(H+HTSTAR)
      YB(3)=XPRIM(J)
      YB(4)=-XPRIM(J)+(H+HTSTAR)
      YB(5)=0.D0
      YB(6)=-XPRIM(J)+(H+HTSTAR)
    END IF
  END DO

```

## A2.1 Fortran Program for Preisach Calculations (General)

```

      CALL INTEG2D(XA,XB,Q,P,J,I,TAG,&5,INTEG,XPRIM,XR,NC,
      *           YA,YB,SUMK,FACTOR,LG)

      INTEG=INTEG + SUMK

      END DO

      IHZ(P) = ((1.D0-f)*INTEG + f*(1.D0-DEXP(-gamma*H)))
      HA(P) = H - C*IHZ(P)
      END DO

      RETURN
      END

C-----
      SUBROUTINE REMCALC
C-----
C This program calculates the magnetizing remanence ir.
C-----

      IMPLICIT NONE
      REAL*8 C,FIELD,MEANC0,MEANC(1000),WIDTHC(1000),MEAN,
      *       WIDTHI,HTSTAR,msat,f,gamma,ALPHA,WEIGHT,INFINITY,
      *       INFINITYI,shift

      COMMON
      /FITPARAMETERS/C,FIELD,MEANC0,MEANC,WIDTHC,MEAN,
      *       WIDTHI,HTSTAR,msat,f,gamma,ALPHA,WEIGHT,INFINITY,
      *       INFINITYI,shift

      REAL*8 rtbis,HPRIM,REMBIS,error,x1,x2,REM(300),IHZ(300),
      *       HA(300),H

      INTEGER*4 COUNT,P,choice

      EXTERNAL REMBIS

      COMMON /NUM/COUNT
      COMMON /REM/REM

      choice=0
      DO P = 1,COUNT
      H=HA(P)+C*IHZ(P)
      if (C.le.0.D0) then
      x1 = C
      x2 = 0.D0
      else
      x1 = 0.D0
      C   x2 = H + 2.D0*HTSTAR
      C   if (x2.gt.C) x2 = C*IHZ(P)
      x2 = C

      endif
      HPRIM = rtbis(REMBIS,x1,x2,error,p,REM,choice)
      END DO

      RETURN
      END

C-----
      FUNCTION REMBIS(HPRIM,P,REM)
C-----
      IMPLICIT NONE

      REAL*8 C,FIELD,MEANC0,MEANC(1000),WIDTHC(1000),MEAN,
      *       WIDTHI,HTSTAR,msat,f,gamma,ALPHA,WEIGHT,INFINITY,
      *       INFINITYI,shift

      COMMON
      /FITPARAMETERS/C,FIELD,MEANC0,MEANC,WIDTHC,MEAN,
      *       WIDTHI,HTSTAR,msat,f,gamma,ALPHA,WEIGHT,INFINITY,
      *       INFINITYI,shift

      REAL*8 DELTAC,NORMC
      REAL*8 DELTAI,NORMI

      COMMON /NORMC/NORMC,DELTAC
      COMMON /NORMI/NORMI,DELTAI

      REAL*8 FACTOR(20),XA(20),XB(20),XPRIM(20),XR(999),
      *       YA(20),YB(20),INTEG,SUMK,H,HA(300),IHZ(300),NC

```

## A2.1 Fortran Program for Preisach Calculations (General)

```

COMMON /MAG/HA,IHZ
INTEGER*4 I,J,P,Q,Q2,TAG,LG
REAL*8 REM(300),REMBIS,REML,HPRIM

H=HA(P)+C*IHZ(P)
REM(P) = 0.D0
INTEG = 0.D0
IF (H.LE.HTSTAR) THEN
  FACTOR(1)= 2.D0
  FACTOR(2)= 2.D0*(1.D0-WEIGHT)
  FACTOR(3)= 2.D0*(1.D0-WEIGHT)
  FACTOR(4)= 2.D0*(1.D0-WEIGHT)
  FACTOR(5)= 2.D0*(WEIGHT)
  FACTOR(6)= 2.D0*(WEIGHT)
  FACTOR(7)= -2.D0*(WEIGHT)
  FACTOR(8)= -2.D0*(WEIGHT)
  FACTOR(9)= -2.D0
  FACTOR(10)= -2.D0
  FACTOR(11)= -2.D0*(WEIGHT)
  FACTOR(12)= -2.D0*(WEIGHT)
  XA(1)=0.D0
  XA(2)=0.D0
  XA(3)=H
  XA(4)=HTSTAR
  XA(5)=0.D0
  XA(6)=H + HTSTAR
  XA(7)=H
  XA(8)=HTSTAR
  XA(9)=0.D0
  XA(10)=HTSTAR
  XA(11)=HTSTAR
  XA(12)=HTSTAR +(H-HPRIM)/2.D0
  XB(1)=H
  XB(2)=H
  XB(3)=HTSTAR
  XB(4)=H + HTSTAR
  XB(5)=H + HTSTAR
  XB(6)=INFINITY
ELSE
  FACTOR(1)= 2.D0
  FACTOR(2)= 2.D0
  FACTOR(3)= 2.D0*(1.D0-WEIGHT)
  FACTOR(4)= 2.D0*(1.D0-WEIGHT)
  FACTOR(5)= 2.D0*(WEIGHT)
  FACTOR(6)= 2.D0*(WEIGHT)
  FACTOR(7)= -2.D0
  FACTOR(8)= -2.D0
  FACTOR(9)= -2.D0*(WEIGHT)
  FACTOR(10)= -2.D0*(WEIGHT)
  XA(1)=0.D0
  XA(2)=HTSTAR
  XA(3)=0.D0
  XA(4)=(H+HTSTAR)/2.D0
  XA(5)=0.D0
  XA(6)=H+HTSTAR
  XA(7)=0.D0
  XA(8)=HTSTAR
  XA(9)=(HTSTAR+H)/2.D0
  XA(10)=HTSTAR +(H-HPRIM)/2.D0
  XB(1)=HTSTAR
  XB(2)=(H+HTSTAR)/2.D0
  XB(3)=(H+HTSTAR)/2.D0
  XB(4)=H+HTSTAR
  XB(5)=H+HTSTAR
  XB(6)=INFINITY
  XB(7)=HTSTAR
  XB(8)=HTSTAR+(H-HPRIM)/2.D0
  XB(9)=HTSTAR+(H-HPRIM)/2.D0
  XB(10)=INFINITY
  Q2=10
END IF

```

## A2.1 Fortran Program for Preisach Calculations (General)

```

DO Q=1,Q2
  SUMK = 0.D0
  J = 1
  I = 1
  TAG = 0
  LG = 0
  CALL INTEG2D(XA,XB,Q,P,J,I,TAG,&5,INTEG,XPRIM,XR,NC,
    YA,YB,SUMK,FACTOR,LG)
5  TAG = 1
  LG = 0
  IF (H.LE.HTSTAR) THEN
    YA(1)=XPRIM(J)
    YA(2)=0.D0
    YA(3)=0.D0
    YA(4)=0.D0
    YA(5)=-XPRIM(J)
    YA(6)=-XPRIM(J)
    YA(7)=H
    YA(8)=XPRIM(J)+(H-HTSTAR)
    YA(9)=HPRIM
    YA(10)=XPRIM(J)+(HPRIM-HTSTAR)
    YA(11)=-XPRIM(J)+(H+HTSTAR)
    YA(12)=XPRIM(J)+(HPRIM-HTSTAR)
    YB(1)=H
    YB(2)=XPRIM(J)
    YB(3)=H
    YB(4)=-XPRIM(J)+(H+HTSTAR)
    YB(5)=0.D0
    YB(6)=-XPRIM(J)+(H+HTSTAR)
    YB(7)=XPRIM(J)
    YB(8)=XPRIM(J)
    YB(9)=H
    YB(10)=-XPRIM(J)+(H+HTSTAR)
    YB(11)=XPRIM(J)+(H-HTSTAR)
    YB(12)=XPRIM(J)+(H-HTSTAR)
  ELSE
    YA(1)=XPRIM(J)
    YA(2)=XPRIM(J)
    YA(3)=0.D0
    YA(4)=0.D0
    YA(5)=-XPRIM(J)
    YA(6)=-XPRIM(J)
    YA(7)=HPRIM
    YA(8)=XPRIM(J)+(HPRIM-HTSTAR)
    YA(9)=-XPRIM(J)+(H+HTSTAR)
    YA(10)=XPRIM(J)+(HPRIM-HTSTAR)
    YB(1)=H
    YB(2)=-XPRIM(J)+(H+HTSTAR)
    YB(3)=XPRIM(J)
    YB(4)=-XPRIM(J)+(H+HTSTAR)
    YB(5)=0.D0
    YB(6)=-XPRIM(J)+(H+HTSTAR)
    YB(7)=H
    YB(8)=-XPRIM(J)+(H+HTSTAR)
    YB(9)=XPRIM(J)
    YB(10)=XPRIM(J)
    END IF
    CALL INTEG2D(XA,XB,Q,P,J,I,TAG,&5,INTEG,XPRIM,XR,NC,
      YA,YB,SUMK,FACTOR,LG)
    INTEG=INTEG+SUMK
  END DO
  REM(P) = INTEG
  CALL RESUB(C,f,gamma,REM,P)
  IF (C.NE.0.D0) THEN
    REML = HPRIM/C
  ELSE
    REML = REM(P)
  ENDIF
  REMBIS = REM(P) - REML
  WRITE(6,*) 'REMBIS',REMBIS, P, HPRIM
  RETURN
END
C-----
SUBROUTINE DEMAGCALC
C-----
C This program calculates the demagnetizing curve. i(h) DEMAG.

```

## A2.1 Fortran Program for Preisach Calculations (General)

```

C-----
      IMPLICIT NONE
      REAL*8 C,FIELDC,MEANC0,MEANC(1000),WIDTHC(1000),MEANI,
      *      WIDTHI,HTSTAR,msat,f,gamma,ALPHA,WEIGHT,INFINITY,
      *      INFINITYI,shift

      COMMON
/FTTPARAMETERS/C,FIELDC,MEANC0,MEANC,WIDTC,MEANI,
      *      WIDTHI,HTSTAR,msat,f,gamma,ALPHA,WEIGHT,INFINITY,
      *      INFINITYI,shift

      REAL*8 DELTAC,NORMC
      REAL*8 DELTAI,NORMI

      COMMON /NORMC/NORMC,DELTAC
      COMMON /NORMI/NORMI,DELTAI

      REAL*8 FACTOR(20),XA(20),XB(20),XPRIM(20),XR(999),
      *
YA(20),YB(20),INTEG,SUMK,H,HAD(300),IHDZ(300),NC,REM(300)

      COMMON /DEMAG/HAD,IHDZ
      COMMON /REM/REM

      INTEGER*4 COUNT,I,J,P,Q,Q2,TAG,LG
      COMMON /NUM/COUNT

      DO P=1,COUNT

      IHDZ(P) = 0.D0
      INTEG = 0.D0

      H=C*REM(COUNT)-(P-1.D0)/13.D0
      FACTOR(1)= 2.D0
      FACTOR(2)= 2.D0
      FACTOR(3)= 2.D0*(1.D0-WEIGHT)
      FACTOR(4)= 2.D0*(1.D0-WEIGHT)
      FACTOR(5)= 2.D0*(WEIGHT)
      FACTOR(6)= 2.D0*(WEIGHT)

      FACTOR(7)= -2.D0
      FACTOR(8)= -2.D0
      XA(1)=0.D0
      XA(2)=HTSTAR
      XA(3)=0.D0
      XA(4)=INFINITY
      XA(5)=0.D0
      XA(6)=INFINITY
      XA(7)=0.D0
      XA(8)=HTSTAR
      XB(1)=HTSTAR
      XB(2)=INFINITY
      XB(3)=INFINITY
      XB(4)=INFINITY
      XB(5)=INFINITY
      XB(6)=INFINITY
      XB(7)=HTSTAR
      XB(8)=INFINITY
      Q2=8

      DO Q=1,Q2
      TAG = 0
      LG = 0
      SUMK = 0.D0
      J = 1
      I = 1
      CALL INTEG2D(XA,XB,Q,P,J,I,TAG,&5,INTEG,XPRIM,XR,NC,
      *      YA,YB,SUMK,FACTOR,LG)
      TAG = 1
      LG = 0
      YA(1)=XPRIM(J)
      YA(2)=XPRIM(J)
      YA(3)=0.D0
      YA(4)=0.D0
      YA(5)=-XPRIM(J)
      YA(6)=-XPRIM(J)
      YA(7)=H
      YA(8)=XPRIM(J)+(H-HTSTAR)
      YB(1)=INFINITYI
      YB(2)=INFINITYI

```

## A2.1 Fortran Program for Preisach Calculations (General)

```

YB(3)=XPRIM(J)
YB(4)=INFINITYI
YB(5)=0.D0
YB(6)=INFINITYI
YB(7)=INFINITYI
YB(8)=INFINITYI

* CALL INTEG2D(XA,XB,Q,P,J,I,TAG,&5,INTEG,XPRIM,XR,NC,
YA,YB,SUMK,FACTOR,LG)

INTEG=INTEG+SUMK

END DO

IF (H.LE.0.D0) THEN
    IHDZ(P) = ((1.D0-f)*INTEG - f*(1.D0-DEXP(+gamma*H)))
ELSE
    IHDZ(P) = ((1.D0-f)*INTEG + f*(1.D0-DEXP(-gamma*H)))
END IF

HAD(P)=H-C*IHDZ(P)
END DO

RETURN
END
C-----
SUBROUTINE DEREMCALC
C-----
C This program calculates the demagnetizing remanence id.
C-----

IMPLICIT NONE
REAL*8 C,FIELD,MEANC0,MEANC(1000),WIDTHC(1000),MEANI,
* WIDTHI,HTSTAR,msat,f,gamma,ALPHA,WEIGHT,INFINITY,
* INFINITYI,shift

COMMON
/FTPARAMETERS/C,FIELD,MEANC0,MEANC,WIDTHC,MEANI,
* WIDTHI,HTSTAR,msat,f,gamma,ALPHA,WEIGHT,INFINITY,
* INFINITYI,shift

REAL*8 rnbis,HPRIM,DEREMBIS,error,x1,x2,DEREM(300),IHDZ(300),
* HAD(300),H
INTEGER*4 COUNT,P,choice

EXTERNAL DEREMBIS

COMMON /NUM/COUNT
COMMON /DEREM/DEREM
COMMON /DEMAG/HAD,IHDZ

choice=1
C write(6,*) 'CHOICE =', choice

DO P = 1,COUNT
H=HAD(P)+C*IHDZ(P)
if (C.le.0.d0) then
x1 = -C
x2 = H - 2.D0*HTSTAR
if (x2.lt.C) x2 = C
else
x2 = -C
C x2 = H - 2.D0*HTSTAR
C if (x2.lt.-C) x2 = -C
x1 = C
endif
HPRIM = rnbis(DEREMBIS,x1,x2,error,P,DEREM,choice)
END DO

RETURN
END
C-----
FUNCTION DEREMBIS(HPRIM,P,DEREM)
C-----

IMPLICIT NONE

REAL*8 C,FIELD,MEANC0,MEANC(1000),WIDTHC(1000),MEANI,
* WIDTHI,HTSTAR,msat,f,gamma,ALPHA,WEIGHT,INFINITY,
* INFINITYI,shift

```



## A2.1 Fortran Program for Preisach Calculations (General)

```

YB(3)=XPRIM(J)
YB(4)=INFINITYI
YB(5)=0.D0
YB(6)=INFINITYI
YB(7)=INFINITYI
YB(8)=INFINITYI
YB(9)=HPRIM
YB(10)=-XPRIM(J)+(HPRIM+HTSTAR)
CALL INTEG2D(XA,XB,Q,P,J,I,TAG,&5,INTEG,XPRIM,XR,NC,
*
YA,YB,SUMK,FACTOR,LG)

INTEG=INTEG+SUMK

END DO

DEREM(P) = INTEG
C WRITE(6,*) 'DEREM =',DEREM(P)
CALL RESUB(C,f,gamma,DEREM,P)
IF (C.NE.0.D0) THEN
  DEREML = HPRIM/C
ELSE
  DEREML = DEREM(P)
ENDIF
DEREMBIS = DEREM(P) - DEREML

RETURN
END

C-----
SUBROUTINE
INTEG1D(XA,XB,N,DELTA,MEAN,WIDTH,NORM,INTEG,LG)
C-----
C This program calculates an integral in one dimension.
C Divides a given range into N parts, and each of these N into ten.
C-----

IMPLICIT NONE
REAL*8 X(10),W(10),Y(10),FUNCP(10),A(9999),B(9999)
REAL*8 XA,XB,DELTA,MEAN,WIDTH,FUNC,INTEG,NORM

COMMON /INTEGRATION/W,X

```

```

INTEGER*4 NJ,K,LG

EXTERNAL FUNC

INTEG=0.D0

DO J=1,N
  A(J) = XA+DFLOAT(J-1)*DELTA
  B(J) = XA+DFLOAT(J)*DELTA
  DO K=1,10
    Y(K) = (B(J)-A(J))*X(K)/2.D0+(B(J)+A(J))/2.D0
    FUNCP(K) = FUNC(Y,K,MEAN,WIDTH,NORM,LG)
    INTEG = INTEG + (B(J)-A(J))*W(K)*FUNCP(K)/2.D0
  END DO
END DO

RETURN
END

C-----
SUBROUTINE INTEG2D(XA,XB,Q,P,J,I,TAG,*,INTEG,XPRIM,XR,NC,
*
YA,YB,SUMK,FACTOR,LG)
C-----
C This program calculates an integral in two dimensions.
C-----

IMPLICIT NONE
REAL*8 W(10),X(10)
REAL*8 C,FIELD,MEANC0,MEANC(1000),WIDTHC(1000),MEANI,
*
WIDTHI,HTSTAR,msat,f,gamma,ALPHA,WEIGHT,INFINITY,
*
INFINITYI,shift

COMMON /INTEGRATION/W,X
COMMON
/FTPARAMETERS/C,FIELD,MEANC0,MEANC,WIDTHC,MEANI,
*
WIDTHI,HTSTAR,msat,f,gamma,ALPHA,WEIGHT,INFINITY,
*
INFINITYI,shift

REAL*8 DELTAC,NORMC
REAL*8 DELTAI,NORMI

COMMON /NORMC/NORMC,DELTAC

```

## A2.1 Fortran Program for Preisach Calculations (General)

```

COMMON /NORMI,NORMI,DELTAI
INTEGER*4 Q,I,J,K,L,P,TAG,LG
REAL*8 FUNC1(10),XA(20),XB(20),X1(999),X2(999),XM(999),XR(999),
* DX(10),XPRIM(10),
* FUNC2(10),YA(20),YB(20),Y1(999),Y2(999),YM(999),YR(999),
* DY(10),YPRIM(10),
* FACTOR(20)
REAL*8 INTEG,SUMK,NC,NI,DELTA1,DELTA2,FUNC
EXTERNAL FUNC
IF (TAG.EQ.1.D0) GO TO 20
NC = IDINT((XB(Q)-XA(Q))/DELTA2)
IF (NC.LT.1.D0) NC=1.D0
DELTA1=(XB(Q)-XA(Q))/NC
DO I=1,NC
  X1(I) = XA(Q)+DFLOAT(I-1)*DELTA1
  X2(I) = XA(Q)+DFLOAT(I)*DELTA1
  XM(I) = 0.5D0*(X2(I)+X1(I))
  XR(I) = 0.5D0*(X2(I)-X1(I))
DO J=1,10
  DX(J)=XR(I)*X(I)
  XPRIM(J)=DX(J)+XM(I)
  IF (XPRIM(J).LT.0.D0) pause 'BAD NUMBER'
  RETURN
C
NI = IDINT((YB(Q)-YA(Q))/DELTA1)
IF (NILT.1.D0) NI = 1.D0
DELTA2 = (YB(Q)-YA(Q))/NI
DO L=1,NI
  Y1(L) = YA(Q)+DFLOAT(L-1)*DELTA2
  Y2(L) = YA(Q)+DFLOAT(L)*DELTA2
  YM(L) = 0.5D0*(Y2(L)+Y1(L))
  YR(L) = 0.5D0*(Y2(L)-Y1(L))
END DO
DO K=1,10
  DY(K)=YR(L)*X(K)
  YPRIM(K)=DY(K)+YM(L)
  FUNC1(K) = FUNC(XPRIM,J,MEANC,WIDTHC,NORMC,1)
  FUNC2(K) = FUNC(YPRIM,K,MEANI,WIDTHI,NORMI,0)
  SUMK=SUMK + W(K)*W(J)*YR(L)*XR(I)*
    FUNC1(K)*FUNC2(K)*FACTOR(Q)
END DO
END DO
END DO
END DO
RETURN
END
C-----
FUNCTION FUNC(Y,K,MEAN,WIDTH,NORM,LG)
C-----
IMPLICIT NONE
REAL*8 FUNC,MEAN,WIDTH,NORM,Y(10),pi
INTEGER*4 K,LG
pi = 3.1415926535D0
C
IF (LG.EQ.0) THEN
  FUNC =DEXP(-(Y(K)-MEAN)**2.D0/(2.D0*(WIDTH**2.D0)))/
    (NORM**((2.D0*(WIDTH**2.D0)*pi)**0.5D0))
C
ELSE IF ((LG.EQ.1).AND.(Y(K).EQ.0.D0)) THEN
  FUNC = 0.D0
C
ELSE
  FUNC =DEXP(-(DLOG(Y(K))**2.D0/(2.D0*(WIDTH**2.D0)))/
    (NORM*Y(K)**(2.D0*(WIDTH**2.D0)*pi)**0.5D0))
C
IF (Y(K).LT.0.D0) PAUSE 'BAD NUMBER'
C
ENDIF
END
C-----

```

## A2.1 Fortran Program for Preisach Calculations (General)

```

C-----
SUBROUTINE RESUB(C,f,gamma,REM,P)
C-----
C      Use resubstitution to determine reversible component of remanences.
C-----
      IMPLICIT NONE
      REAL*8 C,f,gamma,DIFIRZ,REM(300),IRZ,IRZO
      INTEGER*4 P,R
      IRZO = REM(P)
      WRITE(6,*) IRZO
      R = 0
      DO R = 1,50
      IF ((C*IRZO).LE.0.D0) THEN
      IRZ = -f*(1.D0-DEXP(+gamma*(C*IRZO))) + (1.D0-f)*REM(P)
      ELSE
      IRZ = f*(1.D0-DEXP(-gamma*(C*IRZO))) + (1.D0-f)*REM(P)
      END IF
      IF (IRZ.NE.0.D0) THEN
      DIFIRZ = (IRZ - IRZO)/IRZ
      ELSE
      DIFIRZ = (IRZ - IRZO)
      END IF
      IF (DABS(DIFIRZ).LT.1.D-4) THEN
      GO TO 10
      ELSE
      IRZO = IRZ
      END IF
      END DO
      PAUSE 'Did not converge'
      REM(P) = IRZ
      WRITE(6,*) P, 'Converged'
      RETURN
      END
C-----
FUNCTION rbis(rembis,x1,x2,xacc,p,REM,choice)
      INTEGER*4 JMAX
      REAL*8 rbis,x1,x2,xacc,derembis,rembis,REM(300)
      EXTERNAL rembis,derembis
      PARAMETER (JMAX=50)
      INTEGER*4 j,p,choice
      REAL*8 dx,f,fmid,xmid
      xacc = 1.d-4
      if (choice.eq.0) then
      fmid=rembis(x2,p,REM)
      if (fmid.eq.0.d0) return
      f=rembis(x1,p,REM)
      if (f.eq.0.d0) return
      else
      fmid=derembis(x2,p,REM)
      if (fmid.eq.0.d0) return
      f=derembis(x1,p,REM)
      if (f.eq.0.d0) return
      endif
      if(f*fmid.ge.0.d0) pause 'root must be bracketed in rbis'
      if(f.lt.0.d0)then
      rbis=x1
      dx=x2-x1
      else
      rbis=x2
      dx=x1-x2
      endif
      do 11 j=1,JMAX
      dx=dx*.5
      xmid=rbis+dx
      if (choice.eq.0) then
      fmid=rembis(xmid,p,REM)
      else
      fmid=derembis(xmid,p,REM)
      endif
      if(fmid.le.0.d0)rbis=xmid
      if(abs(dx).lt.xacc .or. fmid.eq.0.d0) return
      11 continue
      !! pause 'too many bisections in rbis'

```

## A2.1 Fortran Program for Preisach Calculations (General)

```

END
C-----
SUBROUTINE DEMAGINTERPOL
C-----
C      This program calculates the demagnetizing curve, i(h) DEMAG, using an
C      interpolation routine.
C-----

      REAL*8 HA(300),IHZ(300)
      REAL*8 HAD(300),IHDZ(300),HADP(300),IHDZP(300)

      COMMON /MAG/HA,IHZ
      COMMON /DEMAG/HAD,IHDZ

      INTEGER*4 COUNT

      COMMON /NUM/COUNT

      INTEGER*4 j, k, l, m, n_data, n_interp, n_point, q

c-----j (returned from locate subroutine), l and m are indices

      PARAMETER (n_point = 4) ! n_point interpolation.
      REAL*8 xx(n_point), yy(n_point) ! The data points sent to the
      ! interpolation subroutine.
      REAL*8 dy, x, y ! x is the interpolation point.
      ! y and the uncertainty dy are returned from
      ! the interpolation subroutine

      n_data = COUNT ! Number of data points.
      n_interp = COUNT ! Number of interpolation points.

      do k = 1, n_interp !for each interpolation point

         x = -HA(k)

c-----The subroutine locate finds the position of x such that it lies
c      between xa(j) and xa(j+1). It returns the value "j".
         call locate(HAD,n_data,x,j)

c----- The following if-then-else block contains "magic numbers"
c      particular to n_point = 4.

         if ( (j .EQ. 1) .OR. (j .EQ. 2) ) then
            m = 1 ! The first 4 data points must be used.
         else
            if ((j .EQ. n_data) .OR. (j .EQ. n_data-1)) then
               m = n_data + 1 - n_point !The last 4 data points must
               !be used.
            else
               if ( ABS(HAD(j-2)-x) .LE. ABS(HAD(j+2)-x) ) then
                  m = j-2 !Here there is an ambiguity. If x is
                  !closer to xa(j-2) than to xa(j+2) then
               else
                  m = j+1 !the four points used start with j-2, if
                  !not the first point is the j-1 point.
               end if
            end if
         end if

         do l = 1, n_point
            xx(l) = HAD(m+l-1)
            yy(l) = IHDZ(m+l-1)
         enddo

c-----Call the interpolation subroutine, ratint, for rational function
c      interpolation.

         call ratint(xx,yy,n_point,x,y,dy)

         HADP(k) = x
         IHDZP(k) = y

10      enddo ! Repeat for the next interpolation point, x.

         do q = 1,COUNT
            HAD(q) = HADP(q)
            IHDZ(q) = IHDZP(q)
         end do

70      FORMAT (2G23.16)

```

## A2.1 Fortran Program for Preisach Calculations (General)

C Interpolation routine from Numerical Recipes.  
C-----

RETURN  
end

C-----  
SUBROUTINE LOCATE(xx,n,x,j)  
C-----

C Used for the interpolation routine. From Numerical Recipes.  
C-----

IMPLICIT NONE

INTEGER\*4 j,n  
REAL\*8 x,xx(n)  
INTEGER\*4 j,jm,ju

j1 = 0  
ju = n+1  
if (ju-ji.gt.1) then  
jm = (ju+j1)/2  
if ((xx(n).ge.xx(1)).eqv.(x.ge.xx(jm))) then  
j1 = jm  
else

ju = jm  
endif  
goto 10  
endif  
if (x.eq.xx(1)) then  
j = 1  
else if (x.eq.xx(n)) then  
j = n-1  
else

j = j1  
endif

return  
END

C-----  
SUBROUTINE ratint(xa,ya,n,x,y,dy)  
C-----

IMPLICIT NONE

INTEGER\*4 n,NMAX  
REAL\*8 dy,x,y,xa(n),ya(n),TINY  
PARAMETER (NMAX=10,TINY=1.d-25)  
INTEGER\*4 i,m,ns  
REAL\*8 dd,h,hh,t,w,c(NMAX),d(NMAX)

ns=1  
hh=abs(x-xa(1))  
do 11 i=1,n  
h=abs(x-xa(i))  
if (h.eq.0.d0)then  
y=ya(i)  
dy=0.d0  
return

else if (h.lt.hh) then

ns=i  
hh=h  
endif

c(i)=ya(i)  
d(i)=ya(i)+TINY

11 continue

y=ya(ns)

ns=ns-1

do 13 m=1,n-1

do 12 i=1,n-m

w=c(i+1)-d(i)

h=xa(i+m)-x

t=(xa(i)-x)\*d(i)/h

dd=1-c(i+1)

if(dd.eq.0.d0)pause 'failure in ratint'  
if (dd.eq.0.d0) WRITE (6,\*) t,c(i+1),m

dd=w/dd

d(i)=c(i+1)\*dd

c(i)=1\*dd

12 continue

if (2\*ns.lt.n-m)then

dy=c(ns+1)

## A2.1 Fortran Program for Preisach Calculations (General)

```

else
  dy=d(ns)
  ns=ns-1
endif
y=y+dy
13 continue

return
END

C-----
      SUBROUTINE FILE
C-----
      REAL*8 C,FIELD,MEANC0,MEANC(1000),WIDTHC(1000),MEANI,
*          WIDTHI,HTSTAR,msat,f,gamma,ALPHA,WEIGHT,INFINITY,
*          INFINITYI,shift

      COMMON
/FTTPARAMETERS/C,FIELD,MEANC0,MEANC,WIDTC,MEANI,
*          WIDTHI,HTSTAR,msat,f,gamma,ALPHA,WEIGHT,INFINITY,
*          INFINITYI,shift

      REAL*8 HA(300),IHZ(300)
      REAL*8 HAD(300),IHDZ(300)
      REAL*8 IRZ(300),IDZ(300)

      COMMON /MAG/HA,IHZ
      COMMON /DEMAG/HAD,IHDZ
      COMMON /REM/IRZ
      COMMON /DEREM/IDZ

      INTEGER*4 COUNT,P,Q,R
      COMMON /NUM/COUNT

      OPEN (unit = 7, file = "mag1.o", status = 'OLD')
      OPEN (unit = 8, file = "rem1.o", status = 'OLD')
      OPEN (unit = 9, file = "henkel1.o", status = 'OLD')

      DO Q=1,COUNT
        WRITE (7,70) HAD(COUNT-(Q-1))*FIELD, IHDZ(COUNT-(Q-1))*msat
        WRITE (8,70) HA(P)*FIELD, IHZ(P)*msat
        WRITE (8,70) HA(P)*FIELD, IRZ(P)*msat
        END DO

        DO R=1,COUNT
          WRITE (9,70) IRZ(R)*msat, IDZ(R)*msat
        END DO

70  FORMAT(G23.16, ' ',G23.16)

      END FILE (9)
      END FILE (8)
      END FILE (7)
      CLOSE (9)
      CLOSE (8)
      CLOSE (7)

      RETURN
      END
C-----
      SUBROUTINE CHISQR(shift)
C-----
      IMPLICIT NONE

      REAL*8 mfield(300),mag(300),reman(300), hreman(300),
*          hdereman(300),rfield(300),xm(300),ym(300),xr(300),yr(300),
*          hx(300),hy(300),chisq,difsq,chisqtot,redchisq,shift
      INTEGER*4 kk,m,n,p,q,npts,COUNT,pp,qq,rr,chi,mpts,hnpts

      COMMON /NUM/COUNT
      COMMON /CH11/npts,mpts,hnpts,chi

      OPEN (unit = 3, file = "chi1.o", status = 'OLD')
      OPEN (unit = 7, file = "mag1.o", status = 'OLD')
      OPEN (unit = 8, file = "rem1.o", status = 'OLD')
      OPEN (unit = 9, file = "henkel1.o", status = 'OLD')

```

## A2.1 Fortran Program for Preisach Calculations (General)

```

OPEN (unit = 10, file = "cccr1.m.dat", status = 'OLD')
OPEN (unit = 11, file = "cccr1i.dat", status = 'OLD')
OPEN (unit = 12, file = "cccr1h.dat", status = 'OLD')

DO m = 1, npts
  READ (10,*) xm(m),ym(m)
  xm(m) = xm(m) + shift
enddo
CALL sort2(npts,xm,ym)

DO n = 1, mpts
  READ (11,*) xr(n),yr(n)
  xr(n) = xr(n) + shift
enddo
CALL sort2(mpts,xr,yr)

DO p = 1,COUNT*2
  READ (7,*) mfield(p),mag(p)
  READ (8,*) rfield(p),reman(p)
enddo

DO q = 1,COUNT
  READ (9,*) hcreman(q),hdcreman(q)
enddo

CLOSE (7)
CLOSE (8)
CLOSE (9)

chisqtot = 0.D0
OPEN (unit = 7, file = "polm1.o", status = 'OLD')
OPEN (unit = 8, file = "pol11.o", status = 'OLD')
OPEN (unit = 9, file = "polh1.o", status = 'OLD')

CALL CHINTERPOL(xm,mfield,mag,2*COUNT,npts,chi,shift)
chisq = 0.D0
difsq = 0.D0

DO pp = 1,npts
  WRITE (7,70) xm(pp)-shift,mag(pp)
  difsq = ((ym(pp)-mag(pp))**2.D0)/
    ((5.d-5*0.08d0+0.02d0*ym(pp))**2.D0)
  chisq = chisq + difsq
enddo

OPEN (unit = 10, file = "cccr1.m.dat", status = 'OLD')
OPEN (unit = 11, file = "cccr1i.dat", status = 'OLD')
OPEN (unit = 12, file = "cccr1h.dat", status = 'OLD')

DO m = 1, npts
  READ (10,*) xm(m),ym(m)
  xm(m) = xm(m) + shift
enddo
CALL sort2(npts,xm,ym)

DO n = 1, mpts
  READ (11,*) xr(n),yr(n)
  xr(n) = xr(n) + shift
enddo
CALL sort2(mpts,xr,yr)

DO p = 1,COUNT*2
  READ (7,*) mfield(p),mag(p)
  READ (8,*) rfield(p),reman(p)
enddo

DO q = 1,COUNT
  READ (9,*) hcreman(q),hdcreman(q)
enddo

CLOSE (7)
CLOSE (8)
CLOSE (9)

chisqtot = 0.D0
OPEN (unit = 7, file = "polm1.o", status = 'OLD')
OPEN (unit = 8, file = "pol11.o", status = 'OLD')
OPEN (unit = 9, file = "polh1.o", status = 'OLD')

CALL CHINTERPOL(xm,mfield,mag,2*COUNT,npts,chi,shift)
chisq = 0.D0
difsq = 0.D0

DO pp = 1,npts
  WRITE (7,70) xm(pp)-shift,mag(pp)
  difsq = ((ym(pp)-mag(pp))**2.D0)/
    ((5.d-5*0.08d0+0.02d0*ym(pp))**2.D0)
  chisq = chisq + difsq
enddo

CALL CHINTERPOL(xr,rfield,reman,2*COUNT,mpts,chi,shift)
chisq = 0.D0

DO qq = 1,mpts
  WRITE (8,70) xr(qq)-shift,reman(qq)
  difsq = ((yr(qq)-reman(qq))**2.D0)/
    ((5.d-5*0.08d0+0.02d0*yr(qq))**2.D0)
  chisq = chisq + difsq
enddo

DO qq = 1,mpts
  WRITE (6,*) redchisq
  WRITE (3,*) redchisq
enddo

CALL CHINTERPOL(hx,hreman,hdcreman,COUNT,hnpts,chi,shift)
chisq = 0.D0

DO kk = 1, hnpts
  READ (12,*) hx(kk),hy(kk)
enddo
CALL sort2(hnpts,hx,hy)

chi = 1

CALL CHINTERPOL(hx,hreman,hdcreman,COUNT,hnpts,chi,shift)
chisq = 0.D0

DO rr = 1, hnpts
  if (hx(rr).lt.0.d0) go to 5
  WRITE (9,70) hx(rr),hdcreman(rr)
  difsq = ((hy(rr)-hdcreman(rr))**2.D0)/
    ((5.d-5*0.08d0+0.02d0*hy(rr))**2.D0)
  chisq = chisq + difsq
enddo

```

## A2.1 Fortran Program for Preisach Calculations (General)

```

5          enddo
          redchisq = chisq/(hnpts-9)
          chisqtot = chisqtot + redchisq

          WRITE(6,*) redchisq
          WRITE(6,*) chisqtot
          WRITE(6,*) ' '
          WRITE(3,*) redchisq
          WRITE(3,*) chisqtot

70          FORMAT (2025.16)

          CLOSE (7)
          CLOSE (8)
          CLOSE (9)
          CLOSE (10)
          CLOSE (11)
          CLOSE (12)

          RETURN
          end

C-----
C-----SUBROUTINE CHINTERPOL(xdata,xcalc,ycalc,n_data,n_interp,chi,shift)
C-----
C-----This program calculates magnetization & remanence at data field points
C-----Uses an interpolation routine.
C-----
C-----IMPLICIT NONE
C-----INTEGER*4 j, k, l, m, n_data, n_interp, n_point, q, chi, COUNT
C-----j (returned from locate subroutine), l and m are indices
C-----
C-----PARAMETER (n_point = 4) ! n_point interpolation.
C-----REAL*8 xx(n_point), yy(n_point) ! The data points sent to the
C-----! interpolation subroutine.
C-----REAL*8 dy, x, y ! x is the interpolation point.
C-----! y and the uncertainty dy are returned from
C-----! the interpolation subroutine
C-----REAL*8 xcalc(300),ycalc(300),newx(300),newy(300),shift

          COMMON /NUM/COUNT
          do k = 1, n_interp !for each interpolation point
              x = xdata(k)
              c-----The subroutine locate finds the position of x such that it lies
              c-----between xa(j) and xa(j+1). It returns the value "j".
              if (chi.eq.0) then
                  call locate2(xcalc,n_data,x-shift,j)
              else
                  call locate2(xcalc,n_data,x,j)
              endif
              ! The following if-then-else block contains "magic numbers"
              ! particular to n_point = 4.
              if ( (j .EQ. 1) .OR. (j .EQ. 2) ) then
                  m = 1 ! The first 4 data points must be used.
              else
                  if ( (j .EQ. n_data) .OR. (j .EQ. n_data - 1) ) then
                      m = n_data + 1 - n_point ! The last 4 data points must
                      ! be used.
                  else
                      if ( ABS(xcalc(j-2)-x) .LE. ABS(xcalc(j+2)-x) ) then
                          m = j-2 ! Here there is an ambiguity. If x is
                          ! closer to xa(j-2) than to xa(j+2) then
                      else
                          m = j-1 ! the four points used start with j-2, if
                          ! not the first point is the j-1 point.
                      end if
                  end if
              end if
              if (chi.eq.0) then
                  if ( (j .GE. (COUNT-1)) .AND. (j .LT. (COUNT+1))) m = COUNT-3
                  if (x.eq.-1,d0) m = COUNT+1
              else
                  if ( (j .GE. (COUNT+1)) .AND. (j .LT. (COUNT+3))) m = COUNT+1
              end if
              continue
          end if
      enddo
  
```

## A2.1 Fortran Program for Preisach Calculations (General)

```

do 1 = 1, n_point
  xx(1) = xcalc(m+1-1)
  yy(1) = ycalc(m+1-1)
enddo

c-----Call the interpolation subroutine, polint, for rational function
c interpolation.

call ratint(xx,yy,n_point,x,y,dy)

newx(k) = x
newy(k) = y

10 enddo      ! Repeat for the next interpolation point, x.

do q = 1, n_interp
  xcalc(q) = newx(q)
  ycalc(q) = newy(q)
end do

70 FORMAT (2G23.16)

RETURN
end

C-----
C-----SUBROUTINE polint(xx,yy,n,x,y,dy)
C-----
INTEGER*4 n,NMAX
REAL*8 dy,x,y,xa(n),ya(n)
PARAMETER (NMAX=10)
INTEGER*4 i,m,ns
REAL*8 den,dif,dift,ho,hp,w,c(NMAX),d(NMAX)
ns=1
dif=abs(x-xa(1))
do 11 i=1,n
  dift=abs(x-xa(i))
  if (dift.lt.dif) then
    ns=i
    dif=dift
  endif
enddo

c(i)=ya(i)
d(i)=ya(i)
11 continue
y=ya(ns)
ns=ns-1
do 13 m=1,n-1
do 12 i=1,n-m
  ho=xa(i)-x
  hp=xa(i+m)-x
  w=c(i+1)-d(i)
  den=ho-hp
  if(den.eq.0.d0)pause 'failure in polint'
  den=w/den
  d(i)=hp*den
  c(i)=ho*den
12 continue
  if (2*ns.lt.n-m)then
    dy=c(ns+1)
  else
    dy=d(ns)
  endif
  ns=ns-1
  y=y+dy
13 continue
return
END

C-----
C-----SUBROUTINE LOCATE2(xx,n,x,j)
C-----
C----- Used for the interpolation routine. From Numerical Recipes.
C-----
IMPLICIT NONE
INTEGER*4 j,n
REAL*8 x,xx(n)
INTEGER*4 j1,jm,ju

```



## A2.1 Fortran Program for Preisach Calculations (General)

```
      brr(i)=brr(i+1)
      brr(i+1)=temp
    endif
    i=i+1
    j=ir
    a=arr(i+1)
    b=brr(i+1)
    continue
    i=i+1
3   if(arr(i).lt.a)goto 3
    continue
    j=j-1
    if(arr(j).gt.a)goto 4
    if(j.lt.i)goto 5
    temp=arr(i)
    arr(i)=arr(j)
    arr(j)=temp
    temp=brr(i)
    brr(i)=brr(j)
    brr(j)=temp
    goto 3
5   arr(i+1)=arr(i)
    arr(j)=a
    brr(i+1)=brr(i)
    brr(j)=b
    jstack=jstack+2
    if(jstack.gt.NSTACK)pause 'NSTACK too small in sort2'
    if(ir-i+1.ge.j-1)then
      istack(jstack)=ir
      istack(jstack-1)=i
      i=j-1
    else
      istack(jstack)=j-1
      istack(jstack-1)=i
      i=j
    endif
  endif
  goto 1
END
```

## A2.2 Fortran Program for Preisach Calculations (Nd<sub>2</sub>Fe<sub>14</sub>B)

```

C NdFeB
C THERMALLY demagnetized initial state. One thermal field.
C This program calculates id versus ir to generate Henkel plots, using
C the cumulative technique. Good for k = 0 only.
C
  REAL*8 W(10),X(10),C,MEAN,WIDTH,WIDTHI,HCSTAR,HSCALE,MSCALE,
  * FRCT,WIDTHA,gamma,alpha
  COMMON /DIST/MEAN,WIDTH,WIDTHI,HCSTAR,WIDTHA/C,W,X
  COMMON HSCALE,MSCALE,FRCT,gamma,alpha
C
C Get value for k and coercive field (hc) distribution parameters.
C
  OPEN (FILE='kmw1.dar', UNIT=4, ACCESS='SEQUENTIAL',
  * FORM='FORMATTED', STATUS='OLD')
  READ (4,*) C,WIDTH,MEAN,WIDTHA,WIDTHI,HCSTAR,HSCALE,
  * MSCALE,FRCT,gamma,alpha
C
C X and W values for integration scheme.
C
  X(1) = -0.9739065285D0
  W(1) = 0.0666713443D0
  X(2) = -0.8650633667D0
  W(2) = 0.1494513492D0
  X(3) = -0.6794095683D0
  W(3) = 0.2190863625D0
  X(4) = -0.4333953941D0
  W(4) = 0.2692667193D0
  X(5) = -0.1488743390D0
  W(5) = 0.2955242247D0
  X(6) = -X(5)
  W(6) = W(5)
  X(7) = -X(4)
  W(7) = W(4)
  X(8) = -X(3)
  W(8) = W(3)
  X(9) = -X(2)
  W(9) = W(2)
  X(10) = -X(1)
  W(10) = W(1)
C
C Call subroutines to calculate i(h),ir,i(h)DEMAG,id,iinf, and
C tabulate results.
C
  CALL NORMCALC
  CALL NORMCALC2
  CALL NORMCALC3
  CALL NORMSCALC
  CALL IHCALC
  CALL IRCALC
  CALL IINFCALC
  CALL IHDCALC
  CALL IDCALC
  CALL DELT
C
  CLOSE (4)
  STOP
  END
C
  SUBROUTINE NORMCALC
C This program calculates integral of the hc-gaussian in one dimension.
C Divides a given range into N parts, and each of these N into ten.
C
  REAL*8 FUNC(10),X(10),W(10),Y(10),A(9999),B(9999)
  REAL*8
  INTEG,XA,XB,WIDTH,WIDTHI,MEAN,NORM,C,HCSTAR,DELTAS,DELTAC,
  * HSTART,NORMA,DELTA A,WIDTHA,NORM3,DELTA2
  COMMON
  /DIST/MEAN,WIDTH,WIDTHI,HCSTAR,WIDTHA/NORMAL/NORM,NORMA,
  * NORM3/C,W,X
  COMMON /DEL/ DELTAS,DELTAC,HSTART,DELTA A,DELTA2
C
  N=24
  XA=0.D0
  XB=6.D0
  N=40
  XA=0.D0
  XB=60.D0
  DELTAC=(XB-XA)/DFLOAT(N)
  INTEG=0.D0
  DO 50 J=1,N

```

## A2.2 Fortran Program for Preisach Calculations (Nd<sub>2</sub>Fe<sub>14</sub>B)

```

A(J) = -XA+DFLOAT(J-1)*DELTAC
B(J) = -XA+DFLOAT(J)*DELTAC
DO 50 K=1,10
Y(K) = (B(J)-A(J))*X(K)/2.DO+(B(J)+A(J))/2.DO
C   FUNC(K) = EXP(-(Y(K)-1.DO)**2/((WIDTH**2.DO)*2.DO))/
C   * ((2.DO*(WIDTH**2.DO)*3.14159265D0)**0.5D0)
  FUNC(K) = DEXP(-(DLOG(Y(K)))**2.DO/((WIDTH**2.DO)*2.DO))/
  * (Y(K)*(2.DO*(WIDTH**2.DO)*3.14159265D0)**0.5D0)
  INTEG = INTEG + (B(J)-A(J))*W(K)*FUNC(K)/2.DO
50 CONTINUE
NORM = INTEG
60 FORMAT(1X,G25.16)
WRITE (6,*) NORM
RETURN
END
C
SUBROUTINE NORMCALC2
C This program calculates integral of the hc-gaussian in one dimension.
C Divides a given range into N parts, and each of these N into ten.
C
REAL*8 FUNC(10),X(10),W(10),Y(10),A(9999),B(9999)
REAL*8
INTEG,XA,XB,WIDTH,WIDTHI,MEAN,NORM,C,HCSTAR,DELTAS,DELTAC,
  * HSTART,NORMA,DELTA2,WIDTHA,NORM3,DELTA2
COMMON
/DIST/MEAN,WIDTH,WIDTHI,HCSTAR,WIDTHA/NORMAL/NORM,NORMA,
  * NORM3//C,W,X
COMMON /DEL/ DELTAS,DELTAC,HSTART,DELTA2,DELTA2
C
C   N=20
C   XA=0.D0
C   XB=6.D0
N=80
XA=0.D0
XB=60.D0
DELTA2=(XB-XA)/DFLOAT(N)
INTEG=0.D0
DO 50 J=1,N
  A(J) = -XA+DFLOAT(J-1)*DELTA2
  B(J) = -XA+DFLOAT(J)*DELTA2

```

```

DO 50 K=1,10
Y(K) = (B(J)-A(J))*X(K)/2.DO+(B(J)+A(J))/2.DO
C   FUNC(K) = EXP(-(Y(K)-MEAN)**2/((WIDTHA**2.DO)*2.DO))/
C   * ((2.DO*(WIDTHA**2.DO)*3.14159265D0)**0.5D0)
  FUNC(K) = DEXP(-(DLOG(Y(K)/MEAN))**2.DO/((WIDTHA**2.DO)*2.DO))/
  * (Y(K)*(2.DO*(WIDTHA**2.DO)*3.14159265D0)**0.5D0)
  INTEG = INTEG + (B(J)-A(J))*W(K)*FUNC(K)/2.DO
50 CONTINUE
NORMA = INTEG
60 FORMAT(1X,G25.16)
WRITE (6,*) NORMA
RETURN
END
C
SUBROUTINE NORMCALC3
C This program calculates integral of the hc-gaussian in one dimension.
C Divides a given range into N parts, and each of these N into ten.
C
REAL*8 FUNC(10),X(10),W(10),Y(10),A(9999),B(9999)
REAL*8
INTEG,XA,XB,WIDTH,WIDTHI,MEAN,NORM,C,HCSTAR,DELTAS,DELTAC,
  * HSTART,NORMA,DELTA2,WIDTHA,DELTA2,NORM3
COMMON
/DIST/MEAN,WIDTH,WIDTHI,HCSTAR,WIDTHA/NORMAL/NORM,NORMA,
  * NORM3//C,W,X
COMMON /DEL/ DELTAS,DELTAC,HSTART,DELTA2,DELTA2
C
C   N=20
C   XA=0.D0
C   XB=6.D0
N=80
XA=0.D0
XB=60.D0
DELTA2=(XB-XA)/DFLOAT(N)
INTEG=0.D0
DO 50 J=1,N
  A(J) = -XA+DFLOAT(J-1)*DELTA2
  B(J) = -XA+DFLOAT(J)*DELTA2
DO 50 K=1,10
Y(K) = (B(J)-A(J))*X(K)/2.DO+(B(J)+A(J))/2.DO

```

## A2.2 Fortran Program for Preisach Calculations (Nd<sub>2</sub>Fe<sub>14</sub>B)

```

C   FUNC(K)=EXP(-(Y(K)-1.D0)**2/((WIDTH**2.D0)*2.D0)/
C   • ((2.D0*(WIDTH**2.D0)*3.14159265D0)**0.5D0)
  FUNC(K)=DEXP(-(DLOG(Y(K)/(1.D0+alpha*MEAN)))**2.D0/((WIDTH**2.D0)
  • *2.D0)/(Y(K)*((2.D0*(WIDTH**2.D0)*3.14159265D0)**0.5D0))
    INTEG = INTEG + (B(J)-A(J))*W(K)*FUNC(K)/2.D0
50  CONTINUE
    NORM3 = INTEG
60  FORMAT(1X,G25.16)
    WRITE (6,*) NORM3
    RETURN
    END

C
  SUBROUTINE NORMSCALC
C This program calculates integral of the hs-gaussian in one dimension.
C Divides a given range into N parts, and each of these N into ten.
C
  REAL*8 FUNC(10),X(10),W(10),Y(10),A(9999),B(9999)
  REAL*8
  INTEG,XA,XB,WIDTH,WIDTHI,MEAN,NORM,NORMS,C,HCSTAR,DELTAS,
  • DELTAC,HSTART,NORMA,DELTA,WIDTHA,NORM3,DELTA2
  COMMON
/DIST/MEAN,WIDTH,WIDTHI,HCSTAR,WIDTHA/NORMAL/NORM,NORMA,
  • NORM3//C,W,X
  COMMON /DEL/ DELTAS,DELTAC,HSTART,DELTA,DELTA2

C
  N=50
  XA=-5.D0
  XB=5.D0
  DELTAS=(XB-XA)/DFLOAT(N)
  INTEG=0.D0
  DO 50 J=1,N
    A(J) = XA+DFLOAT(J-1)*DELTAS
    B(J) = XA+DFLOAT(J)*DELTAS
    DO 50 K=1,10
      Y(K) = (B(J)-A(J))*X(K)/2.D0+(B(J)+A(J))/2.D0
      FUNC(K) = EXP(-(Y(K))**2/((WIDTHI**2.D0)*2.D0)/
      • ((2.D0*(WIDTHI**2.D0)*3.14159265D0)**0.5D0)
      INTEG = INTEG + (B(J)-A(J))*W(K)*FUNC(K)/2.D0
50  CONTINUE
    NORMS = INTEG
60  FORMAT(1X,G25.16)
    WRITE (6,*) NORMS
    RETURN
    END

C
  SUBROUTINE IHCALC
C This program calculates the magnetization i(h). (For any k.)
C
  IMPLICIT REAL*8 (A-H,O-Z)
  REAL*8 FUNC1(10),X(10),W(10),X1(999),X2(999),
  • XM(999),XR(999),DX(10),XPRIM(10),FUNC2(10),YA(20),YB(20),
  • YPRIM(10),Y2(10),Y1(999),YM(999),YR(999),DY(10),XA(20),XB(20),
  • FACTOR(20),DELTAS,DELTAC,NUMC,NUM,NC,MS,HSTART,HSCALE,MSCALE
  REAL*8 INTEG,SUMK,IH,H,C,MEAN,WIDTHI,WIDTH,NORM,HCSTAR,P,FRCT,
  • NORMA,DELTA,WIDTHA,DELTA2,NORM3,gamma,alpha
  COMMON /DIST/MEAN,WIDTH,WIDTHI,HCSTAR,WIDTHA/NORMAL/NORM,
  • NORMA,NORM3//C,W,X
  COMMON /DEL/ DELTAS,DELTAC,HSTART,DELTA,DELTA2
  COMMON HSCALE,MSCALE,FRCT,gamma,alpha

C
C Sum the three integrals reading the limits from the following
C
  OPEN (FILE='ihk1.o', UNIT=8, ACCESS='SEQUENTIAL',
  • FORM='FORMATTED', STATUS='NEW')
  IH=0.D0
  DO 80 P=1,60
    H=(P/36.D0)**2.D0
5  FACTOR(1)=2.D0
  FACTOR(2)=1.D0
  FACTOR(3)=1.D0
  XA(1)=0.D0
  XA(2)=0.D0
  XA(3)=H/2.D0
  XB(1)=H/2.D0
  XB(2)=H/2.D0
  XB(3)=60.D0
  Q2=3
10  INTEG=0.D0
  PROB = 0.D0

```

## A2.2 Fortran Program for Preisach Calculations ( $\text{Nd}_2\text{Fe}_{14}\text{B}$ )

```

DO 60 Q=1,Q2
NUMC = (XB(Q)-XA(Q))/DELTAC
NC = IDINT(NUMC)
IF (NC.LT.1.D0) NC=1.D0
DELTA1=(XB(Q)-XA(Q))/NC
SUMK=0.D0
SUM1K=0.D0
DO 50 I=1,NC
  X1(I) = XA(Q)+DFLOAT(I-1)*DELTA1
  X2(I) = XA(Q)+DFLOAT(I)*DELTA1
C
C Calculate a 2D integral.
C
  XM(I)=0.5D0*(X2(I)+X1(I))
  XR(I)=0.5D0*(X2(I)-X1(I))
  DO 50 J=1,10
    DX(J)=XR(I)*X(J)
    XPRIM(J)=DX(J)+XM(I)
    YA(1)=XPRIM(J)
    YA(2)=-XPRIM(J)
    YA(3)=-XPRIM(J)
    YB(1)=-XPRIM(J)+H
    YB(2)=XPRIM(J)
    YB(3)=-XPRIM(J)+H
20  NUM = (YB(Q)-YA(Q))/DELTAS
    MS = IDINT(NUM)
    IF (MS.LT.1.D0) MS=1.D0
    DELTA2=(YB(Q)-YA(Q))/MS
    DO 50 L=1,MS
      Y1(L) = YA(Q)+DFLOAT(L-1)*DELTA2
      Y2(L) = YA(Q)+DFLOAT(L)*DELTA2
      YM(L)=0.5D0*(Y2(L)+Y1(L))
      YR(L)=0.5D0*(Y2(L)-Y1(L))
      DO 50 K=1,10
        DY(K)=YR(L)*X(K)
        YPRIM(K)=DY(K)+YM(L)
        FUNC1(K) = DEXP(-YPRIM(K)**2.D0/((WIDTH**2.D0)*2.D0)/
  * ((2.D0*(WIDTH**2.D0)*3.14159265D0)**0.5D0)
C  FUNC2(K) = DEXP(-(XPRIM(J)-1.D0)**2.D0/((WIDTH**2.D0)*2.D0)/
C  * (NORM**((2.D0*(WIDTH**2.D0)*3.14159265D0)**0.5D0))
        FUNC2(K) =DEXP(-(DLOG(XPRIM(J))**2.D0/((WIDTH**2.D0)*2.D0)/
  * (XPRIM(J)**(2.D0*(WIDTH**2.D0)*3.14159265D0)**0.5D0)
        SUMK=SUMK + W(K)*W(J)*YR(L)*XR(I)*FUNC1(K)*FUNC2(K)*FACTOR(Q)
        SUM1K=SUM1K + W(K)*W(J)*YR(L)*XR(I)*FUNC1(K)*FUNC2(K)
50  CONTINUE
    INTEG=INTEG+SUMK
    PROB = PROB+SUM1K
60  CONTINUE
    IH=INTEG+(1.D0-PROB)*(1.D0-DEXP(-gamma*H))
    IH=FRCT*IH + (1.D0-FRCT)*(1.D0-DEXP(-gamma*H))
    IH=IH*MSCALE
C
C Writing numerical value to a file.
C
    HA = (H - C*IH)*HSCALE
    WRITE (8, 70) HA,IH
70  FORMAT (1X,3G25.16)
80  CONTINUE
    END FILE (UNIT=8)
    CLOSE (UNIT=8)
    CLOSE (UNIT=4)
    RETURN
    END
C
SUBROUTINE IRCALC
C This program calculates the magnetizing remanence ir.(k < 0 only)
C
  REAL*8 FUNC1(10),X(10),W(10),X1(999),X2(999),
  * XM(999),XR(999),DX(10),XPRIM(10),FUNC2(10),YA(20),YB(20),
  * YPRIM(10),Y2(10),Y1(999),YM(999),YR(999),DY(10),XA(20),XB(20),
  * FACTOR(20)
  REAL*8 INTEG,SUMK,H,IR,C,HA,IH,MEAN,WIDTH,NORM,HSCALE,FRCT,
  * WIDTHI,HCSTAR,DELTAS,DELTAC,NUMC,NUM,MS,NC,P,R,HSTART,MSCALE,
  * WIDTHA,DELTA,NORMA,NORM3,DELTA2,gamma,alpha
  COMMON
  /DIST/MEAN,WIDTH,WIDTHI,HCSTAR,WIDTHA/NORMAL/NORM,NORMA,
  * NORM3//C,W,X
  COMMON /DEL/ DELTAS,DELTAC,HSTART,DELTA,DELTA2
  COMMON HSCALE,MSCALE,FRCT,gamma,alpha
C

```

## A2.2 Fortran Program for Preisach Calculations (Nd<sub>2</sub>Fe<sub>14</sub>B)

```

C Sum the three integrals reading the limits from the following
C
  OPEN (FILE='hk1.o', UNIT=7, ACCESS='SEQUENTIAL',
  • FORM='FORMATTED', STATUS='OLD')
  OPEN (FILE='irk1.o', UNIT=8, ACCESS='SEQUENTIAL',
  • FORM='FORMATTED', STATUS='NEW')
  DO 80 P=1,60
  H=(P/36.D0)**2.D0
  READ (7,71) HA, IH
71  FORMAT(1X,2G25.16)
5   FACTOR(1)=2.D0
  FACTOR(2)=1.D0
  FACTOR(3)=1.D0
  FACTOR(4)=-2.D0
  XA(1)=0.D0
  XA(2)=0.D0
  XA(3)=H/2.D0
  XA(4)=0.D0
  XB(1)=H/2.D0
  XB(2)=H/2.D0
  XB(3)=60.D0
  XB(4)=H/2.D0
  Q2=4
10  INTEG=0.D0
  DO 60 Q=1,Q2
  NUMC = (XB(Q)-XA(Q))/DELTA C
  NC = IDINT(NUMC)
  IF (NC.LT.1.D0) NC=1.D0
  DELTA1=(XB(Q)-XA(Q))/NC
  SUMK=0.D0
  DO 50 I=1,NC
  X1(I) = XA(Q)+DFLOAT(I-1)*DELTA1
  X2(I) = XA(Q)+DFLOAT(I)*DELTA1
C
C Calculate a 2D integral.
C
  XM(I)=0.5D0*(X2(I)+X1(I))
  XR(I)=0.5D0*(X2(I)-X1(I))
  DO 50 J=1,10
  DX(J)=XR(I)*X(J)
  XPRIM(J)=DX(J)+XM(I)
  YA(1)=XPRIM(J)
  YA(2)=-XPRIM(J)
  YA(3)=-XPRIM(J)
  YA(4)=XPRIM(J)
  YB(1)=-XPRIM(J)+H
  YB(2)=XPRIM(J)
  YB(3)=-XPRIM(J)+H
  YB(4)=-XPRIM(J)+H
20  NUM = (YB(Q)-YA(Q))/DELTAS
  MS = IDINT(NUM)
  IF (MS.LT.1.D0) MS=1.D0
  DELTA2=(YB(Q)-YA(Q))/MS
  DO 50 L=1,MS
  Y1(L) = YA(Q)+DFLOAT(L-1)*DELTA2
  Y2(L) = YA(Q)+DFLOAT(L)*DELTA2
  YM(L)=0.5D0*(Y2(L)+Y1(L))
  YR(L)=0.5D0*(Y2(L)-Y1(L))
  DO 50 K=1,10
  DY(K)=YR(L)*X(K)
  YPRIM(K)=DY(K)+YM(L)
  FUNC1(K) = DEXP(-YPRIM(K)**2.D0/((WIDTH**2.D0)*2.D0))/
  • ((2.D0*(WIDTH**2.D0)*3.14159265D0)**0.5D0)
C   FUNC2(K) = DEXP(-(XPRIM(J)-1.D0)**2.D0/((WIDTH**2.D0)*2.D0))/
C   • (NORM*((2.D0*(WIDTH**2.D0)*3.14159265D0)**0.5D0))
  FUNC2(K) =DEXP(-(DLOG(XPRIM(J)))**2.1)/((WIDTH**2.D0)*2.D0)/
  • (XPRIM(J)*(2.D0*(WIDTH**2.D0)*3.14159265D0)**0.5D0)
  SUMK=SUMK + W(K)*W(J)*YR(L)*XR(I)*FUNC1(K)*FUNC2(K)*FACTOR(Q)
50  CONTINUE
  INTEG=INTEG+SUMK
60  CONTINUE
C
C Writing numerical value to a file.
C
  IR = FRCT*INTEG*MSCALE
  HA=H*HSCALE
  WRITE (9,*) P,R
65  WRITE (8,70) HA, IR
70  FORMAT (1X,2G25.16)
80  CONTINUE

```

## A2.2 Fortran Program for Preisach Calculations ( $\text{Nd}_2\text{Fe}_{14}\text{B}$ )

```

CLOSE (UNIT=7)
END FILE (UNIT=8)
CLOSE (UNIT=8)
RETURN
END
C
SUBROUTINE IINFALC
C
C This program calculates the saturation remanence, i(infinity).
C (k<0 only).
C
IMPLICIT REAL*8 (A-H,O-Z)
REAL*8 FUNC1(10),X(10),W(10),X1(999),X2(999),
* XM(999),XR(999),DX(10),XPRIM(10), FUNC2(10), YA(20), YB(20),
* YPRIM(10), Y2(10), Y1(999), YM(999), YR(999), DY(10), XA(20), XB(20),
* FACTOR(20)
REAL*8 INTEG,SUMK,IINF,H,C,MEAN,WIDTHI,WIDTH,NORM,HCSTAR,NUM,
* NC,NUMC,MS,R,HSTART,HSCALE,MSCALE,FRCT,WIDTHA,NORMA,
* DELTAA,NORM3,DELTA2,gamma,alpha
COMMON
/DIST/MEAN,WIDTH,WIDTHI,HCSTAR,WIDTHA/NORMAL/NORM,NORMA,
* NORM3/C,W,X
COMMON /DEL/ DELTAS,DELTAC,HSTART,DELTA2,DELTA2/INF/IINF
COMMON HSCALE,MSCALE,FRCT,gamma,alpha
C
C Sum the three integrals reading the limits from the following
C
OPEN (FILE='infk1.o', UNIT=8, ACCESS='SEQUENTIAL',
* FORM='FORMATTED', STATUS='NEW')
H=2.D0
FACTOR(1)=2.D0
FACTOR(2)=1.D0
FACTOR(3)=1.D0
FACTOR(4)=-2.D0
XA(1)=0.D0
XA(2)=0.D0
XA(3)=H/2.D0
XA(4)=0.D0
XB(1)=H/2.D0
XB(2)=H/2.D0
XB(3)=60.D0
XB(4)=H/2.D0
Q2=4
10 INTEG=0.D0
DO 60 Q=1,Q2
NUMC=(XB(Q)-XA(Q))/DELTAC
NC=IDINT(NUMC)
IF (NC.LT.1.D0) NC=1.D0
DELTA1=(XB(Q)-XA(Q))/NC
SUMK=0.D0
DO 50 I=1,NC
X1(I) = XA(Q)+DFLOAT(I-1)*DELTA1
X2(I) = XA(Q)+DFLOAT(I)*DELTA1
C
C Calculate a 2D integral.
C
XM(I)=0.5D0*(X2(I)+X1(I))
XR(I)=0.5D0*(X2(I)-X1(I))
DO 50 J=1,10
DX(J)=XR(I)*X(J)
XPRIM(J)=DX(J)+XM(I)
YA(1)=XPRIM(J)
YA(2)=-XPRIM(J)
YA(3)=-XPRIM(J)
YA(4)=XPRIM(J)
YB(1)=-XPRIM(J)+H
YB(2)=XPRIM(J)
YB(3)=-XPRIM(J)+H
YB(4)=-XPRIM(J)+H
NUM=(YB(Q)-YA(Q))/DELTAS
MS=IDINT(NUM)
IF (MS.LT.1.D0) MS=1.D0
20 DELTA2=(YB(Q)-YA(Q))/MS
DO 50 L=1,MS
Y1(L) = YA(Q)+DFLOAT(L-1)*DELTA2
Y2(L) = YA(Q)+DFLOAT(L)*DELTA2
YM(L)=0.5D0*(Y2(L)+Y1(L))
YR(L)=0.5D0*(Y2(L)-Y1(L))
DO 50 K=1,10
DY(K)=YR(L)*X(K)

```

## A2.2 Fortran Program for Preisach Calculations (Nd<sub>2</sub>Fe<sub>14</sub>B)

```

YPRIM(K)=DY(K)+YM(L)
FUNC1(K) = DEXP(-YPRIM(K)**2.D0/((WIDTH**2.D0)*2.D0))/
• ((2.D0*(WIDTH**2.D0)*3.14159265D0)**0.5D0)
C   FUNC2(K) = DEXP(-(XPRIM(J)-1.D0)**2.D0/((WIDTH**2.D0)*2.D0))/
C   • (NORM*((2.D0*(WIDTH**2.D0)*3.14159265D0)**0.5D0))
FUNC2(K) =DEXP(-(DLOG(XPRIM(J)))**2.D0/((WIDTH**2.D0)*2.D0))/
• (XPRIM(J)*(2.D0*(WIDTH**2.D0)*3.14159265D0)**0.5D0)
SUMK=SUMK + W(K)*W(J)*YR(L)*XR(I)*FUNC1(K)*FUNC2(K)*FACTOR(Q)
50 CONTINUE
INTEG=INTEG+SUMK
60 CONTINUE
C
C Writing numerical value to a file.
C
PREL=INTEG
IINF=FRCT*INTEG*MSCALE
WRITE (9,*) R
WRITE (8,70) IINF,PREL
70 FORMAT (1X,2G25.16)
END FILE (UNIT=8)
CLOSE (UNIT=8)
RETURN
END
C
SUBROUTINE IHDCALC
C
C This program calculates the demagnetizing curve, i(h) DEMAG.
C (any k )
C
IMPLICIT REAL*8 (A-H,O-Z)
REAL*8 FUNC1(10),X(10),W(10),X1(999),X2(999),
• XM(999),XR(999),DX(10),XPRIM(10), FUNC2(10),YA(20),YB(20),
• YPRIM(10),Y2(10),Y1(999),YM(999),YR(999),DY(10),XA(20),XB(20),
• FACTOR(20),AA(10),BB(10),YY(10),FUNC(10)
REAL*8 INTEG,SUMK,IHD,H,C,COUNT,MEAN,WIDTH,WIDTHI,NORM,HCSTAR,
• P,DELTAS,DELTAC,NUMC,NUM,MS,NC,HSCALE,MSCALE,FRCT,WIDTHA,
• DELTAA,NORMA,DELTA2,NORM3,gamma,alpha
COMMON /NUM/COUNT/DIST/MEAN,WIDTH,WIDTHI,HCSTAR,WIDTHA
• /NORMAL/NORM,NORMA,NORM3/DEL/DELTAS,DELTAC,HSTART,DELTAA,
• DELTA2/C,W,X

```

```

COMMON HSCALE,MSCALE,FRCT,gamma,alpha
C
C Sum the three integrals reading the limits from the following
C
OPEN (FILE='ihdk1.o', UNIT=9, ACCESS='SEQUENTIAL',
• FORM='FORMATTED', STATUS='NEW')
OPEN (FILE='iinfk1.o', UNIT=7, ACCESS='SEQUENTIAL',
• FORM='FORMATTED', STATUS='OLD')
READ(7,71) IINF,PREL
71 FORMAT(1X,2G25.16)
DO 80 P=1,60
IHD=0.D0
H=-(P/36.0D0)**2.D0
C
XXA=0.D0
XXB=-H
COUNT=(XXB-XXA)/DELTA
NN=IDINT(COUNT)
IF (NN.LT.1.D0) NN=1.D0
DLT=(XXB-XXA)/NN
RESET=0.D0
DO 55 J=1,NN
AA(J) = -XXA+DFLOAT(J-1)*DLT
BB(J) = -XXA+DFLOAT(J)*DLT
DO 55 K=1,10
YY(K) = (BB(J)-AA(J))*X(K)/2.D0+(BB(J)+AA(J))/2.D0
C   FUNC(K) =EXP(-(YY(K)-MEAN)**2/((WIDTHA**2.D0)*2.D0))/
C   • (((2.D0*(WIDTHA**2.D0)*3.14159265D0)**0.5D0))
FUNC(K) =DEXP(-(DLOG(YY(K)/MEAN))**2.D0/((WIDTHA**2.D0)*2.D0))/
• (YY(K)*(2.D0*(WIDTHA**2.D0)*3.14159265D0)**0.5D0)
RESET = RESET + (BB(J)-AA(J))*W(K)*FUNC(K)/2.D0
55 CONTINUE
WRITE(6,*) RESET
C
FACTOR(1)= -2.D0
FACTOR(2)= -1.D0
FACTOR(3)= -1.D0
XA(1)=0.D0
XA(2)=0.D0
XA(3)=-H/2.D0

```

## A2.2 Fortran Program for Preisach Calculations ( $\text{Nd}_2\text{Fe}_{14}\text{B}$ )

```

XB(1)=-H/2.D0
XB(2)=-H/2.D0
XB(3)=60.D0
Q2 = 3
10  INTEG=0.D0
    PROB=0.D0
    DO 60 Q=1,Q2
    NUMC = (XB(Q)-XA(Q))/DELTA C
15  NC = IDINT(NUMC)
    IF (NC.LT.1.D0) NC=1.D0
    DELTA1=(XB(Q)-XA(Q))/NC
    SUMK=0.D0
    SUM1K=0.D0
    DO 50 I=1,NC
        X1(I) = XA(Q)+DFLOAT(I-1)*DELTA1
        X2(I) = XA(Q)+DFLOAT(I)*DELTA1
    C
    C Calculate a 2D integral.
    C
    XM(I)=0.5D0*(X2(I)+X1(I))
    XR(I)=0.5D0*(X2(I)-X1(I))
    DO 50 J=1,10
        DX(J)=XR(I)*X(J)
        XPRIM(J)=DX(J)+XM(I)
        YA(1)=XPRIM(J)+H
        YA(2)=-XPRIM(J)
        YA(3)=XPRIM(J)+H
        YB(1)=-XPRIM(J)
        YB(2)=XPRIM(J)
        YB(3)=XPRIM(J)
        NUM = (YB(Q)-YA(Q))/DELTAS
        MS = IDINT(NUM)
        IF (MS.LT.1.D0) MS=1.D0
20  DELTA2=(YB(Q)-YA(Q))/MS
    DO 50 L=1,MS
        Y1(L) = YA(Q)+DFLOAT(L-1)*DELTA2
        Y2(L) = YA(Q)+DFLOAT(L)*DELTA2
        YM(L)=0.5D0*(Y2(L)+Y1(L))
        YR(L)=0.5D0*(Y2(L)-Y1(L))
    DO 50 K=1,10
        DY(K)=YR(L)*X(K)
        YPRIM(K)=DY(K)+YM(L)
        FUNC1(K) = DEXP(-YPRIM(K)**2.D0/((WIDTH**2.D0)*2.D0))/
        • ((2.D0*(WIDTH**2.D0)*3.14159265D0)**0.5D0)
    C   FUNC2(K) = DEXP(-(XPRIM(J)-1.D0)**2.D0/((WIDTH**2.D0)*2.D0))/
    C   • (NORM*((2.D0*(WIDTH**2.D0)*3.14159265D0)**0.5D0))
        FUNC2(K) =DEXP(-(DLOG(XPRIM(J)/(1.D0+alpha*MEAN)))**2.D0/((WIDTH
        • **2.D0)*2.D0))/(XPRIM(J)*(2.D0*(WIDTH**2.D0)*3.14159265D0)
        • **0.5D0)
        SUMK=SUMK + W(K)*W(J)*YR(L)*XR(I)*FUNC1(K)*FUNC2(K)*FACTOR(Q)
        SUM1K=SUM1K + W(K)*W(J)*YR(L)*XR(I)*FUNC1(K)*FUNC2(K)
50  CONTINUE
    INTEG=INTEG+SUMK
    PROB=PROB+SUM1K
60  CONTINUE
    IHD=INTEG-(1.D0-PROB)*(1.D0-DEXP(+gamma*H))
    IHD=IHD*RESET
    IHD=IHD+PREL*(1.D0-RESET)
    IHD=IHD*FRCT-(1.D0-DEXP(+gamma*H))*(1.D0-FRCT)
    IHD=IHD*MSCALE
    HAD=(H-C*IHD)*HSCALE
    C
    C Writing numerical value to a file.
    C
    WRITE (9, 70) HAD, IHD
70  FORMAT (1X,2G25.16)
80  CONTINUE
    END FILE (UNIT=9)
    CLOSE (UNIT=9)
    CLOSE(UNIT=7)
    RETURN
    END
    C
    C SUBROUTINE IDCALC
    C
    C This program calculates the demagnetizing remanence id.( k = 0 only).
    C
    IMPLICIT REAL*8 (A-H,O-Z)
    REAL*8 FUNC1(10),X(10),W(10),X1(999),X2(999),AA(10),BB(10),
    • XM(999),XR(999),DX(10),XPRIM(10), FUNC2(10),YA(20),YB(20),

```

## A2.2 Fortran Program for Preisach Calculations (Nd<sub>2</sub>Fe<sub>14</sub>B)

```

* YPRIM(10),Y2(10),Y1(999),YM(999),YR(999),DY(10),XA(20),XB(20),
*
FACTOR(20),YY(10),FUNC(10),NORM,WIDTHA,DELTA,NORMA,DELTA2,NORM3
REAL*8 INTEG,SUMK,H,ID,C,HAD,IHD,MEAN,WIDTH,COUNT,FRCT,gamma,
*
WIDTHI,HCSTAR,DELTAC,DELTAS,NUM,NUMC,MS,NC,HSCALE,MSCALE,alpha
COMMON /NUM2/COUNT2/DIST/MEAN,WIDTH,WIDTHI,HCSTAR,WIDTHA
*
/NORMAL/NORM,NORMA,NORM3/DEL/DELTAS,DELTAC,HSTART,DELTA,DELTA
2
* //C,W,X
COMMON HSCALE,MSCALE,FRCT,gamma,alpha
C
C Sum the three integrals reading the limits from the following
C
OPEN (FILE='infk1.o', UNIT=7, ACCESS='SEQUENTIAL',
* FORM='FORMATTED', STATUS='OLD')
OPEN (FILE='hdk1.o', UNIT=9, ACCESS='SEQUENTIAL',
* FORM='FORMATTED', STATUS='OLD')
OPEN (FILE='dk1.o', UNIT=4, ACCESS='SEQUENTIAL',
* FORM='FORMATTED', STATUS='NEW')
READ (7,72) IINF, PREL
72 FORMAT (1X,2G25.16)
CLOSE(UNIT=7)
ID=0.D0
DO 80 P=1,60
H=-(P/36.0D0)**2.D0
READ (9,71) HAD, IHD
71 FORMAT (1X,2G25.16)
C
XXA=0.D0
XXB=-H
COUNT=(XXB-XXA)/DELTA
NN=IDINT(COUNT)
IF (NN.LT.1.D0) NN=1.D0
DLT=(XXB-XXA)/NN
RESET=0.D0
DO 55 J=1,NN
AA(J) = -XXA+DFLOAT(J-1)*DLT
BB(J) = -XXA+DFLOAT(J)*DLT

```

```

DO 55 K=1,10
YY(K) = (BB(J)-AA(J))*X(K)/2.D0+(BB(J)+AA(J))/2.D0
C FUNC(K) = EXP(-(YY(K)-MEAN)**2/((WII)THA**2.D0)*2.D0)/
C * (((2.D0*(WIDTHA**2.D0)*3.14159265D0)**0.5D0))
FUNC(K) =DEXP(-(DLOG(YY(K)/MEAN))**2.D0/((WIDTHA**2.D0)*2.D0)/
* (YY(K)*(2.D0*(WIDTHA**2.D0)*3.14159265D0)**0.5D0)
RESET = RESET + (BB(J)-AA(J))*W(K)*FUNC(K)/2.D0
55 CONTINUE
C WRITE(6,*) RESET
C
FACTOR(1)= -2.D0
FACTOR(2)= -1.D0
FACTOR(3)= -1.D0
FACTOR(4)= +2.D0
XA(1)=0.D0
XA(2)=0.D0
XA(3)=-H/2.D0
XA(4)=0.D0
XB(1)=-H/2.D0
XB(2)=-H/2.D0
XB(3)=60.D0
XB(4)=-H/2.D0
Q2=4
10 INTEG=0.D0
DO 60 Q=1,Q2
NUMC = (XB(Q)-XA(Q))/DELTAC
15 NC = IDINT(NUMC)
IF (NC.LT.1.D0) NC=1.D0
DELTA1=(XB(Q)-XA(Q))/NC
SUMK=0.D0
DO 50 I=1,NC
X1(I) = XA(Q)+DFLOAT(I-1)*DELTA1
X2(I) = XA(Q)+DFLOAT(I)*DELTA1
C
C Calculate a 2D integral.
C
XM(I)=0.5D0*(X2(I)+X1(I))
XR(I)=0.5D0*(X2(I)-X1(I))
DO 50 J=1,10
DX(J)=XR(I)*X(J)

```

## A2.2 Fortran Program for Preisach Calculations ( $\text{Nd}_2\text{Fe}_{14}\text{B}$ )

```

XPRIM(J)=DX(J)+XM(I)
YA(1)=XPRIM(J)+H
YA(2)=-XPRIM(J)
YA(3)=XPRIM(J)+H
YA(4)=XPRIM(J)+H
YB(1)=-XPRIM(J)
YB(2)=XPRIM(J)
YB(3)=XPRIM(J)
YB(4)=-XPRIM(J)
NUM = (YB(Q)-YA(Q))/DELTAS
MS = IDINT(NUM)
IF (MS.LT.1.D0) MS=1.D0
20 DELTA2=(YB(Q)-YA(Q))/MS
DO 50 L=1,MS
Y1(L) = YA(Q)+DFLOAT(L-1)*DELTA2
Y2(L) = YA(Q)+DFLOAT(L)*DELTA2
YM(L)=0.5D0*(Y2(L)+Y1(L))
YR(L)=0.5D0*(Y2(L)-Y1(L))
DO 50 K=1,10
DY(K)=YR(L)*X(K)
YPRIM(K)=DY(K)+YM(L)
FUNC1(K) = DEXP(-YPRIM(K)**2.D0/((WIDTH**2.D0)*2.D0))/
* ((2.D0*(WIDTH**2.D0)*3.14159265D0)**0.5D0)
C FUNC2(K) = DEXP(-(XPRIM(J)-1.D0)**2.D0/((WIDTH**2.D0)*2.D0))/
C * (NORM*((2.D0*(WIDTH**2.D0)*3.14159265D0)**0.5D0))
FUNC2(K) = DEXP(-(DLOG(XPRIM(J)/(1.D0+alpha*MEAN)))**2.D0/((WIDTH
* **2.D0)*2.D0)/(XPRIM(J)*(2.D0*(WIDTH**2.D0)*3.14159265D0)
* **0.5D0))
25 SUMK=SUMK + W(K)*W(J)*YR(L)*XR(I)*FUNC1(K)*FUNC2(K)*FACTOR(Q)
50 CONTINUE
INTEG=INTEG+SUMK
60 CONTINUE
C
C Writing numerical value to a file.
C
ID = RESET*INTEG+(1.D0-RESET)*PREL
ID = ID*FRCT
ID = ID*MSCALE
65 WRITE (UNIT=4, 70) HAD, ID
70 FORMAT (1X,2G25.16)

80 CONTINUE
END FILE (UNIT=4)
CLOSE (UNIT=4)
CLOSE (UNIT=9)
RETURN
END
C
SUBROUTINE DELT
C
REAL*8 IR(200),HAM(200),ID(200),HAD(200),IINF,DELTAI(200),
* IRP(200),IDP(200)
COMMON IINF
OPEN (FILE='idelt1.o', UNIT=8, ACCESS='SEQUENTIAL',
* FORM='FORMATTED', STATUS='NEW')
OPEN (FILE='ihenk1.o', UNIT=4, ACCESS='SEQUENTIAL',
* FORM='FORMATTED', STATUS='NEW')
OPEN (FILE='irk1.o', UNIT=7, ACCESS='SEQUENTIAL',
* FORM='FORMATTED', STATUS='OLD')
OPEN (FILE='idk1.o', UNIT=9, ACCESS='SEQUENTIAL',
* FORM='FORMATTED', STATUS='OLD')
OPEN (FILE='iinfk1.o', UNIT=5, ACCESS='SEQUENTIAL',
* FORM='FORMATTED', STATUS='OLD')
C
READ (5,60) IINF,PREL
60 FORMAT (1X,2G25.16)
DO 80 J=1,60
READ (7,62) HAM(J),IR(J)
62 FORMAT (1X,2G25.16)
READ (9,63) HAD(J),ID(J)
63 FORMAT (1X,2G25.16)
IRP(J)=IR(J)/IINF
IDP(J)=ID(J)/IINF
DELTAI(J) = IDP(J) - (1.D0-2.D0*IRP(J))
WRITE (8,72) IDP(J),DELTAI(J)
72 FORMAT (2G25.16)
WRITE (4,73) IRP(J),IDP(J)
73 FORMAT (2G25.16)
80 CONTINUE
END FILE (UNIT=8)
END FILE (UNIT=4)

```

## A2.2 Fortran Program for Preisach Calculations (Nd<sub>2</sub>Fe<sub>14</sub>B)

```
CLOSE (UNIT=4)
CLOSE (UNIT=8)
CLOSE (UNIT=7)
CLOSE (UNIT=9)
CLOSE (UNIT=5)
RETURN
END
```

# References

Basso, V. & Bertotti, G. (1994) . Description of magnetic interactions and Henkel plots by the Preisach hysteresis model. IEEE Transactions on Magnetics, 30 (1), 64-72.

Basso, V., Lo Bue, M. & Bertotti, G. (1994) . Interpretation of hysteresis curves and Henkel plots by the Preisach model (invited). Journal of Applied Physics, 75 (10), 5677-5682.

Bate, G. (1980) . Recording Materials . In E. P. Wohlfarth (Ed.), Ferromagnetic Materials: A handbook on the properties of magnetically ordered substances, 2, (pp. 381-507) . Amsterdam: North-Holland Publishing Company.

Becker, J. J. (1969) . Observations of magnetization reversal in cobalt-rare earth particles. IEEE Transactions on Magnetics, 5, 211-214.

Becker, J. J. (1973) . A model for the field dependence of magnetization discontinuities in high-anisotropy materials. IEEE Transactions on Magnetics, MAG-9 (3), 161-164.

Bertotti, G. (1998) . Hysteresis in Magnetism for Physicists, Materials Scientists, and Engineers. San Diego, CA: Academic Press.

Bertram, H. N. & Zhu, J.-G. (1992) . Fundamental Magnetization Processes in Thin-Film Recording Media. In H. Ehrenreich & D. Turnbull (Eds.), Solid State Physics, Advances in Research and Application, 46, (pp. 299-313) . San Diego, CA: Academic Press Inc.

Bulte, J. W. M., Douglas, T., Mann, S., Frankel, R. B., Moskowitz, B. M., Brooks, R. A., Baumgarner, C. D., Vymazal, J., Strub, M.-P. & Frank, J. A. (1994). Magnetoferritin: Characterization of a novel superparamagnetic MR contrast agent. Journal of Magnetic Resonance Imaging, 4, 497-505.

Chikazumi, S. (1964). Physics of Magnetism. New York: John Wiley & Sons, Inc.

Cornejo, D. R., Lo Bue, M., Basso, V., Bertotti, G. & Missell, F. P. (1997). Moving Preisach model analysis of noncrystalline SmFeCo. Journal of Applied Physics, 81 (8), 5588-5590.

Cullity, B. D. (1972). Introduction to Magnetic Materials. Reading, MA: Addison-Wesley Publishing Company.

de Almeida, J. R. L. & Thouless, D. J. (1980). Stability of the Sherrington-Kirkpatrick solution of a spin glass model. Journal of Physics A, 11 (5), 983-990.

Della Torre, E. (1966). Effect of interaction on the magnetization of single-domain particles. IEEE Transaction on Audio Electroacoustics, 14 (86) p. 86-93.

Douglas, T., Bulte, J. W. M., Dickson, D. P. E., Frankel, R. B., Pankhurst, Q. A., Moskowitz, B. M. & Mann, S. (1995). Inorganic-Protein Interactions in the Synthesis of a Ferrimagnetic Nanocomposite. In Mark, J. E., Lee, C. C.-Y. & Bianconi, P. A. (Eds.) Hybrid Organic-Inorganic Composites. Washington D.C.: American Chemical Society, 19-28.

Dunlap, R. A. (1988). Experimental Physics. New York: Oxford University Press.

Ferré, J., Rajchenbach, J. & Maletta, H. (1981) . Faraday rotation measurements of time dependent magnetic phenomena in insulating spin glasses . Journal of Applied Physics 52 (3), 1697-1702.

Fischer, K. H. & Hertz, J. A. (1991) . Spin Glasses. Cambridge: Cambridge University Press.

Fisher, D. S. & Huse, D. A. (1988) . Equilibrium behavior of the spin-glass ordered phase. Physical Review B, 38 (1), 386-411.

Henkel, O. (1964) . Remanenzverhalten und wechselwirkungen in hartmagnetischen teilchenkollektiven. Physica Status Solidi, 7, 919-929.

Huse, D. A. & Fisher, D. S. (1987) . Dynamics of droplet fluctuations in pure and random Ising systems. Physical Review B, 35 (13), 6841-6846.

Jacobs, I. S. & Schmitt, R. W. (1959) . Low-temperature electrical and magnetic behavior of dilute alloys: Mn in Cu and Co in Cu. Physical Review, 113 (2), 459-463.

Jacobs, I. S. & Bean, C. P. (1955) . An approach to elongated fine-particle magnets. Physical Review, 100, 1060-1067.

Jiles, D. (1991) . Introduction to Magnetism and Magnetic Materials. New York: Chapman and Hall.

Köster, E. & Arnoldussen, T. C. (1990) . Recording Media. In C. D. Mee. & E. D. Daniel (Eds.), Magnetic Recording Handbook: technology and applications. (pp. 101-257) . McGraw-Hill Inc., New York, 1990.

Langevin, P. (1905) . Magnétisme et théorie des electrons. Annales de Chemie et de Physique, 5, 70-127.

Li, D. & Strnat, K. J. (1985) . Domain behavior in sintered Nd-Fe-B magnets during field-induced and thermal magnetization change. Journal of Applied Physics, *57* (1), 4143-4145.

Lottis, D. K, Dahlberg, E. D., Christner, J. A., Lee, J. I., Peterson, R. L. & White, R. M. (1988) . Magnetic aftereffect in CoCr films. Journal of Applied Physics, *63* (8), 2920-2922.

Lottis, D., White, R. & Dahlberg, E. D. (1990) . The magnetic aftereffect in CoCr films: A model. Journal of Applied Physics, *67* (9), 5187-5189.

Luborsky, F. E. (1961) . Development of elongated particle magnets. Journal of Applied Physics, *32*, 171S-183S .

Mayergoyz, I. (1986) . Mathematical models of hysteresis. Physical Review Letters, *56* (15), 1518-1521.

Mayergoyz, I. (1991) . Mathematical Models of Hysteresis. New York: Springer-Verlag.

McCurrie, R. A. & Gaunt, P. (1964) . The magnetic properties of platinum-cobalt near the equiatomic composition. Proceedings of the International Conference on Magnetism, 1964. (pp. 780-782) . London: The Institute of Physics.

Mitchler, P. D., Dahlberg, E. D., Engle, E. & Roshko, R. M. (1995) . Henkel plots in a thermally demagnetized scalar Preisach model. IEEE Transactions on Magnetics, *31* (5), 2499-2503.

- Mitchler, P. D., Dahlberg, E. D., Wesseling, E. & Roshko, R. M. (1996a) .  
Anomalous time-induced curvature in Henkel plots based on the Preisach model. Journal of Applied Physics, **79** (8), 5758-5760.
- Mitchler, P. D., Dahlberg, E. D., Wesseling, E. E. & Roshko, R. M. (1996b) .  
Henkel plots in a temperature and time dependent Preisach model. IEEE Transactions on Magnetics, **32** (4), 3185-3194.
- Mitchler, P. D., Roshko, R. M. & Dahlberg, E. D. (1997) . A Preisach model with a temperature and time-dependent remanence maximum. Journal of Applied Physics, **81** (8), 5221-5223.
- Mitchler, P. D., Roshko, R. M. & Dahlberg, E. D. (1998) . Interaction effects in CrO<sub>2</sub> audio tape: Ac versus thermal demagnetization. IEEE Transactions on Magnetics, **34** (4), 4385-4387.
- Mitchler, P. D., Roshko, R. M. & Dahlberg, E. D. (1999) . A Preisach analysis of Nd<sub>2</sub>Fe<sub>14</sub>B. Journal of Applied Physics, **85** (8), 4385-4387.
- Mitchler, P. D., Roshko, R. M., Dahlberg, E. D. & Moskowitz, B. M. (1999) . Interactions and thermal effects in systems of fine particles: A Preisach analysis of CrO<sub>2</sub> audio tape and magnetoferritin. IEEE Transactions on Magnetics, **35** (3), p. 2029-2042.
- Mitchler, P. D., Roshko, R. M., Dahlberg, E. D. & Wesseling, E. (1997) . Preisach model for spin-glass remanences. Physical Review B, **55** (9), 5880-5885.
- Morrish, A. H. (1965) . The Physical Principles of Magnetism. New York: John Wiley & Sons, Inc.

- Moskowitz, B. M., Frankel, R. B., Walton, S. A., Dickson, D. P. E., Wong, K. K. W., Douglas, T. & Mann, S. (1997) . Determination of the preexponential frequency factor for superparamagnetic maghemite particles in magnetoferritin. Journal of Geophysical Research, **102** (B10), 22671-22680.
- Néel, L. (1949) . Théorie du trainage magnétique des ferromagnétiques en grain fins avec applications aux terres cuites. Annales de Géophysique, **5**, 99-136.
- Néel, L. (1950) . Théorie du trainage magnétique des substances massives dans le domaine de Rayleigh. Journal de Physique et Le Radium, **11**(2), 49-61.
- Nordblad, P., Lundgren, L. & Sandlund, L. (1987) . Field dependence of the remanent magnetization in spin glasses. Europhysics Letters, **3** (2), 235-241.
- Préjean, J. J. & Souletie J. (1980) . Two-level-systems in spin glasses: a dynamical study of magnetizations below  $T_G$ , application to CuMn systems. Journal de Physique, **41**, 1335-1352.
- Preisach, F. (1935) . Über die magnetische nachwirkung. Zeitschrift für Physik, **94**, 277-302.
- Press, W. H., Teukolsky, S. A., Vetterling, W. T. & Flannery, B. P. (1996) . Numerical Recipes in Fortran 77 and Fortran 90: The Art of Scientific and Parallel Computing (2<sup>nd</sup> ed.) [Computer software] . Cambridge: Cambridge University Press.
- Princeton Measurements Corporation (1995) . Model 3900 MicroMag™ VSM Magnetometer Instruction Manual. Princeton Measurements Corporation.
- Quantum Design (1992) . Magnetic Property Measurement Systems: Systems and Options. San Diego, CA: Quantum Design.

Quantum Design (1996) . Magnetic Property Measurement Systems: Hardware Reference Manual. San Diego, CA: Quantum Design.

Roshko, R. M., Mitchler, P. D. & Dahlberg, E. D. (1997) . The effect of thermally induced relaxation on the remanent magnetization in a moving Preisach model. In G.C. Hadjipanayis (Ed.), Hysteresis in Novel Magnetic Systems (pp. 147-157) . The Netherlands: Kluwer Academic Publishers.

Roshko, R. M. & Moskowitz, B. M. (1998) . A Preisach analysis of magnetoferritin. Journal of Magnetism and Magnetic Materials, 177-181, 1461-1463.

Sagawa, M., Fujimura, S., Togawa, N., Yamamoto, H. & Matsuura, Y. (1984) . New material for permanent magnets on a base of Nd and Fe (invited). Journal of Applied Physics, 55 (6), 2083-2087.

Samwell, E. O., Bissell, P. R. & Lodder, J. C. (1993) . Remanent magnetic measurements on perpendicular recording materials with compensation for demagnetizing fields. Journal of Applied Physics, 73 (3), 1353-1359.

Screfl, T. (1997) . Micromagnetics of thin films and multilayers. In G.C. Hadjipanayis (Ed.), Hysteresis in Novel Magnetic Systems (pp. 49-68) . The Netherlands: Kluwer Academic Publishers.

Sherrington, D. & Kirkpatrick, S. (1975) . Solvable model of a sin-glass. Physical Review Letters, 35, 1792-1796.

Song, T. & Roshko, R. M. (2000a) . Preisach model for systems of interacting superparamagnetic particles. IEEE Transaction on Magnetics, 36 (1), 223-230.

Song, T. & Roshko, R. M. (2000b) . A Preisach model for systems with magnetic order. Physica B , 275, 24-27.

Souletie, J. (1983) . Hysteresis and after-effects in massive substances. From spin-glasses to the sand hill. Journal de Physique, 44 (9), 1095-1116.

Spinu, L. and Stancu, A. (1998) . Modeling magnetic relaxation phenomena in fine particle systems with a Preisach-Neél model. Journal of Magnetism and Magnetic Materials, 189, 106-114.

Stancu, A. and Spinu, L. (1998) . Temperature and time dependent Preisach model for a Stoner-Wohlfarth particle system. IEEE Transactions on Magnetism, 34 (6), 3867-3875.

Stoner, E. C. & Wohlfarth, E. P. (1948) . A mechanism of magnetic hysteresis in heterogeneous alloys. Philosophical Transactions of the Royal Society (London), A-240, 599-642.

Sugaya, H. & Yokoyama, K. (1990) . Video Recording. In C. D. Mee. & E. D. Daniel (Eds.), Magnetic Recording Handbook: technology and applications. (pp. 884-1014) . McGraw-Hill Inc., New York, 1990.

Vajda, F. & Della Torre, E. (1991) . Measurements of output-dependent Preisach functions. IEEE Transactions on Magnetics, 27, 4757-4762.

Vajda, F. & Della Torre, E. (1992) . Characteristics of magnetic media models. IEEE Transactions on Magnetics, 28 (5), 2611-2613.

Vajda, F. & Della Torre, E. (1993) . Efficient numerical implementation of complete-moving-hysteresis models (invited). IEEE Transactions on Magnetics, 29 (2), 1532-1537.

Vajda, F., Della Torre, E. & McMichael, R. D. (1994) . Demagnetized-state dependence of Henkel plots. I. The Preisach model. Journal of Applied Physics, 75 (10), 5689-5691.

Weiss, P. (1907) . L'hypothèse du champ moléculaire et de la propriété ferromagnétique. Journal de Physique, 6, 661-690.

Wesseling, E. B. E. (1996) . Field dependence of the remanent magnetization of silver manganese and copper manganese spin glasses (Doctoral dissertation, University of Minnesota, 1996) . Dissertation Abstracts International - B, 57, AAT 9615188.

Wohlfarth, E. P. (1958) . Relations between different modes of acquisition of the remanent magnetization of ferromagnetic particles. Journal of Applied Physics, 29, 595-596.

Yaskawa, S. & Heath, J. (1990) . Data Storage on Flexible Disks. In C. D. Mee. & E. D. Daniel (Eds.), Magnetic Recording Handbook: technology and applications. (pp.772-811) . McGraw-Hill Inc., New York, 1990.

Zijlstra, H. (1967) . Experimental Methods in Magnetism, 2. Measurement of Magnetic Quantities Selected Topics. In Solid State Physics, 9, (E. P. Wohlfarth, Ed.) Amsterdam: North-Holland Publishing Company.